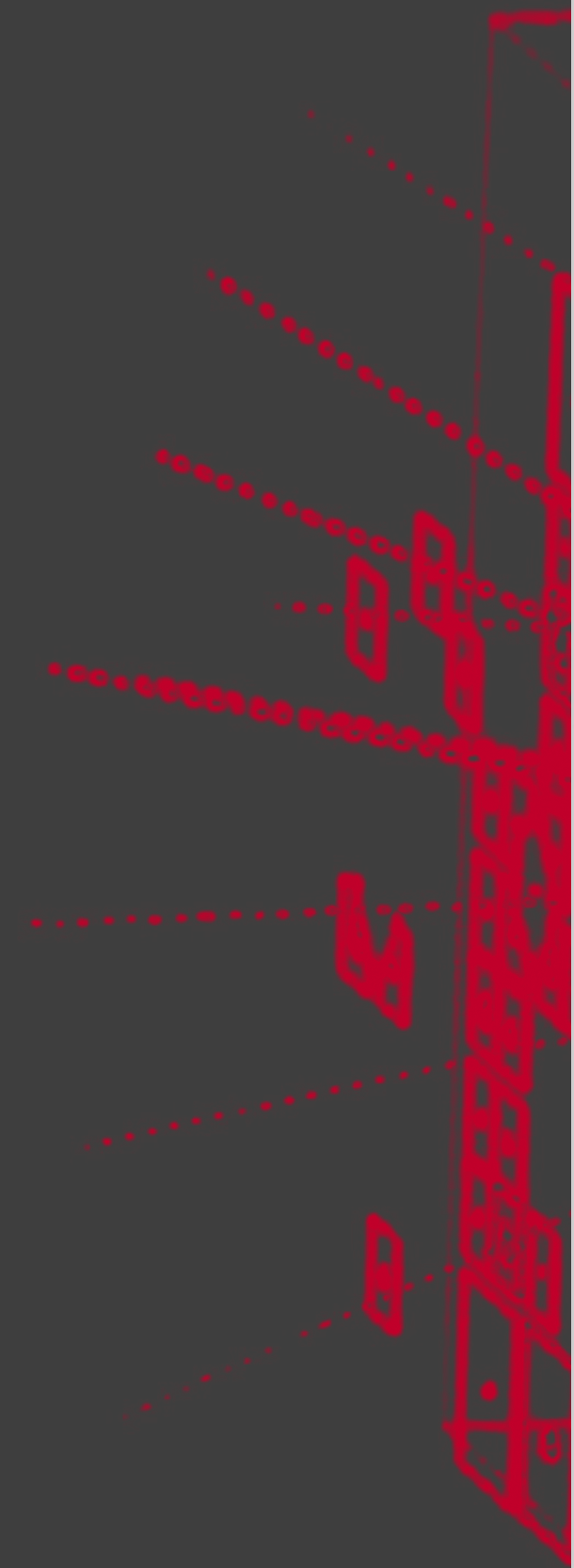

JOHANNES GUTENBERG
UNIVERSITÄT MAINZ

JG|U

Measurement of the W boson mass with the DØ detector and determination of the strong coupling constant with the ATLAS detector

Jakub Cúth

Front cover page: *One of the first recorded Z-boson candidates from 1983. The data were recorded by UA1 detector installed on S$p\bar{p}$S collider in CERN. The plot taken from [1].*

Back cover page: *One of the first measured W-boson candidates from 1982. The data were recorded by UA1 detector installed on S$p\bar{p}$S collider in CERN. The plot is from [2].*

Abstract

A good theoretical description of electroweak boson production in hadronic collisions at high center of mass energies is essential for the measurement of the W boson mass. The DYRES computer program allows for the precise calculation of the relevant production cross section, however, is limited in performance. In this thesis, the DYRES program was significantly improved, leading to a new tool named DYTURBO. In order to test the performance of the DYTURBO program, the transverse momentum spectrum of Z bosons, $p_T(Z)$, produced in proton-proton collisions at a center of mass energy of 13 TeV was measured, using data collected by the ATLAS Experiment at the Large Hadron Collider. Due to the large speed improvements of DYTURBO compared to previous similar theoretical tools, it was possible for the first time to extract the strong coupling constants by fitting the measured $p_T(Z)$ distribution. This approach yields a value of $\alpha_S^{2D}(M_Z^2) = 0.1177 \pm 0.0014_{\text{syst+syst}} \pm 0.0086_{\text{theo}}$, in agreement with other measurements of the ATLAS collaboration. The actual measurement of the W boson mass was developed using data of proton–anti-proton collisions, recorded from 2009 to 2010 at $\sqrt{s} = 1.96$ TeV by the DØ experiment at Tevatron. The W boson mass is extracted using the transverse energy distribution of decay electrons as well as the transverse mass observable, using a novel, two-dimensional fitting technique. The work focused on the estimation of uncertainties due to the limited knowledge of parton density functions, which are the largest theoretical uncertainties of the W boson mass measurement. Since the final W boson mass analysis was not yet approved by the collaboration at the time of the thesis submission, only the expected uncertainty can be made public at this stage. The upcoming measurement of the DØ experiment is expected to have a statistical and systematic uncertainty of 14 MeV and 19 MeV, respectively.

Keywords: Drell-Yan, soft and collinear gluon resummation, W boson mass, strong coupling constant, ATLAS experiment, DØ experiment

Ownership declaration

Hereby I, Jakub Cúth, declare that I have completed the present thesis, entitled: *Measurement of the W boson mass with the DØ detector and determination of the strong coupling constant with the ATLAS detector* independently, making use only of the specified literature and aids. It is entirely the product of my own doctoral work, unless stated otherwise.

In Mainz, 2.3.2018

Signature

Zusammenfassung

Eine gute theoretische Beschreibung der elektroschwachen Prozesse zur Bosonen Produktion in Hadronenkollisionen bei hohen Schwerpunktsenergien ist für die Messung der Masse des W Bosons essentiell. Das DYRES Computerprogramm erlaubt die präzise Berechnung der Wirkungsquerschnitte aller relevanten Prozesse, ist dabei aber nicht sehr performant. Daher wurde im Rahmen dieser Arbeit ein neues Programm, DYTURBO, entwickelt, dass die Performanz signifikant verbessert. Um die Leistungsfähigkeit dieses Programms zu Testen, wurde das Transversalimpuls-Spektrum des Z-Bosons unter Benutzung von Daten, die am ATLAS Detektor am LHC aufgenommen wurden, gemessen. Aufgrund der im Vergleich zu anderen Softwarepaketen hohen Laufzeitverbesserungen durch DYTURBO war es nun das erste Mal möglich die starke Kopplungskonstante durch Fitten des oben genannten Spektrums zu extrakhieren. Diese Methode ergab einn Wert von $\alpha_S^{2D}(M_Z^2) = 0.1177 \pm 0.0014_{\text{syst+syst}} \pm 0.0086_{\text{theo}}$, der mit anderen ATLAS Messungen übereinstimmt. Die eigentliche Messung der W Boson Masse wurde anhand von Tevatron Daten mit einer Schwerpunktsenergie von $\sqrt{s} = 1.96$ TeV am DØ Experiment entwickelt. Die W Boson Masse wurde unter Nutzung der Transversalenergieverteilung zerfallender Elektronen und der Transversalmassen-Observable bestimmt. Dabei wurde eine neue, zweidimensionale Fitmethode verwendet. Diese Arbeit spezialisiert sich auf die Abschätzung sysmtematischer Unsicherheiten aufgrund des begrenzten Wissens der Parton-Verteilungsfunktion, was die größte theoretische Unsicherheit bei der Messung der W Boson Masse darstellt. Da die Analyse zur Zeit des Einreichens dieser Arbeit noch nicht von der ATLAS Kollaboration angenommen wurde, können hier nur vorläufige Unsicherheiten veröffentlich werden. Die kommende Messung am DØ Experiment werden vorrausichtlich eine statistische und systematische Unsicherheit von 14 MeV beziehungsweise 19 MeV haben.

Contents

1 Introduction **2**

I Common theoretical and instrumental concepts **4**

2 Vector boson production at hadronic collisions **6**
2.1 Standard Model particles and their interaction . . . 7
2.2 Born level considerations . . . 11
2.3 Higher orders and resummation . . . 13
2.3.1 Fixed order calculation . . . 14
2.3.2 Soft and colinear gluon resummation . . . 15

3 Hadron colliders and their detectors **20**
3.1 Tevatron . . . 22
3.2 DØ Detector . . . 24
3.2.1 Inner tracker detector and solenoidal magnet . . . 25
3.2.2 Electromagnetic and hadronic calorimeters . . . 27
3.2.3 Muon chambers and toroidal magnet . . . 29
3.2.4 Single electron trigger . . . 30
3.2.5 Event reconstruction . . . 31
3.3 LHC . . . 33
3.4 ATLAS . . . 35
3.4.1 Inner detector and solenoidal magnet . . . 36
3.4.2 Electromagnetic and hadronic calorimeters . . . 37
3.4.3 Muon chambers and toroidal magnet . . . 38
3.4.4 Trigger system . . . 40
3.4.5 Reconstruction of event data . . . 41

II Precision measurements at hadron colliders **44**

4 Development of Drell-Yan integrator **46**
4.1 Available Tools for Vector Boson Predictions . . . 46
4.2 Calculation Strategy and Speed Improvement . . . 49
4.3 Benchmark and Validation . . . 53

5 Detemination of strong coupling constant **60**
5.1 Measurement Strategy . . . 60
5.2 Measurement of Transverse Momentum of Z bosons . . . 67
5.2.1 Signal Selection . . . 67
5.2.2 Used Samples and Background Estimations . . . 70
5.2.3 Detector Level Corrections . . . 72
5.2.4 Measured p_{T}^{Z} and Unfolding to Fiducial Level . . . 77
5.3 Estimation of Strong Coupling Constant . . . 83

6 Measurement of W-boson mass **88**
6.1 Template fit of W boson mass . . . 88
6.2 Event modeling . . . 90
6.3 Estimation of the modeling uncertainties . . . 92
6.3.1 Boson p_{T}-shape uncertainty . . . 92
6.3.2 PDF uncertainty . . . 95
6.3.3 PDF profiling . . . 99
6.4 Detector level parametrization and experimental uncertainties . . . 101
6.5 Data samples and event selection . . . 104
6.5.1 Common selection criteria . . . 105
6.5.2 Selection of $Z \to ee$ events . . . 106
6.5.3 Selection of $W \to e\nu$ events . . . 108
6.6 Results of W boson mass fit . . . 113
6.7 Preservation of W boson mass analysis for future revaluation . . . 115

7 Conclusion **120**

Acknowledgement **123**

III Appendix **126**

References **143**

List of Figures **150**

List of Tables **152**

List of Abbreviations **159**

A ATLAS p_{T}^{Z} control distributions **160**

B W mass control plots **163**
B.1 Comparison of data from RunIIb3 with CTEQ6.6 . . . 163
B.2 Comparison of data from RunIIb3 with CT14nnlo . . . 170

C W boson mass theory uncertainty plots **177**
C.1 Uncertainty estimated from CTEQ6.6 . . . 177
C.2 Uncertainty estimated from CTEQ6.6 profiled . . . 178
C.3 PDF CT14nnlo . . . 180

D CTEQ 6.6 profiling control plots **182**

1. Introduction

One of the most important characteristic of a scientist is his curiosity and the gift to ask the right questions at the right time. The right questions cannot only lead to new answers, but help to focus on the important aspects. An famous example was brought up by Richard P. Feynman in the second section of his lectures on physics [3], where he asks: *"If . . . only one sentence were to be passed on to next generations of creatures, what statement would contain the most information in the fewest words?"* and gives directly the answer *". . . all things are made of atoms – little particles that move around in perpetual motion, attracting each other when they are a little distance apart, but repelling upon being squeezed into one another."*

The majority of scientific fields are focused on consequences of this statement, e.g. chemistry, thermodynamics or material engineering. This thesis, however, is connected to the underlying theory of this statement, i.e. the Standard Model (SM) of particles physics. Developed in the late 1970's, the Standard Model describes phenomena at sub-atomic distances by a mathematical tool known as quantum field theory. It describes the universe around us by twelve matter particles and included a mathematical consistent description of three fundamental interactions, known as the strong force, the weak force as well as the electromagnetic force. Up to now, no consistent formulation of gravity in the framework of quantum field theories has been possible. With the pioneering work of Glashow [4] and Salam [5] in 1959 and Weinberg [6] in 1967, the electromagnetic- and the weak-interaction were unified in a common underlying force, known as electroweak interaction. This force is mediated by the exchange of the three elementary particles, namely the electroweak gauge bosons, $W^{\pm}$, Z and γ.

This thesis aims for a precision measurement of the $W^{\pm}$ boson mass, which is an important parameter to test the consistency of the electroweak sector of the Standard Model. Since the hadron collisions and the subsequent production of W bosons are described by the strong interaction, a large part of this thesis is devoted to further developments on the prediction of the electroweak boson production at hadron colliders. As a result of these studies, a new approach for the extraction of the strong coupling constant was implemented and tested.

This thesis is divided into two main parts. The first part contains a general introduction to particle physics with a special focus on the production of vector bosons (Chapter 2) and a description of the experimental setup used for the measurements in this work (Chapter 3). The second part focusses on the main analyses aspects and the corresponding results, i.e. the Drell-Yan integrator development (Chapter 4), the estimation of the strong coupling constant (Chapter 5) and the measurement of the W boson mass (Chapter 6). The thesis concludes in Chapter 7.

Part I

Common theoretical and instrumental concepts

2. Vector boson production at hadronic collisions

For precision measurements in the electroweak sector at hadron colliders it is not only necessary to precisely understand the detector but also to calculate the fully-differential cross section of the Drell-Yan process. The latter, i.e. the modeling and the calculation of the vector boson production, is described in this chapter. As a first step, the basic definition and the general notation, used in this thesis, is introduced. This is followed by an introduction to the particles and interactions of the quantum field theory of particle physics – Standard Model (SM) in Section 2.1. The following two sections (Section 2.2 and Section 2.3) describe the leading order calculations of Drell-Yan as well as higher order correction, respectively.

General notation remarks

Two- or three-dimensional vectors are noted with arrows, i.e. $\vec{p} = (p_x, p_y, p_z)$ while the absolute size of this vector written without arrow, i.e. $p \equiv ||\vec{p}||$. A four-vector in Minkowski space represented by a greek letter as superscript p^μ, unless otherwise stated. The size of a four-vector is noted without any index, i.e. $p \equiv ||p^\mu|| = \sqrt{p_\mu p^\mu}$. The size of the momentum four-vector is equivalent to the invariant mass $m^2 \equiv p^2 = E^2 - \vec{p}^2$.

In case of two colliding particles with same momentum it is convenient to define observables in laboratory system i.e. the rest frame of colliding particles. The plane perpendicular to axis of the collision is called transverse plane. The momentum projected into this plane is called transverse momentum and it is denoted by low index "T"; the symbol p_T is used for final particles, while the symbol q_T is used for transverse momentum of a vector boson. The angle of the momentum in transverse plane is called azimuthal angle and usually noted as ϕ. The longitudinal angle θ is defined as angle between particle's momentum and the collision axis. A commonly used observable. which depends on longitudinal angle, is the rapidity defined as

$$y = \ln\left(\frac{E + p_z}{E - p_z}\right) , \tag{2.1}$$

The rapidity is equivalent to the pseudo-rapidity, η, for particles with momentum much larger then their invariant mass ($m \ll p$). It is defined by:

$$\eta = -\ln\tan\frac{\theta}{2} \tag{2.2}$$

In all Feynman diagrams shown in this thesis, the time axis is from the left towards to the right hand side. Fermion legs and propagators are shown as solid oriented lines, vector boson legs and propagators are shown as waved solid lines, scalar boson legs and propagators are shown as dashed line and gluon legs and propagators are shown as curled solid lines.

The lower case letters s, t, u are reserved for Lorentz-invariant Mandelstam variables [7], unless otherwise stated. In case of two-by-two collisions with four-momenta p^μ and indices of participants $1 + 2 \to 3 + 4$ the Mandelstam variables are defined by

$$\begin{aligned} s &= (p_1^\mu + p_2^\mu)^2 = (p_3^\mu + p_4^\mu) \\ t &= (p_1^\mu - p_3^\mu)^2 = (p_2^\mu - p_4^\mu) \\ u &= (p_1^\mu - p_4^\mu)^2 = (p_2^\mu - p_3^\mu) \, . \end{aligned} \tag{2.3}$$

In the following, the symbols γ^μ are reserved for four-by-four Dirac gamma matrices $\mu \in 0, 1, 2, 3$. The shorthand notation for the product of gamma matrices is given by $\gamma^5 \equiv i\gamma^0\gamma^1\gamma^2\gamma^3$, where index 5 is a remnant from notation, where time-component 0 had index 4.

2.1 Standard Model particles and their interaction

The electromagnetic interaction of elementary particles is successfully described by a relativistic quantum field theory known as quantum electron dynamics (Quantum Electrodynamics (QED)), developed in the middle of last century [8, 9, 10]. In the last 1970's, the electromagnetic force and the weak force have been unified, i.e. described within one theoretical framework, known as the electroweak (quantum field theory of electromagnetic and weak interaction (Electroweak)) Standard Model.

The Electroweak theory [6, 11] is based on a $SU(2) \times U(1)$ gauge symmetry group with four gauge bosons and two dimensionless coupling constants g, g'. This symmetry is spontaneously broken in nature, which is described by Brout-Engler-Higgs mechanism [12, 13]. This mechanism introduces (in the minimal valid model) one neutral massive scalar field, known as the Higgs field with one associated boson H, i.e. the Higgs Boson. The boson H was first detected by the A Thoroidal LHC AparatuS (ATLAS) and the CMS collaborations in 2012 [14, 15], and allowed for the measurement of its mass as the last missing parameter of the SM.

After symmetry breaking, the massless gauge bosons are mixed into two charged massive fields, $W^\pm$, one neutral massive field Z as well as one neutral massless field A (i.e. photon field γ). The Lagrangian describing the electroweak interaction with fermion fields ψ_i with flavour i can be written as

$$L = \sum_i \bar{\psi}_i \left(i\partial\!\!\!/ - m_i - \frac{m_i H}{v} \right) \psi_i \tag{2.4}$$

$$- e \sum_i Q_i \bar{\psi}_i \gamma^\mu \psi_i A_\mu \tag{2.5}$$

$$- g \frac{g}{2\cos\theta_W} \sum_i \bar{\psi}_i \gamma^\mu (g_{V,i} - g_{A,i}\gamma^5) \psi_i Z_\mu \tag{2.6}$$

$$- \frac{g}{2\sqrt{2}} \sum_i \bar{\Psi}_i \gamma^\mu (1 - \gamma^5)(T^+ W_\mu^+ + T^- W_\mu^-) \Psi_i \tag{2.7}$$

$$\tag{2.8}$$

where m_i are masses of fermions and Q_i are the charges of the fermions. The positron charge e is used as unit of the electric charge in this work unless stated otherwise. The weak mixing angle θ_W is defined here by the relation $\tan\theta_W \equiv \frac{g'}{g}$.

There are three families of fermion fields, which transform as lepton and quark doublets

$$\Psi_i = \underbrace{\begin{pmatrix} \nu_i \\ \ell_i \end{pmatrix}}_{\text{leptons}} \text{ and } \underbrace{\begin{pmatrix} u_i \\ \sum_j V_{ij} d_j \end{pmatrix}}_{\text{quarks}}, \tag{2.9}$$

where the charged massive leptons ℓ_i are electrons e, muons μ and taus τ with the corresponding massless neutral neutrinos $\nu_i = \nu_e, \nu_\mu, \nu_\tau$. The quarks u_i with electric charge $+2/3$ are called up u, charm c, top t , while the quarks d_i with electric charge $-1/3$ are named down d, strange s and bottom b. The term V_{ij} represents the elements of the Cabibbo-Kobayashi-Maskawa mixing matrix (CKM) matrix [16, 17].

The coupling of fermions with flavour i to the neutral weak boson is modified by

vector and axial-vector coupling constants

$$g_{V,i} = t_i - 2Q_i \sin^2 \theta_W \tag{2.10}$$

$$g_{A,i} = t_i \ , \tag{2.11}$$

where the weak isospin of fermions t_i has values of $+1/2$ for u_i and ν_i, and $-1/2$ for d_i and ℓ_i.

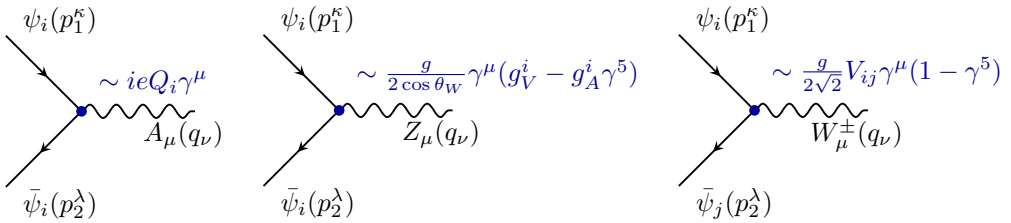

Figure 2.1: *Feynman diagrams for interaction vertices of electroweak bosons and fermions.*

The basic vertices of the fermion electroweak interactions are described by the diagrams shown in Figure 2.1. The first two diagrams Figure 2.1 (a,b) correspond to two terms in Equation 2.5 and Equation 2.6, respectively. They are describing the neutral electroweak current, which conserves the flavour of the interacting fermions. Due to the interference term, it is not possible to distinguish between the production of an off-mass-shell photons and the production of a Z boson. Therefore, these two processes are often noted together as $f\bar{f} \to Z/\gamma^*$ and theoretical predictions are calculated considering both contributions.

The last diagram in Figure 2.1 (c), corresponds to the last term of Equation 2.7 and it describes the charged, flavour changing, electroweak current. The flavour mixing term V_{ij} is equal to one for leptons $i = \ell$ and the corresponding neutrino $j = \nu_\ell$ pair. In case of quark – anti-quark annihilation, the term V_{ij} corresponds to one element of the CKM matrix. The vector bosons γ, W, Z are denoted by the symbol V for the charge-independent statement.

With help of the above described vertices (Figure 2.1), the partial width for leptonic decays of vector bosons can be expressed on tree-level as

$$\Gamma(W^- \to \ell\bar{\nu}) = \frac{G_F M_W^3}{6\sqrt{2}\pi} \tag{2.12}$$

$$\Gamma(Z \to \ell\bar{\ell}) = \frac{G_F M_Z^3}{6\sqrt{2}\pi} \left(g_{V,\ell}^2 + g_{A,\ell}^2\right) \tag{2.13}$$

where the Fermi constant G_F [18] describes the coupling of the effective four-fermion interaction at energies much lower than boson mass $s \ll M_V^2$. The relation $G_F/\sqrt{2} = g^2/8M_W^2$ [7] relates the Fermi constant to the fundamental parameters of Electroweak theory.

The electroweak bosons studied in this thesis are produced in collisions of two hadrons. Hadrons are composite objects, described in the most simplest model by three quarks (baryons), three anti-quarks (anti-baryon) or a pair of quark and anti-quark (meson). The quarks and anti-quarks are interacting via the strong interaction. By the experimental study of hadrons, it was concluded that the strong interaction can be described by the exchange of internal quantized charge called color. Each

(anti-)quark is a carrier of (anti-)color charge. The color charge exchange is mediated by a massless bosons called gluons. The hadrons itself are in nature observed as color singlet (colorless) states. The theory of the strong interaction, called quantum chromo dynamics (quantum field theory of the strong interaction – Quantum Chromodynamics (QCD)) is also a quantum field theory and was formulated for the first time by Harald Fritzch, Heinrich Leutwyler and Murray Gell-Mann in 1973 [19] using a general field theory approach, developed by Chen-Ning Yang and Robert Mills in 1950s[20].

QCD is based on the $SU(3)$ symmetry gauge group, with quarks carrying one of $N_C = 3$ color charges as fundamental representation of this group. The transformation of gluon fields $\mathcal{G}_\mu^C$ is described by the adjoined representation of $SU(3)$. There are eight gluon fields with index C, having values from one to $N_C^2 - 1 = 8$. The generators of the SU(3) group are marked by t_{ab}^C and they are represented by eight 3×3 matrices. The QCD Lagrangian can be schematically written in form [7]

$$L_{\text{QCD}} = \sum_q \bar{\psi}_{q,a} \left(i\gamma^\mu \partial_\mu \delta_{ab} - \frac{\alpha_S}{4\pi} \gamma^\mu t_{ab}^C \mathcal{G}_\mu^C - m_q \delta_{ab} \right) \psi_{q,b} - \frac{1}{4} F^{A,\mu\nu} F_{\mu\nu}^A \,, \tag{2.14}$$

where quark spinors are described by $\psi_{q,a}$ with flavour q color charge a and corresponding mass m_q. It is evident from the Lagrangian that the strong interaction conserves the flavour of quarks. The color dynamics $a \to b$ is represented by term with generators t_{ab}^C. The field tensor $F_{\mu\nu}^A$ is given by

$$F_{\mu\nu}^A = \partial_\mu \mathcal{G}_\nu^A - \partial_\nu \mathcal{G}_\mu^A - \frac{\alpha_S}{4\pi} f_{ABC} \mathcal{G}_\mu^B \mathcal{G}_\nu^C \,, \tag{2.15}$$

where the structure constant of $SU(3)$ group is marked as f_{ABC} and defined by anti-commutator as $if_{ABC}t^C = [t^A, t^B]$. Thanks to the last term on right hand side of Equation 2.15, QCD contains three-gluon and four-gluon vertices, which is the largest difference compared to QED, where photons are not interacting with each other.

There are seven free parameters in QCD: six masses of quarks m_q and dimensionless structure constant α_S representing the strength of strong force. The renormalization group equations for these parameters are given by

$$\frac{\mathrm{d}\alpha_S}{\mathrm{d}t} = -\alpha_S^2 \left(\beta_0 + \beta_1 \frac{\alpha_S}{4\pi} + \beta_2 \left(\frac{\alpha_S}{4\pi} \right)^2 + \dots \right) \tag{2.16}$$

$$\frac{\mathrm{d}m^2}{\mathrm{d}t} = -4\pi m^2 \left(\gamma_0 \frac{\alpha_S}{\pi} + \gamma_1 \left(\frac{\alpha_S}{\pi} \right)^2 + \dots \right) \tag{2.17}$$

where the coefficients β_i and γ_i are known up to 3-loop precision [21]. The expansion is done in terms of $t = \frac{1}{4\pi} \log \frac{\mu^2}{\mu_0^2}$, with μ_0 representing reference point of the chosen scale. Even though, the value of α_S is rather large compared to weak and electromagnetic couplings it still possible to use perturbation theory in terms of α_S, when the involved energies are sufficiently large. The expansion is done in terms of the running coupling $\alpha_S(\mu_\mathsf{R}^2)$ at the renormalization scale μ_R in order to handle ultraviolet divergences in finite order calculations.

The coupling $\alpha_S(\mu_\mathsf{R}^2)$ is not a direct observable and depends on energy scale μ_R of studied process. Many experimental observables are used to determine α_S using next-to-next-to leading order (NNLO) perturbative calculations (see Figure 2.2), but most of them are extracting $\alpha_S(M_Z^2)$ in the $(10^1\text{-}10^3)$ GeV region. The energy regime with the currently highest experimental sensitivity on α_S is the region between $(2\text{-}10)$ GeV (see Chapter 5).

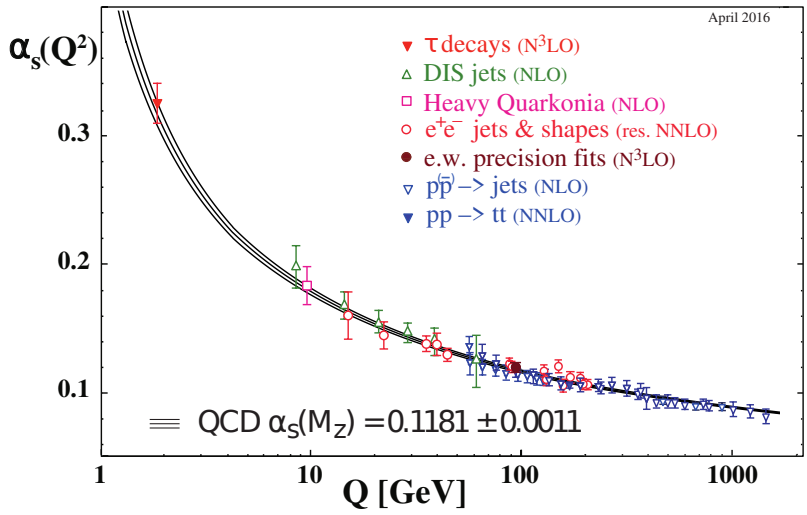

Figure 2.2: *The list of α_S measuements with respect to scaled of studied process. The plot is from [7].*

Following the perturbation theory, the cross section can be expanded into series in powers of $\alpha_S(\mu_R^2)$, i.e.

$$\mathrm{d}\sigma_{ab} = \mathrm{d}\sigma_{ab}^0 + \frac{\alpha_S(\mu_R^2)}{\pi}\mathrm{d}\sigma_{ab}^0 + \left(\frac{\alpha_S(\mu_R^2)}{\pi}\right)^2 \mathrm{d}\sigma_{ab}^0 + \dots \,, \tag{2.18}$$

where terms $\mathrm{d}\sigma_{ab}^i$ for the electroweak boson production are discussed in detail later, starting from the lowest order (or born cross section) $\mathcal{O}\left(\alpha_S^0\right)$ and followed by higher orders corrections.

Perturbative QCD calculations are not applicable for the description of the momentum distributions of quarks and gluons inside of hadrons. Therefore the parton model [22, 23] has to be used. In this model, a momentum p_i^μ of the interacting quarks or gluons (partons) is described as the fraction of the colliding hadron momentum P_i^μ

$$p_i^\mu = x_i P_i^\mu \,, \tag{2.19}$$

where x_i is known as Björken-x and has values between 0 and 1. The probability of finding a parton of flavour a with a momentum fraction x in the hadron h at energy scale μ_F is described by the parton density functions (Parton Distribution Function (PDF)) $f_{a/h}(x, \mu_F^2)$, which have to be estimated experimentally.

The mechanism of the massive lepton pair production in hadron collision using the parton model was described for the first time by Sidney David Drell and Tung-Mow Yan [24] in 1970. This reaction (Equation 2.20) is known as Drell-Yan and it plays a crucial role for precision studies of QCD phenomena. The particle mediating the momentum transfer in the following reaction is electroweak vector boson marked by V:

$$h_1(P_1^\alpha) + h_2(P_2^\beta) \to V(q^\kappa) + X \to \ell_3(p_3^\mu) + \ell_4(p_4^\nu) + X(p_{5,\dots}^\rho) \tag{2.20}$$

The reaction is represented as Feynman diagram in Figure 2.3, where fermions are depicted by solid lines, vector bosons by wavy lines and gluons by curly lines. Symbol X represents the underlying event, i.e. the hadronic activity from the Drell-Yan scattering residuals and from different reactions than the primary Drell-Yan scattering.

The neutral and charged electroweak currents occurs in hadron collisions in a folded manner, i.e. the protons and (anti-)protons are interacting via their partons.

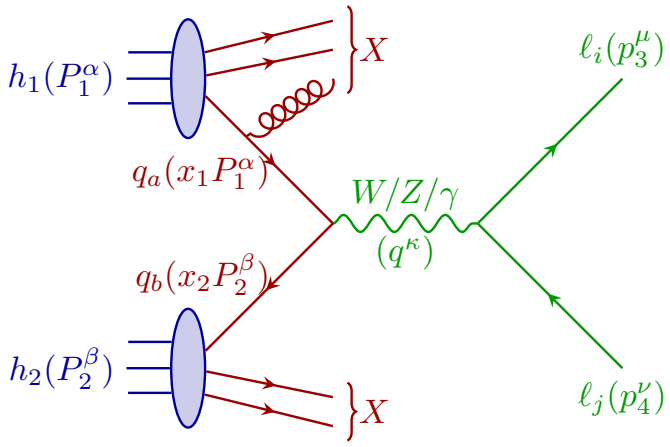

Figure 2.3: *Diagram of the vector boson $W/Z/\gamma$ production in collision of two hadrons $h_{1,2}$ and its decay to lepton pairs $\ell_{i,j}$. The four-momenta of interacting partons $q_{a,b}$ are defined by the four-momenta of colliding hadrons $P_{1,2}^{\alpha,\beta}$ and the fraction $x_{1,2}$. The four-momentum of intermediating boson and four-momenta of leptons are denoted by q^κ and $p_{3,4}^{\mu,\nu}$, respectively. The latin indices a, b, i, j represents the fermion flavour and greek indices α, β, μ, ν represent the bispinor space.*

Using factorization theorem, the fully differential cross section $\mathrm{d}\sigma_{h_1 h_2}$ of the Drell-Yan process can be written as

$$\frac{\mathrm{d}\sigma_{h_1 h_2}}{dp_3^\mu dp_4^\nu} = \sum_{a,b} \int_0^1 \mathrm{d}x_1 \int_0^1 \mathrm{d}x_2 f_{a/h_1}(x_1, \mu_\mathsf{F}^2) f_{b/h_2}(x_2, \mu_\mathsf{F}^2) \frac{\mathrm{d}\hat{\sigma}_{ab}}{dp_3^\mu dp_4^\nu} \,, \tag{2.21}$$

where the cross section $\mathrm{d}\hat{\sigma}_{ab}$ is called partonic cross section. It represents in some sense the probability of vector boson production from the interaction of two incoming partons with respect to the four-momenta $p_{3,4}^\mu$ of the final state leptons. Hence, it is necessary to include the contributions from all possible combinations of all quarks, anti-quarks flavours as well as gluons. This is represented by a sum over flavours a and b in Equation 2.21. The integration over the corresponding Björken-x values in the parton distribution functions takes into account all possible momenta of interacting partons for the final cross section.

In following sections the calculation of Drell-Yan cross section will be described using perturbative QCD as well as the factorization theorem.

2.2 Born level considerations

The leading order Drell-Yan (tree level diagram) calculation has no QCD vertex. Therefore, the calculation of the vector boson production from two interacting partons at leading order is $\mathcal{O}\left(\alpha_s^0\right)$ and the calculation is based purely on electroweak vertices (Figure 2.1).

The QED calculation of muon pair production in electron–positron annihilation $e\bar{e} \to \mu\bar{\mu}$[25] can be used as starting point for the calculation of the process $q\bar{q} \to \ell\bar{\ell}$ at electroweak leading order. The differential cross section, assuming a photon as the mediator, can be expressed as

$$\frac{\mathrm{d}\sigma^{0\gamma}(q\bar{q} \to \ell\bar{\ell})}{\mathrm{d}\Omega_{\mathsf{CMS}}} = \frac{\alpha^2 Q_q^2}{4\hat{s}}(1 + \cos\theta) \,, \tag{2.22}$$

with Q_q as the electric charge of the involved quarks. However, this is not the complete calculation in case of the Drell-Yan process, since also the Z boson contribution has to be taken into account. The vertices defined in Figure 2.1 are applied to the calculation of the $e\bar{e} \to \mu\bar{\mu}$ process. The tree-level cross section for the processes $q\bar{q} \to \ell\bar{\ell}$ has therefore an additional Z boson term, i.e.

$$\frac{\mathrm{d}\sigma^{0Z}(q\bar{q} \to \ell\bar{\ell})}{\mathrm{d}\Omega_{\mathsf{CMS}}} = \frac{\alpha^2 \hat{s}}{4\left[(\hat{s} - M_Z^2)^2 + M_Z^2\Gamma_Z^2\right]} \cdot \cdot \left[(g_{V,\ell}^2 + g_{A,\ell}^2)(g_{V,q}^2 + g_{A,q}^2)(1 + \cos^2\theta) + 8 g_{V,\ell} g_{A,\ell} g_{V,q} g_{A,q} \cos\theta\right] . \tag{2.23}$$

It is necessary to include the Z and γ interference in the calculation, leading to

$$\frac{\mathrm{d}\sigma^{0Z\gamma}(q\bar{q} \to \ell\bar{\ell})}{\mathrm{d}\Omega_{\mathsf{CMS}}} = \frac{\alpha^2 Q_q (\hat{s} - M_Z^2)}{2\left[(\hat{s} - M_Z^2)^2 + M_Z^2\Gamma_Z^2\right]} \left[g_{V,\ell}^2 g_{V,q}^2 (1 + \cos^2\theta) + 2 g_{A,\ell} g_{A,q} \cos\theta\right] , \tag{2.24}$$

The total born cross section of process $q\bar{q} \to Z/\gamma^* \to \ell\bar{\ell}$ is consequently a sum of above mentioned terms

$$\frac{\mathrm{d}\sigma^{0}(q\bar{q} \to Z/\gamma^* \to \ell\bar{\ell})}{\mathrm{d}\Omega_{\mathsf{CMS}}} = \frac{\mathrm{d}\sigma^{0\gamma}(q\bar{q} \to \ell\bar{\ell})}{\mathrm{d}\Omega_{\mathsf{CMS}}} + \frac{\mathrm{d}\sigma^{0Z}(q\bar{q} \to \ell\bar{\ell})}{\mathrm{d}\Omega_{\mathsf{CMS}}} + \frac{\mathrm{d}\sigma^{0Z\gamma}(q\bar{q} \to \ell\bar{\ell})}{\mathrm{d}\Omega_{\mathsf{CMS}}} \tag{2.25}$$

In reactions with a W boson as mediator, there is no γ^* interference term and the cross section is proportional to $q\bar{q} \to Z \to \ell\bar{\ell}$ Equation 2.23, however, with few differences. The first difference is the possible change of flavour, which is quantified by the CKM matrix. Each entry of the matrix corresponds to a quark flavour change $q_i \to \bar{q}_j$. The second difference is due to the vector boson itself, where its mass and width are substituted $M_Z \to M_W$, $\Gamma_Z \to \Gamma_W$ and no further axial-vector contribution to the cross section is further assumed.

$$\frac{\mathrm{d}\sigma^{0W}(q_i\bar{q}_j \to \ell\nu)}{\mathrm{d}\Omega_{\mathsf{CMS}}} = \frac{\alpha^2 \hat{s}}{4\left[(\hat{s} - M_W^2)^2 + M_W^2\Gamma_W^2\right]} (1 + \cos^2\theta) \tag{2.26}$$

The differential cross section is written in terms of the spatial angle $\Omega_{\mathsf{CMS}} = \phi \cos\theta$, which represents the direction of the final state leptons in the center of mass frame. Starting from Eq. 2.22-2.26 the cross section can be written in terms of

$$\mathrm{d}\sigma \approx 1 + A_4 \cos\theta + \cos^2\theta , \tag{2.27}$$

where the coefficient A_4 depends on the vector and axial-vector coupling between a Z boson and fermions, which is sensitive to $\sin^2_W$.

The resonant behaviour of the cross section with respect to the mass of intermediating boson M_V in Equation 2.23 is represented by Breit-Wigner [26] function

$$\frac{1}{4\left[(\hat{s} - M_V^2)^2 + M_V^2\Gamma_V^2\right]}, \tag{2.28}$$

where M_V, Γ_V is the mass and width of boson and $\hat{s}$ is the partonic Mandelstam variable of the event. This term can be completely factorized out from all orders of the QCD calculation.

At leading order, the vector bosons have no transverse momentum other than the intrinsic transverse momentum k_T of the partons within the proton. This intrinsic k_T is typically small, i.e. in the order of $< k_{\mathrm{T}} > \sim 0.70$ GeV. Further contributions to the vector boson transverse momentum q_{T} are due to the emissions of addition partons, appearing in higher order QCD calculations.

2.3 Higher orders and resummation

In the previous section, the born level process of the vector boson production in hadronic collisions was described without any explicit contribution of the strong interaction in the initial reaction, i.e. the corresponding order in terms of powers of α_S was $\mathcal{O}\left(\alpha_S^0\right)$. In order to improve the precision of the cross section calculation of a given processes, higher order corrections to the born-level process have to be taken into account.

The fixed order calculation of the vector boson production in hadronic collisions is described by Equation 2.20, where one or more additional partons are radiated from the initial quark or gluon states. Such process at Leading order (LO) is $\mathcal{O}\left(\alpha_S\right)$ and referred as LO vector boson plus jet (Vj) process. Consequently, Next-to-Leading order (NLO) Vj is a process of $\mathcal{O}\left(\alpha_S^2\right)$.

A summary of fixed order diagrams and their corresponding order $\mathcal{O}\left(\alpha_S^n\right)$ is shown in Table 2.1. Example diagrams of the Vj calculation up to $\mathcal{O}\left(\alpha_S^2\right)$ are shown in Figure 2.4. The quarks, gluons and α_S vertices are indicated as blue for LO, light blue for NLO and faint blue for Next-to-Next-to-Leading order (NNLO) in the corresponding diagrams.

Order	Process	Note
$\mathcal{O}\left(\alpha_S^0\right)$:	$q + \bar{q} \to V$	born level Figure 2.4 (a)
$\mathcal{O}\left(\alpha_S^1\right)$:	$q + \bar{q} \to V$	one loop correction Figure 2.4 (a)
	$q + \bar{q} \to V + g$	Vj LO Figure 2.4 (b)
	$q(\bar{q}) + g \to V + q(\bar{q})$	Vj LO Figure 2.4 (c)
$\mathcal{O}\left(\alpha_S^2\right)$:	$q + \bar{q} \to V$	two-loop correction Figure 2.4 (a)
	$q + \bar{q} \to V + g$	one-loop correction Figure 2.4 (b)
	$q + \bar{q} \to V + g + g$	Vjj LO
	$q(\bar{q}) + g \to V + q(\bar{q})$	one-loop correction Figure 2.4 (c)
	$q(\bar{q}) + g \to V + q(\bar{q}) + g$	Vjj LO
	$q + \bar{q} \to V + q + \bar{q}$	Vjj LO
	$q(\bar{q}) + q(\bar{q}) \to V + q(\bar{q}) + q(\bar{q})$	Vjj LO
	$gg \to V + q + \bar{q}$	Vjj LO

Table 2.1: *List of fixed order calculation diagrams up to $\mathcal{O}\left(\alpha_S^2\right)$. Taken from [27].*

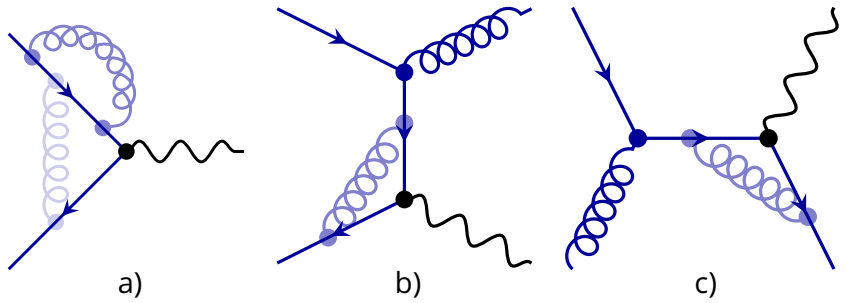

Figure 2.4: *Example of diagrams contributing to born level (a), boson and gluon (b), boson and quark (c). The leading order is indicated as blue, one-loop correction as light blue and two-loop correction as faint blue. The Electroweak vertex and boson are shown as black.*

2.3.1 Fixed order calculation

To calculate a spectrum of non-zero transverse momentum of the intermediate boson (q_{T}) it is necessary to include real emission of jets and virtual loops into the partonic cross section. Within perturbation theory this is achieved by including all possible Feynman diagrams. The momentum of emitted partons is balanced by the momentum of the vector boson. The challenging part of the calculation is the region of small q_{T}, where the effect of multiple soft and collinear gluon emission is driving the boson momentum.

The angular distributions of the final state leptons provide information about the production mechanism. These distributions are experimentally well defined and they can be measured with good precision. Since the partons entering to the vector boson production vertex are not measurable, the suitable reference frame needs to be chosen. The problem lies in the fact that the direction of incoming quarks nor their transverse momentum is known. Therefore, the rest frame of the vector boson is chosen to reduce the impact of the boson momentum on angular distributions. The so-called Collins-Soper frame allows for a unique definition on the orientation of the rest frame.

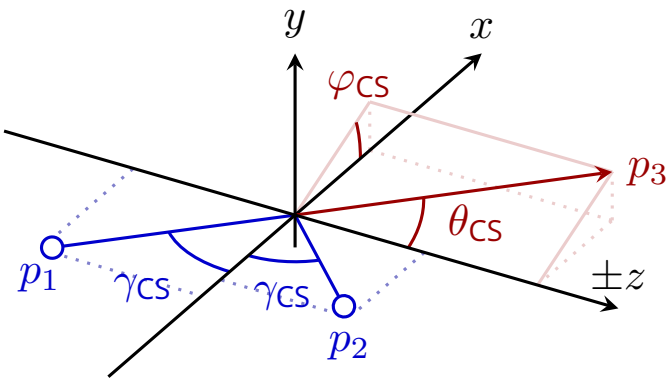

Figure 2.5: *Illustration of Collins-Soper frame. Blue lines represents the incoming partons, red vectors represents the outgoing lepton. The other lepton momentum vector is symmetric with respect to origin of coordinates.*

The Collins-Soper frame is the rest frame of vector boson, where the z-axis was chosen to be perpendicular to the bisector of the angle $2\gamma_{\mathrm{CS}}$ between incoming partons [28]. The incoming partons create a plane, which can be chosen to be the xz-plane

without loss of any generality. Therefore, the vector of total recoil momentum also lies in this plane. The lepton momenta have the same size and direction but opposite sign, therefore, it is sufficient to describe one of the leptons by two angles. The polar angle θ_{CS} is defined as angle between lepton momentum vector and z-axis; the azimuthal ϕ_{CS} angle defined as angle between lepton momentum vector and xz-plane.

The lepton momentum vector $\vec{p}_3^{\,\text{CS}}$ in Collins-Soper frame is then calculated by

$$\begin{aligned} p_{3,x}^{\text{CS}} &= \frac{1}{2}\frac{M_V}{\sqrt{M_V^2 + q_{\text{T}}^2}}(2p_{3,x} - q_{\text{T}}) \,, \\ p_{3,y}^{\text{CS}} &= p_{3,y} \,, \\ p_{3,z}^{\text{CS}} &= \pm\frac{M_V}{2}\sqrt{1 - \frac{(p_{3,x}^{\text{CS}})^2 + (p_{3,y}^{\text{CS}})^2}{M_V^2/4}} \,. \end{aligned} \tag{2.29}$$

The Collins-Soper angles are calculated from lepton momentum $\vec{p}_3^{\,\text{CS}}$ by

$$\begin{aligned} \varphi_{\text{CS}} &= \arctan\left(\frac{p_{3,y}^{\text{CS}}}{p_{3,x}^{\text{CS}}}\right) \,, \\ \cos\theta_{\text{CS}} &= \frac{||\vec{p}_3^{\,\text{CS}}||}{p_{3,z}^{\text{CS}}} \,. \end{aligned} \tag{2.30}$$

Higher order calculations of the lepton angular distributions are non-trivial due to helicity and polarization effects. The angular cross section can be factorized in similar way as it can be done at leading order (Equation 2.27), including more terms depending lepton angles. The angular coefficients up to $\mathcal{O}\left(\alpha_s^2\right)$ for the Drell-Yan process where calculated in [29]. The dependence can be written in terms of spherical harmonics $\mathcal{P}_i$ of Collins-Soper frame (CS) angles θ_{CS}, φ_{CS} as

$$\begin{aligned} \mathrm{d}\hat{\sigma}^{(\text{ang})} &\approx (1 + \cos^2\theta_{\text{CS}}) + \sum_{i=0}^{7} A_i \mathcal{P}_i(\theta_{\text{CS}}, \varphi_{\text{CS}}) \\ &\approx (1 + \cos^2\theta_{\text{CS}}) + A_0\frac{1}{2}(1 - 3\cos^2\theta_{\text{CS}}) + A_1 \sin 2\theta_{\text{CS}} \cos\varphi_{\text{CS}} \\ &+ A_2\frac{1}{2}\sin^2\theta_{\text{CS}} \cos 2\varphi_{\text{CS}} + A_3 \sin\theta_{\text{CS}} \cos\varphi_{\text{CS}} + A_4 \cos\theta_{\text{CS}} \\ &+ A_5 \sin^2\theta_{\text{CS}} \sin 2\varphi_{\text{CS}} + A_6 \sin 2\theta_{\text{CS}} \sin\varphi_{\text{CS}} + A_7 \sin\theta_{\text{CS}} \sin\varphi_{\text{CS}}, \end{aligned} \tag{2.31}$$

where vector and axial-vector couplings control the angular moments A_i as follows: the moments A_0, A_1, A_2 origin from the $(g_{V,\ell}^2 + g_{A,\ell}^2)(g_{V,q}^2 + g_{A,q}^2)$ coupling combination, while the moments A_3, A_4 origin from the $g_{V,\ell}g_{A,\ell}g_{V,q}\ g_{A,q}$ couplings. The higher coefficients $A_{5,6,7}$ are influenced by parity conserving and violating terms. The factorization to spherical harmonics allows to measure the angular coefficients A_i from $Z \to \ell\ell$ events as moments of the cross section. The orthogonality of the spherical harmonics also allows to correct the calculated angular distributions by reweighting to higher order prediction.

2.3.2 Soft and colinear gluon resummation

The transverse momemtum of bosons is balanced by partons radiated from initial state. The low-q_{T} region is dominated by multiple emmison of soft or collinear gluons. Since the gluon emmisions are independent from each other, the total probability of emitting an invite series of gluons is complementary to the probability of emitting no gluon. Based on this fact, an alternative to the fixed order calculation

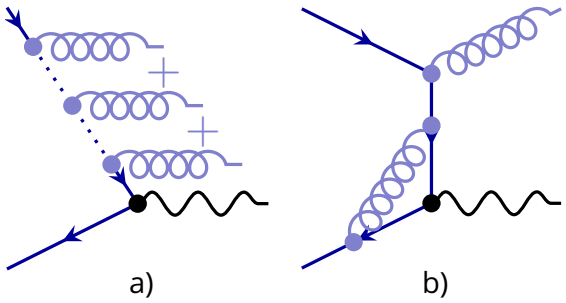

Figure 2.6: *Comparison of resummation (a) and fixed order (b) diagrams. The dotted line represents the infinite series of gluon emmisions, which is resummed.*

is to exponentiate the soft and collinear gluon contribution to cross section and resum the leading logarithmic terms. The schematic representation of resummation is shown in Figure 2.6 (a). An example diagram of a fixed order calculation is shown in Figure 2.6 (b). While resummation better describes the beginning of the spectrum ($q_{\mathrm{T}} < 30\,\mathrm{GeV}$), the fixed order calculations is more accurate for larger values of q_{T}. Therefore, these two calculation approaches are combined for a prediction of the full q_{T} spectrum. The two diagrams shown in Figure 2.6 can have overlapping final state configurations (e.g. one gluon emission), which need to be estimated and subtracted to avoid double counting in the cross section calculation.

As previously discussed, the prediction calculation is divided into two terms: resummed cross section $\mathrm{d}\hat{\sigma}^{(\mathrm{res.})}$ and finite contribution of fixed order $\mathrm{d}\hat{\sigma}^{(\mathrm{fin.})}$

$$\frac{\mathrm{d}\hat{\sigma}^{(\mathrm{tot.})}}{\mathrm{d}q_{\mathrm{T}}^2} = \frac{\mathrm{d}\hat{\sigma}^{(\mathrm{res.})}}{\mathrm{d}q_{\mathrm{T}}^2} + \frac{\mathrm{d}\hat{\sigma}^{(\mathrm{fin.})}}{\mathrm{d}q_{\mathrm{T}}^2}\,. \tag{2.32}$$

The illustration of the vector boson spectrum is shown on Figure 2.7, where the black solid line is the total cross section $\mathrm{d}\hat{\sigma}^{(\mathrm{tot.})}$. The finite part $\mathrm{d}\hat{\sigma}^{(\mathrm{fin.})}$ is shown by the blue dotted line and it is calculated from fixed order $\mathrm{d}\hat{\sigma}^{(\mathrm{f.o.})}$ (red dashed line) subtracted by contributions already counted in resummed term $\mathrm{d}\hat{\sigma}^{(\mathrm{res.})}$.

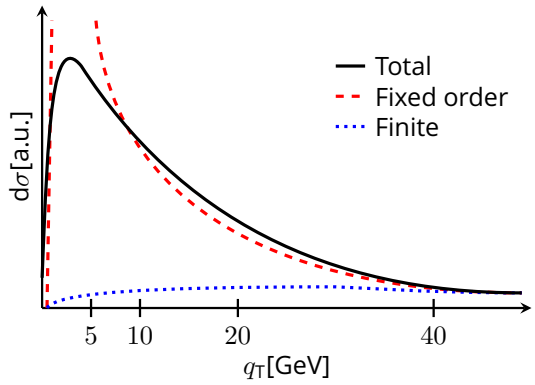

Figure 2.7: *A sketch of the differential cross section with respect to the transverse momentum of the vector boson* q_{T}.

The commonly used formalism for soft and collinear gluon resummation was firstly described by John Colins, Davison Sopper and George Sterman [30] in 1984. The calculation using the Collins-Soper-Sterman resummation formalism (CSS) approach is done in the impact parameter b space. The impact parameter is the Fourier transformation of boson transverse momentum q_{T}. For large values of b, i.e. $\lim_{b\to\infty} q_{\mathrm{T}} = 0$,

the resummed and total cross section are going to zero. The resummed cross section is also vanishing for small value of $b \to 0$, i.e. high q_{T}, where the physical effects are dominated by fixed order calculations that incorporate hard parton emissions. The general form of the resummed cross section can be found in Equation 2.33. It consists of two parts: the perturbative Wilson function $\mathcal{W}$ and the non-perturbative Sudakov formfactor $\mathcal{S}_{\mathsf{NP}}$ and can be schematically written as

$$\frac{\mathrm{d}\hat{\sigma}^{(\mathsf{res.})}}{\mathrm{d}q_{\mathrm{T}}^2} = \frac{M_V^2}{\hat{s}} \int_0^\infty \mathrm{d}b \frac{b}{2} J_0(bq_{\mathrm{T}}) \mathcal{W}(b, M_V, \hat{s} \mid \alpha_s(\mu_{\mathsf{R}}^2), \mu_{\mathsf{R}}^2, \mu_{\mathsf{F}}^3) \mathcal{S}_{\mathsf{NP}}(b, Q, \mu_{\mathsf{res.}}, x_1, x_2) \ . \quad (2.33)$$

The function $\mathcal{S}_{\mathsf{NP}}$ in the CSS formalism, is a process independent form factor, which depends only on the initial state. The Sudakov form factor modifies the shape of p_{T}^Z, forming the characteristic Sudakov peak in beginning of the spectrum. The most general form of $\mathcal{S}_{\mathsf{NP}}$ depends on the parton flavour a and its momentum fraction y within the hadron h as well as an arbitrary momentum scale $\mu_{\mathsf{res.}}$, representing the upper scale where the resummation approach is applied. The general form can be written as [30]

$$\mathcal{S}_{\mathsf{NP}} = \exp\left[-S_0(b)\ln(Q/\mu_{\mathsf{res.}}) - S_{a/h1}(x_1, b) - S_{b/h2}(x_2, b)\right] \ , \quad (2.34)$$

where both functions S_0, $S_{a/h}$, must be estimated experimentally. Currently, two parametrizations of $\mathcal{S}_{\mathsf{NP}}$ are widely used. The first is used by Broke, Nadolsky, Ladinsky, Yuan (BNLY) [31] and given by

$$\mathcal{S}_{\mathsf{NP}}^{\mathsf{BNLY}} = \exp\left\{\left[-g_1 - g_2\ln(Q/\mu_{\mathsf{res.}}) - g_1 g_3 \ln(100 x_1 x_2)\right] b^2\right\} \ , \quad (2.35)$$

with the three parameters $g_{1,2,3}$ are estimated also in [31]. The simplified form of BNLY can be obtained by setting $g_2 = g_3 = 0$ (used by Guzzi, Nadolsky, Wang [32] or Catani, de Florian, Ferrera, Grazzini [33]) i.e. leaving only one free parameter:

$$\mathcal{S}_{\mathsf{NP}}^{\mathsf{Gauss}} = \exp\left\{-gb^2\right\} \ . \quad (2.36)$$

In this case, the function is using a general Gaussian smearing parameter of perturbative part. It was shown [32] that this parameterization is sufficient to describe the measured distribution of vector boson transverse momentum in hadron collisions.

The perturbative part of the function $\mathcal{W}$ handles the soft and collinear gluon emission by resuming the large logarithms from all orders of perturbative QCD. Since the calculation is done in the impact parameter space, a representation of parton momentum fraction in the impact parameter space is required. This is done by so-called Mellin transformations [34] of the parton distribution functions, written as

$$\mathcal{F}_{a/h}(M, \mu_{\mathsf{F}}^2) = \int_0^1 \mathrm{d}x \ f_{a/h}(x, \mu_{\mathsf{F}}^2) \cdot x^{M-1} \ , \quad (2.37)$$

where the complex number M is called Mellin moment. The function $\mathcal{W}$ can be therefore calculated as product

$$\begin{aligned}\mathcal{W}_{MN}(b, M_V \mid \alpha_s(\mu_{\mathsf{R}}^2), \mu_{\mathsf{R}}^2, \mu_{\mathsf{F}}^2) = \mathcal{F}_{a/h_1}(M, \mu_{\mathsf{F}}^2) \cdot \mathcal{F}_{b/h_2}(N, \mu_{\mathsf{F}}^2) \cdot \\ \cdot \mathcal{H}_{MN}(M_V, \alpha_s(\mu_{\mathsf{R}}^2) \mid M_V^2/\mu_{\mathsf{R}}^2, M_V^2/\mu_{\mathsf{F}}^2, M_V^2/\mu_{\mathsf{res.}}^2)\end{aligned} \quad (2.38)$$

where the moments M and N correspond to the momentum fractions x_1 and x_2, respectively. The function $\mathcal{H}_{MN}$ represents the truncation of fixed order hard-virtual

and collinear contributions. It is expanded in terms of α_s and the coefficients $\mathcal{H}^{(i)}$ are known up to $\mathcal{O}\left(\alpha_s^2\right)$ [35]:

$$\mathcal{H}_{MN} = 1 + \frac{\alpha_S}{\pi}\mathcal{H}^{(1)} + \left(\frac{\alpha_S}{\pi}\right)^2 \mathcal{H}^{(2)} \tag{2.39}$$

The last term on right hand side of Equation 2.32 $\mathrm{d}\hat{\sigma}^{(\text{fin.})}$ has two contributions: Since the fixed order prediction $\mathrm{d}\hat{\sigma}^{(\text{f.o.})}$ is divergent for $q_\mathrm{T} = 0$, a counter term $\frac{\mathrm{d}\hat{\sigma}^{(\text{res.}\to\text{f.o.})}}{\mathrm{d}q_\mathrm{T}^2}$ has to be subtracted, which is estimated using above mentioned $\mathcal{H}_{MN}$ truncation.

$$\frac{\mathrm{d}\hat{\sigma}^{(\text{fin.})}}{\mathrm{d}q_\mathrm{T}^2} = \frac{\mathrm{d}\hat{\sigma}^{(\text{f.o.})}}{\mathrm{d}q_\mathrm{T}^2} - \frac{\mathrm{d}\hat{\sigma}^{(\text{res.}\to\text{f.o.})}}{\mathrm{d}q_\mathrm{T}^2} \,. \tag{2.40}$$

Hence, this divergence is treated by the resummed term of Equation 2.32.

3. Hadron colliders and their detectors

In this thesis the data from two experiments is analysed. The data from the ATLAS experiment is used for the extraction of the value of α_S in Chapter 5. The measurement of the W boson mass (Chapter 6) was done with data recorded by DØ experiment. Each experiment is located at a different hadron collider situated in different laboratory. The technical specification of both colliders and both experiments is discussed in this chapter. Namely, the $p\bar{p}$ collider Tevatron at Fermilab is described in Section 3.1 and the pp collider Large Hadron Collider (LHC) at European Organization for Nuclear Research (CERN) is described in Section 3.3. The technical parameters of the detectors, the trigger and the data acquisition system are described in sections Section 3.4 and Section 3.2 for ATLAS and DØ respectively. Common principles of both high energy physics experiments used are presented in following text.

A particle accelerator is device, which increases the momentum of a charged particles using static or dynamic electric fields. Both above mentioned accelerators are complex toroidal structures with the size reaching up to tens of kilometers in circumference.

Two main parameters of accelerators are the beam energy and the beam luminosity. The luminosity represents the number of particles which travel through a given unit area per unit of time:

$$\mathcal{L} = \frac{N_b \cdot f}{A} \,, \tag{3.1}$$

where N_c is number of colliding particle with the rate f in an area A. The unit of luminosity is $\mathrm{cm}^{-2}\mathrm{s}^{-1}$. The total luminosity delivered by a collider to its detectors is quantified in the integrated luminosity $\int \mathrm{d}t\mathcal{L}$, which is integrated over the complete runtime. In order to calculate the expected number of produced events it is necessary to multiply the luminosity by the cross section of the observed event σ

$$N = \int \mathcal{L}\sigma \,. \tag{3.2}$$

The number of events N is unitless therefore the cross section is an area. The most frequent unit used for cross section is barn b which is defined by $1\,\mathrm{b} = 2{\cdot}10^{-13}\,\mathrm{cm}^2$. The integrated luminosity can be expressed in units of inverse barns but more frequent are derived units, e.g. inverse femto-barn $1\,\mathrm{fb}^{-1} = 10^{-15}\,\mathrm{b}^{-1}$.

The second parameter of a collider is the maximum reachable collision energy. It defines the regime of physical processes which can be studied at the experiment. The most frequent type of high energy beam accelerators is a synchrotron. Both hadron colliders discussed in this thesis are synchrotrons. The synchrotron is a circular accelerator, which uses radio frequency (RF) alternating electric field for accelerating charged particles, while a magnetic field is used to keep the beam on circular trajectory and to keep beam focused.

Since the synchrotron needs particles with an initial momentum, an accelerator chain is installed at each laboratory to extract charged particles from a medium and create a focused and pre-accelerated beam. More details of each accelerator chain is discussed in the dedicated sections.

The first powerfull particle accelerators (by Widerœ[36] in 1928) were used for fixed target experiments. However, the energy in the center of mass system with respect to the beam energy is $\sqrt{s} = \sqrt{2mE_{\text{beam}}}$. On the other hand, when two beams collide with each other the center of mass energy is $\sqrt{s} = 2E_{\text{beam}}$, where E_{beam} is the energy of one beam. Hence, the particle collider can produce a larger center of mass energy than the fixed target experiment with the same beam energy. In colliders with same charged particles the two beams are circulated in opposite directions inside separated tubes next to each other, while in case of e.g. $p\bar{p}$ one tube can be used to host both beams using the same magnetic field.

There are several points along the collider circumference, where beams are bended from their trajectory and are focus to collide with each other. Such a place is called an interaction point. A system of particle detectors is build around an interaction point.

The usual structure of a detector is a cylindrical tube along the beam line. The detectors are built up in an onion-shaped structure separated into central region (barrel) and forward region (end cap). Two basic coordinate systems are used to describe position of detector and particle: the Cartesian system and the spherical system, where both have their origin in the center of the detector.

The right-handed Cartesian system has its z-axis defined along beam line and the y axis pointing upwards. The x coordinate definition is different between ATLAS and DØ. While in the case of the ATLAS detector the x-axis is pointing to the middle of LHC ring (z-axis is pointing to anti-clockwise direction), in case of the DØ experiment the x-axis is pointing away from the Tevatron ring (z-axis is pointing to clockwise direction).

The spherical coordinate system has also three parameters: the distance from center point and two angles (r, ϕ, θ). The radius r is defined as the distance from the beam line in the transversal xy-plane. The azimuthal angle ϕ is defined in the transversal plane with $\phi = 0$ pointing along the positive x-axis. The longitudinal angle θ is defined as the opening angle from beam line. Both coordinate systems are shown in Figure 3.1.

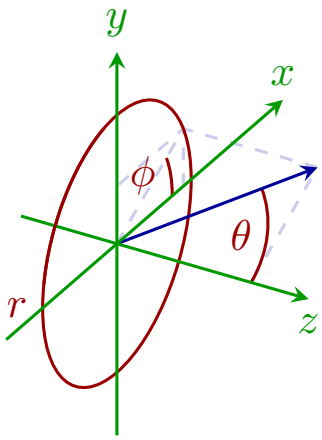

Figure 3.1: *Coordinate systems: Cartesian depicted by green, spherical is red. Blue color represents described vector.*

General purpose detectors for high-energy physics, like ATLAS and DØ, are designed to identify and measure a wide range of long-lived particles produced during collision. The detectors have three main parts: an inner tracking system, a calorimeter and a muon spectrometer.

The trajectory of a charged particle (track) is detected by the inner tracker. The tracks are bent by a solenoidal magnetic field applied in the inner detector, which

makes it possible to measure the momentum of the particle from its curvature.

The calorimeter is a detector designed to stop the particle inside its volume and measure the energy deposited by the particle. The calorimeter is divided into two parts. The electrons and photons are stopped in the electromagnetic calorimeter due to shorter attenuation length. The massive hadrons need more interaction material to be fully absorbed. Therefore, the hadronic calorimeter needs more material to extend its radiation length and is therefore build around the electromagnetic calorimeter.

All particles, except muons and neutrinos, are stopped inside calorimetric system. The muons are not interacting strong enough to be stopped inside the calorimeter, hence, the muons pass through both calorimeters with only a very small amount of energy deposited in the calorimeter. Therefore their tracks are measured with same principle as the inner tracker works, using the bending radius in a known magnetic field.

The neutrinos are only weakly interacting particles and they can not be measured inside detector directly. However, using the momentum conservation it is possible to measure the transverse neutrino momentum by the total energy imbalance of the event.

The high collision rate increases the statistical precision of the measurements. On the other hand, not every collision is a hard scattering event containing physics data of interest. Therefore, a trigger system is installed to select the physics processes of interest. The final trigger decision is combined from dedicated hardware for fast and course filtering of events and from multiple more advanced decision algorithms. After the trigger selects the event, the Data AcQuisition system (DAQ) collects the measured data from each detector subsystem and stores them on magnetic tapes. The magnetic tapes are used in both experiments, due to their write speed and robustness of storage technology. The experiment-wise software framework was developed to provide tools for processing measured data, generating predictions and simulating detector response. Detailed specifics to each experiments are discussed in the corresponding sessions.

3.1 Tevatron

The Tevatron collider is situated at Fermilab near Batavia, IL, USA. The Fermilab was founded in 1967 [37]. The main project was the production and study of high energy proton – anti-proton collisions with the Tevatron collider, which was finished in September 2011. The current main research at Fermilab is focused on neutrino physics, but there are also smaller experiments which profit from the wide accelerator complex, see Figure 3.2. This section introduces the Fermilab accelerators with a focus on the Tevatron collider.

A bottle of hydrogen gas H^2 is connected to the magnetron chamber [39], which creates hydrogen ions H^- from the gas. These ions are accelerated to 750 keV using a static electric field generated inside a Cockroft-Walton chamber. The beam is then injected through LINear ACcelerator in Fermilab (LINAC). The LINAC consists of RF cavities and drift tube segments with a total length of 150 m. As a particle is accelerated, in each cavity the drift tube length is increased to keep particles travel time through each drift tube the same. The H^-, ions with an energy of 400 MeV, are sent trough a carbon stripping foil to remove both electrons from the ion. The resulting proton beam is directed to a synchrotron ring with an output energy 8 GeV called Booster.

Next in chain is the Main Injector - a proton synchrotron with a circumference of approximately 3.3 km and typical focusing and defocusing quadrupole magnet lattice (FODO). The magnets are in order that first quadrupole magnet (F) is focusing the beam in horizontal plane. The next dipole magnet (O) is used to keep the beam on

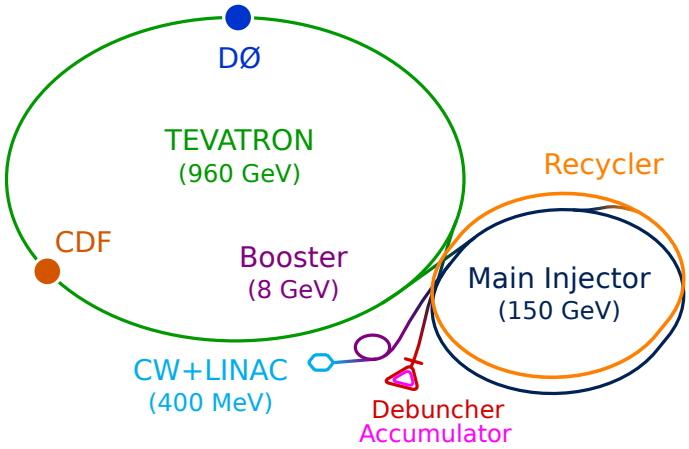

Figure 3.2: *Schematic view of the Fermilab accelerator complex. Plot adapted from [38] data from [39].*

circular trajectory. The next quadrupole magnets (D) is defocusing the beam in the horizontal plane and it is followed again by a bending dipole (O). The order of focusing magnets from the vertical plane perspective is opposite, i.e. Magnets opposite to the FODO lattice (DOFO). The maximal output energy of the Main Injector is 150 GeV, and from there a proton beam with this energy is injected into Tevatron. However, part of the beam with an energy of 120 GeV is used to create the anti-proton beam.

In order to create the anti-proton beam, the proton beam from the Main Injector is directed to a nickle target once every 1.47 s, with an anti-proton being created once per fifty protons and with an outgoing anti-proton energy of about 8 GeV. A charge-mass spectrometer build from a lithium lens and a pulse magnet separates the anti-protons from other particles. The raw anti-proton beam from the spectrometer has a high emittance, i.e. too high perpendicular spread of particles in the beam. The magnetic optics are not sufficient for focusing the beam. Therefore, a technique called stochastic cooling (developed in 1960 [40]) is used in the synchrotron called Debuncher. The Debuncher also minimizes the longitudinal momentum spread of the anti-protons by a RF bunch rotation with a working energy 8 GeV. The anti-protons are then filled to another synchrotron called Accumulator, where they are cooled down further. The final anti-proton beam with an energy of 8 GeV is finally filled to the Main Injector and circulates next to the proton beam but in the opposite direction.

The production of an anti-proton beam with the necessary luminosity for Tevatron collisions is very energy and time consuming. It takes about three hours. Therefore, during the `runII` upgrade an additional storage ring named Recycler was installed. This fixed energy anti-proton storage ring provides additional stochastic and electronic cooling. The Recycler can be filled from the Accumulator or from the Main Injector. The filling from the Main Injector happens when the anti-proton beam after Tevatron collision is directed back to the Main Injector and at ramp down to store and recycle the anti-proton beak for the next Tevatron collisions inside Recycler.

The last stage of accelerator complex at Fermilab is Tevatron. Tevatron is filled from Main Injector with proton and anti-proton beams both with energy of 150 GeV. The time from beam fill to beam dump is called store. The beams are circulating inside one tube next to each other in opposite direction. The highest possible beam energy at Tevatron is of 980 GeV. The fact that it is almost one TeV is the origin of name Tevatron.

The beams consists of 36 bunches with 396 ns bunch spacing organized into twelve

bunches per three trains. The number of particles inside the proton bunch is $2.5{\cdot}10^{11}$-$3{\cdot}10^{11}$ while an anti-proton bunch only has $0.4{\cdot}10^{11}$-$1{\cdot}10^{11}$ anti-protons. The beams are intentionally crossed at the two collision points Bo and Do, where the detectors CDF and DØ are installed, respectively. The beam conditions allow to reach collision rate about 2.5 MHz with the beams squeezed to a transverse area of $5{\cdot}10^{-3}$ mm^2[39] at the interaction points to increase instantaneous luminosity.

The operation of Tevatron and its detectors can be divided into three periods called runs: `runI`, `runIIa` and `runIIb`. The `runI` collisions at Tevatron started in 1992 and lasted until the first shutdown in 1996. During this run, the first observations of the top quark were confirmed independently by both experiments. Both detectors and accelerators were updated during the five year long shutdown. The collisions started again in 2001 as the `runIIa` period which continued until April 2006. The last period, `runIIb` is further divided by short technical shutdowns into four parts: runIIb1, runIIb2, runIIb3 and runIIb4. The corresponding years are respectively: from June 2006 to July 2007, from November 2007 to June 2009, from September 2009 to July 2010 and from August 2010 to September 2011. The last collision was delivered in September 2011. The integrated luminosity of runIIb is shown in Figure 3.3 where the exponential increase of the luminosity is clearly visible.

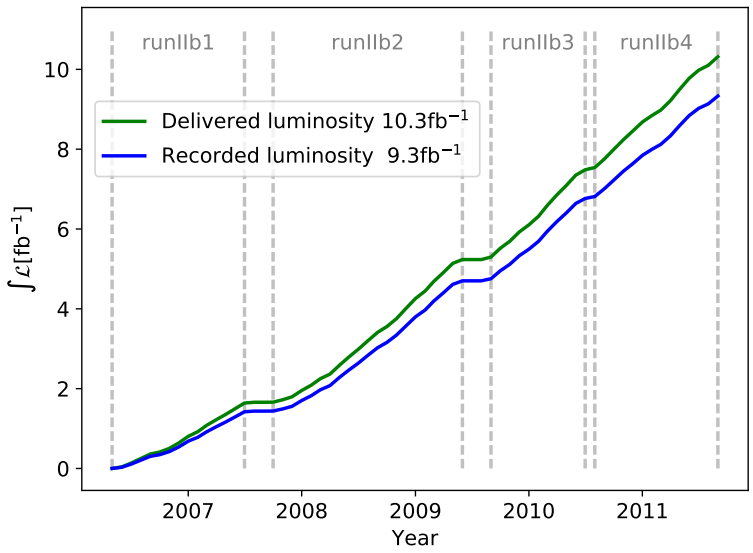

Figure 3.3: *Integrated luminosity of runIIb delivered by Tevatron (green) and recorded by DØ experiment (blue). The data was taken from [41].*

The W mass measurement was published and later updated with data from several runs. The first Tevatron measurement was published using data recoded during `runIIa` [42]. The next measurement [43] was combined with CDF results in [44]. It is currently the best world estimation of the W boson mass. The update from DØ including data from runIIb3 is expected in summer of 2018. The analysis of the data collected by DØ in runIIb3 is presented in this thesis (Chapter 6). The description of detection system of the DØ follows.

3.2 DØ Detector

The DØ is general-purpose cylindrical detector for the studies of $p\bar{p}$ collisions in the Tevatron collider. The detector is situated around the Tevatron beam pipe at the

interaction point DO (hence the name). The apparatus itself is a complex machine with many parts, which must be synchronized and controlled in challenging time, voltage, temperature and radiation conditions. The total detector length measured along the beam axis is 20 m. It is about 13 m high and its weight is about 5500 t[39]. The detector is divided into three parts: the innermost tracking system is surrounded by calorimetric system and the muon spectrometer is installed in the outermost layer. Two magnets are present: a solenoidal magnet between the tracker and the calorimeter and a toroidal magnet between the calorimeter and the muon spectrometer. The schematic view detector is shown in Figure 3.4. Each detector part is described in the following sections.

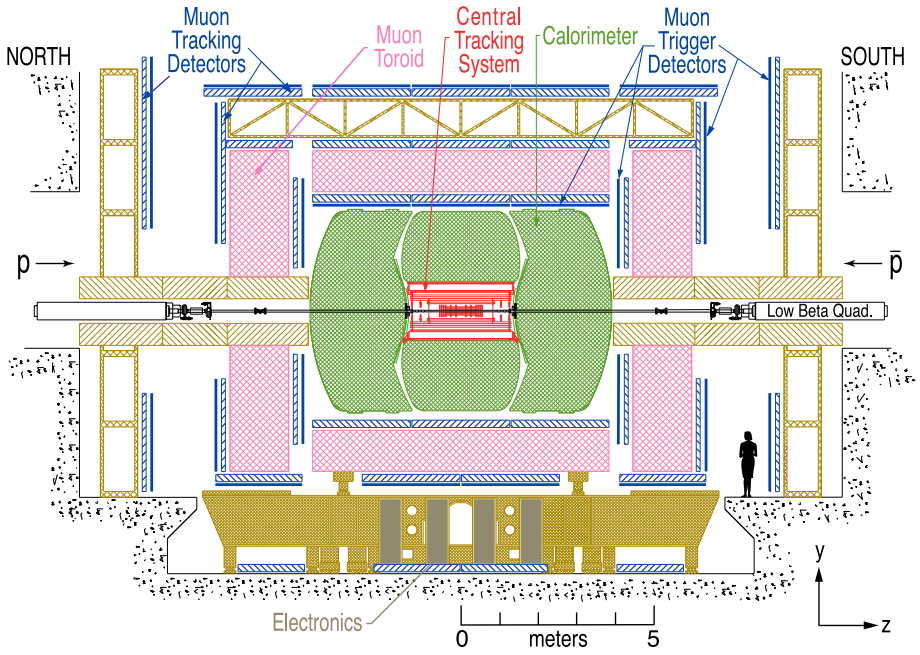

Figure 3.4: *Cross section view of the DØ showing the sub-detector parts. Plot from [45].*

3.2.1 Inner tracker detector and solenoidal magnet

The tracker is the first detector which is reached by particles created in a collision. In the W mass analysis, the information from the inner tracker is used to reconstruct the vertex of the interaction with a resolution of 35 µm and to identify electrons using measured tracks. The DØ inner tracker consists of two parts the Silicon Microstrip Tracker (SMT) and the Central Fiber Tracker (CFT). The tracks of charged particles are bend in the $x - y$ plane by magnetic field from the solenoidal magnet. From the curvature of the track it is possible to calculate the momentum of the particle. A schematic view of the inner detector including the solenoidal magnet is shown in Figure 3.5.

A brief description of the detector with information from [45] follows. More detailed descriptions can be found in these citations.

The innermost detector of the whole DØ is the silicon micro-strip tracker. It has a typical cylindrical design and is symmetric with respect to the center of the detector $z = 0$. It has tree barrel modules next to each other on each side of the z-axis. Four modules closest to the center are called central barrels. The last two modules are called outer barrels. In total there are six barrel modules with a z-length of 12 cm each.

Except at $z = 0$, there is a disk module between each barrels. These four modules,

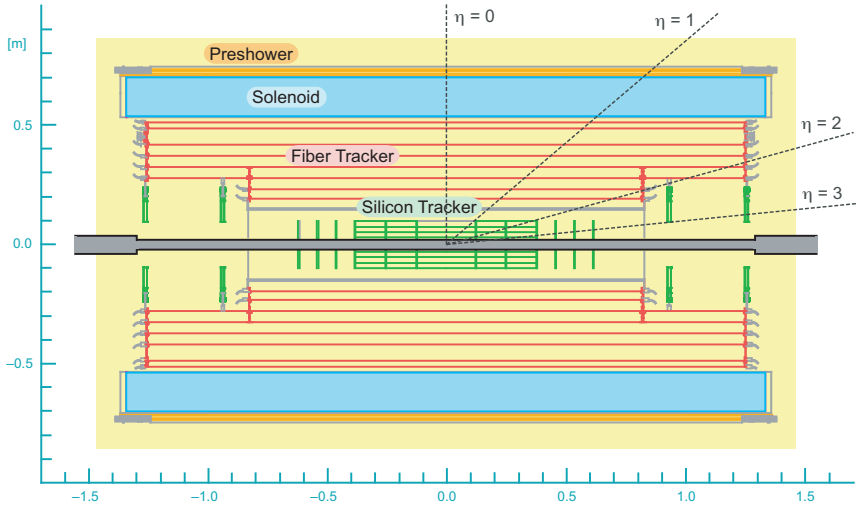

Figure 3.5: *Schematic view of the tracking detector. Plot colorized and taken from [46]*

called inner F-disks, are installed at $|z|$ =12.5 cm and 25.3 cm. At the ends of the last barrels there are four more disks modules. These eight modules, called outer F-disks, are installed at $|z|$ =38.2 cm, 43.1 cm, 48.1 cm and 53.1 cm. Two more disk modules are installed on each side further along beam axis at $|z|$ =100.4 cm and 121.0 cm. These four modules,called H-disks. In total there are 16 disk modules. The precision of the position measurement is defined by the pitch distance between the strips.

Each of the barrel modules has four coaxial layers in different r distances 2.7 cm, 4.6 cm, 7.6 cm and 10.5 cm. Each layer is covered in the full ϕ-range by rectangular sensors with strips in ϕ-direction with a pitch of (50-153) µm. Consequently, the barrels provide $r - \phi$ track measurement for pseudo-rapidity up to $|\eta| < 2$. The F- and H-disks are covered fully-ϕ by wedge sensors with strips in both phi and r with a pitch of (40-80) cm. Consequently the disks provide $r - \phi$ and $r - z$ track measurement with pseudo-rapidity coverage up to $|\eta| < 3$.

The CFT is a scintillating fiber tracker installed right around the SMT. It is composed of eight coaxial barrels located $r = (20 - 52)$ cm from the beam-line. The barrels are 2.5 m long, except the two innermost barrels which are only 1.7 m long to create space for SMT H-disks.

Each barrel is covering the full ϕ range by two doublets of 835 µm thick scintillating fibers with the first one parallel to z and second tilted by a small stereo angle $\pm 3°$. Thanks to overlay and stereo angle the resolution is better than the thickness of each individual fiber. Since the position can be determined to 50 µm precision, it yields a final resolution of 100 µm. The CFT provides a $r - \phi$ and $r - z$ track measurement in the pseudo-rapidity range up to $|\eta| < 1.7$.

The electronic signal from SMT as well as the light from the Semiconductor Tracker (SCT) fibers is guided outside the detector through a gap between the forward and the central calorimeter.

There were several technical challenges for the design of the inner detector magnetic system. A solenoid magnet is installed before the calorimeter measurement system. The coil of electromagnet consists of superconductive wires from copper doped niobium-tungsten alloy, which is cooled down by liquid helium. The coil is 2.73 m long and has a diameter of 1.42 m. Its main goal is to provide a solenoidal magnetic field of 2 T, which makes it possible to measure a wide range of track momenta. The thickness of the magnet is supposed to be approximately one radiation length at $\eta = 0$

to reduce the possible effects on the calorimeter energy resolution. The size of the magnet is limited by the space between the calorimeter cryostats and the central tracker.

3.2.2 Electromagnetic and hadronic calorimeters

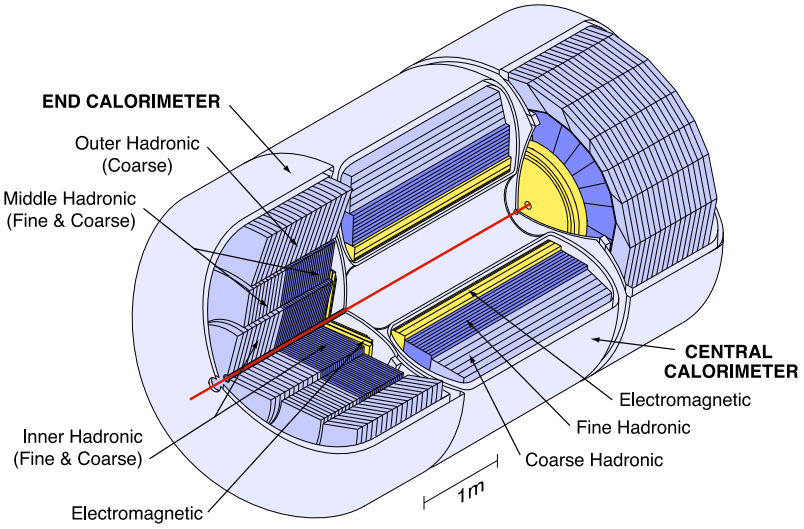

Figure 3.6: *Cut-away view of DØ calorimeters. The beam line is marked by thin red line. For more information see text. Plot taken from [46]*

The measurement from the calorimeter is the most crucial information for the W boson mass measurement. The DØ calorimeters measure the momentum vector of the electrons and the missing transversal energy in the event. Naturally, the signal from the calorimeter is used to trigger events with electrons. The DØ calorimeters are divided into the Central Calorimeter (CC) and forward End-cap Calorimeter (EC) and both are energy sampling Liquid-Argon Calorimeter (LAr) detectors. Additional detectors improving the performance of the calorimetric system are Central Pre-Shower (CPS), Forward Pre-Shower (FPS) and Inter-Cryostat Detector (ICD). The pre-showering detectors are placed between the tracking and the calorimetry systems and improve matching of information between them. The last mentioned ICD is installed to cover the gap in the calorimeter acceptance in the transition region from the CC to the EC.

The DØ calorimeter parts are encapsulated in one central barrel cryostat and two forward end-cap cryostats (one per each side)[45]. The cut-away view in Figure 3.6 shows the positions of the cryostats and the calorimeters inside them. The cryostats are double-walled stainless steel containers filled with liquid Argon. Continuous measurements and flow of the liquid argon maintain desired argon purity and temperature at level of 90 K.

The DØ calorimeters are designed as energy sampling detectors. The particle interacts with material of the absorber plates and creates electromagnetic and hadronic showers. The particles from the showers drift through the liquid argon gap to the signal board. The drifting field is created between grounded absorber plates and signal boards with positive voltage (2-2.5) kV. The typical drift time in the 2.3 mm long gap is about 450 ns. The absorber, LAr gap and read-out plate form one calorimeter cell, as depict by schema in Figure 3.7).

The cells are installed in a tower-like structure one cell after another in direction pointing away from the detector center. The size and shape of the towers are designed

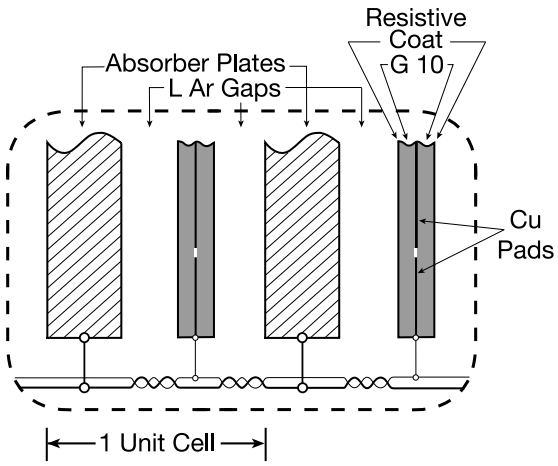

Figure 3.7: *Schematic view of calorimeter cell. Plot taken from [47].*

to provide positional measurement in $\eta \times \phi$ with a precision of 0.1×0.1. The towers are colorized and empty spaces in Figure 3.8.

According to the type of the dominating showers the calorimeter is divided into electromagnetic EM (closer to beam-line) and hadronic part (further from beam-line). There are two types of hadronic towers: fine hadronic towers with more cells with shorter absorbers and coarse hadronic towers with less cells but with longer absorbers.

The electromagnetic towers (yellow in Figure 3.8) have depleted uranium sampler and copper read-out structure. It covers the full ϕ region and pseudo-rapidity range of $|\eta_{\text{det}}| < 1.1$ and $1.3 < |\eta_{\text{det}}| < 4$ for the CC and EC, respectively. The amount of material in the electromagnetic calorimeter is about 20.5 units of the radiation length.

The fine hadronic towers (dark blue in Figure 3.8) have uranium-niob sampler and copper read-out structure. It covers the full ϕ-angle and pseudo-rapidity range $|\eta_{\text{det}}| < 1.0$ and $1.1 < |\eta_{\text{det}}| < 4$ in the EC and CC, respectively. The coarse hadronic towers (light blue in Figure 3.8) have copper plate samplers and copper read-out structure. Again, it has full ϕ-angle coverage and pseudo-rapidity range $|\eta_{\text{det}}| < 0.7$ and $0.7 < |\eta_{\text{det}}| < 4$ in the EC and CC, respectively.

The total amount of material in the calorimeter is 7.2-10.3 units of nuclear absorption length. The tower size defines spatial resolution and the energy resolution for electrons is discussed in Section 6.4.

Pre-shower detectors improve electron and photon identification as well as background rejection. DØ have three pre-shower detectors. The one CPS is measuring in full ϕ angle in the pseudo-rapidity region $|\eta_{\text{det}}| < 1.3$ and two FPS (one on each side) are measuring in full ϕ angle in pseudo-rapidity region $1.5 < |\eta_{\text{det}}| < 2.5$. Both detectors are built up by three (four) layers in central (forward) region. The layers consists of triangular scintillating strips with a light-guide fiber in its center. The position of pre-shower modules is marked by red in Figure 3.8.

There is reduced detector coverage in the transition region between the CC and EC calorimeters. To improve the coverage an ICD was installed covering pseudo-rapidity region $1.1 < |\eta_{\text{det}}| < 1.4$. The detector is situated in the space between the CC and EC on the outside wall of the forward cryostat (green color Figure 3.8). The ICD works as scintillating sampler with same granularity in $\eta - \phi$ as it is in calorimeter. In addition, there are detectors within central and forward cryostat called Zero mass sampler, which were installed in order to improve the measurement for pseudo-rapidity region $0.8 < |\eta| < 1.3$

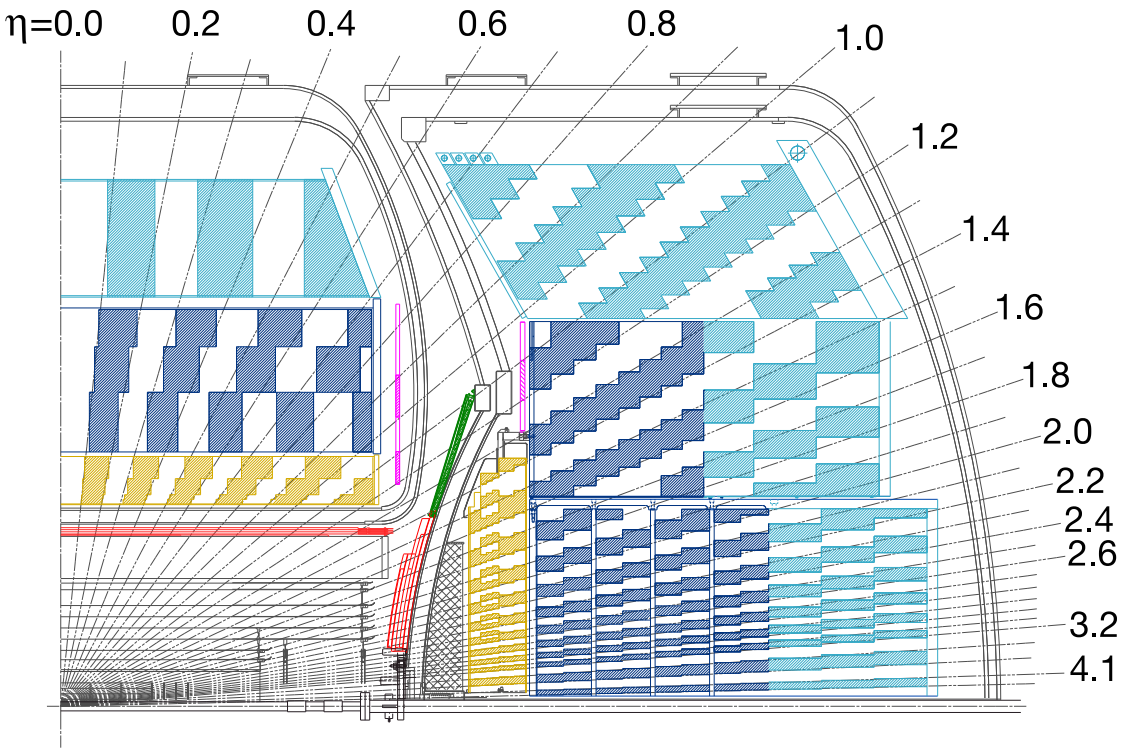

Figure 3.8: *Technical drawing of calorimeter cells with pseudo-rapidity lines. The cells shading pattern follows the read-out structure. The electromagnetic cells are yellow, blue are fine hadronic cells, faint blue are coarse hadronic cells. The pre-shower detectors are marked red, the position of ICD is marked green. Plot taken from [47] and colorized.*

3.2.3 Muon chambers and toroidal magnet

The muons are the only charged particles which pass through the calorimeter. The calorimeter and toroidal magnet radiation thickness is so large that only muons above 3.5 GeV are able to reach all layers of the muon spectrometer. The tracking method used in the muon spectrometer is similar to the inner detector, but the magnetic field is toroidal in muon spectrometer, therefore the tracks are bent in $r - z$ plane. The position of muon chambers is depicted by blue color in Figure 3.4. The pink color in the same figure represents the toroidal magnet.

The magnetic field for the muon spectrometry is generated by five solid-iron toroidal electromagnets. Three central parts occupy the barrel region in a distance of (317-425) cm from the beam line and installed next to each other they are circa 750 cm long. The end-cap parts (one on each side) are created by a disk with 417 cm in diameter situated circa 450 cm from center of detector. The full operating current 1.5 kA is able to generate a magnetic field of 1.8 T (1.9 T) in the central (end-cap) region.

The detection modules of the muon system are organized in three regions: one central and one forward on each side. All regions have three layers, which contain scintillator counters and wire drift tubes. The measurement of the hit position from the scintillators and the drift tubes is combined with precise knowledge of the alignment and consequently, the muon track is reconstruct.

Layers in the central region have a pseudo-rapidity coverage $|\eta_{\text{det}}| < 1$. The azimuthal coverage (angle ϕ) in the bottom part is reduced due to the construction support for the calorimeter and the inner tracker. The rectangular layers are installed in the $y - z$ (two side caps) and $x - z$ (top and bottom caps) planes. The first layer is placed between the calorimeter and the central toroidal magnet. The two last layers

are the outermost detectors of DØ placed outside the central toroidal magnet.

The Proportional Drift Tubes (PDT) are used to measure the trajectory of muons in all three central layers, each layer consists of multiple modules. These modules have three to four rows of twenty-four tubes. The aluminium square tubes are filled with gas mixture of argon, methane and tetrafluoromethane. An anode wire is positioned in the center of each tube and is used to measure the difference of the arrival times on each side of the tube. A vernier cathode pads are installed above and under the wire to provide the hit position along the wire and to measure the total charge of the drifted ions. The drift distance resolution is in the order of 1 cm. The position of the hit along the tube is measured with a precision of (10-50) cm, which depends on the distance between the hits and the electronics.

The drift time is in the order of 750 ns, which is longer than the bunch-crossing frequency. Therefore, scintillating muon counters are installed above or below the drift chambers. The main purpose of the counters is to to trigger muon measurement. This rejects other particles than muons coming from the calorimeter and reduces the cosmic muon background. In the central region there are two scintillator modules: one behind the innermost drift chambers and one before the outermost drift chambers. The active part of the counter chambers are scintillating fibers orientated perpendicular to beam axis.

The forward region, which has full ϕ-angle coverage and $1 < |\eta_{\text{det}}| < 2$ pseudo-rapidity coverage, is also divided into three rectangular layers. The first layer is situated between the forward toroidal magnet and the calorimeter and the last two layers, placed after the forward toroidal magnet, are the outermost detectors of DØ in the forward region.

Drift tubes in the forward region have a smaller tube diameter than the PDT, therefore, they are called Mini Drift Tubes (MDT). The drift time inside the MDT is around 60 ns. Each rectangular tube is divided into eight square cells with an anode wire inside each cell. This arrangement result in a hit position precision of about 0.7 mm.

The forward scintillator modules consist of trapezoidal shaped scintillation pads. The granularity in the azimuthal angle is matched to the CFT $\Delta\phi \sim 4^\circ$ while in the pseudo-rapidity it is $\Delta\eta = 0.07 - 0.12$.

The PDT and MDT are depicted by blue rectangles with a diagonal pattern in Figure 3.4 while the muon scintillator modules are depicted by solid blue rectangles. No information from muon system was used in the W mass analysis. Therefore, the description of the muon triggers, data acquisition and reconstruction is skipped in next sections and can be found elsewhere [47].

3.2.4 Single electron trigger

The Tevatron bunch-crossing rate is about 1.7 MHz [48]. In a model case, when the full detector information could be stored for every bunch-crossing, the data flow would be hundreds of gigabytes per second, which would be an enormous amount of data to store and process. During measurement there is no motivation to record all events, because not every bunch-crossing yields an event containing physics of interest. Therefore, a trigger system is installed to make the decision, whether information from the bunch-crossing should be stored or not, in a short amount of time.

The DØ trigger system has three levels (L1, L2 and L3). The first two, L1 and L2 are hardware triggers using low-level physical observables. The last one, L3, is a software trigger running on a dedicated computer farm using fast reconstruction algorithms of the high-level physical objects. The trigger system efficiently reduces the raw detection frequency of 1.7 MHz down to a storage rate of 100 Hz. The data

is stored on tapes and then processed by off-line reconstruction algorithms. The schematic view of the trigger system with the corresponding frequencies for each stage is shown in Figure 3.9.

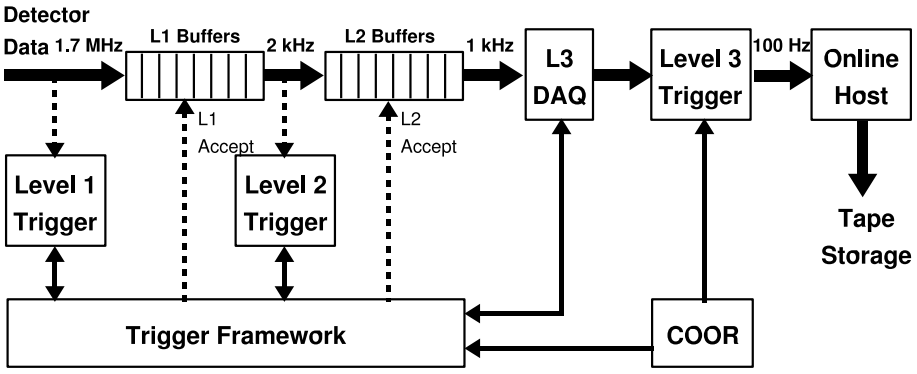

Figure 3.9: *DØ trigger with the corresponding rates at each stage. Plot taken from [48].*

Each part of the detector, (tracker, calorimeters and muon system), has its own trigger system. The following paragraphs are focused on the description of the calorimeter triggers used during W mass analysis, namely E1_SHT25 and E1_SHT27.

The trigger chain starts with the L1 trigger, where electronics receives analog signals from the calorimeter trigger towers, which is converted to the corresponding transverse energy using look-up tables. The trigger towers have a size of 0.2×0.2 in the $\eta - \phi$ space (twice the detector granularity). The sliding window algorithms look for a position of the deposited energy local maximum (window). The window size is 0.4×0.4 and the searched Region of Interest (RoI) is 1×1 large.

A minimum energy of 19 GeV is required by the L1 trigger in any region of interest with $|\eta_{\text{det}}| < 3.2$. The L2 trigger automatically accepts events with a deposited energy of at least 25 GeV. For energies between 19 and 25 GeV, the decision is based on a likelihood of the deposited energy coming from an electromagnetic shower. The selection within L3 trigger requires a reconstructed electron with a transverse energy larger than 25 GeV and 27 GeV for E1_SHT25 and E1_SHT27, respectively.

3.2.5 Event reconstruction

The events selected by the trigger are stored on a tape. Information is written in raw format containing direct digital output from sub-detector parts. This format is processed by the collaborations software framework called `cafe` [49]. The `cafe` framework is developed to read collected data and reconstruct the physical event objects. For the M_W measurement it is necessary to reconstruct the position of the interaction vertex, the momentum of the electrons and the missing transversal energy $\not\!\!E_{\text{T}}$.

Since the vertex and electron identification uses track information, the basic principle of track reconstruction is described here. The tracking detectors provide the positions of hits - points where particles crossed the active area of the detector. Clusters of hits are processed by a pattern recognition software to identify tracks, which are bent while crossing the magnetic field. From curvature of a track and a precise knowledge of the magnetic field, it is possible to reconstruct the momentum vector of particle. The higher the energy of a particle the more straight is its track. Consequently, it is more convenient to use the calorimeter information for high-momentum electron measurements. The track information used for the M_W analysis are: the position of the closest track point to the beam-line and the spatial angles θ

and ϕ.

Several interactions happen along the beam line during one bunch crossing. The precise z-position of the interaction vertex is crucial for the spatial measurement. The standard DØ procedure for the determination of the primary vertex position uses a Kalman filter. The closest point of the electron track is taken as the vertex z-position in case that this value is more than 2 cm away from Kalman-z value. The same is applied in Z events, but the average value from two electron tracks is used then. The additional criteria $|z| < 60$ cm is applied on the reconstructed vertex.

The signal of an electron and a photon inside the electromagnetic calorimeter are very similar. However, a photon being a neutral particle travels trough the tracking detectors without leaving any signal. This is used for identifying electrons. Firstly, the raw energy of an electron $E^{\text{raw}}_{\text{EM}}(\Delta R)$ needs to be estimated. It is defined as the sum of the energies from all electromagnetic cells within a radius of $\Delta R = 0.2$ around the cell with the highest energy. The distance ΔR is calculated between the center points of the cells in the $\eta - \phi$ coordinates. The total energy $E^{\text{raw}}_{\text{tot}}(\Delta R)$ is defined as the sum of the energy from all cells (electromagnetic and hadronic) within the radius ΔR. Four basic properties of electron shower are used to identify electron:

- *EM fraction*: The energy of electrons is mostly deposited in EM layers of calorimeter. The electromagnetic fraction $f^{\text{EM}}_{0.2}$ is defined to address this as

$$f^{\text{EM}}_{0.2} = \frac{E^{\text{raw}}_{\text{EM}}(0.2)}{E^{\text{raw}}_{\text{tot}}(0.2)} \,. \tag{3.3}$$

  The value of $f^{\text{EM}}_{0.2}$ is expected to be very close to 1.

- *Isolation*: The shower created by an electron has a narrow profile in the $\eta - \phi$ plane, therefore the isolation can be defined as

$$E^{\text{iso}}_{2\to4} = \frac{E^{\text{raw}}_{\text{tot}}(0.4) - E^{\text{raw}}_{\text{EM}}(0.2)}{E^{\text{raw}}_{\text{tot}}(0.2)} \tag{3.4}$$

  with values for electrons expected to be close 0.

- *Track match*: A track from the inner tracking system is extrapolated to the third EM layer using the knowledge of the magnetic field distribution. The track and the calorimeter values of the azimuthal angle ϕ and z position in the third EM layer are compared and the track match quality is calculated by

$$\chi^2_{\text{TM}} = \left(\frac{\Delta\phi}{\sigma\phi}\right)^2 \left(\frac{\Delta z}{\sigma z}\right)^2 \,, \tag{3.5}$$

  where σ_x is the resolution of the variable Δx.

- *H-matrix*: The longitudinal profile of an electron shower is modelled by Monte-Carlo simulation. A set of seven parameters is used to describe it: EM fractions per each EM layer, the weighted RMS in ϕ direction, $log(E^{\text{raw}}_{\text{tot}}(0.2))$ and the vertex $\frac{z}{\sigma_z}$. The covariance matrix is created by comparing the EM cluster and Monte-Carlo simulation. This matrix is used to determine the χ^2_{HM} value, which should be small for electron-like showers.

The raw electron energy $E^{\text{raw}}_{\text{e}}$ is defined as the sum of the deposited energy in all EM layers and the first hadronic layer within the radius $\Delta R < 0.2$. The values of the electrons ϕ and θ angles are taken from the associated track.

Neutrinos leave the detector without any deposited energy. Since the calorimeter system is able to detect particles in full ϕ-angle the momentum conservation can be used to estimate the transversal momentum and the direction of escaped neutrinos. The vector of imbalance is called missing transverse energy $\not{E}_{\mathrm{T}}$ and is defined as

$$\vec{\not{E}}_{\mathrm{T}}^{\,\mathrm{raw}} = -\sum_i E_{\mathrm{i}}^{\mathrm{raw}} \sin\theta_i \left(\cos\phi_i \sin\phi_i\right) \tag{3.6}$$

where i is an index running over all the calorimeter cells except the coarse hadronic calorimeter (due to noise). The parameters ϕ_i, θ_i and $E_{\mathrm{i}}^{\mathrm{raw}}$ are the corresponding cell azimuthal, longitudinal angles and energy.

The information about the total deposited energy in the transversal plane is quantified by the $\sum E_{\mathrm{T}}$ variable. It is defined as the scalar sum of the transverse energies from all clusters i except the coarse hadronic layers

$$\sum E_{\mathrm{T}} = \sum_i E_{\mathrm{i}}^{\mathrm{raw}} \sin\theta_i \ , \tag{3.7}$$

This variable is useful because of its dependence on the instantaneous luminosity.

The reconstructed events are then stored in object-oriented branches inside ROOT trees. These files are stored on tapes and can be analysed inside `cafe` framework. The Monte-Carlo simulation uses the same reconstruction procedure as the data, but the digital signal from the detector is simulated using the GEANT [50] framework. The first step is the generation of particles using PYTHIA [51] or RESBOS [52]. The generated particles are used as the input to the full detector simulation in GIANT. The program has full three dimensional models of the detectors and their supporting constructions including the type of material used. Further in this thesis a different approach for the simulation is described. This method is using parametrization of the detector response. To distinguish these two simulation methods full Monte-Carlo simulation (FullMC) is used for the `cafe+GIANT` approach and Parameterised Monte-Carlo Simulation (PMCS) for the other one described in Section 6.1.

3.3 LHC

The data used in Chapter 5 is from the ATLAS experiment, which is situated at LHC at CERN, Geneva. The LHC is installed in the tunnel which was build for the Large Electron-Positron collider (LEP). For both accelerators it is necessary to provide pre-accelerated particles. Therefore, CERN has an accelerator complex to support LHC experiments as well as many other projects.

The LHC can be used to collide protons with protons, protons with lead ions or lead ions with lead ions. The filling of the accelerator is different for each type of collision. The following text is focused on the proton-proton filling of the LHC, which is schematically shown in Figure 3.10.

The whole acceleration procedure starts with a bottle of hydrogen gas which is used to fill the duoplasmatron device [53]. The duoplasmatron strips off the electrons from the hydrogen and directs a beam of protons into the LINear ACcelerator at CERN (LINAC2). The LINAC2 accelerates the protons to an energy of 50 MeV in cavities with a total length of 32 m. The proton beam is transferred 80 m into the circular accelerator Proton Synchrotron Booster (PSB). The four PSB rings provide a 1.4 GeV proton beam to the Proton Synchrotron (PS). After a ramp up in the PS, the proton beam, with an energy of 26 GeV, is filled into the Super Proton Synchrotron (SPS). The SPS is the last accelerator before the LHC. Multiple injection-extraction cycles are necessary to reach the requested beam luminosity in both direction of the LHC beam-lines. After a

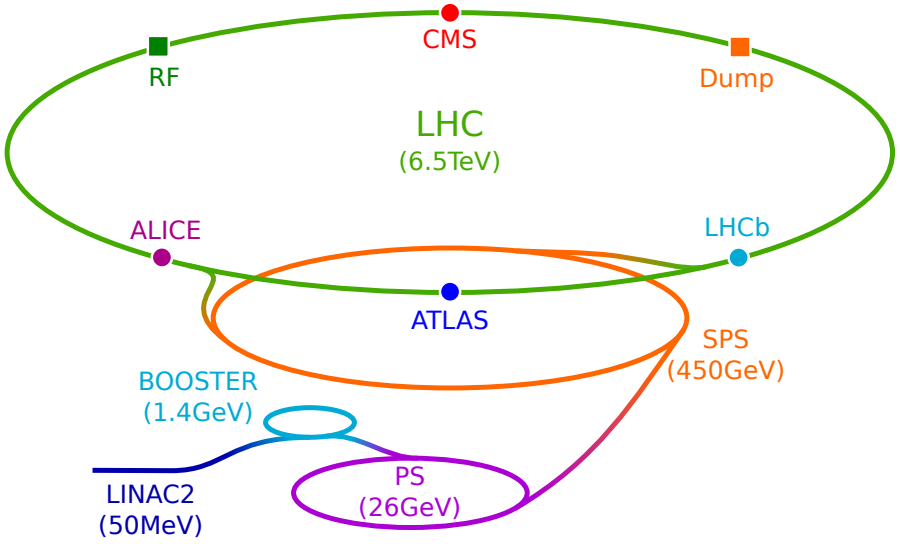

Figure 3.10: *Schematic view of CERN accelerator complex*

successfull LHC filling, the protons are accelerated from 450 GeV up to 6.5 TeV (in 2015). From the year 2015 the LHC holds the world record of the highest proton-beam energy and consequently for the highest center-of-mass energy in proton-proton collision [54].

Two proton beams are counter-rotating in the LHC in separated pipes. The LHC is divided by eight access points (numbered from 1 to 8) regularly distributed over it's circumference. Between the access points, the beam is transferred through a set of straight modules containing beam-tubes, magnets and a cryogenic system. Every beam-line is surrounded by bending (dipole) and focusing (quadrupole and higher multipole) magnets. The material used for the electromagnetic coils is super-conductive at temperature near absolute zero. The cryogenic system of the LHC is based on the exceptional heat-transfer efficiency of super-fluid liquid helium. The cryogenics sustain the niob-titanium magnets at a temperature of 1.9 K. The coils are able to operate at a current of 8 kA which generates a magnetic field of 7.8 T in the case of the dipole magnets.

The LHC access points hosts facilities for beam operations. At four of them the beams are focused and directed to cross each other and provide collisions. The others are used for accelerating, cleaning and dumping the beams. The beam-crossing points with numbers 1,2,5 and 8 hosts the experiments ATLAS, A Large Ion Collider Experiment (ALICE), Compact Muon Solenoid (CMS) and Large Hadron Collider beauty (LHCb), respectively. While CMS and ATLAS are general purpose detectors with very similar physics program, the other two are more specialized. The ALICE experiment focuses on high-energy heavy-ion collisions. Theses collisions have high particle multiplicities, therefore the detector is designed with a high granularity in the tracking system. The measurement of multiplicities in ion-ion collisions is an important observable for quark-gluon confinement studies. The LHCb detector focuses on the production of hadrons containing b-quark (hence beauty) which has an important place in studies of strong or heavy flavor physics. The acceleration and beam optics along the beam line is provided by RF cavities situated at access point 4. The beam is directed into a carbon prism in the event of an unexpected or planned termination of the run at

access point 6. To reduce the necessary prism length the beam is defocused and bended by a set of electromagnets.

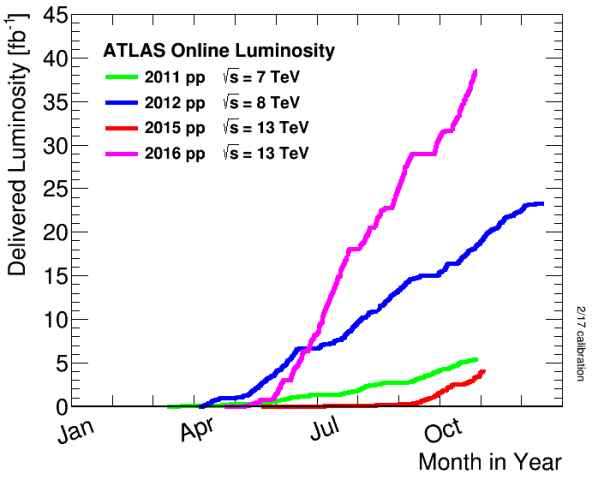

Figure 3.11: *Integrated luminosity with respect to time for different production years. Figure taken from [55].*

After the first collision in 2011, the LHC had one long technical stop in years 2013-2014. During this stop the necessary accelerator and detector upgrades were performed in order to increase the energies from 3.5 TeV to 6.5 TeV during first running period. The delivered luminositiies of proton-proton collision per each production year are shown in Figure 3.11. The data collected during 2015 by the ATLAS detector is used in Chapter 5.

3.4 ATLAS

The ATLAS detector is a general purpose detector built around an interaction point at the LHC. The ATLAS detector was designed to focus on a wide-range of physical measurements as well as to search for new phenomena. With a total length of 46 m and a diameter 25 m it is one of the largest particle detectors ever build by mankind. A cut-away view of the detector is shown in Figure 3.12. It has a cylindrical structure with three main detection systems ordered from inside to outside: Inner Detector (ID), calorimeters and Muon Spectrometer (MS). The detector parts together with the trigger and the data acquisition system are described in following sections.

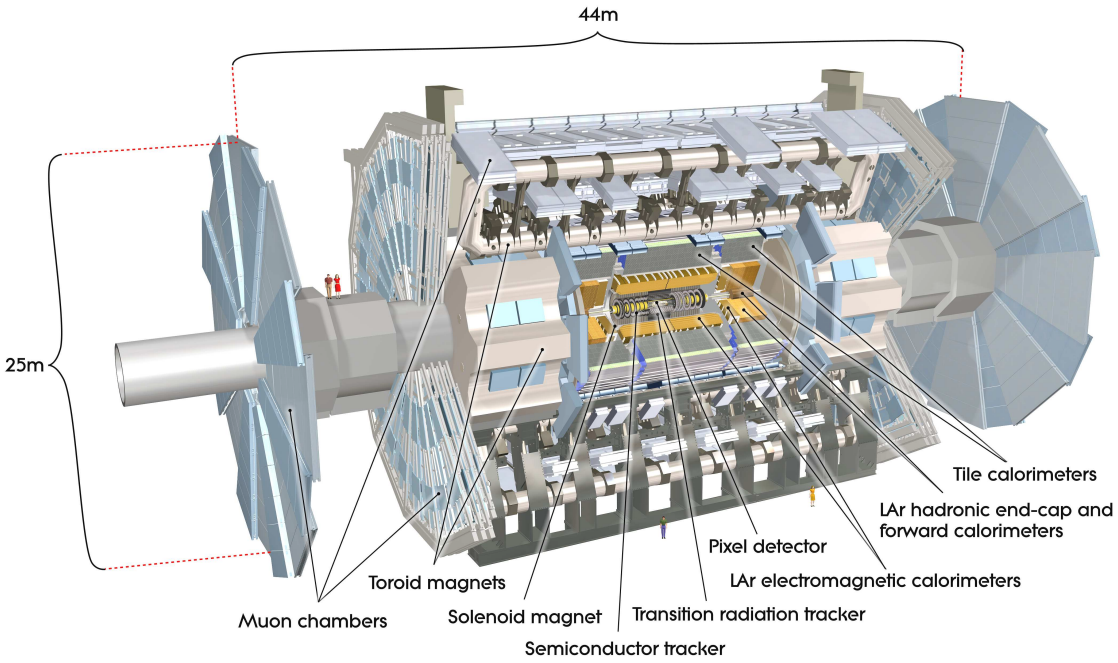

Figure 3.12: *Cut-away view of ATLAS detector.Figure taken from [56].*

3.4.1 Inner detector and solenoidal magnet

The ID of ATLAS measures the trajectories of charged particles and from the bending of the track in the solenoid magnetic field it is possible to determine the particle momentum. The ID consists of tree parts: The Pixel detector (Pixel), the SMT and the Transition Radiation Tracker (TRT). The placement of the components is depicted in Figure 3.13.

The Pixel detector is installed as the first detector layer around the beam axis. The central part has four barrel layers and three disk layers on each side. The innermost barrel layer was installed during the long technical stop. It is called Insertable b-layer (IBL), because it improves the measurement of secondary vertices from long-lived B-hadrons. The layers are design to cover the full ϕ-angle and reach the pseudo-rapidity region up to $|\eta| < 2.5$ with at least three layers (barrel or end-cup). The Pixel detector is named by it's detecting technology. It is a rectangular semiconductor detector with a pixel size of $50 \times 400\,\mu m^2$, oriented such that the ϕ-coordinate is measured by the coordinate with the smaller pixel size and such higher resolution.

Around the Pixel detector the SCT is installed. It has four layers in the barrel region and nine disks in the end-cap region on each side. The SCT consists of semiconductor strips with a pitch of about 80 µm. In the barrel layers the readout is double-sided and oriented to the beam-line with a relative stereo angle of ± 20 mrad. The end-cap disks have strips organized perpendicular to the beam-line with repeating ± 20 mrad stereo angle among different layers. The SCT has a full ϕ-angle coverage and detects particle with a pseudo-rapidity of $|\eta| < 2.5$ with at least four layers. Both Pixel and SCT operate at a temperature range of $(-10\text{-}-5)\,°C$.

The last and the outermost part of the ID is the TRT. It consists of three modules in the barrel and twenty end-cap modules. The detector is build out of straws with a diameter of 4 mm which are filled with a Xe-CO_2 gas mixture. The xenon absorbs low-energy transition radiation photons and amplifies them to measurable signal amplitudes. The gold plated anode tungsten wires, which are in the center of each

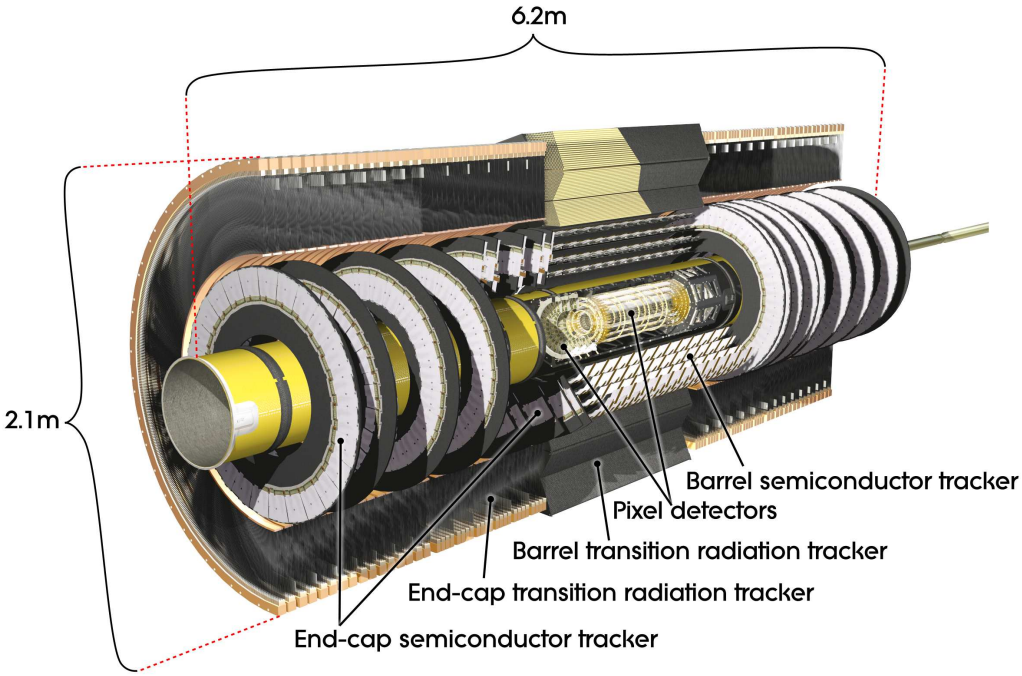

Figure 3.13: *Cut-away view of ATLAS inner detector system.*

straw, are read-out on each side of the straw. Each module consists of many layers of tubes which assures typically 36 hits per track. The TRT provides only $r-\phi$ information in full ϕ-angle coverage and particles up to $|\eta| < 2.0$ pass at least three modules of the TRT.

Key ingredient for the momentum measurement of charged particle with tracking detectors is the magnetic field. The magnetic field with a strength of 2 T for the ATLAS ID is generated by a current of 7.73 kA in a superconducting coil. The coil has a zylindrical shape with 5.3 m length and 2.4 m diameter. It is placed between the ID and the electromagnetic calorimeter inside a cryostat which keeps the operating temperature of 4.2 K.

3.4.2 Electromagnetic and hadronic calorimeters

The information of the calorimeter is not used in the p_{T}^{Z} analysis in Chapter 5, therefore the ATLAS calorimeter system is discussed very briefly. The most important function for the p_{T}^{Z} measurement is that it provides enough shielding material, hence only muons are able to pass through and reach the MS. The cut-away view of the ATLAS calorimeters is shown in Figure 3.14.

The ATLAS calorimeter consists of the electromagnetic in the inner part and the hadronic calorimeter in the outer part. The electromagnetic calorimeter is a LAr sampling calorimeter with lead absorber and accordion structure over its full coverage in both barrel ($|\eta| < 1.475$) and end-cap ($1.375 < |\eta| < 3.2$) regions. The electromagnetic calorimeter has more than 22 radiation length.

The hadronic calorimeter has three barrels with a steel-scintillator-tile structure, one in the center region $|\eta| < 1$ and one per each side of $0.8 < |\eta| < 1.7$, sharing the cryostat with the end-cap calorimeters. The hadronic end-cap and forward calorimeter are LAr energy-samplers installed in the region $1.5 < |\eta| < 3.2$ and $3.1 < |\eta| < 4.9$. The total material thickness including the electromagnetic calorimeter material is more than 4.5 interaction lengths.

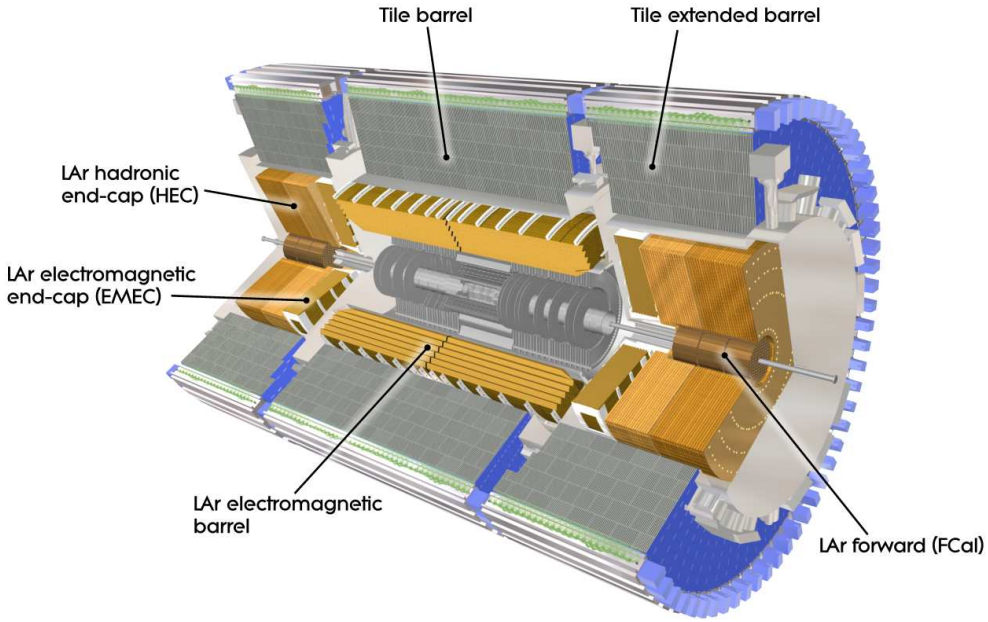

Figure 3.14: *Cut-away view of ATLAS calorimeter system.*

3.4.3 Muon chambers and toroidal magnet

The principle of the muon identification is the same for ATLAS and DØ. It is based on the fact that muons are the only high-momentum charged particles leaving the calorimeter system. Therefore, it is possible to use the same track momentum measurement principle as in the ID. The only difference is the orientation of the magnetic field, which is toroidal. Consequently the detectors are designed to be more sensitive in the longitudinal angle θ than the ϕ-angle.

Every part of the ATLAS muon spectrometer consists of a barrel in the central region and wheels in the end-cap regions on each side. There are four types of detectors: Monitored Drift Tubes (MDT), Cathode Strip Chambers (CSC), Resistive Plate Chambers (RPC) and Thin Gap Chambers (TGC). While, the last two, RPC and TGC, are working as trigger chambers, the first two are installed to provide a precise muon momentum measurement. The MS detectors and the toroidal magnet are shown in Figure 3.15.

The muon spectrometer magnet system is divided into a barrel region and an end-cap region on each side. A toroidal magnetic field with a strength of 4 T is created by supper conductive coils with a current of 20.5 kA. The barrel part is 25.3 m long and the outer diameter is 20.1 m. The inner diameter is defined by the size of the hadronic calorimeter. One end-cap toroid is 5 m long and it has a diameter of 10.7 m. The cryostat system ensures that all superconductive component are cooled down to it's operating temperature of 4.7 K

The barrel region is organized in three layers. Each layer consist of sixteen overlapping MDT modules. Each module consist of three to eight layers of drift tubes oriented parallel to the beam axis. The tubes have a diameter of 3 cm and are filled with an Ar-CO_2 gas mixture. The main measurement is done in the z-plane with a precision of 30 µm. The MDT modules cover almost the full ϕ-angle, except region where support structures for the toroid magnet and the MS are placed. All three barrel layers (i.e. twenty measurements per track) covers a pseudo-rapidity range of $|\eta| < 1.05$.

The RPC provide a fast measurement time (1.5 ns) with track hit information in

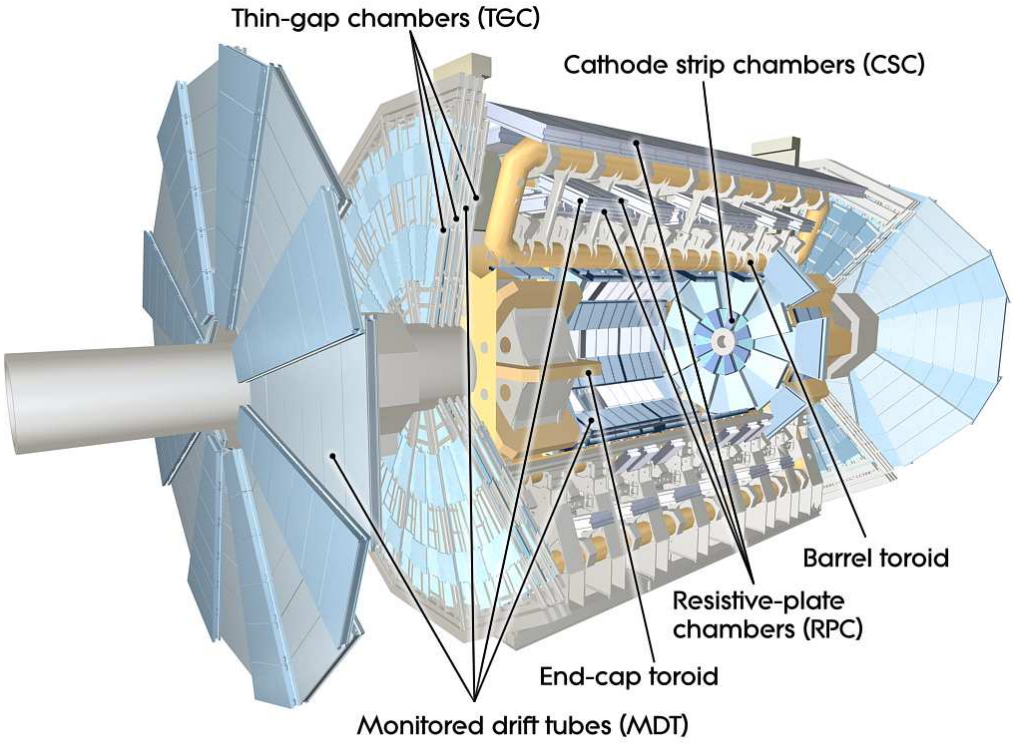

Figure 3.15: *The cut-away view of ATLAS muons spectrometer*

both z and ϕ coordinates. Consequently, the RPC modules are used for triggering and also provide additional information of the ϕ coordinate to the MDT. The RPC modules are installed in three layers: above and below the middle MDT modules and above the last MDT modules. Each module consists of parallel electrode plates and the gas volume is divided by a resistive plate, hence the name of detector. The resolution in both ϕ and z directions is 10 mm. The $\eta - \phi$ coverage is the same as for the barrel MDT with six measurements per track.

The MS end-caps are organized in three disk-shaped layers on each side of the detector. The θ angle precision measurement in the end-cap region is mostly provided by MDT chambers in a pseudo-rapidity region of $1.1 < |\eta| < 2.7$. Only the first layer in the forward region $2.0 < |\eta| < 2.7$ is occupied by CSC. The particle densities are higher in this region and therefore a faster detection is needed. The CSC is a multi-wire chambers with cathode strips perpendicular to the wires. The sixteen modules with two chambers back-to-back provide four measurements of the η and ϕ coordinate per track with 30 µm precision.

The muon trigger detectors in the end-cap region are organized in a similar way as in the barrel, but with TGC modules in four layers. One layer is mounted before each innermost and middle MDT chambers and two layers are mounted after the middle MDT chamber. The TGC, in addition to triggering, provide a supplementary measurement of ϕ-angle for the MDT chambers in end-cap. The detector is a multi-wire proportional chamber with a specific smaller wire-to-plate distance than wire-to-wire distance. The spatial coverage is the same as for the end-cap MDT and the measurement resolution of r and phi is $(2\text{-}6)$ mm and $(3\text{-}7)$ mm, respectively.

The knowledge of the muon chambers alignment on long distances is crucial for a precise track-momentum measurement. Therefore, each detector module was constructed with high precision and measured after production. The module-to-

module alignment is measured by a laser system and imaging sensors. It measures the deviations from a straight line for three points. This can be done online during data taking and therefore it can provide a hit position correction for each run.

3.4.4 Trigger system

The trigger system of the ATLAS detector has two stages, a hardware trigger stage L1, and a software trigger stage High Level Trigger (HLT). The triggers are designed [57] to reduce the number of recorded events and keep only events with interesting physics. The trigger system has decision chains which corresponds to different criteria on each level. The trigger conditions before and during 2015 are different. The average trigger rates are increased by a factor 2-2.5 between $\sqrt{s} = 7$ and 13 TeV for the same luminosity and the same trigger criteria. More details about trigger changes after the detector upgrade can be found [57]. Since in Chapter 5, only the muon trigger is used, only muon-related details are described below. More information about triggers menus can be found in [57].

The main requirement for the L1 trigger is to provide an event rate reduction from almost 40 MHz down to 100 kHz (75 kHz before 2015) In the first stage, L1, needs to be quick. Therefore, it was designed and manufactured on specialized electronic card for each detector part.

The L1 muon trigger starts with the identification of muons by a time and space coincidence in the muon trigger chambers. The muon momentum is estimated by comparing the deviation from a straight-line trajectory with expected deviations from six pre-calculated momentum thresholds in a range of (5-35) GeV. The decisions, together with the RoI are seeded to the HLT.

The HLT consisted of two stages before 2015, the fast, less accurate Fast software trigger (L2) and the slower, more precise Event Filter - precise software trigger (EF). From 2015 onwards these two stages are executed as one step, while the algorithm stays the same. The HLT decision is software based and distributed over a computing farm. On the first load, the event is reconstructed only partially and a fast decision is made, this corresponds to the previous L2 stage. If the event fulfilled the criteria, the remaining data is loaded and the event is fully reconstructed. This stage corresponds to the previous EF. Due to the sequential loading of data and partial reconstruction the trigger has the same processing but shorter loading time.

The information from L1 is seeded into the HLT processing. The event rate of 100 kHz from L1 is reduced to an output rate of 1 kHz (400 Hz before 2015). This is possible due to the data acquisition system bandwidth of approximately 1 GB/s.

The HLT muon trigger uses information from the MDT chambers to refine the estimated muon momentum for each L1 RoI. The hit position inside the MDT is calculated from the drift times and the track momentum is estimated by look-up tables. This fast estimation (corresponding to L2) is done only with information form the MS.

The precision reconstruction stage (former EF) uses the previous MS-only RoI and momentum and it extrapolate them to the ID. If no matching with a ID track is found the algorithm extrapolates ID tracks to the MS and it tries to find combined muon candidates. The combined muon information is used for the trigger decisions in most of the muon triggers.

For the p_{T}^{Z} analysis an inclusive set of events was used from two single muon trigger menus [57]: `HLT_mu20_iloose_L1MU15` or `HLT_mu50`. The first one requests at L1 a muon with p_{T} at least 15 GeV. The HLT cuts on 20 GeV include loose isolation cuts of combined muon. The second menu uses 20 GeV muons from the L1 trigger and HLT cuts on 50 GeV with no isolation cuts.

3.4.5 Reconstruction of event data

The accepted data is stored on magnetic tapes in a raw stream from detector electronics (RAW), i.e. the digitalized output from all parts of the detector. The RAW data are processed by the ATLAS main software framework ATHENA [58]. The reconstruction described below is implemented inside the ATHENA packages. The Monte-Carlo simulation of the detector from the RAW format has identical processing steps as the data processing. The RAW Monte-Carlo event information is obtained from the generation of the physics events and the simulation of the detector response.

All steps for the Monte-Carlo simulations are incorporated into the ATHENA framework. Numerous generator are interfaced in this framework including configuration files tuned to LHC collisions. The GEANT [50] interface, with an up-to-date geometry of the detector and the used materials, is used to simulate the transition of particles through material and to simulate the response for each piece of the detector.

The reconstruction of tracks is a key ingredient for the $Z \to \mu\mu$ event reconstruction. The ID and MS are measuring the position of points (hits) where particles pass through the detector volume. A set of hits is gathered together into clusters which improves the spatial information. The trajectory of charged particle is bended in the magnetic field. A set of algorithms find the curved trajectory by fitting the cluster positions. The track momentum is calculated from the track bending radius and a precise modeling of the magnetic field.

The track is described by six parameters: a spatial point and a momentum vector. The momentum vector is frequently described in ϕ, η and p_{T} coordinates. The spatial point is chosen as the closest point of the track to the beam-line. This is usually described in detector Cartesian coordinates. The distance of the track along the beam-line z_0 is defined with respect to the beam spot, i.e. the point where both beams are focused to. The perpendicular distance d_0 is defined as the distance between the beam-line and the track.

A vertex is defined as the point in space which has at least three intersecting tracks. The primary vertex is the one with the highest scalar momentum sum of tracks associated to this vertex.

The muon reconstruction starts from measured hits in the MS. Cluster are created by a straight line fit of hits per each MDT module in η direction. The ϕ coordinate is estimated by the measurements from the trigger-chambers. The search algorithm reconstructs the tracks from three layers starting with the middle one.

To improve the spatial and momentum measurement of muons, the track is combined with the track reconstructed in the ID. The combination of the ID and the MS tracks is done after both tracks were indecently reconstructed. Afterwards, the MS track is extrapolated to the ID region and associated to one ID track. During the association procedure MS hits can be added or removed in order to improve the fit results. If no ID track is found for the MS track the reverse approach is used, i.e. the ID tracks are extrapolated to MS and associated to MS tracks.

Part II

Precision measurements at hadron colliders

4. Development of Drell-Yan integrator

The main topic of this chapter is the development of software for the cross section calculation of vector boson production in hadron-hadron collisions. Since fully differential calculations are not available on a analytical basis, complex numerical integration algorithms are used in particle physics.

The chapter gives first a brief overview of selected, publicly available computer programs and describes their approaches to the modeling of the $h_1 + h_2 \to V \to \ell_1 + \ell_2$ process (Section 4.1). The Section 4.2 is focused on the DYRES program as well as the developed improvements of its performance. In the last section, the benchmark of DYRES against its improved version DYTURBO is presented and discussed.

4.1 Available Tools for Vector Boson Predictions

Monte-Carlo generators in high energy physics are typically used to calculate the cross section of defined particle reactions. The general purpose of a Monte Carlo event generator is the integration a scattering matrix over given phase space interval. Every modern event generator that aims at the description of hadron collisions is based on the QCD factorization theorem Equation 2.21, however, the integration itself is performed by different numerical and semi-numerical methods. For the Drell-Yan process, the simple integration of the transverse momentum of vector boson q_{T} is divergent for $q_{\mathrm{T}} \to 0$. Clearly, this is not observed in nature due to the soft and collinear gluon emission from the incoming parton. Two techniques are used within modern event generators to treat this phenomena: parton showering (PS) and analytical q_{T} resummation.

Typically, the general purpose Monte-Carlo generators [59, 60] are based on parton showering models (POWHEG [61], HERWIG [62], SHERPA [63]). Here, the calculation starts by generating partons from two hadron beams described by parton distribution functions. The next step is to simulate the parton splitting based on the QCD splitting functions. This splitting processes can be interpreted as Initial State Radiation (ISR). The partons after the ISR are used for the calculation of the hard scattering process. This hard scattering processes can be described by perturbation theory using fixed order calculations. One of the simplest examples is the born-level Drell-Yan production process, i.e. $q\bar{q} \to V \to \ell\ell$.

Many programs, which model only the hard scattering, can be interfaced to parton shower generators. Consequently, the information about the underlying event is available and can be used in detector response modeling. The complication with this approach origins from higher-order calculations, where additional parton splitting is predicted within the hard scattering (e.g. $qg \to qV$) itself. Here, a matching between the parton shower and the matrix element calculation has to be performed in order to avoid double counting. The general strategies are based on re-weighting methods, veto-algorithms or their combinations. Tree-level generators typically use the CKKW [64] or MLM [65] schemes. further higher-order parton shower corrections are process dependent. For example, the PYTHIA uses correction only for first parton branching, while HERWIG corrects for hardest emission. Several groups (POWHEG, MiNLO [66] and GENEVA [67]) advanced these matching techniques to higher-order calculations. In

particular, the POWHEG algorithm extends the CKKW formalism to NLO level and it is currently widely used at the LHC.

Another approach (described in more detail in Section 2.3) for the treatmeant of soft and collinear gluon emission relies on the resummation formalism. The analytical resummation uses the expansion of all α_S orders inside scattering matrix. The matching of a resummed prediction to the real parton emission is complicated, leading to the fact that most resumed-based generators (e.g. RESBOS [52], DYRES [68], CUTE [69], etc) have no event information on the recoiling hadronic activity.

An overview of the available tools for the prediction of the Drell-Yan process is given in Table 4.1. The second column shows the highest implemented order in the strong coupling constant. The actual process is given in the third column, where nj refers to number of modeled jets and PS indicates that the underlying shower is modeled. When the output of a certain program can be interfaced to a parton shower program, it is indicated by +PS in the third column. A fully differential lepton cross section can be predicted by listed programs except CUTE.

Program name	Hard scattering highest order	Generated information	Calculation method
PYTHIA [51]	$\mathcal{O}(1)$	$W/Z + PS$	Matrix-element correction for first branching
HERWIG [62]	$\mathcal{O}(1)$	$W/Z + PS$	Matrix-element correction for hardest branching
SHERPA [63]	$\mathcal{O}(\alpha_S^n)$	$W/Z + nj + PS$	CKKW, large n available
MC@NLO [70]	$\mathcal{O}(\alpha_S)$	$W/Z(+PS)$	PS matching, interface to HERWIG
POWHEGBOX [71]	$\mathcal{O}(\alpha_S)$	$W/Z(+PS)$	PS matching, interface to PYTHIA or HERWIG
POWHEG+MiNLO [66]	$\mathcal{O}(\alpha_S^2)$	$W/Z(+PS)$	NNLOPS matching
GENEVA [67]	$\mathcal{O}(\alpha_S^2)$	$W/Z(+PS)$	interface to PYTHIA, NNLL' thrust resummation
ALPGEN [72]	$\mathcal{O}(\alpha_S^n)$	$W/Z + nj(+PS)$	interface to PYTHIA or HERWIG, large n available
MADGRAPH [73]	$\mathcal{O}(\alpha_S^n)$	$W/Z + nj(+PS)$	interface to PYTHIA, large n available
MCFM [74]	$\mathcal{O}(\alpha_S^3)$	$W/Z + nj$	up to $n = 2$ available
FEWZ [75]	$\mathcal{O}(\alpha_S^2)$	W/Z	
DYRES [68]	$\mathcal{O}(\alpha_S^2)$	W/Z	NNLL q_{T} resummation
RESBOS [52]	$\mathcal{O}(\alpha_S^2)$	W/Z	NNLL q_{T} resummation
CUTE [69]	$\mathcal{O}(\alpha_S^2)$	W/Z	NNLL q_{T} resummation, no lepton kinematics

Table 4.1: *Selected Drell-Yan generators with the highest implemented order and used method of calculation. A possible interface to a parton shower program is marked by $(+PS)$. The table is adapted from [76], with data obtained from reference present in each row.*

The two main Drell-Yan programs used in this thesis are the Drell-Yan Monte-Carlo generator using resummation calculation (RESBOS) and the Drell-Yan Monte-Carlo integrator (DYTURBO), both based on q_{T} resummation. While RESBOS is used for the W mass measurement, DYTURBO is a newly developed program, which implements various numerical and optimization techniques on top of the Drell-Yan Monte-Carlo integrator (DYRES). Both generators are described in more detail in the following text.

The calculation used in the RESBOS generator is based on the CSS formalism (see Section 2.3.2). The computation uses an effective method to separate the actual calculation into two steps. The first step used the LEGACY [77] code and evaluates the matrix element coefficients W and Y (see Equation 2.33) for a dense grid of different values of q_{T}, Q, y. The resulting grid file serves as input for the second program RESBOS [78], which generates random boson kinematics according to the grid. The program generates phase-space points for leptons from the boson decay and it calculates the cross section for each point. This cross section is taken as weight and given to the Monte-Carlo integration method (Vegas) [79] , which assures the optimization of the phase space generation. The program RESBOS itself is very fast. The model parameters of this code have been tuned to data recorded at the Tevatron. A serious disadvantage of RESBOS is the fact, that the LEGACY itseld is not public[1]. Without access to LEGACY, external users cannot modify the model parameters, i.e. cannot fit and tune the predictions to new measurements at the LHC. This triggered to development of DYRES and DYTURBO, described in the following.

The DYRES program is also based on CSS q_{T} resummation formalism for the Drell-Yan process at hadron collision. It is written in `Fortran`. Also here, the actual cross section calculation is separated into two terms: The resummed and the finite part, schematically written as

$$\frac{\mathrm{d}\hat{\sigma}^{()}}{\mathrm{d}q_{\mathrm{T}}^2} = \frac{\mathrm{d}\hat{\sigma}^{(\mathrm{res.})}}{\mathrm{d}q_{\mathrm{T}}^2} + \frac{\mathrm{d}\hat{\sigma}^{(\mathrm{fin.})}}{\mathrm{d}q_{\mathrm{T}}^2} \,. \tag{4.1}$$

The resummation of logarithms is carried out in the impact parameter space b, which is the conjugated variable to q_{T} via Fourier transformation. The resummed cross section $\frac{\mathrm{d}\hat{\sigma}^{(\mathrm{res.})}}{\mathrm{d}q_{\mathrm{T}}^2}$ is obtained by a zero-order Hankel transformation, given by

$$\frac{\mathrm{d}\hat{\sigma}^{(\mathrm{res.})}}{\mathrm{d}q_{\mathrm{T}}^2} = \int_0^\infty \frac{\mathrm{d}b}{2\pi} b J_0(bq_{\mathrm{T}}) \cdot \mathcal{H}^{N_1,N_2} \cdot \exp \mathcal{G}^{N_1,N_2} \tag{4.2}$$

where the function $\mathcal{G}^{N_1,N_2}$ includes the Sudakov form factor and further process independent collinear-evolution terms. Here the resummed logarithms are calculated up to leading log, next-to-leading log and next-to-next-to-leading log accuracy in the strong coupling constant. The function $\mathcal{H}^{N_1,N_2}$ includes hard-virtual and collinear contributions for a given specific process, but is independent from the impact parameter b and contains NLO/NNLO corrections to the born level process. Both functions $\mathcal{G}^{N_1,N_2}$ and $\mathcal{H}^{N_1,N_2}$ are defined in the so-called double Mellin-space[2] [80].

The fixed order prediction is divergent for $q_{\mathrm{T}} \to 0$. To obtain the finite term from Equation 4.1 it is necessary to subtract the expansion of resummed part at same perturbative order, i.e.

$$\frac{\mathrm{d}\hat{\sigma}^{(\mathrm{fin.})}}{\mathrm{d}q_{\mathrm{T}}^2} = \frac{\mathrm{d}\hat{\sigma}^{(\mathrm{f.o.})}}{\mathrm{d}q_{\mathrm{T}}^2} + \frac{\mathrm{d}\hat{\sigma}^{(\mathrm{res.}\to\mathrm{f.o.})}}{\mathrm{d}q_{\mathrm{T}}^2} \,. \tag{4.3}$$

[1] It was announced that `RESBOS-v2.0` will include a public version of LEGACY

[2] defined by the two momentum fractions of incoming partons

The counter-term $\frac{\mathrm{d}\hat{\sigma}^{(\text{res.}\to\text{f.o.})}}{\mathrm{d}q_{\mathrm{T}}^2}$ has the structure of a truncated $\frac{\mathrm{d}\hat{\sigma}^{(\text{res.})}}{\mathrm{d}q_{\mathrm{T}}^2}$ from Equation 4.2, where the terms inside $\mathcal{G}^{N_1,N_2}$ are not resummed to all $\mathcal{O}\left(\alpha_S^n\right)$, but only up to $\mathcal{O}\left(\alpha_S\right)$/$\mathcal{O}\left(\alpha_S^2\right)$ for the NLO/NNLO counter term.

The fixed order cross section $\frac{\mathrm{d}\hat{\sigma}^{(\text{f.o.})}}{\mathrm{d}q_{\mathrm{T}}^2}$ is calculated by using the published code of the `MCFM` [74] generator package. This program is able to calculate the W/Z prediction up-to NNLO (i.e. $\mathcal{O}\left(\alpha_S^2\right)$). The NLO calculation (program option `order=1`) contains one 7-dimensional integral, denoted as as `VJ` or `VJLO` in the following. For the calculation of the NNLO prediction (`order=2`) two integrals, i.e. terms, have to be calculated. The two-loop virtual correction are calculated in the first 8-dimensional integral. This integral has a positive contribution to the cross section for $q_{\mathrm{T}} < 30\,\mathrm{GeV}$ and it is labeled as `VJVIRT`. The second integral `VJREAL` has ten-dimensional integration domain and apart from real parton emission it includes also Catani-Seymour subtraction mechanism to avoid double counting between real and virtual contributions. This subtraction method has large impact on convergence speed of the integral, since the corresponding term has a negative contribution to the cross section for $q_{\mathrm{T}} < 30\,\mathrm{GeV}$ and it cancels out with virtual part. Consequently, the overall convergence speed of NNLO prediction depends largely in the treatment of this term.

To summarize the structure of calculations used in DYRES at Next-to-Next-to-Leading logarithms (NNLL) +NNLO, it is convenient to write schematically the cross section as

$$\begin{aligned}\frac{\mathrm{d}\hat{\sigma}^{(\text{NNLL+NNLO})}}{\mathrm{d}q_{\mathrm{T}}^2} &= \frac{\mathrm{d}\hat{\sigma}^{((\text{res.}))}}{\mathrm{d}q_{\mathrm{T}}^2} - \frac{\mathrm{d}\hat{\sigma}^{((\text{f.o.,real}))}}{\mathrm{d}q_{\mathrm{T}}^2} + \frac{\mathrm{d}\hat{\sigma}^{((\text{f.o.,virt}))}}{\mathrm{d}q_{\mathrm{T}}^2} - \frac{\mathrm{d}\hat{\sigma}^{((\text{f.o.}\to\text{res.}))}}{\mathrm{d}q_{\mathrm{T}}^2} \\ &= \frac{\mathrm{d}\hat{\sigma}^{(\text{BORN})}}{\mathrm{d}q_{\mathrm{T}}^2} - \frac{\mathrm{d}\hat{\sigma}^{(\text{VJREAL})}}{\mathrm{d}q_{\mathrm{T}}^2} + \frac{\mathrm{d}\hat{\sigma}^{(\text{VJVIRT})}}{\mathrm{d}q_{\mathrm{T}}^2} - \frac{\mathrm{d}\hat{\sigma}^{(\text{CT})}}{\mathrm{d}q_{\mathrm{T}}^2}\end{aligned} \tag{4.4}$$

where the signs before terms represents the sign of contribution to the total cross section. The superscripts of terms in first row follow the name convention used in DYRES [68], while the superscripts of terms in the second row are following name-convention used in DYTURBO. Each term represents one Vegas numerical integration and is consequently uncorrelated between phase space points.

4.2 Calculation Strategy and Speed Improvement

In order to create a DYRES prediction that has a comparable statistical precision as the current LHC data sets, approximately 10^8 CPU hours are required. Even by using a parallelization scheme to allow the usage of ten thousand cores, the calculation would still require 10^7 s, i.e. approximately three months. Therefore, the program DYTURBO was developed as a speed and precision improved version of the original DYRES code.

Although, `Fortran` has several computational advantages over other programming languages, it is not suitable for larger projects or front-end frameworks. Therefore, as a first step, a C++ framework was developed, which is in control of the program execution, the calculations, the processing of input files and the interpretation of command-lines. It allows for a simple interface for additional user-specific calculations. The framework itself is not directly linked to the actual speed-optimization of the underlying calculations, however it makes it easier to introduce the speed improvements in a second step. The program is controlled by a text input file with an intuitive syntax.

The original DYRES program is able to split the actual calculation into a resummation term and a finite order term. However, as is shown in Equation 4.4 there are four independent integrals at NNLL+NNLO. Therefore, it was chosen to calculate each term separately at a given order to fully control the calculation process itself. This

also allows to parallelize the calculation per each term and test the optimal number of iterations per each term separately. The predictions can therefore be calculated at several orders independently, e.g. it can be chosen to only calculate to a given finite order or also to include resummed predictions. The complete list of options including the corresponding settings is given in Table 4.2.

Calculation	`order`	`fixedorder`	List of terms
LO	0	`false`	`BORN`
NLO	1	`false`	`BORN+VJ+CT`
NLL+NLO	1	`true`	`BORN+VJ+CT`
NNLO	2	`false`	`BORN+VJREAL+VJVIRT+CT`
NNLL+NNLO	2	`true`	`BORN+VJREAL+VJVIRT+CT`

Table 4.2: *List of terms needed per each order and input settings of parameters `order` and `fixedorder`.*

The first significant speed optimization is based on the improvement of `BORN` and `CT` integrands by loop unrolling (i.e. longer code but less iterations), code hoisting (i.e. move code outside of loops) and reusing quark-flavour symmetries (e.g. $\sigma(u\bar{u} \to Z) = \sigma(u\bar{u} \to Z)$). The high-level part of integrands were rewritten in `C++`, while low-level calculations of Sudakov exponent $\mathcal{G}^{N_1,N_2}$ are implemented in `Fortran`. The execution time of one integrand evaluation was improved by a factor of roughly one hundred by these code changes.

The functions $\mathcal{H}^{N_1,N_2}$ and $\mathcal{G}^{N_1,N_2}$ from equation Equation 4.2 are defined in double Mellin space of complex numbers N_1 and N_2. The Mellin moment of parton distribution functions are required for the cross section prediction and can be calculation by

$$F(N) = \int_0^1 \mathrm{d}x\; x^N f(x)\;, \tag{4.5}$$

where $f(x)$ is the relevant parton density function. After the convolution of Mellin-PDF $F(N)$ with the function $\mathcal{H}^{N_1,N_2}$, it is transformed back to x space. This is solved in DYRES by fitting the PDF at a scale μ, which equals to vector boson mass M_V, with the function

$$f(x) = x^a(1-x^b)\cdot A\left(1 + Bx + Cx^{0.5} + Dx^{1.5} + Ex^2 + Fx^3\right) \tag{4.6}$$

where $a, b, A, \ldots, F$ are fitting parameters. The calculation of Mellin moments of the polynomial function is based on the relation

$$\int_0^1 \mathrm{d}x\; x^a(1-x)^b = \frac{\Gamma(a+1)\Gamma(b+1)}{\Gamma(a+b+1)}\;. \tag{4.7}$$

with $\mathrm{Re}(a) > -1$ and $\mathrm{Re}(b) > -1$. This approach has two bottlenecks. The first one is that the polynomial approximation might be insufficient for some PDF sets e.g. those from the NNPDF group. The second bottleneck is that the fitting of PDF takes approximately 20 min during program initialization. Therefore, the Mellin moments of the PDF in DYTURBO are calculated numerically using Gaussian quadrature rules. With this approach, the numerical integration for 120 moments can be achieved in less than one second.

In general, Monte-Carlo methods can be seen as a class of algorithms for the numerical integration using random sampling techniques. In high energy physics, Monte-Carlo methods are used for n-dimensional integrationa by generating random inputs following a certain probability density function, defined on the domain of the integration. This approach is very useful since the underlying domain is usually the kinematic phase space of the produced particles, i.e. it allows to produce various kinematic distributions during one integration. In addition, it is possible to save the phase-space point under consideration together with the integrand value as weights and create a n-tuple[3] which stores this information. The resulting n-tuple can then be treated as physical event and the generated distributions can be passed to a detector simulation, finally allowing to compare theoretical predictions of the Standard model with the actual measured distributions at the experiment.

The `Vegas` [79] algorithm is a common method for numerical integrations and uses the basic principle described above. In the ideal case, the sampling probability density function (p.d.f.) is described by the absolute value of the integrand. Since one needs to know the value of the integral $\int |f|$ for this ideal case, which is typically unknown, the p.d.f. is approximated with an iterative procedure.

DYTURBO uses four iterations to optimize the sampling probability function. The number of random points N_i in each iteration i is $N_i = \frac{i}{10} \cdot N$. The number of total used random points used in all iterations, N_{calls}, is set for each `TERM`-parameter `vegasncallsTERM`. From each iteration i a sampling grid is created and it is used as input sampling for the iteration $i + 1$. Only the last iteration $i = 4$ is used to create the final distributions. It implies that 60 % of N_{calls} is used during the pre-conditioning, i.e. during the sampling of the phase space, and only 40 % of N_{calls} is used in final distributions, however, with a significantly improved sampling convergence.

The `Vegas` implementation in DYTURBO is taken from the `CUBA` [81] package. The `CUBA` library implements parallelization methods based on the fact that the random points are independent to each other within one iteration. Therefore, integrands are evaluated in parallel on multi-core machines, which shortens the necessary time to reach the required precision. This can be illustrated by the following example, when the sum of one hundred integrations with 10^6 calls has a lower numerical precision than one integration with 10^8 calls parallelized to 100 cores, even though they have exactly same amount of integrand evaluations and both integrations take approximately the same real time. This is caused by the different number of calls used during pre-conditioning stage.

The `Vegas` algorithm is very versatile and robust against the many-dimensional domains. However, more efficient numerical methods are available for small number of dimensions $d \leq 3$. In our application, the lowest dimensionality $d = 6$ has resummed term,

$$\mathrm{d}\hat{\sigma}^{(\text{res.})} = \frac{\mathrm{d}\hat{\sigma}^{(\text{born})}}{\mathrm{d}\Omega} \hat{W}(q_{\mathrm{T}}, Q, y), \tag{4.8}$$

where the born level cross section $\frac{\mathrm{d}\hat{\sigma}^{(\text{born})}}{\mathrm{d}\Omega}$ depends on three angles: the polar angle $\cos\theta_{\text{CS}}$ and azimuthal angle φ_{CS} of lepton decay in the CSS frame, as well as, the azimuthal angle of the boson ϕ_V in its rest frame. However, the latter is trivial due to the global symmetry of rotations around beam axis. The azimuthal angle φ_{CS} enters the cross section only via the lepton kinematic cuts, i.e. is a step function with a value of one within the fiducial phase-space and zero otherwise. The born cross section dependence on $\cos\theta_{\text{CS}}$ is proportional to $(A + B\cos\theta_{\text{CS}} + C\cos^2\theta_{\text{CS}})$. Therefore, the angular dependence of $\frac{\mathrm{d}\hat{\sigma}^{(\text{born})}}{\mathrm{d}\Omega}$ can be substituted by a semi-analytical integration over the first three $\cos\theta_{\text{CS}}$ moments and the same can be applied to the counter term

[3] An n-tuple stores the event kinematics per generated event.

$\mathrm{d}\hat{\sigma}^{(\text{res.}\to\text{f.o.})}$. This means that the residual dimension of the integral is three and the quadrature rule integration can be used instead of Vegas.

The Gauss quadrature rule is a numerical method for definite integral calculations, where the integrand is approximated by a weighted sum of polynomials in several points of the integration domain. The calculation of the finite integral of polynomials is not performance expensive. The Gauss quadrature method is implemented inside of the `CUBA` packages as well as in DYTURBO. Another method of quadrature rule is the Cleshaw-Curtis cubature approach, which is implemented in the `cubature` [82] package.

As previously described, the version of DYTURBO, which was partially developed and used within this thesis, relies on several methods for term integrations. A summary of all available methods is given in Table 4.3.

Function name	Term	Dimension	Integration
`bornintegr2d`	Born level	2	Cubature rule
`bornintegrMC4d`	Born level	4	`VEGAS`
`bornintegrMC6d`	Born level	6	`VEGAS`
`resintegr2d`	Resummation	2	Cubature rule
`resintegr3d`	Resummation	3	Cubature rule
`resintegrMC`	Resummation	6	`VEGAS`
`ctintegr2d`	Counter term	2	Cubature rule
`ctintegr3d`	Counter term	3	Cubature rule
`ctintegrMC`	Counter term	6	`VEGAS`
`ctintegr`	Counter term	8	`VEGAS`
`vjintegr3d`	$V+j$ LO	3	Cubature rule
`vjlointegr5d`	$V+j$ LO	5	Cubature rule
`vjlointegr7d`	$V+j$ LO	7	`VEGAS`
`vjrealintegr`	$V+j$ NLO Real	10	`VEGAS`
`vjvirtintegr`	$V+j$ NLO Virtual	8	`VEGAS`

Table 4.3: *List of available integrand implementations inside DYTURBO.*

The missing implementation of creating n-tuples for the further analyses during the integration process might look as a time-ineffective approach to estimate the desired prediction on an event-by-event basis. However, the calculation of vector boson production cross section involves a huge amount of data that needs to be stored in order to allow for a reasonable statistics precision due to the large cancellation of several terms. Therefore, DYTURBO contains a very simple, but powerful interface to create any distribution which should be studied further. Three key options needed to be implemented:

- to define a new observable,
- to control and define kinematic cuts,
- to define a new histogram or profile.

Internally, it has to be implemented that

- the interface is available for both `Fortran` and `C++` integrands,
- the calculation of all observables is done only when requested and only once per change of kinematics,
- the definition and treatment of statistically correlated variations (e.g. PDF) is automatically performed (i.e. per each histogram),
- the correct treatment of weights from color dipoles inside `VJREAL` term is implemented,
- the ability to collect results from both `Vegas` and `Cubature` integration is foreseen,
- the any dependency on `ROOT` [83] is dropped.

The main component is the kinematic observable `Histo::Observable`, from which all observable classes are derived. This class assures that every observable is calculated only once per event (or when any kinematic cuts are changed). There are many predefined kinematic observables are available for user. The observable is not just used to fill histograms, but also to define fiducial cuts. The last part of the implementation was done for the booking and the filling of histograms and profiles. Currently, one-, two- and three-dimensional histograms are implemented as well as one- and two-dimensional profiles. Even though ROOT is a widely used tool and it is also interfaced to DYTURBO, the idea was to keep the output format extendible. Therefore, new histogram objects where developed based on `STL`.

4.3 Benchmark and Validation

Since DYTURBO contains calculation optimizations at many different stages, it is necessary to prove that the overall results of predictions are not affected by the developed improvements. Therefore, detailed benchmark tests of DYTURBO have been performed with respect to original DYRES program. The first test is to evaluate the resummation term integral for defined points within a given phase space. The chosen points are: rapidity $y = 0$, mass m equals to invariant mass of modeled vector boson and a set of vector boson p_{T}'s ranging from 1 to 30 GeV. The angular angles of leptons are integrated out. This is test has been performed for W^+, W^- and Z separately. The results are presented in Table 4.4 and confirm a full agreement between the DYTURBO and the DYRES predictions.

The next benchmark test is limited by the available computational power due to the slow convergence of original DYRES program. The results are represented by plots of differential cross section with respect to boson p_{T} on Figure 4.1 (a,c,e) for Z, W^+, W^-, respectively. The prediction of DYRES is marked as green, the DYTURBO prediction is shown as orange. The agreement is always within statistical precision of DYRES.

A further benchmark test compares two approximations of parton density functions, which are used in DYTURBO for the transformation of PDFs into Mellin space Figure 4.1 (b,d.f). The first one, used also in DYTURBO, is polynomial approximation (see Equation 4.6). It is indicated as orange and is exactly equivalent to the prediction shown in Figure 4.1 (a,c,e). The second and faster method is to calculate the transformed PDF for a given set of Mellin moments using the quadrature rule during the numerical integration. The corresponding results are marked as blue color. The difference is in the order of $0.5\,\%$ which is caused by the incorrect matching of different flavours in calculation. This problem was fixed at later stage.

The last benchmark test compares the numerical integration algorithms. This is tested by differential cross section with respect to Z boson p_{T} in Figure 4.2. The blue color is represents the results of the VEGAS, while the green color indicates the results of the Gauss quadrature rule integration. The observed differences are within the statistical uncertainties, mainly caused by the VEGAS integration.

In summary, DYTURBO is able to calculate the precise prediction of fully differential cross section significantly faster than the original DYRES. The speed improvements can be illustrated on a calculation of p_{T}^{Z} distribution. While the original code would require approximately 10^8 CPU hours to produce the p_{T}^{Z} distribution with statical accuracy comparable to the data, the same precision can be obtained with DYTURBO in less than ten CPU hours.

The program is publicly available and it is possible to tune most of the physical and computational parameters. This allows for the application of a large variety of physics problems. In fact, the developed improvements make DYTURBO a versatile tool which can be applied to studies demanding a precise prediction for the modeling of the vector boson production in hadron collisions.

One example is the evaluation of theoretical uncertainties of W boson mass. Here, it can be used to estimate the effect of QCD modeling as well as the effects of limited knowledge of parton distributions inside the colliding protons.

Also, the speed improvement of the differential cross section calculations allows to generate multiple predictions with altered parameters, e.g. α_S. This feature is used in Chapter 5 to compare predictions to the measured distribution of the Z boson transverse momentum and thus extract the value of α_S.

p_T	Z		W^-		W^+	
(GeV)	DYRES	DYTURBO	DYRES	DYTURBO	DYRES	DYTURBO
1	5.865 45	5.865 45	44.0897	44.0897	37.4086	37.4087
2	10.1664	10.1664	77.2641	77.2641	65.8491	65.8491
3	12.3898	12.3898	95.1492	95.1492	81.5767	81.5767
4	12.986	12.9861	100.196	100.196	86.4266	86.4266
5	12.655	12.655	97.4765	97.4765	84.527	84.527
6	11.9066	11.9066	91.1827	91.1827	79.4076	79.4076
7	11.0183	11.0183	83.7393	83.7393	73.1715	73.1715
8	10.1199	10.1199	76.2878	76.2878	66.8395	66.8395
9	9.2632	9.2632	69.2812	69.2812	60.8356	60.8356
10	8.473 34	8.473 34	62.8858	62.8858	55.322	55.322
11	7.753 89	7.753 89	57.1207	57.1207	50.3299	50.3299
12	7.102 96	7.102 96	51.954	51.954	45.8405	45.8405
13	6.515 73	6.515 74	47.3337	47.3337	41.8147	41.8147
14	5.986 38	5.986 39	43.2023	43.2023	38.2066	38.2066
15	5.508 98	5.508 98	39.5044	39.5044	34.9709	34.9709
16	5.077 92	5.077 92	36.1891	36.1891	32.065	32.065
17	4.688 09	4.688 09	33.2108	33.2108	29.4506	29.4506
18	4.334 89	4.334 89	30.5295	30.5295	27.094	27.094
19	4.014 27	4.014 27	28.1101	28.1101	24.9651	24.9651
20	3.722 66	3.722 66	25.9224	25.9224	23.038	23.038
21	3.4569	3.4569	23.9397	23.9397	21.2898	21.2898
22	3.214 24	3.214 24	22.1391	22.1391	19.7008	19.7008
23	2.992 27	2.992 27	20.5006	20.5006	18.2537	18.2537
24	2.788 84	2.788 84	19.0066	19.0066	16.9332	16.9332
25	2.602 09	2.602 09	17.6419	17.6419	15.7261	15.7261
26	2.430 37	2.430 37	16.3931	16.3931	14.6208	14.6208
27	2.272 22	2.272 22	15.2485	15.2485	13.6071	13.6071
28	2.126 34	2.126 34	14.1977	14.1977	12.6758	12.6758
29	1.991 59	1.991 59	13.2315	13.2315	11.8191	11.8191
30	1.866 95	1.866 95	12.3419	12.3419	11.0298	11.0298

Table 4.4: *Comparison between DYRES and DYTURBO differential cross section of resummed term at fixed values of $y = 0$, $m = m_V$, $\cos\theta = 0$, and various values of p_T. The differential cross section are given in fb/GeV^2.*

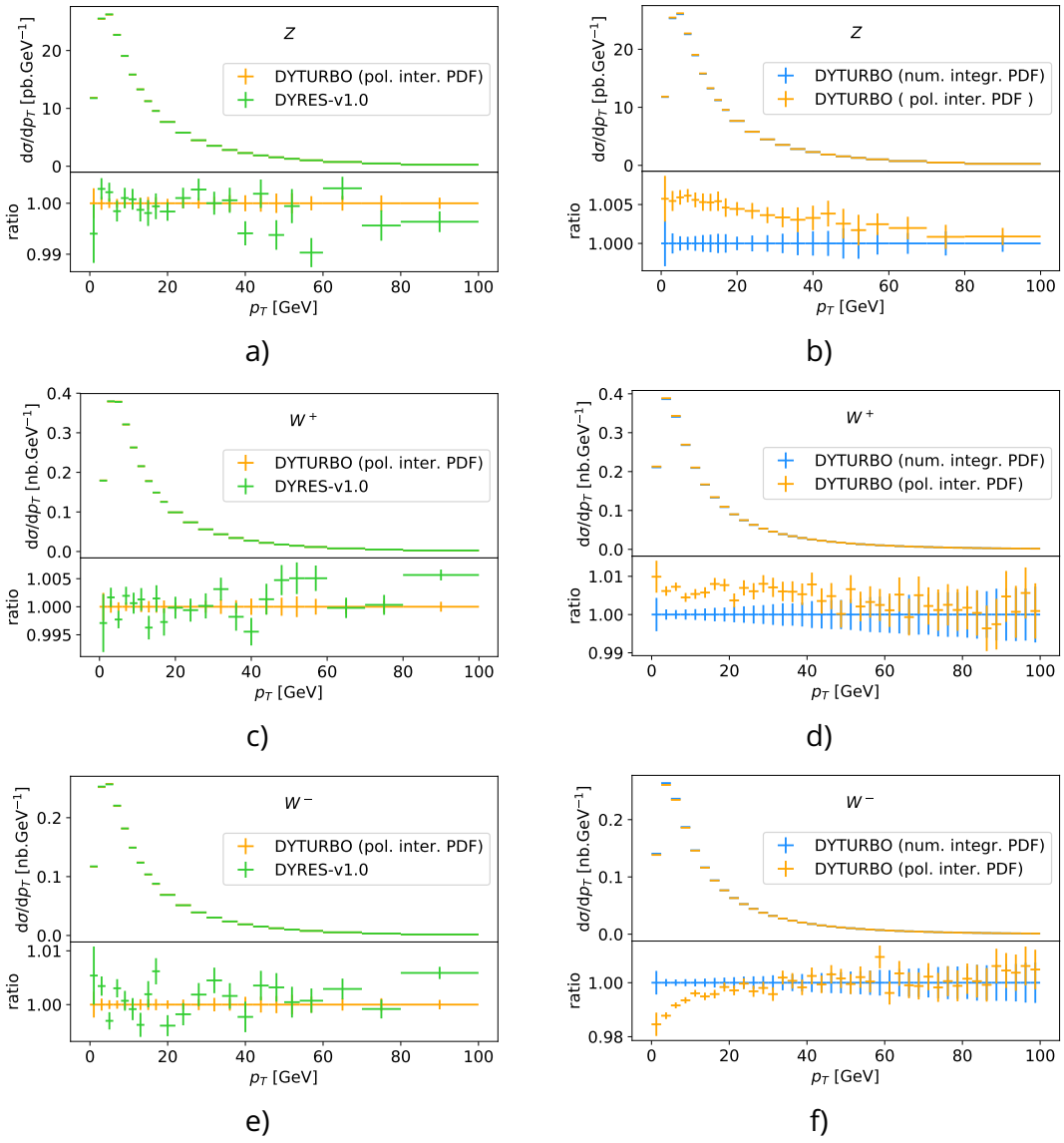

Figure 4.1: *Differential cross section (upper part) and ratio (lower part) with respect to p_{T} of the Z (a,b), W^+ (c,d) and W^- (e,f) bosons. The prediction of DYRES, DYTURBO with polynomial and DYTURBO with numerical transformation of PDF is marked by green, orange and blue color. Further information is given in the text.*

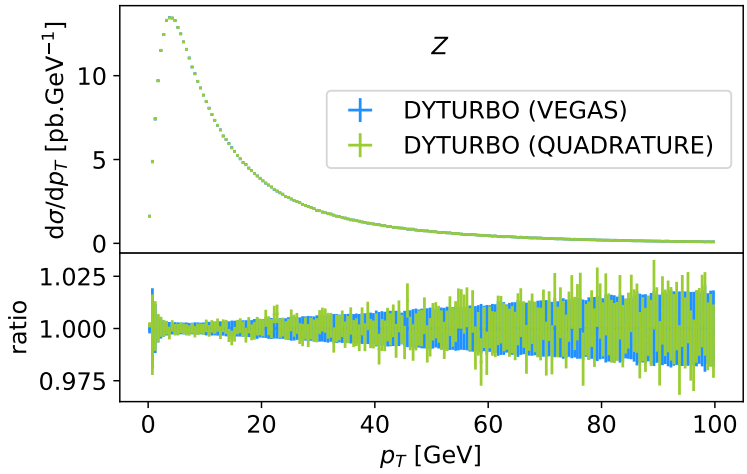

a)

Figure 4.2: *Differential cross section (upper part) and ratio (lower part) with respect to p_{T} of the Z boson. The integration using VEGAS and quadrature rule is marked by blue and green color, resp.*

5. Detemination of strong coupling constant

The strength of the strong interaction is represented by the fundamental coupling constant α_S. The transverse momentum of a vector boson which is produced during a hadron collision, depends dominantly on the initial state parton radiation, i.e. a QCD process involving directly the strong coupling constant. Consequently, the Z boson transverse momentum distribution p_{T}^{Z}, which can be reconstructed from the di-muon decay of Z, is sensitive to the value of α_S. This is the main idea of the $\alpha_S(M_Z^2)$ extraction from the p_{T}^{Z} distribution which is presented in this chapter.

There are three main steps for the estimation of the $\alpha_S(M_Z^2)$ value from p_{T}^{Z} distribution:

1. Measurement of the p_{T}^{Z} distribution with the ATLAS detector and unfolding of the spectrum to the fiducial region.
2. Calculation of the p_{T}^{Z} prediction for different values of $\alpha_S(M_Z^2)$.
3. Extraction of the α_S value by comparing predictions to the unfolded p_{T}^{Z} distribution.

This chapter describes the extraction of the strong coupling constant $\alpha_S(M_Z^2)$ as follows: the methodology and terminology for the measurement of $\alpha_S(M_Z^2)$ is introduced in Section 5.1. The measurement of Z boson transverse momentum p_{T}^{Z} with ATLAS detector using the muon decay channel is described in Section 5.2. The result of the $\alpha_S(M_Z^2)$ value extraction is discussed in Section 5.3.

5.1 Measurement Strategy

In the following text the terminology and methods used in the analysis are defined.

The distribution of the Z transverse momentum is measured in a series of N intervals called bins. The counting of observed events is done per bin and therefore the result (histogram) is a discrete representation of a continuous distribution. Since the histogram and distribution represent the same information, they are often interchanged. In this analysis the shape of p_{T}^{Z} distribution is of interest, hence the number of observed events in each bin is divided by the total number of observed events.

The choice of number of bins usually reflects the resolution of the detector. An ideal detector with unlimited precision and coverage would be able to measure the real continuous physical distribution without any instrumentation or physical background. This is called the true distribution. Obviously, the real detector is not ideal and the measured distribution contains noise, distortions or more general finite resolution effects compared to true physical distribution. Folding the true distribution by the detector response, results in the actual reconstructed distribution.

The distortions imply different number of events between bins of the truth and reconstruction level histograms. By a numerical simulation of a physical event it is possible to estimate the migration of events between truth and reconstruction bins. This information is represented by a response matrix $\mathcal{R}$. The element of the response matrix $\mathcal{R}_{ij}$ is defined as number of events which can be found in the truth histogram bin i and the reconstructed histogram bin j. The response matrix is constructed from

Monte-Carlo simulation where truth and reconstructed distributions are available. The Monte-Carlo sample that is used for building response matrix is called a training sample.

The real detector has limited acceptance i.e. certain regions of physical distribution cannot be measured. This can be reflected in the truth distribution by applying the same detector-acceptance selection on certain truth variables e.g. muon pseudorapidity and muon transverse momentum. The distribution obtained after application of the detector-motivated selection criteria is called the fiducial distribution.

Unfolding

To be able to compare results between different experiments and to theoretical predictions it is necessary to correct the measured data for detector inefficiencies and resolution effects. This procedure is called unfolding. The information contained in the response matrix can be used to unfold the measured data and estimate the true distribution. In order to avoid model-dependent bias, the unfolding is often done to the fiducial level i.e. the response matrix is created from events which pass the fiducial and reconstructed level selection criteria.

The unfolding is defined as follows: let $t(\alpha)$ be the continuous truth distribution of truth observable α, $m(a)$ be the measured distribution of the measured observable a and $\mathcal{R}(\alpha, a)$ be the response function defined by the equation

$$m(a) = \int \mathrm{d}\alpha \mathcal{R}(\alpha, a) \cdot t(\alpha); . \tag{5.1}$$

With respect to the previous statements, the unfolding is the process of finding the unfolding function $\mathcal{R}^{-1}(\alpha, a)$ so that the following equation holds

$$\tau(\alpha) = \int \mathrm{d}a \mathcal{R}^{-1}(\alpha, a) \cdot m(a) \ . \tag{5.2}$$

where $\tau(\alpha)$ is the unfolded distribution. Frequently, the general definition for continuous distributions is specialized for discrete distributions represented by histograms:

$$\tau_i = \sum_j \mathcal{R}^{-1}_{ij} m_j \ , \tag{5.3}$$

where τ_i is number of events in bin i in the truth distribution, m_j is number of events in bin j in the measured distribution. The number $\mathcal{R}_{ij}$ is the element of the response matrix. There are many methods which can be used to find the unfolding matrix and the symbol $\mathcal{R}^{-1}$ does not necessarily represents the inverted $\mathcal{R}$ matrix.

The following text describes two methods which were used to unfold the measured p_{T}^{Z} distribution. In the following these symbols are used:

- m represents the measured distribution
- τ represents the unfolded distribution
- t represents the truth level distribution obtained from the Monte-Carlo training sample
- r represents the reconstructed level distribution obtained from the Monte-Carlo training sample

If not stated otherwise, the index i is reserved for the bin index of truth (t) or unfolded (τ) distributions and the index j is reserved for the bin index of measured (m) or reconstructed (r) distributions. The distribution symbol with index represents the

number of events in the corresponding bins e.g. m_j represents the number of events in bin j of the measured distribution m.

The first unfolding method used is called bin-by-bin. It is an elementary method assuming that migrations between bins are minimal and the measured distribution can be corrected by a multiplicative factor

$$\tau_i = \frac{t_i}{r_i} m_i \ , \tag{5.4}$$

where the symbols follow their earlier definitions. Equation 5.4 shows clearly that this method is not using the full information available i.e. it is underestimating the effect of all non-diagonal elements of $\mathcal{R}$.

The second method used is called Bayesian iterative unfolding [84]. The response matrix can be used to derive the conditional probability $P(r_j|t_i)$ of the reconstructed distribution r that has the number of events r_j in bin j given that the generated distribution t has the number of events t_i in bin i. However, the conjugated conditional probability is needed to calculate the unfolded distribution τ from measured distribution m

$$\tau_i = \sum_j P(\tau_i|r_j) \cdot m_j \tag{5.5}$$

The Bayesian theorem is used to find the conditional probability

$$P(\tau_i|r_j, 0) = \frac{P(r_j|t_i)P(\tau_i^{(0)})}{\sum_i P(r_j|t_i)P(\tau_i^{(0)})} \ , \tag{5.6}$$

where $P(\tau_i|m_i, 0)$ is the conditional probability that the number of events τ_i in bin i of the unfolded distribution τ would cause observation of the number of events r_j in bin j in reconstructed distribution r assuming the prior distribution $\tau^{(0)}$. The prior distribution is an arbitrary distribution which represents a first guess of the expected unfolded distribution e.g. a uniform distribution or the truth distribution of teaching sample. Since, the influence of the prior on the unfolded distribution is very strong Equation 5.6 is used repeatedly, where the prior of iteration a is chosen as the result of previous iteration $a-1$. The conditional probability from Equation 5.6 is used to calculate the unfolded iteration $\tau^{(a)}$ from the measured distribution m.

Template fit

The unfolded distribution is used to estimate the α_S value and it is in the following called measured data. The measured data are compared to a set of generated distributions, where each distribution corresponds to a different value of the $\alpha_S(M_Z^2)$. This set of distributions is called templates, hence, the method of $\alpha_S(M_Z^2)$ extraction is called a template fit. This method is described in the following text.

In this analysis the templates are generated by DYTURBO (see Chapter 4) with NNLL+NLO precision for a set of $\alpha_S(M_Z^2)$ values: 0.1150, 0.1160, 0.1170, 0.1173, 0.1177, 0.1180, 0.1182, 0.1183, 0.1187, 0.1194 and 0.1200. The $\alpha_S(M_Z^2)$ was changed by modifying the configuration header of the Les Houches Parton Distribution Function format (LHAPDF) files. This effectively results in the creation of a new LHAPDF file for each α_S value. The ordinary differential equation is used in DYTURBO to evolve $\alpha_S(M_Z^2)$ to an arbitrary scale $\alpha_S(\mu^2)$.

The shape of the measured distribution is compared to each distribution of the α_S-templates and the χ^2 value is calculated by the formula:

$$\chi^2(\alpha_S) = \sum_{i=1}^{N} \frac{(d_i - t_i(\alpha_S))^2}{\sigma^2} \ , \tag{5.7}$$

where i is the index of each bin, N is the total number of bins, d_i and t_i are values in the bin i for the measured distribution and template respectively. The squared sum of both prediction and measurement uncertainties is represented by σ^2.

A parabolic dependence on α_S is expected according to the theory of maximal likelihood estimator for Gaussian distributed random variables. Consequently, the χ^2 can be parameterised with respect to α_S by

$$\chi^2(\alpha_S) = \left(\frac{\Delta\alpha_S}{\sigma_\alpha}\right)^2 + \chi^2_{\text{min}} \tag{5.8}$$

where σ_α represents the uncertainty of the method and minimal chi-square parameter χ^2_{min} is used to estimate the goodness of fit. The term $\Delta\alpha_S \equiv \alpha_S - \hat{\alpha}_S$ is the difference between the input value α_S and the position of the parabola minimum $\hat{\alpha}_S$. The values of χ^2 from Equation 5.7 for each α_S are fitted by parameterization from Equation 5.8. The estimated parameters from the fit are easily represented as a result of the α_S measurement by:

$$\hat{\alpha}_S \pm \sigma_\alpha \text{ with } p - \text{value}(\chi^2_{\text{min}}|N-1)\ . \tag{5.9}$$

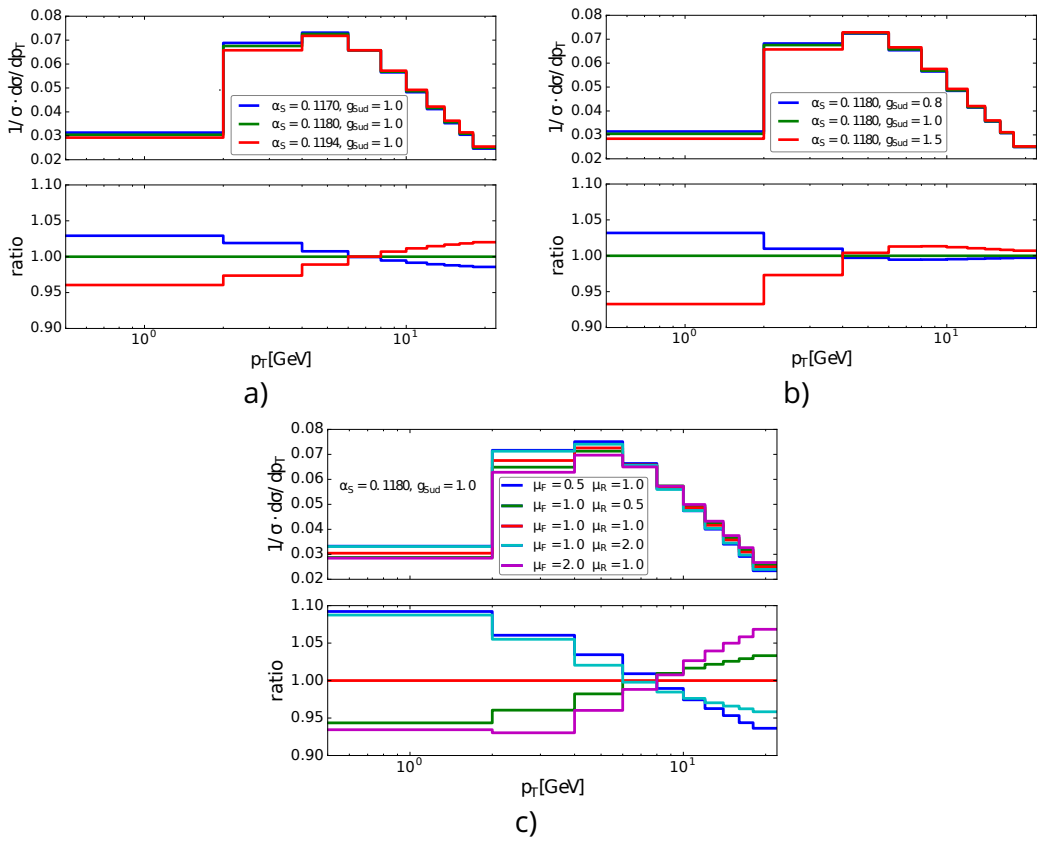

Figure 5.1: *Comparison of p_{T}^Z distribution shapes for different values of α_S (a), g_{NP} (b) parameters and variation of renormalization and factorization scales (c). The lower part of each plot shows the ratio with respect to $\alpha_S = 0.1180$, $g_{NP} = 0.8\,\text{GeV}^2$ and $\mu_R = \mu_F = 1$.*

The shape dependence of p_{T}^Z with respect to the $\alpha_S(M_Z^2)$ values is shown in Figure 5.1(a). A larger impact of the $\alpha_S(M_Z^2)$ variation would be visible for distributions, which are normalized to the calculated total cross section. However, the experimental measurement would be affected by the large uncertainty from the luminosity estimation. Therefore, only shape variations are used in this analysis.

The position of the Sudakov peak (see Section 2.3.2) is controlled, by the non-perturbative parameter g_{NP}. The effect of the g_{NP} parameter on the p_{T}^{Z} distribution is demonstrated in Figure 5.1(b). Since the g_{NP} value affects the extracted value of α_S, the additional variation of the non-perturbative parameter g_{NP} is included into the templates. This additional degree of freedom should compensate the effects in the soft part of the p_{T}^{Z} distribution. The templates were created as a two-dimensional grid for the previously listed values of α_S and this set of g_{NP} values: 0.2 GeV^2, 0.5 GeV^2, 0.8 GeV^2, 1.1 GeV^2, 1.2 GeV^2 and 1.5 GeV^2. The fitting $\chi^2(g_{\text{NP}})$ function needs to be extended by an additional parameter $\epsilon^{\pm}$ due to the non-symmetric parabolic behaviour of χ^2 the in case of the g_{NP} variation. The extended function is defined by

$$\chi^2(g_{\text{NP}}) = \left(\frac{\Delta g_{\text{NP}}}{\Sigma_g(\Delta g_{\text{NP}})}\right)^2 + \chi^2_{\text{min}} \,, \tag{5.10}$$

where terms are defined analogically to Equation 5.8. The step function $\Sigma_g(\Delta g_{\text{NP}})$ is defined as

$$\Sigma_g(\Delta g_{\text{NP}}) = \begin{cases} \sigma_g & \text{if} \Delta g_{\text{NP}} < 0 \\ \epsilon^{\pm} \cdot \sigma_g & \text{if} \Delta g_{\text{NP}} \geq 0 \end{cases} \tag{5.11}$$

where the positive parameter $\epsilon^{\pm}$ reflects the asymmetry between the left and right hand side of the χ^2 parabola. The fit result in terms of parameters is then

$$(\hat{g}_{\text{NP}})^{+\epsilon^{\pm}\cdot\sigma_g}_{-\sigma_g} \text{ with } p - \text{value}(\chi^2_{\text{min}}|N-1) \,. \tag{5.12}$$

Subsequently, to evaluate effects from both α_S and g_{NP} variation, a two-dimensional modification of the parabolic $\chi^2(\alpha_S, g_{\text{NP}})$ formula is required. The covariance matrix (Equation 5.13) of estimated quantities is chosen as a natural starting point to derive the interpretation of the fit result analogously to the one-dimensional case

$$\mathbb{V} \equiv \begin{pmatrix} \sigma_\alpha^2 & \rho\sigma_\alpha\Sigma_g \\ \rho\sigma_\alpha\Sigma_g & \Sigma_g^2 \end{pmatrix} \,, \tag{5.13}$$

where the parameter σ_α (see Equation 5.8) and the function $\Sigma_g(\Delta g_{\text{NP}})$ (see Equation 5.12) are correlated uncertainties of α_S, g_{NP} respectively, and ρ is a correlation coefficient between them. The two dimensional parabola function $\chi^2(\alpha_S, g_{\text{NP}})$ can be written in a matrix form:

$$\chi^2(\alpha_S, g_{\text{NP}}) = \begin{pmatrix} \Delta\alpha_S & \Delta g_{\text{NP}} \end{pmatrix} \mathbb{V}^{-1} \begin{pmatrix} \Delta\alpha_S \\ \Delta g_{\text{NP}} \end{pmatrix} + \chi^2_{\text{min}} \,. \tag{5.14}$$

The vector elements $\Delta\alpha_S$ and Δg_{NP} are defined by:

$$\begin{pmatrix} \Delta\alpha_S \\ \Delta g_{\text{NP}} \end{pmatrix} = \begin{pmatrix} \alpha_S - \hat{\alpha}_S \\ g_{\text{NP}} - \hat{g}_{\text{NP}} \end{pmatrix} \,, \tag{5.15}$$

where $(\hat{\alpha}_S, \hat{g}_{\text{NP}})$ represents the point of parabola minimum χ^2_{min}. Subsequently, the fit result in terms of estimated parameters is

$$\alpha_S = \hat{\alpha}_S \pm \sigma_\alpha \tag{5.16}$$

$$g_{\text{NP}} = (\hat{g}_{\text{NP}})^{+\epsilon^{\pm}\cdot\Sigma_g}_{-\Sigma_g} \tag{5.17}$$

The last assumed effect is variation of the renormalization and factorization scales. The shape effects on the p_{T}^{Z} distribution are shown in Figure 5.1(c). The templates

were created with renormalization and factorization scales varied by 0.5, 1 and 2 times M_Z for each of the above listed α_S and g_{NP} values. These variations are taken as model uncertainties of the templates. This is the largest contribution to the uncertainty of the α_S extraction. To improve the precision of the fit a bin-by-bin correlation for scale variations is assumed. Therefore, Equation 5.7 is modified to

$$\chi^2(\alpha_S, g_{\text{NP}}) = \left(\vec{d} - \vec{t}(\alpha_S, g_{\text{NP}})\right)^T \cdot \mathbb{C}^{-1} \cdot \left(\vec{d} - \vec{t}(\alpha_S, g_{\text{NP}})\right) \ , \tag{5.18}$$

where data $\vec{d}$ and template $\vec{t}$ vectors represent the number of events inside bins analogously to Equation 5.7 and the covariance matrix $\mathbb{C}$ contains scale variation correlations between bins. The experimental and template statistics uncertainties are considered as uncorrelated between bins, therefore they are added in quadrature to the diagonal of $\mathbb{C}$.

Template fit closure test

A closure test was done as a proof of concept, where one generated distribution with known values of α_S and g_{NP} was fitted by the template method and the fit results were compared to the known, generated values.

Firstly, the generated distribution with values of $\alpha_S = 0.1182$ and $g_{\text{NP}} = 1.1\,\text{GeV}^2$ is excluded from templates. This distribution is treated as the measured data and it is further marked as pseudo-data. Secondly, the χ^2 value is calculated using the pseudo-data and each template distribution. Finally, the χ^2 values are fitted to the one-dimensional functions $\chi^2(\alpha_S)$ (Equation 5.8) and $\chi^2(g_{\text{NP}})$ (Equation 5.10) as well as the two-dimensional function $\chi^2(\alpha_S, g_{\text{NP}})$ (Equation 5.14).

The shapes of p_{T}^Z distribution which correspond to the fitted values of α_S and g_{NP} are created by using cubic (bi-cubic) splines [85] for the one-dimensional (two-dimensional) variation. The interpolated distributions are normalized to unity and they are compared to pseudo-data using the ratio plot in Figure 5.2 (b,d,f).

The closure test shows that the extracted values (the position of parabola minimum) fully agree with the input values (pseudo-input) for the one-dimensional α_S (Figure 5.2 (a)) and g_{NP} (Figure 5.2 (c)) as well as the two-dimensional (Figure 5.2 (e)) case. The methodology described above is implemented in the `python` [86] program `alphaS.py` [87] using the `scipy` [88] and `matplotlib` [89] libraries.

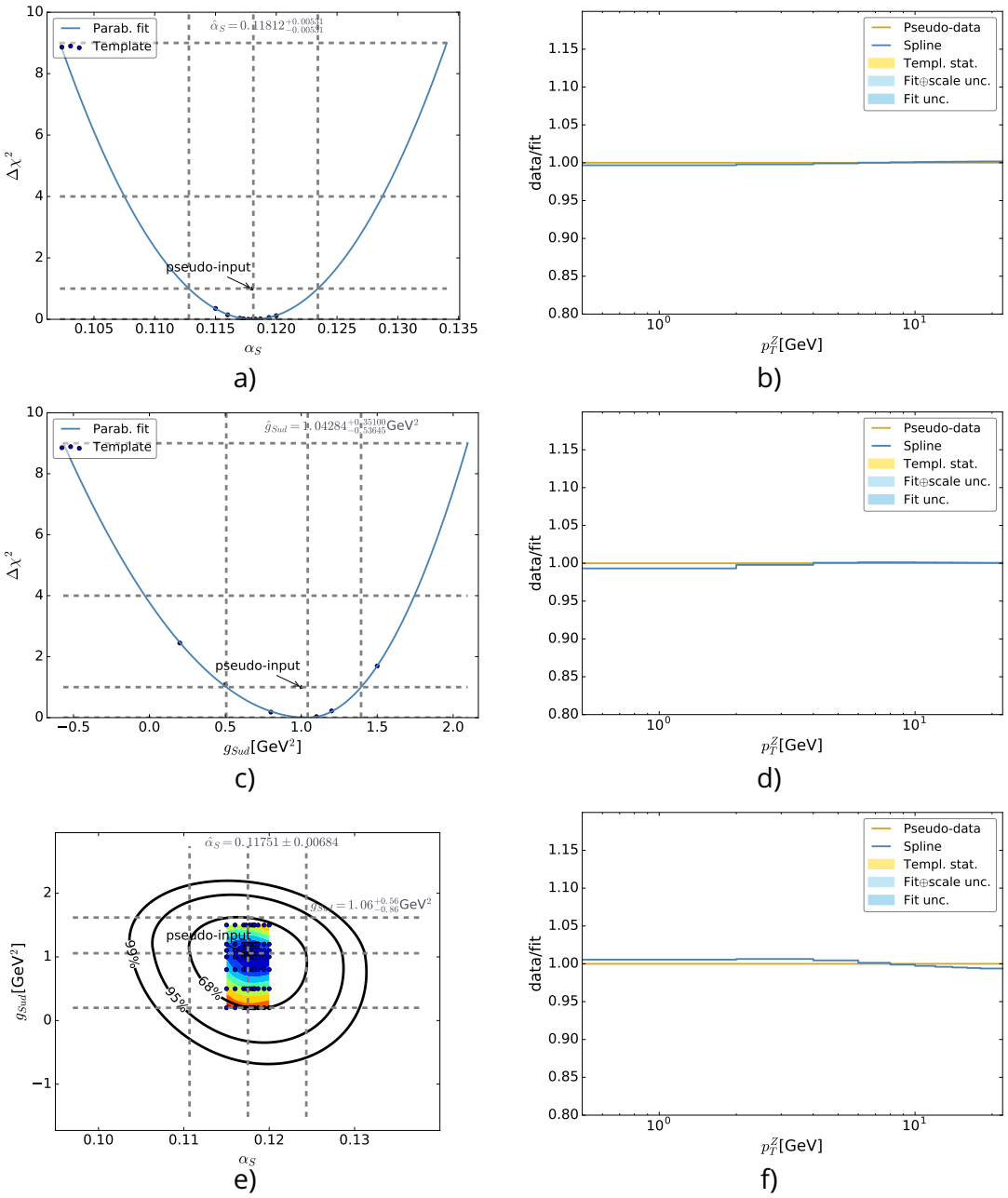

Figure 5.2: *Plots on the left hand side show the fitted $\Delta\chi^2$ parabola w.r.t α_S (a) and g_{NP} (c) and the 68%, 95% and 99% Confidence Level (CL) regions of the 2D α_S-g_{NP} fit (e). The blue points mark the value of the template where χ^2 was evaluated. The pseudo-data is the MC prediction with values $\alpha_S = 0.1182$ and $g_{NP} = 1.1\,\text{GeV}^2$. The plots on the right hand side show the ratio of the p_{T}^Z shape between the pseudo-data and the spline from the best fitted value of α_S (b) g_{NP} (d) and both (f). The yellow line and band represent the pseudo-input uncertainty from the statistics of the prediction. The blue band and line represent the uncertainty on the fitted shape.*

5.2 Measurement of Transverse Momentum of Z bosons

To reach a sufficient level of sensitivity for the α_S extraction, using the method described in chapter Section 5.1, it is necessary to measure the p_{T}^{Z} distribution with per-cent precision level within all bins. Such a measurement is described in this section. The data used for the measurement was collected by the ATLAS detector during proton-proton collisions with $\sqrt{s} = 13\,\mathrm{TeV}$ and with a 25 ns bunch-crossing gap in the year 2015. This dataset corresponds to an integrated luminosity $L = 2.7\,\mathrm{pb}^{-1}$. The luminosity was estimated by an online tool [90] using the standard Good-Runs-List (GRL).

The analysis follows the official recommendations based on release `20.7`[91]. Hence, the official `RootCore` [92] package with a set of preconfigured and tuned tools is used and only configurations different from the recommendations are mentioned in the corresponding section.

5.2.1 Signal Selection

Collisions with various physical processes are measured and analysed by the ATLAS DAQ (see Section 3.4.4). Hence, it is necessary to filter the events, where Z bosons, which then decayed into muon pairs, have been produced.

Several observables and event properties are used in the cut-based selection of signal candidate events in this analysis. These cuts and their motivation are described in this section. Firstly, the used trigger and event quality selection is described. After this, the required properties of the muons are summarized. Finally, observables which are used to define the Z boson candidate are described in the last part of this section.

In this analysis Extended Analysis Objects Data format (xAOD) files containing the `STDM3` Standard Model derivation were used as input. These already provide preselected datasets with events containing at least two leptons (ee, $e\mu$ or $\mu\mu$) [93]. The number of events passing the individual selection criteria are summarized in the cutflow table Table 5.1 below. The first row of this table, the number of events in the xAOD file is obtained from the `CutBookKeeper` information inside the xAOD derivation. For sake of simplicity the xAOD in further text will be defined as the sample before any cuts and Extended Analysis Objects Data format derivation (DxAOD) is the sample with applied selection criteria of the `STDM3` derivation.

The initial event selection is done by the detector trigger electronics. The trigger purpose and a technical description were described in Section 3.4.4. The single muon triggers `HLT_mu20_iloose_L1MU15` or HLT_mu50 were used in this analysis.

These triggers are not pre-scaled and are available for all 25 ns collisions of the year 2015 [94]. These triggers require a muon $p_{\mathrm{T}}^{\mu} > 15$ or $p_{\mathrm{T}}^{\mu} > 50$ respectively on L1. While the second trigger still has the same p_{T}^{μ} threshold for HLT, the first one requires $p_{\mathrm{T}}^{\mu} > 20$ during HLT processing and it uses looser criteria for isolation.

The operational status of each part of the detector can change during data-taking. The conditions of each sub-detector is monitored and stored in a database. These conditions are cross checked by automated algorithms together with detector experts, which decide about the quality of the taken data per Lumi-block. This data quality information is stored in goodrun lists called GRL. In this selection the `StandardGRL` [95] is used. This file is used by the `GoodRunsList` [96] package, which decides whether to keep or skip an event. Moreover, the same GRL file was used to calculate the total luminosity of the processed data [90].

Even though the GRL is filtering events with non-adequate detector conditions, good-practice dictates to apply additional quality checks [97]. All events showing an error in the Tile Calorimeter (Tile) calorimeter or are affected by noise bursts in the LAr and consequent data corruption were rejected. Additionally all events affected

by recovery procedures in SCT were removed. Events with missing or incomplete information were also not used in this analysis. Since only muons were used in this analysis, no event duplications were expected and therefore no duplicate removal was applied.

The events used in this analysis need to contain at least one interaction vertex that is reconstructed form more than three good-quality tracks. The vertex with the largest $\sum p_{\mathrm{T}}^{track}$ is marked as primary vertex. All other vertices are called pile-up vertices. Only muons with tracks associated to the primary vertex are used in this analysis. This is done by the track-to-vertex-association criteria [98], which for purpose of this analysis is defined as:

$$|S(d_0)| < 1 \text{ and } |\Delta z_0 \sin\theta| < 0.5\,\text{mm}\,, \tag{5.19}$$

where d_0 is the distance of the muon track-to-vertex distance projected to the plane parallel to the beam-line, z_0 the longitudinal track-to-vertex distance, θ the longitudinal angle of the track. The significance $S(x) \equiv \frac{x}{\sigma_x}$ is defined as the fraction of the observable x and the measured uncertainty σ_x of this observable. This selection criteria is applied on the tracks to remove all muons originating from pile-up.

The muons are selected from events matching the criteria mentioned above. The Muon selection package `MuonSelectorTools` [99] was used to filter the muons. The tool criteria are split into two groups: Muon identification quality and ID track quality. The tool also preselects muons with $|\eta| < 2.7$ [100]. This will be later replaced by a more strict $|\eta|$ cut in the later stages of the analysis.

All muons require to pass the following standard ID track criteria:

- At least one pixel hit or at least one crossed dead pixel sensor
- Number of SCT hits plus number of crossed dead SCT sensors more than four
- Number of crossed Pixel holes and SCT holes less then three.
- Expected TRT extension, i.e. for tracks in $0.1 < |\eta| < 1.9$ is required that $n_{\mathrm{TRT}}^{\mathrm{expected}} > 5$ and $n_{\mathrm{TRT}}^{\mathrm{outliers}} > 0.9 \cdot n_{\mathrm{TRT}}^{\mathrm{expected}}$, where $n_{\mathrm{TRT}}^{\mathrm{expected}} = n_{\mathrm{TRT}}^{\mathrm{hits}} + n_{\mathrm{TRT}}^{\mathrm{outliers}}$, $n_{\mathrm{TRT}}^{\mathrm{hits}}$ denotes the number of TRT hits on the track and $n_{\mathrm{TRT}}^{\mathrm{outliers}}$ is the number of TRT outliers on the track

The medium quality requirements are used for muon identification, which is described by the following criteria:

- q/p-significance must be less then seven.
- tracks must pass more than one precision layer
- tracks in the $|\eta| < 0.1$ region are accepted with one precision layer only if it passed through less than two layer holes.

Since the final $|\eta| < 2.5$ cut is applied on muons it is not necessary to take the stand-alone MS muons into account. Consequently, only combined muons are used in this analysis. The corrected muon transverse momentum p_{T}^{μ} (see Section 5.2.3) is used to veto muons below 25 GeV.

Measuring the detector activity around the η,ϕ coordinate of the muon candidate provides informations about the isolation of the muon. It is helpful to define a cone in the $\eta - \phi$ space $R = \sqrt{\Delta\phi^2 - \Delta\eta^2}$, where $\Delta\phi$, $\Delta\eta$ is the difference between ϕ and η of two points, respectively. The isolation represents the fraction of the energy deposited inside the muon cone of size R originating from the muon itself. This isolation is a powerful criteria to reject the semi-leptonic decays of the multi-jet background. The

deposited energy can be calculated using the relative track-based $p_{\mathrm{T}}^{\text{varcone30}}/p_{\mathrm{T}}^{\mu}$ or the relative calorimeter-based $E_T^{\text{topocone20}}/p_{\mathrm{T}}^{\mu}$ isolation variable. A detailed definition is given in [101]. The `IsolationSelection` [102] package was used to estimate the isolation of the muons. This tool can work with seven working points and for this analysis the `"Gradient"` working point was used. This means that instead of one fixed value a map of cuts were prepared and used to fulfill the targeted efficiency gradient

$$\varepsilon = \left(0.1143 \cdot \frac{p_{\mathrm{T}}^{\mu}}{1\ \text{GeV}} + 92.14\right)\% \tag{5.20}$$

for both track- and calorimeter-based isolation variables. The combined isolation efficiency is then $\varepsilon = 90(99)\%$ at $25(60)$ GeV [103]. If the criteria of isolation are not passed, i.e. other than muon energy inside cone is too large we say the muons are marked as non-isolated.

There are several Standard Model processes with more than one isolated high-p_{T}^{μ} muon in the final state. Therefore, additional criteria for the Z candidate events are used to reduce the background. Exactly two muons with opposite charge are required to be present in an event to pass the selection. This removes combinatorial background as well as it suppresses di-boson processes. An invariant mass of the two muons $m_{\mu\mu}$ is calculated and only events with mass $m_{\mu\mu} = (66 - 116)$ GeV are selected. This di-muon kinematic system in final-selection events is considered as Z candidate. The number of events passing the above mentioned criteria are summarized in Table 5.1. The last row of this table represents the number of Z candidates.

	Data Events	Fraction [%]	Total Fraction [%]
xAOD	2 849 786 624	100.00	100.00
DxAOD	39 688 616	100.00	1.39
Good Event, GRL	35 407 087	89.21	1.24
Vertex	35 406 861	89.21	1.24
Trigger	16 897 527	42.58	0.59
Medium quality	3 450 907	100.00	0.12
Track selection	3 420 434	99.12	0.12
Track to PV - d_0	2 142 200	62.08	0.08
Track to PV - z_0	2 137 010	61.93	0.07
$p_{\mathrm{T}} > 20$ GeV	1 662 627	48.18	0.06
$\lvert\eta\rvert < 2.5$	1 662 627	48.18	0.06
Isolation	1 437 616	41.66	0.05
Opposite sign	1 437 455	41.65	0.05
Veto extra muons	1 437 329	41.65	0.05
Inv. mass	1 378 678	39.95	0.05

Table 5.1: *Event selection table for data (cut-flow). The number of events in data (second column) fulfilling the cut is shown in the first column. From the second to the last column the fraction calculated with respect to first row below the horizontal line is shown. The values in the last column are calculated as fraction with respect to first row (xAOD).*

5.2.2 Used Samples and Background Estimations

This analysis used the RootCore release Base,2.4.22. This corresponds to xAOD files with production tag p2666 or p2667 for Monte-Carlo[1]. As it is mentioned above the derived xAOD STDM3 of the Standard Model working group was used, which features a di-lepton pre-selection [93]. The data sample for this analysis is provided by the physics_muons stream. The dataset names for Monte-Carlo and data are listed in Table 5.2.

Sample	Dataset name, used generator and PDF
Data	data15_13TeV.periodX.physics_Main.PhysCont.DAOD_STDM3.grp15_v01_p2667
$Z \to \mu\mu$	PowhegBox Pythia (CTEQ6L1) NLO
	mc15_13TeV.361107.PowhegPythia8EvtGen_AZNLOCTEQ6L1_Zmumu.merge.DAOD_STDM3.e3601_s2576_s2132_r7725_r7676_p2666
$Z \to \tau\tau$	PowhegBox Pythia (CTEQ6L1) NLO
	mc15_13TeV.361108.PowhegPythia8EvtGen_AZNLOCTEQ6L1_Ztautau.merge.DAOD_STDM3.e3601_s2726_r7725_r7676_p2666
$t\bar{t}$	PowhegBox Pythia (CT10NLO) NLO
	mc15_13TeV.410000.PowhegPythiaEvtGen_P2012_ttbar_hdamp172p5_nonallhad.merge.DAOD_STDM3.e3698_s2608_s2183_r7725_r7676_p2666
$WW \to \ell\nu\ell\nu$	PowhegBox Pythia (CT10NLO) NLO
	mc15_13TeV.361600.PowhegPy8EG_CT10nloME_AZNLOCTEQ6L1_WWlvlv.merge.DAOD_EXOT5.e4616_s2726_r7772_r7676_p2719
$WZ \to \ell\nu\ell\ell$	PowhegBox Pythia (CT10NLO) NLO
	mc15_13TeV.361601.PowhegPy8EG_CT10nloME_AZNLOCTEQ6L1_WZlvll_mll4.merge.DAOD_STDM3.e4475_s2726_r7772_r7676_p2719
$WZ \to qq\ell\ell$	Sherpa (CT10) NLO
	mc15_13TeV.361094.Sherpa_CT10_WqqZll_SHv21_improved.merge.DAOD_STDM3.e4607_s2726_r7725_r7676_p266
$ZZ \to qq\ell\ell$	Sherpa (CT10) NLO
	mc15_13TeV.361096.Sherpa_CT10_ZqqZll_SHv21_improved.merge.DAOD_STDM3.e4607_s2726_r7725_r7676_p2666

Table 5.2: *List of used samples with full dataset name. In the case of a data sample the periodX is substituted by corresponding period from D-J.*

Even though the selection criteria are used to filter everything but $Z \to \mu\mu$ events, the final data contains other physical processes than $Z \to \mu\mu$. To estimate the amount of this background in the selected data two techniques are widely used: Monte-Carlo method and data-driven method.

The same simulation, reconstruction and selection is applied to Monte-Carlo background samples for all possible physical processes which could have the same signature as $Z \to \mu\mu$ in the final state. Final fractions of the background contamination per each sample are listed in Table 5.4. A brief summary of possible backgrounds is given in the following paragraphs.

Tauonic decay of Z

The $Z \to \tau^+\tau^-$ process is very similar to the process under investigation, but the produced Z decays into a pair of τ-leptons. The majority of the produced τ leptons

[1]During the analysis a new production tag was released and as a result old datasets were removed. After reprocessing of the background studies only the EXOT6 derivation was available for $WW \to \ell\nu\ell\nu$ dataset for the RootCore version of the analysis. This derivation has too low statistics of any events passing the selection criteria and this background is expected to have low impact on shape. Therefore, it was decided not to use this background.

decay into hadrons, however, a significant number of τ-leptons decay into muons and as a result the final state is identical to the one of the signal events. As neutrinos can not be detected by the detector, the two neutrinos from τ decays are not measured by the detector and therefore the di-muon invariant mass peak is expected to be shifted to lower values. A cut on $\not{E}_{\mathrm{T}}$ is not considered, as it would propagate large uncertainties to the p_{T}^{Z} measurement, hence the background contribution is estimated using simulated Monte-Carlo sample.

Dibosons WW,WZ,ZZ

Processes producing two electroweak bosons during proton-proton collision have a smaller cross section than single boson production process. There are three possible combinations: WW, WZ and ZZ. Fully hadronic decays have not been considered. The $WW \to \ell\nu\ell\nu$ process is dominated by $e\mu$ channel and thus it is suppressed by the two-muon-selection criteria. The same selection rejects also most of $WZ \to \ell\nu\ell\ell$ events. Moreover, in this channel the distribution of the two-lepton invariant mass is flat, which reduces the fraction of this background. On the other hand $WZ \to qq\ell\ell$ and $ZZ \to qq\ell\ell$ have have a similar signature as the signal events, resulting in a mass peak in the background contribution.

Top-quark production

The top-quark pair production is also contributing to the irreducible background. As mentioned above only two-muon top-pair decays contribute to the background and the shape of the invariant mass is non-resonant in the di-boson case.

Mult-jet background

The multi-jet background or sometimes called QCD background is a process, when two muons are a decay product of heavy flavour jets, kaons or pions and their di-muon invariant mass is within the Z selection range. Due to high statistical requirements for the Monte-Carlo samples it is more convenient to use a data-driven estimation of this background. In our case this technique is based on two facts: the muons which origins from jets are produced within the $\eta \times \phi$ cone of the jet together with other charged particles; the sign of the charge of these two muons coming from this process is independent i.e. it is equally probable to find the same sign and the opposite sign muon pairs. This data-driven method in general estimates the background from measured data. Based on the above mentioned facts, four control regions are defined, where the data are selected using the cuts as described in Section 5.2.1, except isolation and opposite sign cut are reversed. This is summarized in Table 5.3.

Region	Sign	Isolation	Number of events
A (signal)	opposite-sign	both isolated	1 378 678
B (background)	same-sign	both isolated	51
C (background)	opposite-sign	both non-isolated	9581
D (background)	same-sign	both non-isolated	1229
A (background)	opposite-sign	both isolated	397

Table 5.3: *Definition of regions for the multi-jet background estimation together with the number of observed events in each region. The last row represents the estimated multi-jet background.*

The estimation of the multi-jet background contribution relies on so-called ABCD method. While the region A is dominated by signal events the other regions mostly contain multi-jet events. This method generally assumes that the ratio of background contribution between samples A and B is equal to the ratio of background contribution between samples C and D. Hence we can write that

$$n_A^{\text{bkg}} = n_B^{\text{bkg}} \cdot \frac{n_C^{\text{bkg}}}{n_D^{\text{bkg}}} \tag{5.21}$$

Assuming that the sample with inverted isolation criteria (region C) is background dominated, the shape of multi-jet background is estimated by this region and it is scaled to the estimated number of events from Equation 5.21.

Sample	σ [pb]		xAOD events	Selected events	C-factors
$Z \to \mu\mu$	1901±72	[104]	57 541 433	4 242 895	0.000 197
$Z \to \tau\tau$	1906±72	[104]	94 559 320	2047	0.000 120
$WZ \to jj\ell\ell$	3.423±0.075	[105]	1 570 784	43 523	0.326 004
$WZ \to \ell\nu\ell\ell$	4.50±0.13	[105]	512 240	4159	0.022 554
$ZZ \to \ell\ell jj$	16.45±0.52	[106]	1 564 816	44 552	0.178 685
$t\bar{t} \to bb\ell\ell\nu\nu$	696±34	[107]	158 110 304	112 263	0.049 926

Table 5.4: *Used Monte-Carlo samples for each process. The cross section are obtained from the AMI [108] database and the uncertainties are from stated reference. Number of xAOD events is taken from DxAOD CutBookKeeper and the C-factor represents the scale applied to histograms before comparing with data.*

To estimate the final background of this measurement it is necessary to properly combine the signal and background samples. Firstly, the Monte-Carlo samples are scaled by a factor calculated as ratio of the corresponding cross section obtained from the AMI [108] database and the sum of event weights inside all used DxAOD. Secondly, the scaled Monte-Carlo samples are added and the result is normalized to the number of events observed in data subtracted by the number of estimated multi-jet events. The Table 5.4 summarizes the fractions of all background samples used in this measurement including final background contamination fraction. The C-factor in Table 5.4 is the final normalization factor of Monte-Carlo samples.

5.2.3 Detector Level Corrections

Both the beam conditions and detector performance can change during the production year. The off-line corrections, which are described in the section, are applied on Monte-Carlo events to improve the agreement between simulated and collected data.

The number of interaction per bunch-crossing $\langle\mu\rangle$ influences the detector response and consequently, affects the studied event as well. Since the beam conditions are the main factor influencing $\langle\mu\rangle$ it is not possible to prepare Monte-Carlo prediction before the measurement. Consequently, predictions are created with well-defined distributions of $\langle\mu\rangle$ spectrum and events are reweighted according to the measured data. To provide this reweighting the official PileupReweighting [109] tool was used. Its performance is shown in Figure 5.3.

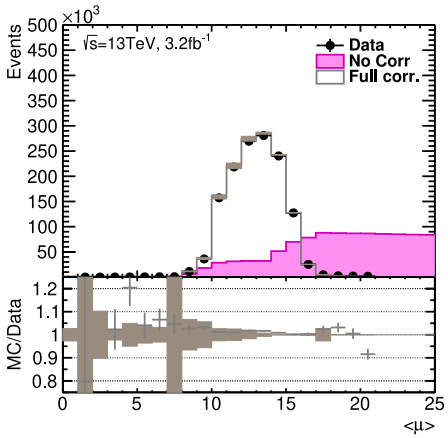

Figure 5.3: *The number of observed events with respect to the average number of interactions per bunch crossing $\langle\mu\rangle$. The collected data is compared to Monte-Carlo predictions including backgrounds. The lower part of the plot shows the ratio of Monte-Carlo and data. Grey bands represent systematic uncertainties and error bars represent statistic uncertainty on both parts of the plot.*

Even though the p_{T}^{Z} measurement is not depending on the luminosity measurement and $Z \to \mu\mu$ kinematic distributions are independent from $\langle\mu\rangle$, many calibration tools require this information from the `PileupReweighting` tool to apply proper corrections and scale factors.

When comparing the measured muon transverse momentum and its Monte-Carlo prediction, a discrepancy can be observed. To correct for this, the invariant mass peaks of the Z boson or J/ψ meson can be used to calibrate Monte-Carlo to match data. The width and peak position of the di-muon invariant mass in $Z \to \mu\mu$ or $J/\psi \to \mu\mu$ is a well-defined observable and is therefore used to compare Monte-Carlo and Data. Using this comparison, correction factors and smearing factors are estimated and then applied to the predicted p_{T}^{μ} (Equation 5.22) distribution.

The muon momentum scale and resolution correction is implemented in the `MuonMomentumCorrection` [110] tool. This tool is able to correct muons with $p_{\mathrm{T}}^{\mu} > 5\,\mathrm{GeV}$ (based on $J/\psi \to \mu\mu$ and $Z \to \mu\mu$). Its basic principle is described in following paragraph, while a detailed description of this tool can be found in [111].

Since combined muons are used in this analysis, their transverse momentum $p_{\mathrm{T}}^{\mathrm{MC,Det}}$ is corrected for tracks reconstructed in each part of detector separately. The corrected transverse momentum is calculated as

$$p_{\mathrm{T}}^{\mathrm{Corr,Det}} = \frac{p_{\mathrm{T}}^{\mathrm{MC,Det}} + \sum_{n=0}^{1} s_n^{\mathrm{Det}} \cdot \left(p_{\mathrm{T}}^{\mathrm{MC,Det}}\right)^n}{1 + \sum_{m=0}^{2} \Delta r_m^{\mathrm{Det}} \cdot \left(p_{\mathrm{T}}^{\mathrm{MC,Det}}\right)^{m-1} g_m} , \tag{5.22}$$

where g_m is a random variable following a normal distribution and correction factors s_n and smearing factors r_n, which depend on muon η and ϕ. Afterwards the transversal momentum is combined assuming the factor f stays the same as it was before applying the correction

$$p_{\mathrm{T}}^{\mathrm{Corr,CB}} = f \cdot p_{\mathrm{T}}^{\mathrm{Corr,InDet}} + (1-f) \cdot p_{\mathrm{T}}^{\mathrm{Corr,MS}} . \tag{5.23}$$

The performance of both the resolution and the scaling for this analysis is shown in plots Figure 5.4.

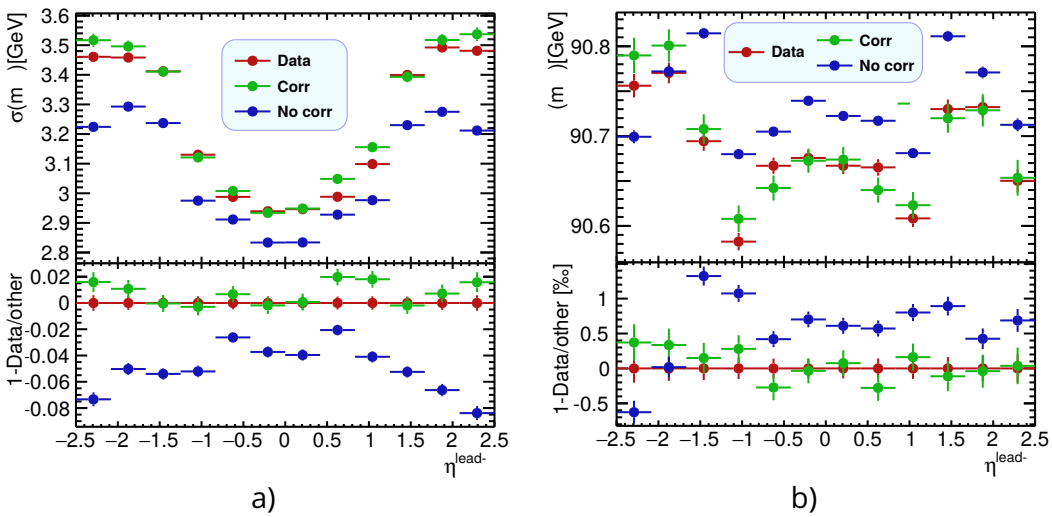

Figure 5.4: *Muon resolution $\sigma(m_{\mu\mu})$ (a) and muon scale $\mu(m_{\mu\mu})$ (b) with respect to $\eta^{\text{lead-}\mu}$ before (blue) and after (green) p_{T}^{μ} corrections compared to data (red). The lower part of the plot shows the ratio of data and Monte-Carlo.*

The muon reconstruction efficiency is slightly overestimated by the Monte-Carlo predictions compared to the reconstruction efficiency in data. In order to achieve better agreement between data and Monte-Carlo a correction has to be applied. The efficiency can be measured by the tag-and-probe method in $Z \to \mu\mu$ events. In this method the first (tag) muon reconstructed with medium quality criteria fires the trigger. The second (probe) object is then used to estimate efficiency of both ID and MS detector systems separately. Detailed information about this method can be found in [101]. The ratio of data and Monte-Carlo efficiency is used as muon reconstruction scale factor to re-weight the Monte-Carlo muons. The scale factors are stored in $\eta - \phi$ map which is provided by `MuonEfficiencyCorrections` [112] package, together with an interface to retrieve them. The `"Medium"` setting was used as muon reconstruction scale factor working point.

The isolation working point is already mentioned in Section 5.2.1. As in the case of the reconstruction efficiency, the isolation efficiency shows slight disagreement between data and Monte-Carlo predictions. The tag-and-probe method mentioned above was used to estimate the isolation scale factors [101]. The same tool `MuonEfficiencyCorrections` is used to retrieve the isolation scale factors. The muon isolation scale factor working point was set to `"GradientIso"`. This mode varies the size of the isolation cone in order to keep the efficiency at a constant value with respect to the momentum of the muon.

The trigger efficiency of data and Monte-Carlo predictions [113] were also compared. The tag-and-probe method was used and the efficiency was calculated for both L1 and HLT. The scale factors are available from the `CP::MuonTriggerScaleFactors` class inside `MuonEfficiencyCorrections` [112] using the `"Medium"` quality criteria.

Since pairs of muons are used for the analysis, the scale factors of both muons were multiplied for each efficiency i.e. reconstruction, isolation and trigger efficiency. Consequently the corrected transverse momentum of the muons were used for the Z candidate kinematics calculations. The average of the applied scale factor corrections is approx. 15.00 %. The distribution with respect to η and p_{T} of the highest-p_{T} (leading) muon is shown in plot Figure 5.5 for each efficiency.

As shown in Figure 5.6, there are minor discrepancies between Monte-Carlo pre-

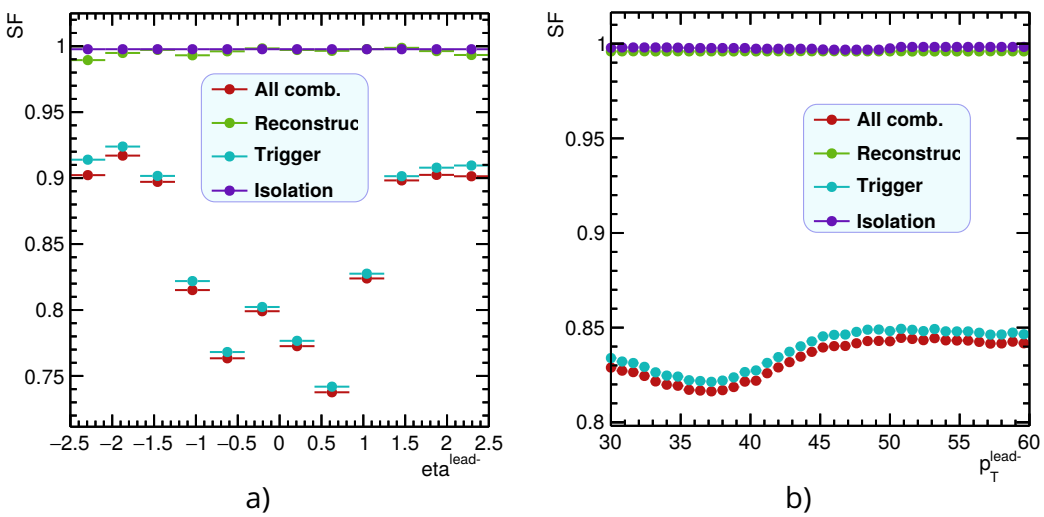

Figure 5.5: *Scaling factors for reconstruction (green), isolation (violet) and trigger (cyan) efficiencies with respect to the $\eta^{lead-\mu}$ (a) and $p_{\mathrm{T}}^{lead-\mu}$ (b) used for the analysed events. The combined correction are depicted in red.*

dictions and the collected data. In order to improve the unfolding performance, additional corrections are applied to Monte-Carlo to match the data. The events according to the Z candidate rapidity and transverse-momentum (p_{T}^{Z}-y^{Z}) were re-weighted by the ratio of the number of events in data and in Monte-Carlo (including background).

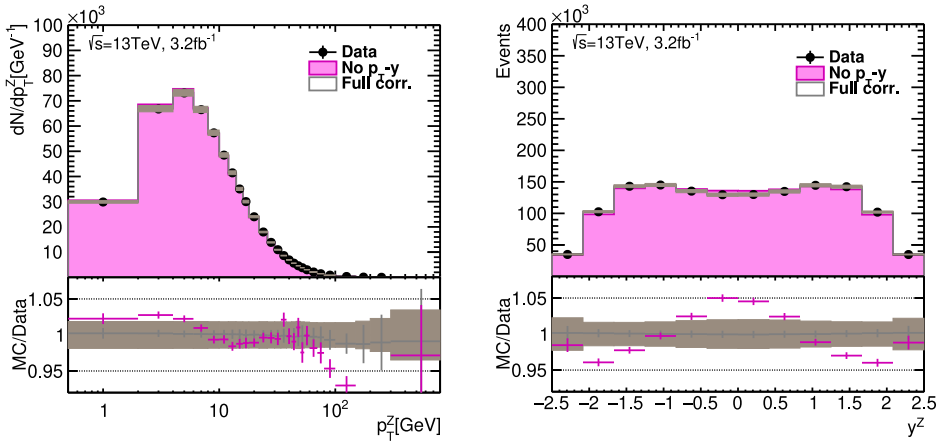

Figure 5.6: *Distribution of p_{T}^{Z} (a) and y^{Z} (b) before (fuchsia) and after (grey) the application of p_{T}^{Z}-y^{Z} re-weighting. The collected data is compared to Monte-Carlo predictions including backgrounds. The lower part of the plot shows the ratio of Monte-Carlo and data. Grey bands represent systematic uncertainties and error bars represent statistic uncertainty on both parts of the plot.*

The plots in Figure 5.7 compare the observed data events and Monte-Carlo predictions for the muon p_{T}^{μ}, η^{μ} distributions. The control plots show good agreement between prediction and observation after include p_{T}^{Z}-y^{Z} reweighting.

The measured data is then unfolded using information from Monte-Carlo predictions after applying all corrections. The unfolded results are used to fit the α_s

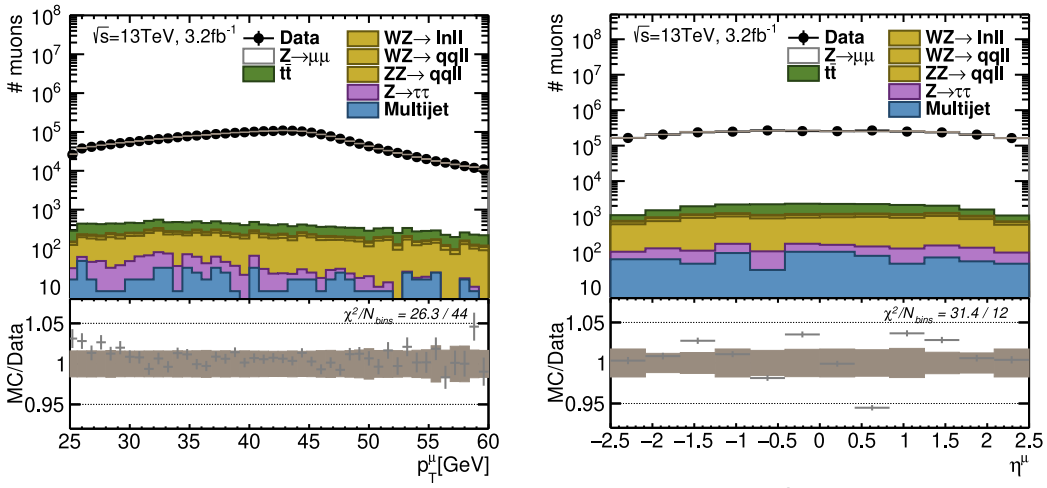

Figure 5.7: *Number of observed muons with respect to muon transverse momentum (a) and muon pseudorapidy (b). The collected data is compared to Monte-Carlo predictions including backgrounds. The lower part of the plot shows the ratio of Monte-Carlo and data. Grey bands represent systematic uncertainties and error bars represent statistic uncertainty on both parts of the plot.*

value.

5.2.4 Measured p_{T}^{Z} and Unfolding to Fiducial Level

The plots in Figure 5.8 show the basic Z distributions from selected data events (Section 5.2.1) compared to their Monte-Carlo predictions including the full background estimation (Section 5.2.2) and all mentioned corrections (Section 5.2.3). The estimation of the statistical and systematic uncertainties are described in this section.

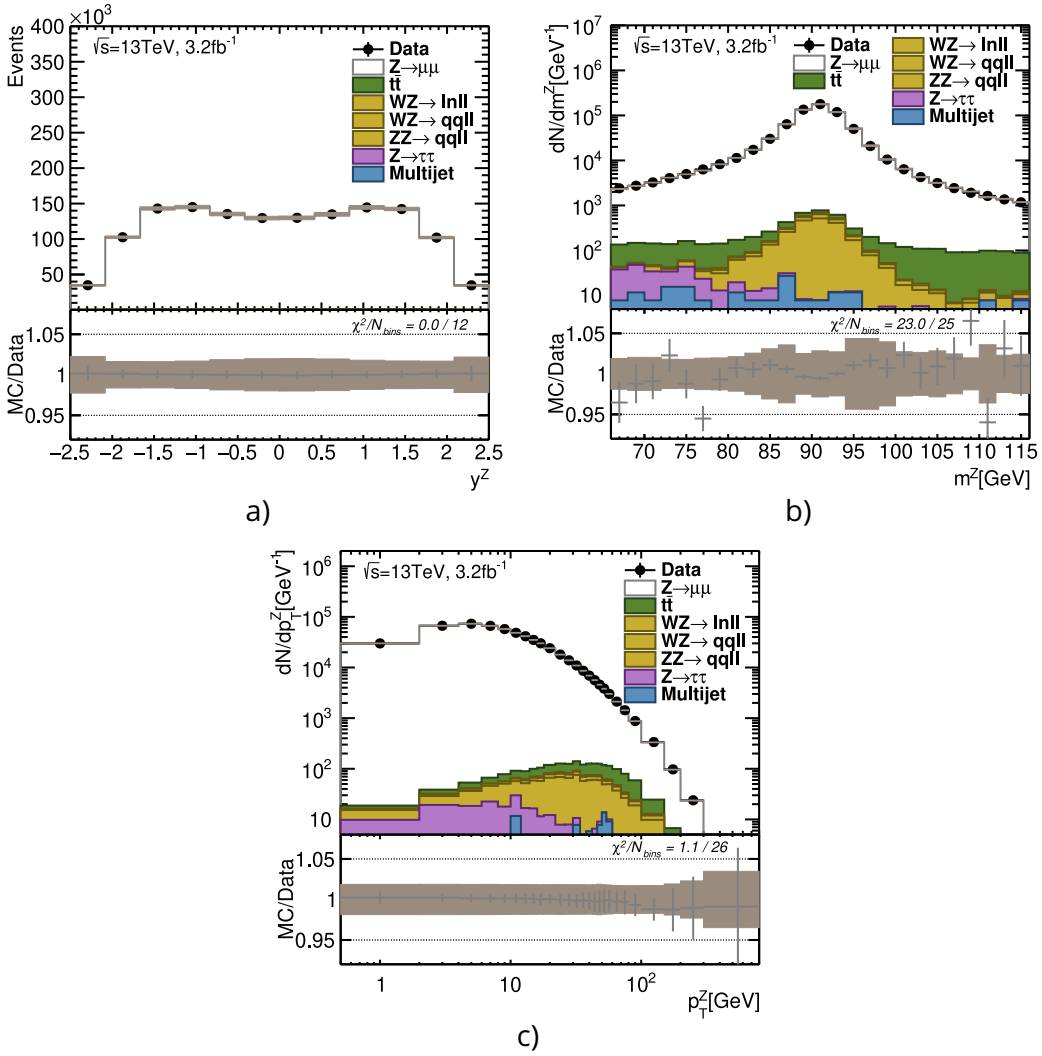

Figure 5.8: *The number of observed events with respect to rapidy (a), mass (b) and transverse momentum (c) of the Z candidate.The collected data is compared to Monte-Carlo predictions including backgrounds. The lower part of the plot shows the ratio of Monte-Carlo and data. Grey bands represent systematic uncertainties and error bars represent statistic uncertainty on both parts of the plot.*

A predicted spectrum contains unavoidable migrations of events between generator and reconstruction level. To be able to compare the measurement with other theoretical predictions it is necessary to extract the fiducial spectrum from the measurement.

The fiducial spectrum is the truth Monte-Carlo spectrum with applied detector cuts on the corresponding observables. The fiducial space for this analysis is defined to exclude muons with p_{T}^{μ} below 25 GeV and $|\eta^{\mu}|$ below 2.5 and select events with a di-muon invariant mass in the range of (66-116) GeV.

To study the migration of events among bins from the truth to the reconstruction

level, it is necessary to be able to account for numerous detector effects. The response matrix $\mathcal{R}$ collects all these informations. It is defined as a two-dimensional histogram of events with reconstructed and truth p_{T}^{Z} distributions (see Figure 5.9 (a)).

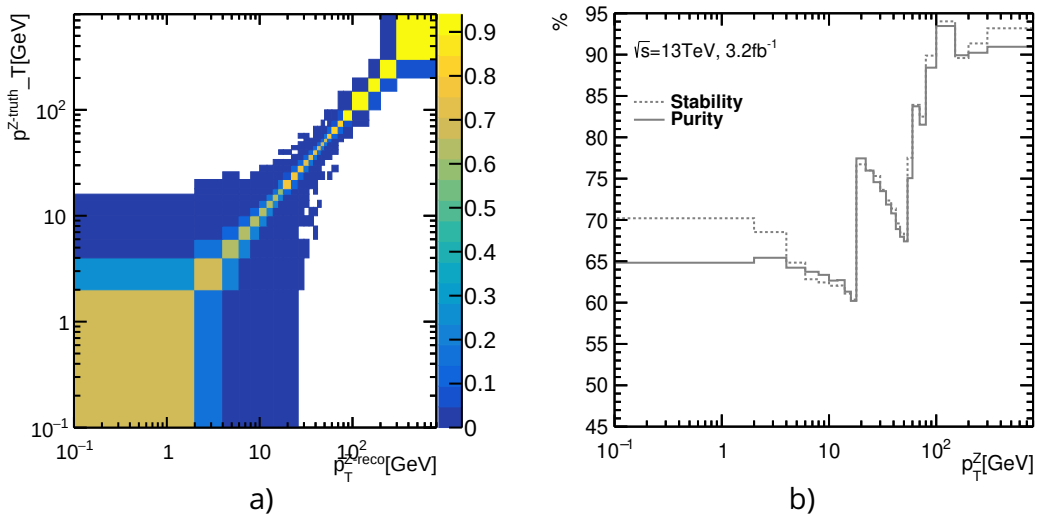

Figure 5.9: *Two-dimensional representation of the response matrix (a) normalized to number of events in reconstructed bin and Purity and stability (b) per p_{T}^{Z} bin in percent.*

In order to estimate the event migration mentioned above, Purity and stability are used. These are defined as:

- **Purity** represents the amount of migration into bin i from other bins. It is defined as the ratio of events, which are reconstructed and generated in bin i over the number of all events reconstructed in this bin. Using the response matrix $\mathcal{R}$ it can be written as

$$\mathcal{P}_i = \frac{\mathcal{R}_{ii}}{\sum_{j=1}^{N} \mathcal{R}_{ij}} \,. \tag{5.24}$$

- **Stability** represents the amount of migration from studied bin i into other bins. It is defined as the ratio of number of events which were reconstructed and generated in the studied bin over the number of events generated in studied bin, which pass the reconstruction criteria. This can be written using the response matrix $\mathcal{R}$ as:

$$\mathcal{S}_i = \frac{\mathcal{R}_{ii}}{\sum_{j=1}^{N} \mathcal{R}_{ji}} \,. \tag{5.25}$$

The optimal bin size should correspond to the detector resolution. The binning of p_{T}^{Z} in this study was inherited from previous measurement [114]. This binning leads to a stability above 60%, a purity above 50% and stable results of the unfolding (see Figure 5.9 (b)). Consequently, the response matrix is mostly diagonal, which can be seen in Figure 5.9 (a).

The unfolding of the p_{T}^{Z} spectrum was achieved using the `RooUnfold` [115] package. To gain full control on the unfolding procedure it was divided into two stages. At first, the `RooUnfoldResponse` object was created from the two-dimensional histogram containing only fiducial events which pass the selection on reconstructed level. The second part, the correction of fiducial efficiency, is applied afterwards as a relative change to the unfolded distribution.

Two tests (called closure and sanity check) were done to prove the concept of unfolding. The closure check of the unfolding method was done using two separate samples. The signal Monte-Carlo events was split into two statistically equivalent samples. The events with even event number are used in tests as training sample and the events with odd event number are used as pseudo-data. Since the pseudo-data contains both fiducial and reconstructed distributions, the fiducial distribution is compared to the unfolded reconstructed distribution, which provides the closure check in Figure 5.10 (b,d) for bin-by-bin and Bayesian iterative method unfolding, respectively.

The sanity check of unfolding was done with the same training and pseudo-data sample i.e. the whole signal Monte-Carlo sample were used to fill both the response matrix and the pseudo-data distributions. The fiducial and unfolded distributions of the sanity test are compared in Figure 5.10 (a,c) for bin-by-bin and Bayesian iterative unfolding, respectively.

In Figure 5.10 the fiducial distribution of the pseudo-data sample is marked with red points. The ratio plot below this is done with respect to this distribution. The reconstructed distribution is marked by cyan points. The unfolded distribution is marked by violet points. The fiducial distribution needs to be as similar as possible to the unfolded distribution retrieved from the reconstructed pseudo-data.

In closure plots a small discrepancy between red and violet distributions is expected. However, the closure test for the Bin-by-Bin method Figure 5.10 (b) shows unwanted behaviour. The unfolded spectrum (voilet) is in full agreement with the fiducial distribution of the training sample (green) which would create irreducible bias. This leads to distribution strongly biased by the training sample (prediction) containing little information from the measurement (data). Consequently, only the Bayesian method, which does not show such behaviour, is used further analysis.

The unfolding uncertainty was estimated as the difference between the two unfolded distributions: First a distribution using the signal Monte-Carlo as training and second with signal Monte-Carlo reweighted to fully describe data used as training.

Several sources of uncertainties are considered in the p_{T}^{Z} measurement. These are described in the following. Simulated events are used to estimate the detector and reconstruction uncertainties using the off-set method. This method varies the correction and efficiency parameters within its estimated uncertainty $\pm 1\sigma$:

- muon reconstruction efficiency variations for systematic and statistical effects in low-p_{T} and high-p_{T} regions separately
- muon trigger efficiency variations for systematic and statistical effects
- muon isolation efficiency variations for systematic and statistical effects
- track momentum correction variations for inner detector and muon spectrometer effects
- muon momentum resolution variation

This analysis procedure is repeated to create a response matrix for each variation. The data is then unfolded with each of these response matrices. The difference between the unfolded variations is then used as the uncertainty.

All but multi-jet background uncertainties were calculated by varying the normalization of each sample within its theoretical uncertainties (see Table 5.4). In case of the multi-jet background, the relative uncertainty in each bin i, calculated as ratio $N_i^{\mathrm{Data}}/\sqrt{N_i^{\mathrm{bkg}}}$, where N^{Data} is number of events observed in data and N^{bkg} is predicted number of all background events, is used as uncertainty. The uncertainty rising

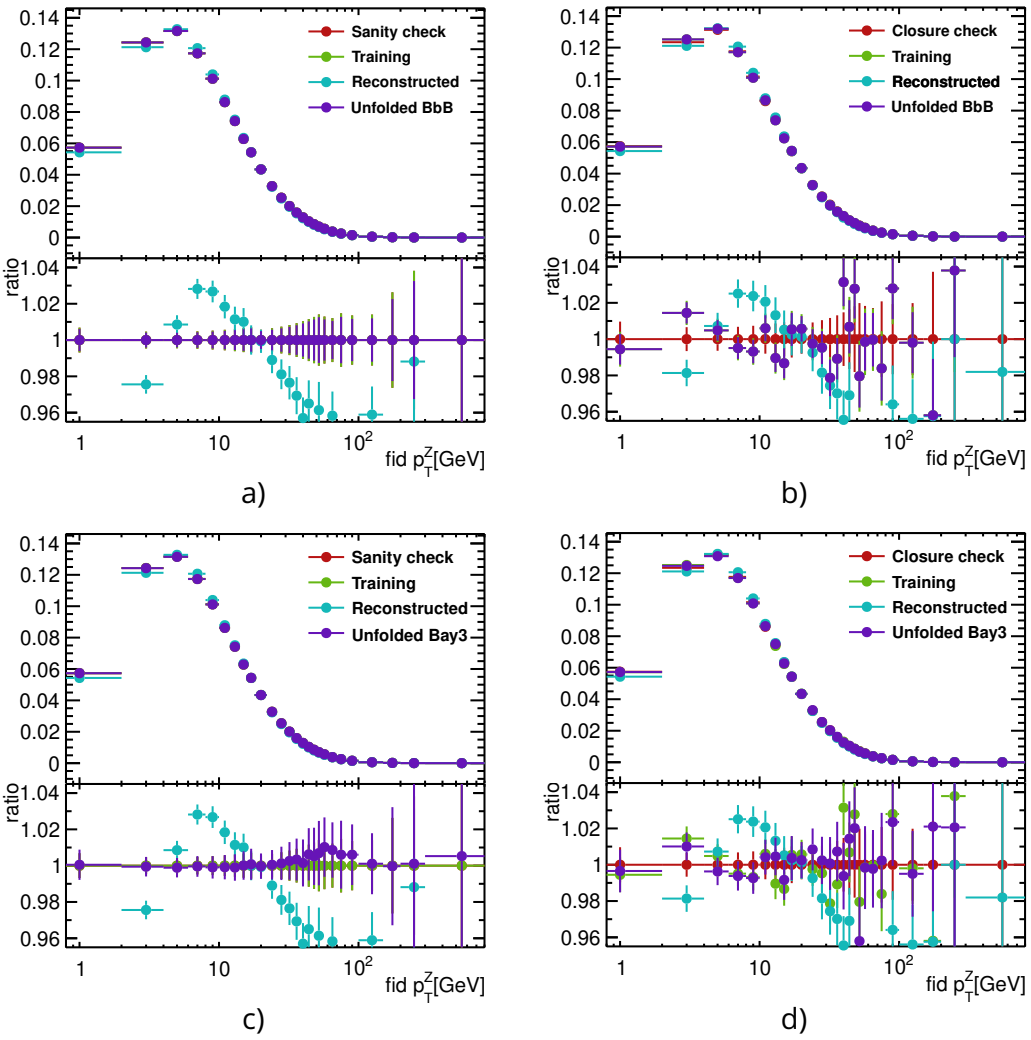

Figure 5.10: *Sanity (a,c) and closure (b,d) tests of Bin-by-Bin (a,b) and Bayesian unfolding (c,d). The pseudo-data fiducial (red) and reconstructed (cyan) distributions are compared to the fiducial distributions of training (green) and unfolded (voilet) shapes of the p_{T}^{Z} distribution. The lower part of each plot shows the ratio of shapes with respect to the fiducial of the pseudo-data.*

from modeling of the background was combined from each channel and treated as uncorelated.

The statistical uncertainty was estimated by generating random histograms called toys. A toy is a histogram which content is generated as a random variable following a Poison distribution. The number of events is hereby given by the corresponding bin content of the measured distribution. One thousand toys were generated and unfolded using the same method and response matrix as used for the measured data. The statistical uncertainty in each bin is calculated as root mean square of the unfolded toys values.

All estimated backgrounds were substracted from the observed data and the resulting spectrum then unfolded using the Bayesian method with five iterations according to the shape convergence between iterations. The obtained shape of the unfolded p_{T}^{Z} distribution is listed in Table 5.5.

The comparison between the unfolded distribution and the two theoretical pre-

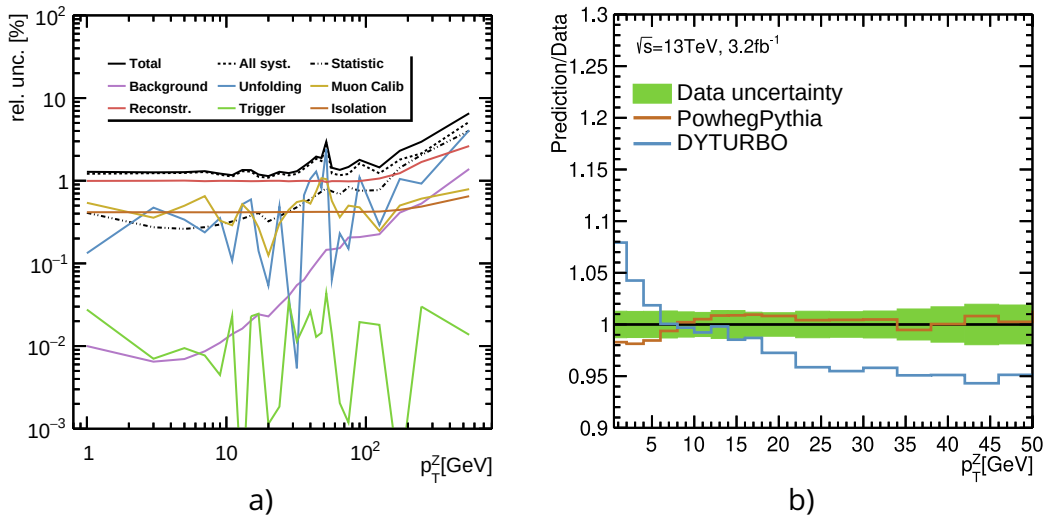

Figure 5.11: *Relative uncertainty contribution to the unfolded p_{T}^{Z} distribution from each source (a). Comparison of the theory predictions to the unfolded data (b), with a predicted value of α_S = 0.1182.*

dictions is shown in Figure 5.11. The Pythia denotes `PowhegPythia8` with `AZNLO` tune and PDF set `CTEQ6L1` (i.e. ATLAS Standard model Monte-Carlo sample). The DYTURBO denotes prediction created with NNLL +NLO using `CT10nnlo` PDF set with nominal value of α_S =0.1182.

p_{T}^{Z} [GeV]	Unfolded $\frac{1}{\sigma_{\text{fid.}}}\frac{d\sigma_{\text{fid.}}}{dp_{\mathrm{T}}^{Z}}$	Rel. stat. unc [%]	Rel. syst. unc. [%]	Rel. tot. unc. [%]
0-2	$4.585\,56\cdot10^{-2}$	1.19	0.41	1.26
2-4	$9.940\,76\cdot10^{-2}$	1.24	0.27	1.27
4-6	$1.052\,62\cdot10^{-1}$	1.18	0.26	1.21
6-8	$9.396\,22\cdot10^{-2}$	1.17	0.27	1.20
8-10	$8.099\,62\cdot10^{-2}$	1.16	0.30	1.19
10-12	$6.904\,41\cdot10^{-2}$	1.09	0.32	1.14
12-14	$5.940\,55\cdot10^{-2}$	1.24	0.35	1.29
14-16	$5.033\,80\cdot10^{-2}$	1.26	0.38	1.31
16-18	$4.357\,03\cdot10^{-2}$	1.09	0.41	1.17
18-22	$6.958\,19\cdot10^{-2}$	1.09	0.32	1.13
22-26	$5.254\,40\cdot10^{-2}$	1.21	0.37	1.27
26-30	$4.079\,06\cdot10^{-2}$	1.12	0.42	1.20
30-34	$3.231\,82\cdot10^{-2}$	1.15	0.48	1.24
34-38	$2.563\,09\cdot10^{-2}$	1.34	0.54	1.44
38-42	$2.067\,57\cdot10^{-2}$	1.56	0.60	1.67
42-46	$1.669\,09\cdot10^{-2}$	1.77	0.67	1.89
46-50	$1.375\,77\cdot10^{-2}$	1.53	0.74	1.69
50-54	$1.125\,72\cdot10^{-2}$	2.73	0.81	2.85
54-60	$1.358\,04\cdot10^{-2}$	1.16	0.74	1.37
60-70	$1.543\,41\cdot10^{-2}$	1.16	0.69	1.35
70-80	$1.030\,96\cdot10^{-2}$	1.20	0.84	1.46
80-100	$1.241\,45\cdot10^{-2}$	1.62	0.76	1.79
100-150	$1.169\,72\cdot10^{-2}$	1.23	0.77	1.45
150-200	$3.413\,34\cdot10^{-3}$	1.80	1.43	2.30
200-300	$1.639\,54\cdot10^{-3}$	2.14	2.05	2.96
300-800	$4.227\,08\cdot10^{-4}$	5.15	4.03	6.54

Table 5.5: *Table of bin-edges, unfolded shape and relative uncertainty (statistical, systematic and total) per each bin of p_{T}^{Z}.*

5.3 Estimation of Strong Coupling Constant

The distribution of the Z boson transverse momentum p_{T}^{Z} is sensitive to the value of the strong coupling constant α_s. Therefore, it is possible to extract the value of α_s from the measured p_{T}^{Z} distribution and such a study is published for the first time in this thesis. The method (see Section 5.1) of α_s estimation is based on a set of theoretical predictions with varied values of α_s, which are then compared to the measured spectrum. The theoretical prediction with NLO+NNLL precision were calculated using DYTURBO generator, which was partially developed within this thesis (see Chapter 4). The measured spectrum of p_{T}^{Z} was estimated from ATLAS data with luminosity $L = 2.7\,\mathrm{pb}^{-1}$ collected from $\sqrt{s} = 13\,\mathrm{TeV}$ LHC collisions in the year 2015.

The fit was repeated two times, i.e. with and without scale variations. This allows the separation theoretical uncertainties (marked as theo in Equations 5.26 - 5.29) from all other effects. The experimental and statistical uncertainties are in the following results marked as syst+stat and this uncertainty covers all effects as they were estimated in the p_{T}^{Z} measurement Section 5.2.

The template method was used to estimate α_s and g_{NP} value separately (one-dimensional method) and simultaneously (two-dimensional method, see Section 5.1 for details). The results of the template fit are shown in Figure 5.13. The shapes of $\Delta\chi^2$ for the case of the one-dimensional extraction and the CL bands for the case of two-dimensional extraction are shown in Figure 5.13 (a,c,e). The fitted shape of p_{T}^{Z} is created by a spline interpolation from templates for the extracted value and compared to the measured distribution in Figure 5.13 (b,d,f).

The fitted value of α_s for the one-dimensional method is

$$\alpha_s^{\mathrm{1D}}(M_Z^2) = 0.1170 \pm 0.0010_{\mathrm{syst+stat}} \pm 0.0076_{\mathrm{theo}}\ , \tag{5.26}$$

and the in case of the two-dimensional method it is

$$\alpha_s^{\mathrm{2D}}(M_Z^2) = 0.1177 \pm 0.0014_{\mathrm{syst+syst}} \pm 0.0086_{\mathrm{theo}}\ . \tag{5.27}$$

The estimation of g_{NP} has limited precision where model uncertainties are dominated by scale variation. The g_{NP} and α_s are very strongly anti-correlated ($\rho = -0.97$). The extracted value of g_{NP} is

$$g_{\mathrm{NP}}^{\mathrm{1D}} = 1.02\ \left(^{+0.42}_{-0.28}\right)_{\mathrm{syst+stat}}\ \left(^{+0.52}_{-0.65}\right)_{\mathrm{theo}}\ \mathrm{GeV}^2 \tag{5.28}$$

for the one-dimensional fit, and in the case of the two-dimensional method it is

$$g_{\mathrm{NP}}^{\mathrm{2D}} = 0.89\ \left(^{+0.51}_{-0.35}\right)_{\mathrm{syst+stat}} \pm \left(^{+0.81}_{-0.92}\right)_{\mathrm{theo}}\ \mathrm{GeV}^2\ . \tag{5.29}$$

The methodology for the study of parton distribution functions effects on the α_s fit were not implemented in this analysis. The estimated size of the p_{T}^{Z} PDF variation envelope is within 0.1% relative uncertainty (see [114]). Therefore, the theoretical uncertainty would be dominated by the scale variation. However, such an estimation does not include the effect of the fitted α_s to the PDF variations. By including the PDF into the fitting χ^2 definition (Equation 5.7) it is possible to constrain the PDF with the new measurement and simultaneously estimate the α_s and g_{NP} values. This strategy is under development using a DYTURBO implementation into the `Xfitter` [116] program. The preliminary α_s measurement presented in this chapter together with the above mentioned improvements indicates that this technique could result in the most precise measurement of α_s at the LHC.

The measurement of $\alpha_s(Q^2)$ is mostly sensitive at the Sudakov peak $Q = (4-6)$ GeV, which is a region where there is no current estimation of α_s contributing to the global

average (see Figure 2.2). The experimental uncertainty of this study is at the same level as the current ATLAS measurement using a transverse energy-energy correlation function $\alpha_s^{\text{TEEC}}(M_Z^2) = 0.1173 \pm 0.0010_{\text{exp.}} \left(^{+0.0065}_{-0.0026}\right)_{\text{theo}}$ [117]. An improvement of the theoretical uncertainties is expected when using higher order prediction than the NNLL+NLO prediction, which is the one that was used in this chapter. However, with DYTURBO it is possible to calculate the prediction up to NNLL +NNLO. The current PDG [7] average value $\alpha_S(M_Z^2) = 0.1181 \pm 0.0011$ does not consider any NLO results from DIS or hadron collider experiments. Therefore, after an improvement to NNLL +NNLO such a measurement would meet the requirements of the Particle Data Group [7] to be used in the α_S world average. Our measurement of $\alpha_S(M_Z^2)$ is compared to the world average and a few selected measurements in Figure 5.12.

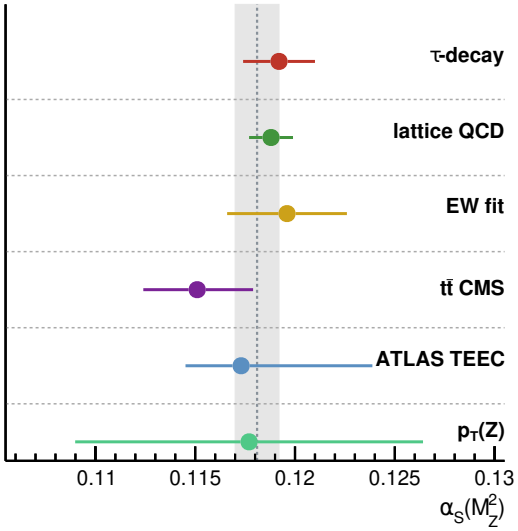

Figure 5.12: *A comparison of $\alpha_S(M_Z^2)$ measurements with the world average (gray band and line). The value from this measurement is named $p_{\text{T}}(Z)$. The other values are taken from [7].*

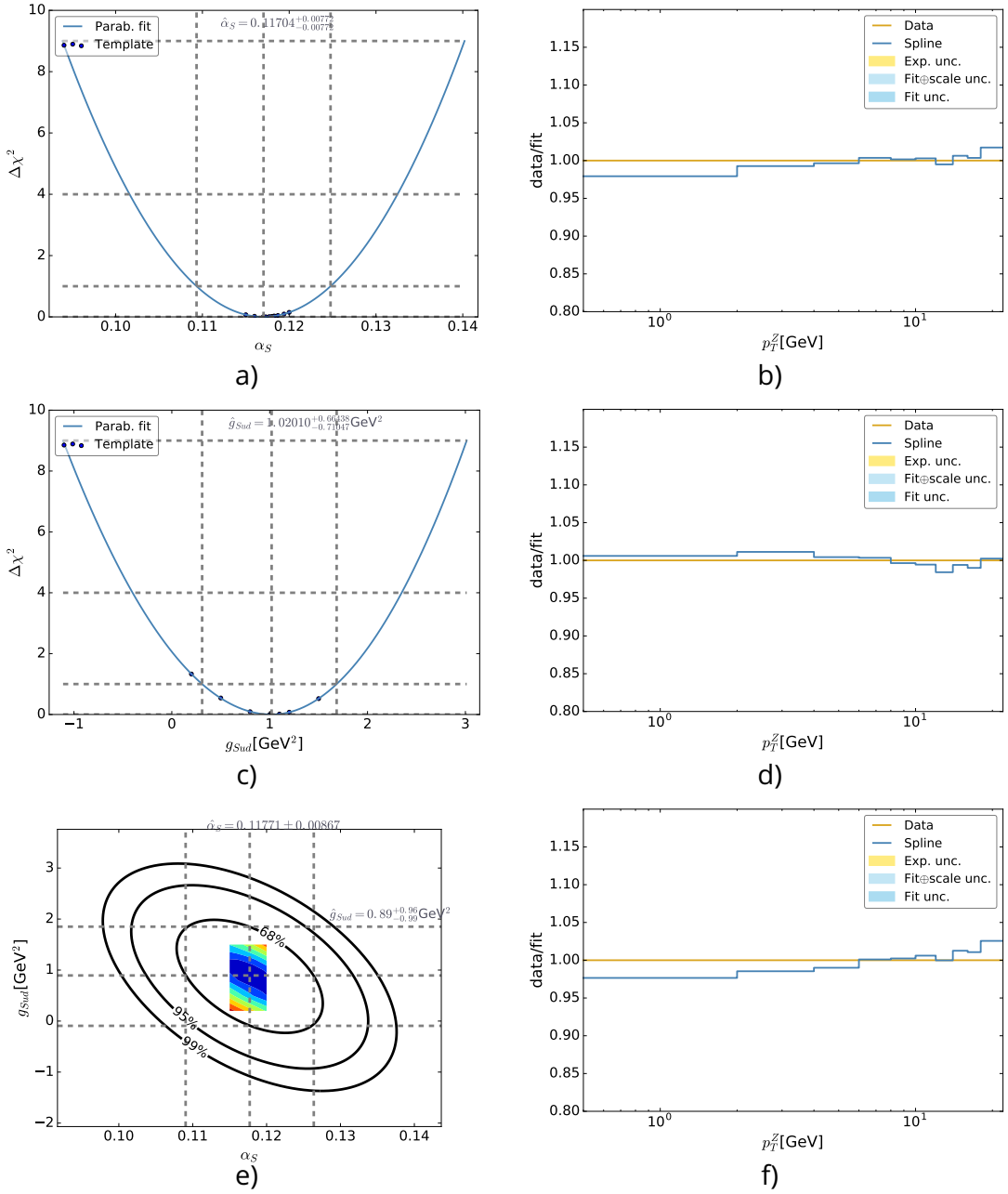

Figure 5.13: *The plots on the left hand side: Fitted $\Delta\chi^2$ parabola w.r.t α_S (a) and g_{NP} (c), and the 68%, 95% and 99%CL regions of the 2D α_S-g_{NP} fit (e). The blue points (1D) and colored areas (2D) mark values of the template where the χ^2 was calculated. The plots on the right right hand side: The ratio of the p_{T}^Z shape between the data (yellow line) and spline (blue line) from the best fitted value of α_S (b) g_{NP} (d) and both simultaneously (f). The yellow band represents the experimental uncertainty. The blue bands represent the uncertainty of the prediction (dark blue) and the total prediction uncertainty including scale uncertainties.*

6. Measurement of W-boson mass

The electroweak sector of the Standard Model is over-constrained once the the Higgs boson mass is fixed. Therefore, the global electroweak fits can used to check the consistency of the SM, after the discovery of the Higgs boson and its mass determination in 2012 [14, 15]. One of the parameters which can be tested by using its indirect estimation is the mass of the charged electroweak boson M_W. Figure 6.1 shows that the current world average (orange point) and the indirect estimation of M_W (blue parabola) differ by $\sim 1.4\sigma$. The first ATLAS M_W measurement with $\sqrt{s} = 7$ TeV data [118] (blue square) appears to be more compatible to the indirect estimation. However, there is still an ongoing analysis of data from collisions delivered by Tevatron during the last two years of its operation. This will further constrain the experimental M_W uncertainty which is currently larger than the uncertainty of the indirect estimation.

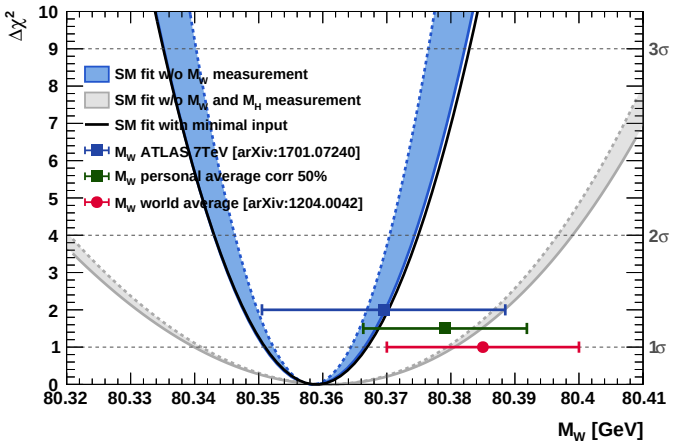

Figure 6.1: *The indirect estimation of M_W with a global electroweak fit (blue parabola) compared to the world average (orange point), new ATLAS measurement [118] (blue square) and personal combination with an assumption of a 50% correlation (green square).*

The measurement of M_W with the DØ detector including a new approach of fitting two-dimensional distributions is described in this chapter as follows. First, the measurement strategy and event modeling are summarized in Section 6.1. The estimation of theoretical uncertainties is described in Section 6.3 and the estimation of experimental uncertainties is described in Section 6.4. The $Z \to ee$, $W \to e\nu$ and background samples, the event selection and comparison of data and predictions are presented in Section 6.5. Results of the M_W estimation from one and two-dimensional distributions are presented in Section 6.6. The preservation of the published DØ M_W measurement is described in Section 6.7 in the end of this chapter.

6.1 Template fit of W boson mass

The mass M_W is estimated from events where a W boson decays into an electron (positron) and an electron anti-neutrino (neutrino). Due to the missing z-coordinate

of the neutrino momentum it is impossible to reconstruct the invariant mass M_W directly for every event. Therefore, the measurement of M_W is done indirectly via kinematic observables defined in the transversal plane which are sensitive to the M_W value. A natural choice for a M_W-sensitive variable is to define the invariant mass equivalent in the transversal plane, i.e. transversal mass

$$m_{\mathrm{T}} = \sqrt{2p_{\mathrm{T}}^{e}\not{E}_{\mathrm{T}}(1-\cos\Delta\varphi)}\,, \tag{6.1}$$

where p_{T}^{e} is the measured electron transverse momentum, $\not{E}_{\mathrm{T}}$ is the energy imbalance in the transversal plane and $\Delta\varphi$ is the opening angle between the p_{T}^{e} and $\not{E}_{\mathrm{T}}$ vectors. Another example of a M_W-sensitive variable is the electron transverse momentum. Distributions for m_{T} and p_{T}^{e} have a characteristic Jacobian peak at a value of M_W and $\frac{M_W}{2}$, respectively.

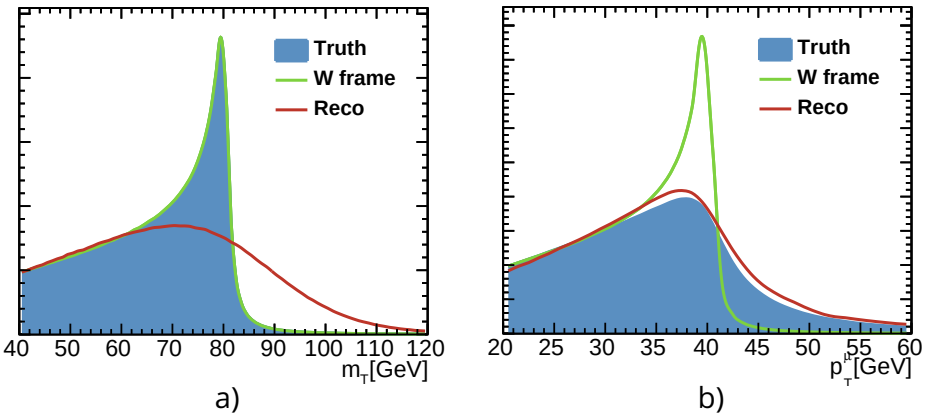

Figure 6.2: *Shapes of the transverse mass m_{T} (a) and the lepton transverse momentum p_{T}^{ℓ} (b) distributions. The blue filled area shows the truth distribution in the lab system ($q_{\mathrm{T}} \neq 0$), the green line shows the distribution in the W rest frame ($q_{\mathrm{T}} = 0$) and the red line shows the distribution after the detector simulation. The plots were created with RESBOS and PMCS (see text). All distributions are scaled to unity.*

The Jacobian peak of the p_{T}^{e} distribution (Figure 6.2(b)) is sharp in the boson center-of-mass system, but the peak is smeared by boosting to the laboratory system due to the transverse momentum of the W boson. On the other side, the Jacobian peak of m_{T} (Figure 6.2(a)) is sharp even after boosting to the laboratory system. The smearing is apparent in the distribution with included detector effects. The origin of the smearing is in the measurement resolution of $\not{E}_{\mathrm{T}}$. A newly suggested distribution for the extraction of M_W is the two-dimensional m_{T}-p_{T}^{e} distribution. The two-dimensional distribution inherits the Jacobian peak and consequently a sensitivity to M_W. The advantage of this approach is the combination of measurements and uncertainties with a proper correlation by construction.

A similar template method to Chapter 5 is used for the extraction of the W mass from three distributions: m_{T}, p_{T}^{e} and a two-dimensional m_{T}-p_{T}^{e} distribution. These distributions are measured by the DØ detector from W events produced during proton–anti-proton collisions. The measured distributions are compared to the set of predictions called templates. Each template represents a distribution for a certain value of M_W. By comparing the measured distribution with all templates it is possible to calculate the likelihood function and estimate the value of M_W.

Templates for every distribution are produced for the range of one hundred equidistant values $M_{W,i}$ with 5 MeV steps. The templates with varied boson masses

$M_{W,i}$ are adjusted by reweighting the generated events. The reweighting factor $r_i(\hat{s})$ is obtained as the ratio of the two Breit-Wiegner functions

$$r_i(\hat{s}) = \frac{(\hat{s} - M_{W,i}^2)^2 + M_{W,i}^2 2\Gamma_W^2}{(\hat{s} - M_{W,0}^2)^2 + M_{W,0}^2 2\Gamma_W^2} \tag{6.2}$$

where $M_{W,0}$ is the nominal generator value and $\hat{s}$ is the partonic squared center-of-mass energy of the event. Afterwards, the templates are interpolated with respect to M_W per each bin and by using cubic splines. This allows to create distributions for any value of M_W continuously in a very short time, which is necessary for the minimization of the likelihood function. The effect of the M_W variation is visible in Figure 6.3, where the distribution shapes are compared for M_W values of 78.439 GeV, 80.399 GeV and 82.359 GeV.

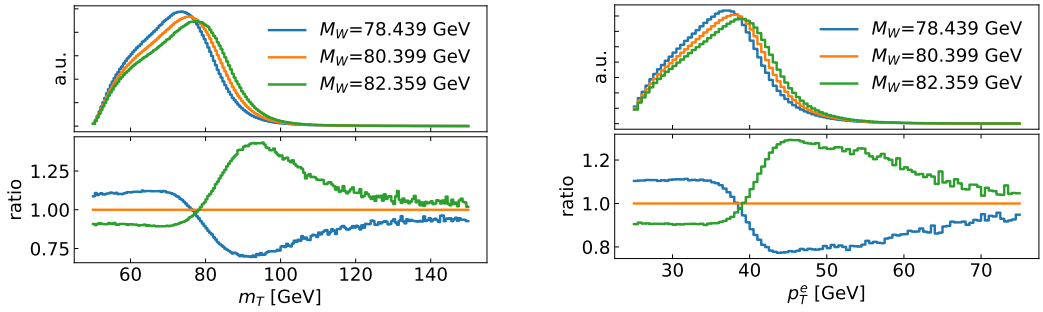

Figure 6.3: *The reconstructed distribution of the W transverse mass (a) and electron transverse momentum (b) for different values of M_W. The upper part of each plot shows distributions normalized to unity. The lower part of each plot shows the ratio with respect to $M_W = 80.399$ GeV.*

The spline templates and distribution from data (or Monte-Carlo variations) are given to the `wzfitter` [119] package. For purposes of this study `wzfitter` was extended and re-designed to be able to fit two-dimensional distributions, fit PDF variations and run ToyMC for estimation of statistical uncertainties within one program. Internally `wzfitter` uses `Minuit` [120] to minimize the negative log-likelihood function ($-\ln \mathcal{L}$).

6.2 Event modeling

The momentum transfer in a Drell-Yan process is intermediated by the electroweak boson: a charged W or a neutral Z. Due to similarity of these two processes the $Z \to ee$ events can be used to calibrate and tune the detector modeling. Afterwards, the modeling is adjusted for the $W \to e\nu$ analysis. The reason for using Z events is that it is possible to measure the complete kinematic information of both leptons at reconstruction level, which is not available in W events due to the undetected neutrino. A schematic view of $p\bar{p} \to W \to e\nu + X$ and $p\bar{p} \to Z \to ee + X$ events is shown on Figure 6.4, with the reconstructed hadronic activity X shown as blue area and the reconstructed electron energy as red area.

Because the templates are compared directly to the measured distribution (no unfolding is applied) the detector effects have to be applied to the template distributions. The detector effects on the shape of the studied distributions are visible in Figure 6.2. The modeling of detector effects for M_W analysis is done by PMCS. It does not simulate the passing of particles through the detector. Instead it rejects or

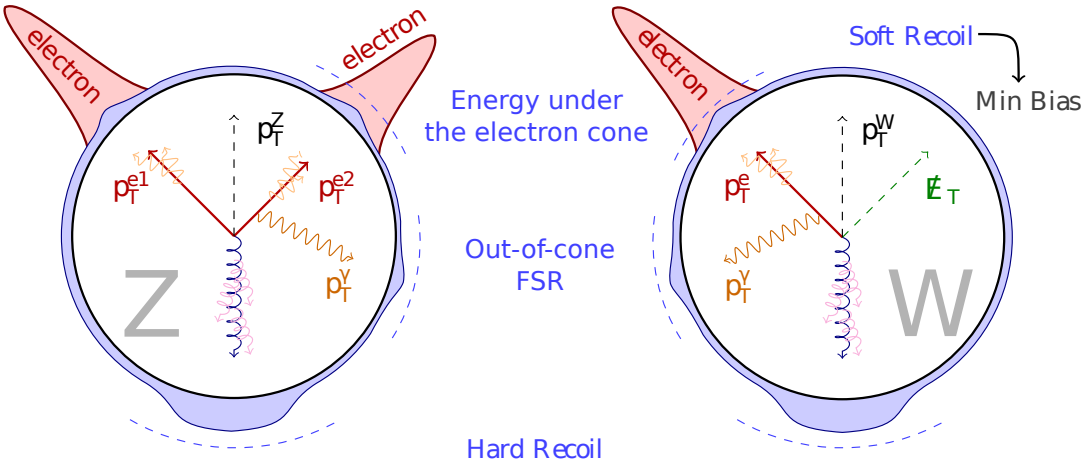

Figure 6.4: *Schematic view of a $Z \to ee$ (left) and a $W \to e\nu$ (right) event in the transversal plane. The inner part of each schema shows the truth momentum vectors and the outer part shows the simulated detector response. The electron response in the calorimeter is depicted as a red area, while the blue area represents the rest of measured activity in the calorimeter (hadronic recoil). The plot was taken from [43] and extended.*

accepts the generator events randomly following the measured and parametrized efficiency distributions. Together with the smearing of generated values this procedure simulates the detector response. The details were already described in several publications [43, 121, 122] and the basic description of the PMCS model can be found in this section. Naturally, every part of the PMCS detector response simulation has a level of precision, which needs to be estimated and propagated to the W mass measurement. The largest expected experimental uncertainties are discussed in Section 6.4.

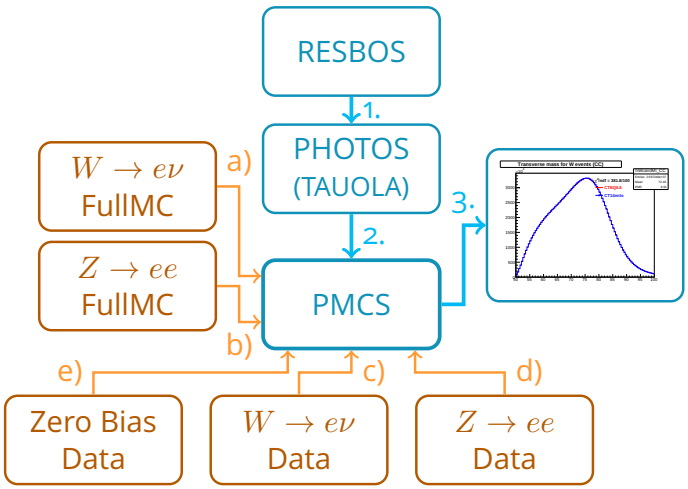

Figure 6.5: *Block diagram of PMCS inputs and outputs. Orange arrows represent inputs to parametrization and tuning. Blue arrows represent the event processing. More description is in the text.*

The structure of PMCS procedures is described by a schema in Figure 6.5. The RESBOS program is used to generate $W/Z \to \ell\ell$ events (Figure 6.5 1.). The predictions from RESBOS were tuned to Tevatron p_{T}^{Z} measurement [77, 52, 31]. The output of

RESBOS are four-momenta of leptons from vector boson decays, which are then processed by PHOTOS [123] (and TAUOLA [124] in case of $W \to \tau\nu$ events) where QED Final State Radiation (FSR) is calculated. The modeling of photons irradiated from final state electrons are necessary to properly simulate the reconstruction performance of the calorimeter in next step. The momenta of leptons and photons are processed by the PMCS program (Figure 6.5 2.).

There is no available information about the underlying event from the RESBOS generator. Consequently, the hadronic response based on generated kinematics is added to PMCS in order to restore hadronic activity measured in W or Z data. The PMCS simulation smears the electron momentum (Figure 6.5 c,d). The pile-up, minimum bias and detector noise are added to hadronic recoil (Figure 6.5 e,d) based on the truth kinematics vector boson (Figure 6.5 b) and the measured instantaneous luminosity (Figure 6.5 c,d). Finally, the electron identification and reconstruction efficiencies are applied (Figure 6.5 a,d).

The PMCS program applies the same cuts on reconstructed objects as those which are applied on data. Afterwards, all histograms necessary for control plots and fitting distributions are filled. At this stage, each event is re-weighted by a Breit-Wiegner function [26] for a range of M_W values in order to create templates per each fitted distribution. The output histograms are used to check the consistency between data and FullMC, and to provide templates for the M_W fitting program (Figure 6.5 3.).

The PMCS combines the detailed detector simulation with information from control data samples. This allows to fine-tune the detector response modeling to fully match the data. Also the PMCS has reduced computational time compared to FullMC. Therefore, it is possible to repeat the analysis for several systematic variations separately using large statistics. The current performance of the PMCS simulation allows us to study the effect on the W mass at MeV-level, which is not possible with FullMC. The dominant uncertainties are discussed in the next section.

The used analysis code is based on W-mass-group tools and official `cafe` repositories [125, 119, 126, 127]. The `cafe` packages were mirrored into one git repository `cafe_2D` [128]. This repository contains all changes which were done to finish this analysis.

6.3 Estimation of the modeling uncertainties

The event modeling starts with a RESBOS prediction which is using the CSS formalism to calculate a fully differential cross section for the Drell-Yan process. The formalism is described in Section 2.3 and the program properties are described in Chapter 4. This section is focused on the estimation of the theoretical model uncertainties and their propagation to M_W.

The modeling uncertainties on M_W are divided into three separated studies. The first uncertainty, which origins from soft and collinear gluon modeling is mostly affecting the shape of the p_{T}^W distribution. Therefore, in the further text it is described as p_{T}-shape uncertainty and is discussed in Section 6.3.1. The second and largest theoretical uncertainty origins from limited information about the momentum of incoming partons and is discussed in Section 6.3.2. A method for PDF information improvement is described in Section 6.3.3 as PDF profiling. The third uncertainty describing the precision of QED modeling is not discussed in this thesis, but can be found in [129].

6.3.1 Boson p_{T}-shape uncertainty

The RESBOS prediction of the vector boson production is split into two parts. The perturbative part is calculated by fixed order QCD and is divergent in the low-p_{T}^W

region. Therefore, the second part includes corrections to soft and collinear gluon emission. The calculation is using the resummation formalism and it is the most contributing part to the prediction for bosons with $p_{\mathrm{T}}^{W} < 30\,\mathrm{GeV}$ (see Figure 2.7).

To be able to test shape uncertainties of QCD modeling with the RESBOS program it is necessary to have corresponding grids with parameter variations. The description of available grids and corresponding results are presented in this section.

The M_W measurement is done with events with $u_{\mathrm{T}} < 15\,\mathrm{GeV}$, which is a region dominated by non-perturbative contribution. The resummation calculation is controlled by a non-perturbative parameter (see Section 2.3) and therefore the uncertainty of the p_{T}^{W}-modeling is estimated by varying this parameter.

RESBOS uses a non-perturbative form factor BNLY (Brock, Nadolsky, Landry, Yuan) [31] form, which has three parameters (see Tab Table 6.1). It is the most general form of a non-perturbative form factor from the RESBOS authors:

$$\mathcal{S}_{\mathrm{NP}}^{\mathrm{BNLY}} = \exp\left[-b^2\left(g_{\mathrm{NP}}^{(1)} + g_{\mathrm{NP}}^{(2)}\ln\left(\frac{Q}{2Q_0}\right) + g_{\mathrm{NP}}^{(3)}\ln\left(\frac{x_1 x_2}{0.001}\right)\right)\right]. \tag{6.3}$$

However, it was shown that mostly the $g_{\mathrm{NP}}^{(1)}$ term is sensitive to measurement. Therefore, the form factor was further simplified and it was used for the study of variations and correlation between non-perturbative and perturbative parameters. The simplified form factor is marked as GNW by Guzzi, Nadolsky and Wang [32].

$$\mathcal{S}_{\mathrm{NP}}^{\mathrm{GNW}} = \exp\left[-b^2 g_{\mathrm{NP}}\right] \tag{6.4}$$

Consequently, when only one non-perturbative parameter is varied in the analysis described in this thesis, it means we are using a sample with GNW (or Gaussian) parameterization. The perturbative parameters are written as $C_{1,\ldots,4}$ and they represent renormalization and factorization scales in RESBOS formalism. The perturbative parameters are usually fixed in a way that $C_1 = C_3$ and $C_2 = C_4$. In RESBOS, the b_{max} represents a numerical parameter controlling integration boundaries in Mellin space. The values of parameters which were used to created CTEQ6.6 grid files are summarized in Table 6.1.

b_{max}	$g_{\mathrm{NP}}^{(1)}$	$g_{\mathrm{NP}}^{(2)}$	$g_{\mathrm{NP}}^{(3)}$	C_1	C_2	C_3	C_4
0.5	0.21	0.68	−0.6	1.122 919	1	1.122 919	1

Table 6.1: *Values of perturbative and non-perturbative parameters of CTEQ6.6 grid files [130]. The values of parameters were taken from the grid file header.*

The main sample for the M_W measurement is CTEQ6.6 BNLY. However, there is no available parameter variation for this sample. Therefore, CT10nnlo GNW grids were used to study the p_{T}-shape uncertainty. The first available sample [131] for a g_{NP} parameter variation had non-consistent values of the integration parameter b_{max}. The effect of this issue is shown in Figure 6.6, where the Sudakov peak of the p_{T}^{W} distribution is not only shifted to softer values, but also a non-physical shape after the peak (marked by "kink"), which is caused by an incorrect $b_{\mathrm{max}} = 0.5$ value with respect to other variations with $b_{\mathrm{max}} = 1.5$.

A new study and new grids were produced by RESBOS authors [132] and used in this study. There are different regimes to estimate the non-perturbative GNW parameter g_{NP} from Tevatron p_{T}^{Z} data [133]. The estimated values are summarized in Table 6.2. To simplify the method description, the regimes of the perturbative part are

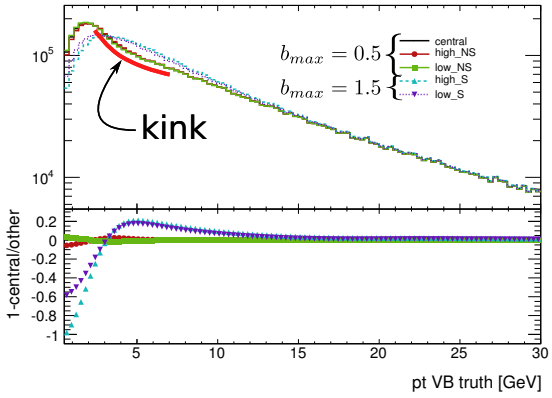

Figure 6.6: *The shapes of the p_{T}^{W} distribution without any fiducial cut as obtained from RESBOS CT10nnlo g_{NP} variations for fixed (red and green) and varied (cyan and violet) perturbative scales. The non-physical shape is marked by "kink".*

named according to the color-convention in Fig.9 of [133]. The nominal is the sample used as central PDF sample of CT10nnlo grids and it is identical to the fixed $C_{1,3} = 2b_0$ approach. The value and uncertainty of g_{NP} in this case was fitted with templates using fixed perturbative scales $C_{1,2,3} = (2 \cdot b_0, 1/2, 2 \cdot b_0)$[1]. These values were estimated before the g_{NP} fit. The other available g_{NP} estimation was done with free $C_{1,2,3}$ parameters during the fit. The estimated perturbative parameters are $C_{1,2,3} = (1.42, 0.33, 1.23)$ and the values of the non-perturbative parameter are listed in Table 6.2.

Grid name	b_{max}	g_{NP}	C_1	C_2	C_3	C_4
nominal CT10nnlo	1.5	1.1	2.245 837 9	0.5	2.245 837 9	0.5
Free C_i center	1.5	0.82	1.594 544 9	0.33	1.381 190 3	0.33
Free C_i high	1.5	1.04	1.594 544 9	0.33	1.381 190 3	0.33
Free C_i low	1.5	0.71	1.594 544 9	0.33	1.381 190 3	0.33
Fixed $C_{1,3} = 2b_0$ center	1.5	1.12	2.245 837 9	0.5	2.245 837 9	0.5
Fixed $C_{1,3} = 2b_0$ high	1.5	1.19	2.245 837 9	0.5	2.245 837 9	0.5
Fixed $C_{1,3} = 2b_0$ low	1.5	1.05	2.245 837 9	0.5	2.245 837 9	0.5
Fixed $C_{1,3} = b_0$ (missing) center	1.5	0.82	1.42	0.33	1.23	0.33
Fixed $C_{1,3} = b_0$ (missing) high	1.5	1.04	1.42	0.33	1.23	0.33
Fixed $C_{1,3} = b_0$ (missing) low	1.5	0.71	1.42	0.33	1.23	0.33

Table 6.2: *Values of parameters for updated CT10nnlo grids [132] with different perturbative regimes. The values were taken from the header of available grid files except for the values for fixed $C_{1,3} = b_0$ which were taken from [32].*

The above described grids were used and a total of $3{\cdot}10^9$ events (generator level) were produced in order to meet required sub-MeV fit sensitivity. The W mass was fitted for each parameter variation for fixed and free scales. The difference of fitted values is used as the estimated uncertainty. Since no parameter correlation were

[1]The value $b_0 = 2e^{-\gamma_E} = 1.123\ldots$ is defined by the Euler-Mascheroni constant $\gamma_E = 0.577\ldots$.

available uncertainties are considered to be fully uncorrelated. Hence, the p_{T}-shape uncertainties, which have been propagated to the M_W measurement were estimated as squared sum of the two results. The values are presented in Table 6.3

Uncertainty [MeV]	m_{T}	p_{T}^{e}	$m_{\mathrm{T}} - p_{\mathrm{T}}$
Free $C_{1,2,3}$	$2.71^{+3.60}_{-1.82}$	$12.05^{+16.05}_{-8.06}$	$2.45^{+3.24}_{-1.65}$
Fixed $C_{1,2,3}$	$1.48^{+1.48}_{-1.48}$	$6.10^{+6.10}_{-6.11}$	$2.20^{+2.19}_{-2.20}$
p_{T}-shape final	3.09	13.51	3.36

Table 6.3: *Calculated p_{T}-shape uncertainties from available non-perturbative parameter variations. The main value is the symmetric uncertainty and the subscript (superscript) is the negative (positive) difference from the central sample. The last row represents a conservative squared sum of these uncertainties.*

6.3.2 PDF uncertainty

The largest model uncertainty contributing to the M_W measurement origins from the limited knowledge of the parton distribution functions of the proton. The authors of parton distribution functions publish the central values together with variations of internal parameters. The space of internal parameters is usually diagonalized and a final PDF set contains variations of eigenvalues rather than variations of physical quantities. Each eigenvalue has positive and negative variation and the eigenvalues are uncorrelated between each other as a result of the diagonalization.

The estimation of the size of the PDF uncertainty is done by using the PDF set CTEQ6.6 [134], which was also used in a previous publication [43]. Each of the PDF variations were used to create a histogram with a M_W sensitive distribution (m_{T}, p_{T}^{e}, $m_{\mathrm{T}} - p_{\mathrm{T}}$). Afterwards, the distributions were fitted with templates created by a central PDF eigenvalue.

The Hessian envelope was used to obtain the final uncertainty from all PDF eigenvalues. The envelope is defined as

$$\sigma_{68\%} = \sqrt{\sum_{i}^{n_{eigen}} \frac{(\Delta M_i)^2}{2.705}}, \tag{6.5}$$

where n_{eigen} is the number of all eigenvalues. The CTEQ group uses variations at a 90% confidence level. Therefore, a scaling factor 2.705 was used to obtain a 68% confidence level uncertainty, which is compatible with 1σ variations of other uncertainties. The term ΔM_i is defined by

$$(\Delta M_i)^2 \equiv \frac{(M_i^+ - M_i^-)^2}{4} \tag{6.6}$$

where M_i^+ and M_i^- are fitted masses for positive and negative variation of the eigenvalue i. This is a symmetric definition of uncertainty. The estimation of positive and negative uncertainty separately from terms $\Delta^{\pm} M_i$ is calculated by

$$\Delta^+ M_i \equiv +\max\left((M_i^+ - M_0), (M_i^- - M_0), 0\right) \tag{6.7}$$

$$\Delta^- M_i \equiv -\min\left((M_i^+ - M_0), (M_i^- - M_0), 0\right) \tag{6.8}$$

where $M_i^{\pm}$ are the fitted masses from positive (negative) variations of eigenvalue i and M_0 is the central value. The individual square differences $(\Delta M_i)^2$, $(\Delta^{\pm} M_i)^2$ are shown per each eigenvalue in Figure 6.7, to highlight the most contributing eigenvalue. It was shown in [135] that eigenvalue number twelve is mostly controlling the ratio between valence u and d quarks. This is expected to have largest influence on M_W and it is confirmed in Figure 6.7.

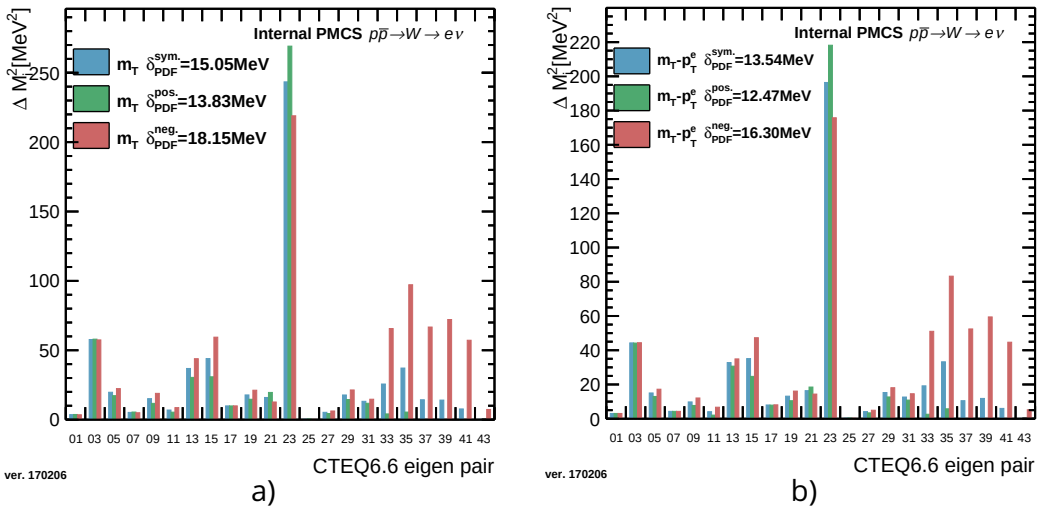

Figure 6.7: *Squared contribution $(\Delta M_i)^2$ to PDF envelope of m_{T} (a) and $m_{\mathrm{T}} - p_T$ (b) per each eigenvalue. The symmetric term $(\Delta M_i)^2$ is represented as blue bars and positive (negative) term $(\Delta^{\pm} M_i)^2$ is represented as green (red) bars.*

The envelope is then calculated by Equation 6.5 and it is illustrated in Figure 6.8 as blue band. Each green point represents a fitted value including the error bar representing the uncertainty of the fit, i.e. mainly statistical uncertainty of the generated sample. The fit uncertainty is at a level of 1.3 MeV. The variations of eigenvalues are plotted in order: first positive and then negative. The impact on M_W can be opposite e.g. a positive PDF variation reduces the fitted value of M_W. In this case the plots (Figure 6.8) show an area which is crossed, instead of continuously filled.

Despite the fact that the p_{T}^Z distribution shows good agreement between CT14nnlo, CTEQ6.6 prediction and $Z \to ee$ data (see Figure 6.9), the discrepancy is clear between $W \to e\nu$ data and PMCS modeled from CT14nnlo prediction (see Figure 6.10 (b)). This is in contrast to CTEQ6.6 PMCS, which shows good agreement with data.

These facts point to a possible problem during production of $W \to e\nu$ CT14nnlo grids. This issue with W grids were discussed with RESBOS authors. For this thesis it is not reasonable to use the CT14nnlo sample to estimate the PDF uncertainty. Therefore, a different approach to constrain the PDF uncertainties is discussed in the next section Section 6.3.3. The final comparison of all PDF studies is summarized in this section and more plots can be found in Appendix C.

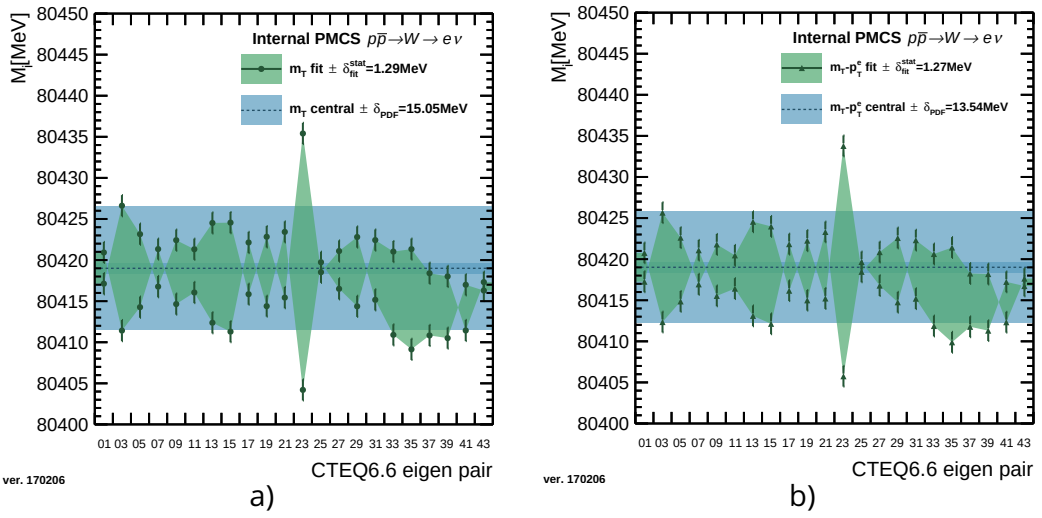

Figure 6.8: *Fitted values of M_W from m_{T} (a) and $m_{\mathrm{T}} - p_T$ (b) per each eigenvalue (points and green band) with the central value (black dashed line) and final scaled PDF envelope (blue band). Error bars and dark blue band represent the statistical uncertainty of the generated sample.*

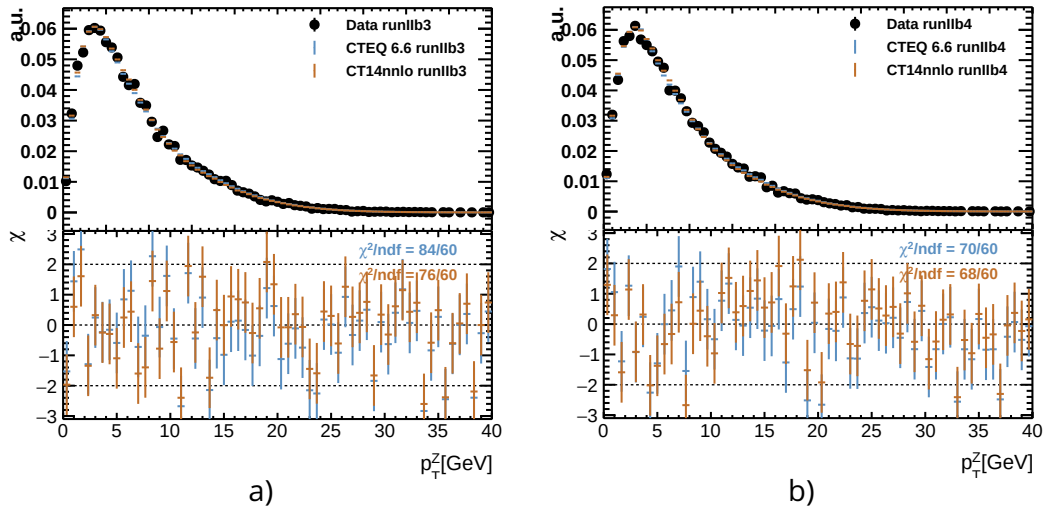

Figure 6.9: *Distribution of Z transverse momentum from (black points) runIIb3 (a) and runIIb4.b) data compared to PMCS predictions using CT14nnlo (brown points) and CTEQ6.6 (blue points) PDF set.*

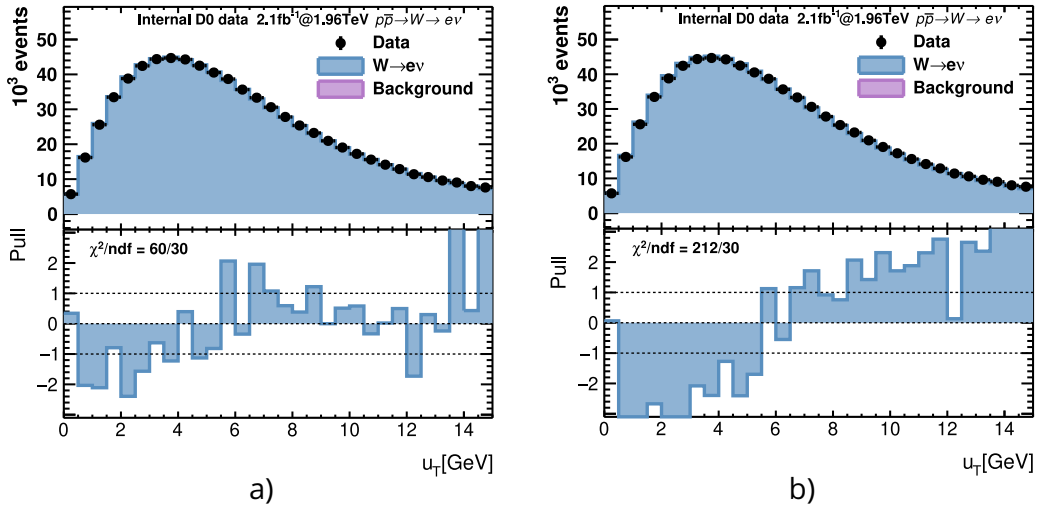

Figure 6.10: *Distribution of hadronic recoil in $W \to e\nu$ events from runIIb3 data compared to CTEQ6.6 (a) and CT14nnlo (b) PMCS prediction. The lower part shows a pull plot between data as PMCS.*

6.3.3 PDF profiling

A published PDF set is fixed, i.e. it has information only from measurements, which were available at the time of its correlation. Additional measurements could improve (constrain) the PDF set. Usually, it is done by the PDF set authors via a new version of certain PDF together with theoretical model improvements. However, older PDF versions can be constrained by new measurements via Hessian reweighting method [136]. As result of this procedure a new PDF set is obtained as linear combination of the original eigenvalues. The calculation of this linear combination is called PDF profiling and this technique is further described and used to constrain the already mentioned CTEQ6.6 sample using the `Xfitter` [116] program.

The measurement from Tevatron [137] was used to constrain the CTEQ6.6 PDF set. The profiling is done by definition of χ^2 with nuisance parameter vectors for theoretical (PDF) $\boldsymbol{\beta_{th}}$ and experimental (measurements) $\boldsymbol{\beta_{exp}}$:

$$\begin{aligned}\chi^2(\boldsymbol{\beta_{exp}}, \boldsymbol{\beta_{th}}) &= \boldsymbol{\chi^2_{exp}} + \boldsymbol{\chi^2_{th}} \\ &= \sum_{i=1}^{N_{\text{data}}} \frac{\left(\sigma_i^{\text{exp}} + \sum_j \Gamma_{ij}^{\text{exp}} \beta_{j,\text{exp}} - \sigma_i^{\text{th}} - \sum_k \Gamma_{ik}^{\text{th}} \beta_{k,\text{th}}\right)^2}{\Delta_i^2} + \\ &+ \sum_j \beta_{j,\text{exp}}^2 + \sum_k \beta_{k,\text{th}}^2 \,,\end{aligned}$$

where Γ_{ij}^{exp} and Γ_{ik}^{th} describes the nuisance vectors influence on the data and theory respectively. Experimental measurements, theory predictions and uncorrelated experimental uncertainties are represented by σ_i^{exp}, σ_i^{th} and Δ_i^2, respectively. After a χ^2 minimization new values of Γ_{ik}^{th} and $\beta_{k,\text{th}}$ are obtained. A simple algebraic calculation is performed in order to find the shift and rotation for the new-eigenspace with respect to the original PDF

$$\begin{aligned}\boldsymbol{\beta_{th}}^T C \boldsymbol{\beta_{th}} &= \boldsymbol{\beta_{th}}^T G^T D G \boldsymbol{\beta_{th}} \\ &= \boldsymbol{\beta_{th}}^T (\sqrt{D} G)^T \sqrt{D} G \boldsymbol{\beta_{th}} \\ &= (G' \boldsymbol{\beta_{th}})^T G' \boldsymbol{\beta_{th}} \\ &= (\boldsymbol{\beta'_{th}})^T \boldsymbol{\beta'_{th}} \,,\end{aligned} \tag{6.9}$$

where the orthogonal matrix G and the positive-definite matrix D is calculated from eigenvectors and eigenvalues of the matrix C. The term $\sqrt{D}$ represents the diagonal matrix elements $\sqrt{D_{ii}}$. Further orthogonal operations would transform G' into triangular form, which leaves the new eigenvalues aligned as much as possible along the original basis.

The new central value of f'_0 is calculated by

$$f'_0 = f_0 + \sum_k \beta_{k,\text{th}}^{\text{min}} \left(\frac{f_k^+ - f_k^-}{2} - \beta_{k,\text{th}}^{\text{min}} \frac{f_k^+ + f_k^- - 2f_0}{2} \right) \tag{6.10}$$

where f_0 is the original central value and $f_k^\pm$ are up and down variations of the original eigenvector k. In a similar way new values $f_i'^\pm$ can be obtained by

$$f_i'^+ = f'_0 + \sum_k G'_{ik} \left(\frac{f_k^+ - f_k^-}{2} + G'_{ik} \frac{f_k^+ + f_k^- - 2f_0}{2} \right) \tag{6.11}$$

$$f_i'^- = f'_0 - \sum_k G'_{ik} \left(\frac{f_k^+ - f_k^-}{2} - G'_{ik} \frac{f_k^+ + f_k^- - 2f_0}{2} \right) \tag{6.12}$$

where f_0, $f_k^{\pm}$, f_0' have same meaning as in Equation 6.10; they were calculated in Equation 6.9.

The measurements which were used for constraining the PDF set are listed in Table 6.4. The largest constrain is expected from the measurement of a differential cross section of the Z boson with respect to rapidity $\mathrm{d}\sigma(Z)/\mathrm{d}y$ and charge asymmetry of W production measured by the leptons pseudo-rapidity A_C^{μ} or by the boson rapidity A_C^W. Most of the time, the statistical uncertainties are considered to be uncorrelated between bins. The only exception is the DØ measurement of W boson production charge asymmetry, where a correlation matrix is provided. In general, the correlation model of the experimental uncertainties which is recommended by the Tevatron experiments is adapted and followed, with the exception of the experimental systematic uncertainties related to trigger and lepton identification efficiencies which are treated as completely uncorrelated.

Observable	Experiment	Integrated luminosity	Kinematic requirements	Ref.
$d\sigma(Z)/dy$	Do	0.4 fb^{-1}	$71 < m_{ee} < 111$ GeV	[138]
$d\sigma(Z)/dy$	CDF	2.1 fb^{-1}	$66 < m_{ee} < 116$ GeV	[139]
A_C^{μ} in $W \to \mu\nu$	Do	7.3 fb^{-1}	$p_{\mathrm{T}}^{\mu} > 25$ GeV, $p_{\mathrm{T}}^{\nu} > 25$ GeV	[140]
A_C^W in $W \to e\nu$	CDF	1.0 fb^{-1}	$E_T^e > 25$ GeV, $p_{\mathrm{T}}^{\nu} > 25$ GeV	[141]
A_C^W in $W \to e\nu$	Do	9.7 fb^{-1}	$E_T^e > 25$ GeV, $p_{\mathrm{T}}^{\nu} > 25$ GeV	[142]

Table 6.4: *List of Tevatron measurements used for constraining the CTEQ6.6 PDF set.*

For more details about profiling see Appendix C. The fit results from original CTEQ6.6 where used and combined with the results from profiling. The new central value and eigenvectors were calculated by Equation 6.10 and Equation 6.12. The comparison of original and profiled envelope is shown in Figure 6.11.

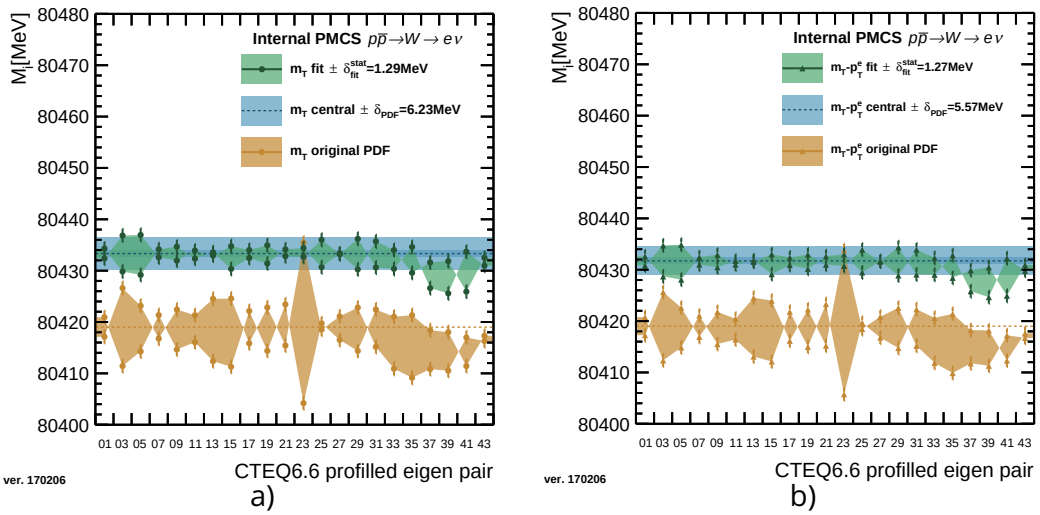

Figure 6.11: *Fitted values of M_W from m_{T} (a) and $m_{\mathrm{T}} - p_{\mathrm{T}}$ (b) per each eigenvalue are represented by points. Original and profiled CTEQ6.6 is depicted by orange and green color, respectively. The blue band represents the scaled symmetric PDF envelope.*

$\Delta M_W^{fit} \pm \delta_{PDF}$[MeV]	m_T	p_T^e	$m_T - p_T^e$
CTEQ6.6	0.00 ± 15.26	0.00 ± 21.91	0.00 ± 14.49
CTEQ6.6 profilled	14.49 ± 6.27	15.82 ± 13.51	13.50 ± 5.89
CT14nnlo	35.30 ± 12.89	71.07 ± 24.30	33.45 ± 12.16

Table 6.5: *Estimated PDF uncertainty δ_{PDF} and fitted M_W from central sample of each PDF set using templates from CTEQ6.6 prediction ΔM_W^{fit}*

The final comparison of original CTEQ6.6, profiled CTEQ6.6 and CT14nnlo samples is summarized in Table 6.5. The ΔM_W^{fit} represents the difference between fitted values using original CTEQ6.6 templates per each row. The profiled ΔM_W^{fit} value is consistent within CTEQ6.6. On the other hand, the CT14nnlo issue with p_{T}^W modeling is visible here as large discrepancy of the p_{T}^e fit. The values from the table are represented as plot on Figure 6.12. The profiled uncertainties are reduced approximately by factor 2 compared to original CTEQ6.6. The origin of M_W PDF uncertainty improvement is most probably in the reduction of valence parton function difference $u_v - d_v$ uncertainty, which is contributing to the largest eigenvalue variation in case of the original CTEQ6.6 PDF set (see Figure 6.11 variation 23). The results from profiled CTEQ6.6 PDF set were taken as final W mass PDF uncertainty (see Table 6.10).

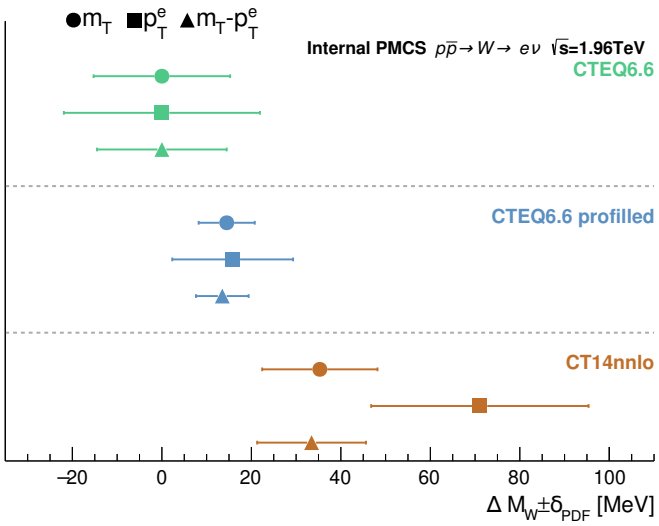

Figure 6.12: *Comparison of original (green) and profiled CTEQ6.6 (blue) and CT14nnlo (brown) PDF uncertainties for m_{T} (circle) p_{T}^e (square) $m_{\text{T}} - p_T$ (triangle) distributions. The shift ΔM_W is estimated by fitting central distributions of each PDF sample with CTEQ6.6 templates.*

6.4 Detector level parametrization and experimental uncertainties

The simulation of the detector response needs to be applied on top of the generated events to be able to compare predictions directly with measured distributions. The PMCS is using parametrizations derived from the full detector simulation and is tuned to fully describe the data. The parametrization model has several stages and each stage has parameters which are estimated with a certain precision. By varying these parameters within their level of precision it is possible to propagate uncertainties to

the M_W measurement. The detector simulation and detector related uncertainties are described in the following text.

The first step of the detector response simulation is to generate the spatial position of the primary vertex in the event. The z-coordinate is simulated exactly as in FullMC i.e. by Gaussian distribution with mean at zero and width of 25 cm with the additional requirement that the z-coordinate of the primary vertex must be within $|z| < 60\,\text{cm}$. The x and y vertex coordinates are assumed to be zero (again same as in FullMC).

Two components were prepared to be able to describe the underlying event and luminosity response. First, the database describing the contribution from spectator parton interactions called Minimum Bias Library (MBLibrary) is obtained from General purpose Monte-Carlo generator (PYTHIA) [143] and it is independent from the luminosity. Second, the contribution from additional $p\bar{p}$ interactions (pile-up) is stored in Zero Bias Library (ZBLibrary) which was obtained from $Z \to ee$ data events [144]. The PMCS program generates luminosity to match the distribution observed in data. Afterwards, the libraries are used to simulate the scalar sum of energy deposited in the calorimeter $\sum E_{\mathrm{T}}$ with respect to generated luminosity and generated vector boson transverse momentum p_{T}^{W}. The measured and simulated luminosity is compared on Figure 6.15 (a).

The hadronic recoil modeling $\vec{u}_{\mathrm{T}}$ is modelled as sum of four terms

$$\vec{u}_{\mathrm{T}} = \vec{u}_{\mathrm{T}}^{\mathsf{Hard}} + \vec{u}_{\mathrm{T}}^{\mathsf{Soft}} + \vec{u}_{\mathrm{T}}^{\mathsf{Elec}} + \vec{u}_{\mathrm{T}}^{\mathsf{FSR}} \,, \tag{6.13}$$

where $\vec{u}_{\mathrm{T}}^{\mathsf{FSR}}$ is the out-of-cone FSR photon contribution to the hadronic recoil and $\vec{u}_{\mathrm{T}}^{\mathsf{Elec}}$ models the hadronic energy inside of the electron cone. The soft term $\vec{u}_{\mathrm{T}}^{\mathsf{Soft}}$ is described by the ZBLibrary and MBLibrary. The dominant term $\vec{u}_{\mathrm{T}}^{\mathsf{Hard}}$ represents the smeared recoil balancing the generated vector boson transverse momentum p_{T}^{Z}.

A pair of random values – bare recoil u_{T}^{0} and tilt angle of recoil $\Delta\phi_0$– are generated from the evector boson recoil $\vec{q}_{\mathrm{T}} \equiv -\vec{p}_{\mathrm{T}}^{Z}$ in the beginning of modeling. The probability density function for $(u_{\mathrm{T}}^{0}, \Delta\phi_0)$ is obtained from the FullMC $Z \to \nu\bar{\nu}$ sample [122], which assures that effects from the two last terms on right hand side of Equation 6.13 i.e. $\vec{u}_{\mathrm{T}}^{\mathsf{Elec}}$ and $\vec{u}_{\mathrm{T}}^{\mathsf{FSR}}$ are not contributing.

The hard recoil smearing is calculated separately in terms of parallel $u_{\parallel}^{0} = u_{\mathrm{T}}^{0} \cdot \cos(\Delta\phi_0)$ and perpendicular $u_{\perp}^{0} = u_{\mathrm{T}}^{0} \cdot \sin(\Delta\phi_0)$ projection to the boson recoil direction $\vec{q}_{\mathrm{T}}$. The parametrization of the main recoil part $\vec{u}_{\mathrm{T}}^{\mathsf{Hard}}$ follows these equations

$$u_{\parallel}^{\mathsf{Hard}} = \left(a + b \cdot e^{-q_{\mathrm{T}}/\tau}\right) \cdot q_{\mathrm{T}} \langle \frac{u_{\mathrm{T}}}{q_{\mathrm{T}}} \rangle_{\parallel} + c \cdot \left(u_{\parallel}^{0} - q_{\mathrm{T}} \langle \frac{u_{\mathrm{T}}}{q_{\mathrm{T}}} \rangle_{\parallel}\right) \,, \tag{6.14}$$

$$u_{\perp}^{\mathsf{Hard}} = u_{\perp}^{0} \,, \tag{6.15}$$

where the mean value $\langle \frac{u_{\mathrm{T}}}{q_{\mathrm{T}}} \rangle_{\parallel}$ is calculated from the probability density function for a given value of q_{T} and $\Delta\phi_0$. The parameters used in this model are: relative scale a, relative offset b, exponential term τ and relative sampling c.

The parametrization of the soft term $\vec{u}_{\mathrm{T}}^{\mathsf{Soft}}$ follows the equation

$$\vec{u}_{\mathrm{T}}^{\mathsf{Soft}} = -\sqrt{\alpha}\vec{u}_{\mathrm{T}}^{\mathsf{MB}} - \vec{u}_{\mathrm{T}}^{\mathsf{ZB}} \,, \tag{6.16}$$

where α_{MB} is a parameter for tuning the minimum bias component $\vec{u}_{\mathrm{T}}^{\mathsf{MB}}$. Both terms $\vec{u}_{\mathrm{T}}^{\mathsf{MB}}$ and $\vec{u}_{\mathrm{T}}^{\mathsf{ZB}}$ are randomly generated from MBLibrary and ZBLibrary, respectively.

The determination of five hadronic recoil parameters with $Z \to ee$ data is done by comparing the hadronic recoil response and the resolution using the eta-imbalance η_{imb} distribution mean and the root-mean-square, respectively. The motivation to this parametrization is to avoid an explicit dependence on the electron energy scale.

Therefore, an observable $\hat{\eta}$ is defined as unit vector of the the electron-positron system bisector. The eta-imbalance is written as

$$\eta_{\text{imb}} \equiv (\vec{u}_{\text{T}} + \vec{p}_{\text{T}}^{ee}) \cdot \hat{\eta} \tag{6.17}$$

The parameters controlling the response a, b, τ from Equation 6.14 and the parameters controlling the resolution c, α_{MB} from Equation 6.14 and Equation 6.16 were fitted separately [129]. The results of the fit, the uncertainties and the correlations between them are summarized in Table 6.6.

Correlations	a	b	τ	c	α_{MB}
a	1.0000	0.3021	−0.4881	0	0
b	0.3021	1.0000	−0.9039	0	0
τ	−0.4881	−0.9039	1.0000	0	0
c	0	0	0	1.0000	−0.6751
α_{MB}	0	0	0	−0.6751	1.0000
Values	0.9845	0.6480	5.1003	1.1056	0.6460
Uncertainties.	0.0077	0.3900	0.3200	0.0400	0.0640

Table 6.6: *Fitted values with uncertainties of the hadronic recoil parameters and their correlation.*

The energy response of the DØ EM calorimeter is the largest experimental uncertainty of the M_W measurement. The calibration of the electron energy scale is done by a comparison of simulated and measured di-electron invariant mass from $Z \to ee$ events. The reconstructed electron energy E is simulated by

$$E = R_{EM}(E_0) \otimes \sigma_{EM}(E_0) + \Delta E \,, \tag{6.18}$$

where E_0 is the generated electron energy after including in-cone FSR photons, σ_{EM} the resolution of calorimeter and ΔE the electron window term. The calorimeter energy response R_{EM} is modeled by

$$R_{EM}(E_0) = F_{\eta-eq}(\eta_{det}) \times F_{HV-loss}(L, \eta_{det}) \times \left(\alpha \times (E_0 - \bar{E}_0) + \beta + \bar{E}_0\right) \,, \tag{6.19}$$

where $F_{\eta-eq}(\eta_{det})$ describes η-non-uniformity as observed in $Z \to ee$ events with both electrons in the central calorimeter, $F_{HV-loss}(L, \eta_{det})$ models the luminosity-dependence of the calorimeter gains due to high-voltage loss. Instead of correcting the electron reconstruction the high-voltage loss effects are modeled by parametrization, which was developed and it is further explained in M_W runIIb12 analysis [129]. Finally the parameters α and β are defined as scale and offset respectively and they are relative to an arbitrary point $\bar{E}_0$. The value of $\bar{E}_0 = 43$ GeV was chosen as mean energy of electrons in $Z \to ee$ events [145].

The measured invariant mass of two electrons with energies E_{e1} and E_{e2} and an opening angle between them, noted as $\Delta\varphi$, is calculated by

$$M_Z = \sqrt{2E_{e1}E_{e2}(1 - \cos\Delta\varphi)} \,. \tag{6.20}$$

This can be approximated as a Taylor expansion in terms of $\beta \ll (E_{e1} + E_{e2})$ as

$$M_Z \approx \alpha M_Z^{\text{true}} + f_Z\beta + \mathcal{O}\left(\beta^2\right) \,, \tag{6.21}$$

where M_Z^{true} is the generator level value of the Z-boson mass and a kinematic variable f_Z defined as

$$f_Z = \frac{(E_{e1} + E_{e2})\,(1 - \cos\Delta\varphi)}{M_Z^{\text{true}}}\ . \tag{6.22}$$

Using the measurement of M_W vs the f_Z distribution it is possible to extract values of the scale α and the offset β. This was evaluated in bins of instantaneous luminosity including correlation between parameters. The estimated parameters for runIIb3 are summarized in Table 6.7 [129].

	$\mathcal{L} < 2$	$2 < \mathcal{L} < 4$	$2 < \mathcal{L} < 6$	$6 < \mathcal{L}$
α	1.0272±0.0043	1.0296±0.0030	1.0315±0.0047	1.0291±0.0074
β[GeV]	0.268±0.032	0.224±0.022	0.192±0.034	0.213±0.053
Correlation	−0.80	−0.79	−0.78	−0.76

Table 6.7: *Results of the fits for electron energy scale and offset to the data runIIb3. The instantaneous luminosity unit $\mathcal{L}$ is* $36{\cdot}10^{30}\ \text{cm}^{-2}\text{s}^{-1}$.

Two main experimental uncertainty sources are evaluated in this analysis: those due to the modelling of hadronic recoil and those due to electron energy scale. The generated sample was processed by PMCS per each variation of the parameter by $\pm1\sigma$ and $\pm2\sigma$ to propagate the systematic variations to the M_W value. Afterwards, the M_W-dependent distributions with varied parameter were fitted by the templates generated with the nominal value of the parameters. The values of M_W with respect to the parameter variations were determined.

Assuming that the M_W variation is linear with respect to variations of the parameter x in a small region around the central value, the variation of M_W is fitted by line and the slope of this line $\frac{\partial M_W}{\partial x}$ is used to propagate the uncertainty to M_W. The combined W mass uncertainty σ_{M_W} from a set of N parameters x_i is calculated by

$$\sigma_{M_W}^2 = \sum_{i,j}^{N} \rho_{ij}\sigma_i\sigma_j \frac{\partial M_W}{\partial x_i}\frac{\partial M_W}{\partial x_j}\ , \tag{6.23}$$

where σ_i is the uncertainty of parameter x_i and ρ_{ij} is the element of correlation matrix. The uncertainties σ_i and correlations ρ_{ij} for the hadronic recoil are taken from Table 6.6. For electron energy scale the average of the uncertainties $\sigma_\alpha = 0.004\,85$ and $\sigma_\beta = 0.035\,25$ with a correlation $\rho = -78.25\,\%$ is used. The propagated uncertainties per each distribution are summarized in Table 6.10.

For a proper propagation of the statistical fluctuations the ToyMC method was used. In our case, one hundred new distributions (toys) which are statistically identical to the measured distribution were created. The probability density function used for each toy follows the generated distribution, assuming the weighted Poison distribution per each bin. The distribution of the toy fit results is expected to follow a Gaussian distribution with the width σ representing the statistical uncertainty propagated to M_W. The mean value of the Gaussian is identical with the generated W mass.

6.5 Data samples and event selection

As it is mentioned in previous sections, the $Z \to ee$ events are used for support studies of $W \to e\nu$ modeling and reconstruction. The event selection of these two processes

have several identical definitions of quality criteria. Therefore in the first part of this section the common event and object selection criteria are described. Then, the $Z \to ee$ event selection with data-to-prediction comparison plots is presented. The $W \to e\nu$ event selection, background estimation and data-to-prediction comparison plots are presented in the last part of this section.

The standard way of visualization of the difference between data and Monte-Carlo in the DØ M_W analysis is the χ-plot. It is sometimes called pull-plot or Δ-over-σ and it is defined as the fraction of the difference between data and Monte-Carlo (Δ) divided by the total uncertainty σ per each bin. All control plots in this chapter are illustrated with this type of comparison to visualize the level of agreement between the measurement and the prediction.

6.5.1 Common selection criteria

The M_W analysis described in this thesis uses collision data from September 2009 to June 2010 corresponding to integrated luminosity of $\mathcal{L} = 2.06\,\text{fb}^{-1}$[41] (runIIb3) delivered by the Tevatron. The measured datasets are available as common sample group "EM Inclusive" skims. The production label of skims is `PASS5-p21.18.00-p20.16.0X` where the letter `X` substitutes the versions 7 and 8. The software version which is used to analyse these events has the reconstruction tag `p21.26.00`.

The main trigger for $W \to e\nu$ and $Z \to ee$ events is the single electron trigger `E1_SHT27`. More details about the trigger system of DØ are described in Section 3.2.4. The final trigger criteria at L3 level are $E_\text{T} > 27\,\text{GeV}$ and standard shower shape requirements. The performance of the detector is changing during the data-taking. The status of the detector is evaluated after recording all events from the beam filling. A non negligible number of events is not suitable to be used for physics measurements because of insufficient detector conditions. Hence, these events are rejected. The integrated luminosity corresponding to triggered events recorded while good detector conditions during period runIIb3 is $1.9\,\text{fb}^{-1}$.

Firstly, the events are selected based on the trigger and the status of the detector. Afterwards, the electron candidates are reconstructed and selected based on measured properties. In addition to the electron transverse energy p_T, the electron pseudorapidity η_det and the azimuthal angle ϕ_det there are more observables used for electron selection: The $f_{0.2}^\text{EM}$ is the fraction of energy stored in the electromagnetic calorimeter with respect to the total deposited energy. The isolation $E_{2\to4}^\text{iso}$ corresponds to the fraction outside a $\Delta R < 0.2$ cone with respect to $\Delta R < 0.4$. The traverse and longitudinal shape of an electromagnetic shower is used to identify an electron. The measured shape is compared to simulated shapes and the value χ^2_HM is calculated. The lower the value of χ^2_HM the more likely it is to correctly identify an electron. The detailed definitions of $f_{0.2}^\text{EM}$, $E_{2\to4}^\text{iso}$, and χ^2_HM are listed in Section 3.2.5. The collected datasets are pre-selected into three streams following these requirements :

- `2EM` for study of $Z \to ee$ events: two EM objects with $p_\text{T} > 20\,\text{GeV}$, $|\eta_\text{det}| < 1.2$, $f_{0.2}^\text{EM} > 0.9$ and $E_{2\to4}^\text{iso} < 0.2$
- `EMMET` for study of $W \to e\nu$ events : one EM object with $p_\text{T} > 20\,\text{GeV}$, $|\eta_\text{det}| < 1.2$, $f_{0.2}^\text{EM} > 0.9$ and raw $\not\!\!E_\text{T} > 20\,\text{GeV}$
- `EMJET` for jet-faking-electron studies : one EM object with $p_\text{T} > 20\,\text{GeV}$, $|\eta_\text{det}| < 1.2$, $f_{0.2}^\text{EM} > 0.9$, and $E_{2\to4}^\text{iso} < 0.2$

The analysis is performed using electron candidates with a transverse momentum $p_\text{T}^e > 25\,\text{GeV}$ which are detected by the central calorimeter only. This selection implies

a limit on the electron pseudo-rapidity of $|\eta^e| < 1.1$. Also an electron isolation of $E^{\text{iso}}_{2\to4} < 0.15$ and an EM-fraction of $f^{\text{EM}}_{0.2} < 0.9$ are required.

The calorimeter object is associated to the inner detector track. The track association is performed requiring a matching significance of $P(\chi^2_{\text{TM}}) > 0.001$, with $\chi^2 = \left(\frac{\Delta\phi}{\sigma_\phi}\right)^2 + \left(\frac{\Delta z}{\sigma_z}\right)^2$, where $\Delta\phi$ and Δz are the azimuthal angle and the longitudinal position differences between the calorimeter and a track extrapolated to the third EM layer. The σ_ϕ and σ_z are the corresponding measurement resolutions. The associated track must have at least one SMT hit and fullfil $p^{\text{trk}}_{\text{T}} > 10\,\text{GeV}$.

The electron candidate must fulfil the shower shape criteria of $\chi^2_{\text{HM}} < 12$. The ϕ-fiducial region of the calorimeter is applied to exclude electrons in and near the ϕ_{Calo} cracks. This means that an electron candidate value of $\frac{32\phi_{\text{trk}}}{2\pi} \mod 1$ must be within 0.1-0.9, where ϕ_{trk} is the reconstructed ϕ-coordinate of the associated track at the radius corresponding to the entrance into the electromagnetic calorimeter.

6.5.2 Selection of $Z \to ee$ events

The event and electron selection criteria mentioned above were applied to preselect the events. Additional requirements for $Z \to ee$ candidates are

- At least two electrons. For events with more than two electrons the pair with the highest p^e_{T} is selected.
- Hadronic recoil value of $u_{\text{T}} < 15\,\text{GeV}$
- Electron pair invariant mass within $70 < m_{ee} < 110\,\text{GeV}$

The data measured during runIIb3 contains 47 279 Z candidate events after the application of all selection criteria mentioned above. The Z candidate kinematics are calculated from two selected electrons.

The plots in Figure 6.13 show the general control distributions for $Z \to ee$ events. The prediction is done using PMCS tuned to $Z \to ee$ data. The comparison to the data shows very good agreement for all control distributions. The irreducible background in measured events is expected to be negligible and therefore it is not considered.

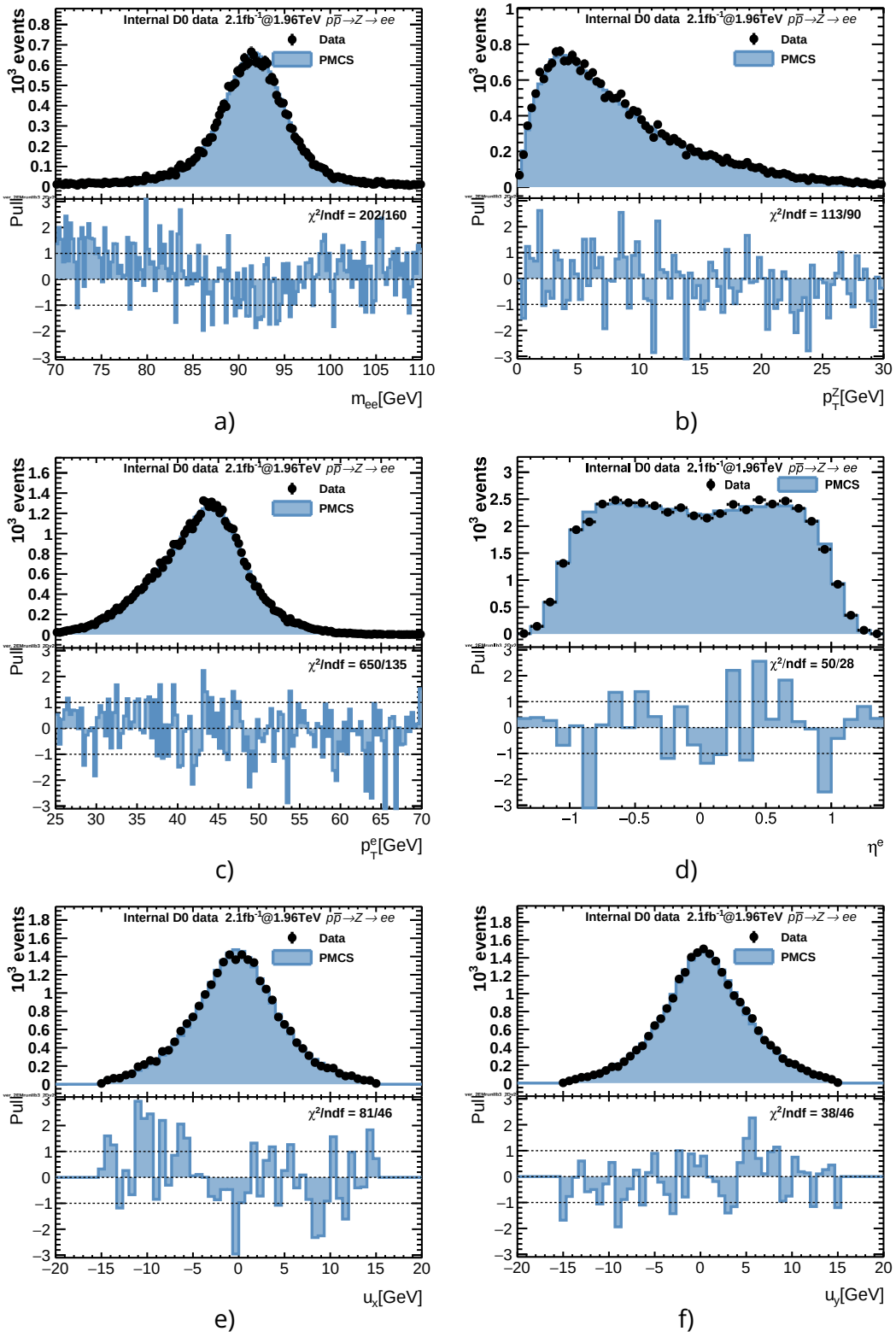

Figure 6.13: *Comparison of measured (black points) and predicted distributions (filled area) of Z-candidate invariant mass (a), Z-candidate transverse momentum (b), electron transverse momentum (c), electron pseudo-rapidity (d), and hadronic recoil x- (e) and y- (f) components in runIIb3 $Z \to ee$ events. Lower part of each figure shows pull-plot between data and prediction. Prediction was done by PMCS.*

6.5.3 Selection of $W \to e\nu$ events

The above mentioned event and electron selection criteria (Section 6.5.1) were applied to preselect the events. Additional requirements for $W \to e\nu$ candidates are

- At least one electron. The electron with the highest p_{T}^{e} is selected in events with more than one electron.
- Hadronic recoil value of $u_{\mathrm{T}} < 15$ GeV
- Transverse mass within $50 < m_{\mathrm{T}} < 200$ GeV

The number of observed events after application of $W \to e\nu$ selection criteria is presented in Table 6.8. The rightmost column represents the fraction of events per each row with respect to the number of events recorded in the EMMET stream.

	Events	Fraction
All events	13 815 825	-
EM≥ 1	2 617 955	100.00 %
$\not\!\!E_{\mathrm{T}} > 25$ GeV	1 913 354	73.09 %
Triggered	1 908 799	72.91 %
$u_{\mathrm{T}} < 15$ GeV	1 425 410	54.45 %
$50 < m_{\mathrm{T}} < 200$ GeV	1 424 659	54.42 %
EC+CC	1 046 143	39.96 %
CC	749 404	28.63 %

Table 6.8: *Number of selected data in runIIb3 and fraction to events recorded in EMMET stream. All events means all collected by minimum bias trigger.*

In case of $Z \to ee$ the contamination of data with background processes is not significant, therefore it is neglected. On the other hand, $W \to e\nu$ events require the estimation of contributions from three different background sources. These are the tau-decay channel of the W boson, Z boson events with only one electron reconstructed and events with one jet misidentified as an electron.

The $W \to \tau\nu$ events are modeled with RESBOS which generates the momenta of τ-leptons and the corresponding neutrinos. The TAUOLA [124] program, which is included into RESBOS code, receives the τ kinematics and generates the kinematics of an electron and two neutrinos from a τ decay. On the top of this calculation, the QED FSR Monte-Carlo generator (PHOTOS) program applies QED radiative corrections to both decay vertices. The final momenta of all decay products are processed by PMCS to obtain the shape of the $W \to \tau\nu$ background for the studied distributions. The shape is scaled by the fraction obtained from the background analysis during runIIb12 [146]. The uncertainty of this background on M_W is studied in two ways: by changing the scale variation by the estimated uncertainty and by variation of the M_W value using event re-weighting (the same technique is used for template generation). The M_W distribution is fitted with a varied background distribution and the difference is taken as the uncertainty. Both studies have shown that the effect of this distribution on the M_W fit is in order of 10 keV and therefore it is considered as negligible [146].

The $Z \to ee$ events contribute to the $W \to e\nu$ background when one of Z electrons is not reconstructed e.g. due to the limited acceptance of the detector. These events

mimic the signal definition and pass all the selection criteria. Therefore, it is possible to estimate the $Z \to ee$ fraction inside the selected $W \to e\nu$ events by studying one fully reconstructed electron (tag) and a second object (probe), which could be a EM object, track or jet. This study was done in the runIIb12 M_W analysis to estimate the fraction as well as the shape of the background distribution. In this analysis the background fraction is taken from the results of the note [146]. The shape of the background is estimated by $Z \to ee$ events generated with RESBOS and processed by PMCS expecting W events. The uncertainty of this background is estimated by scaling the $Z \to ee$ background by $\pm 0.02\,\%$ based on uncertainty of the background fraction estimation obtained from tag-and-probe method. The M_W distribution was fitted varying the background and the difference was taken as the uncertainty. The estimated uncertainty of this background on M_W is 1 MeV, 2 MeV and 1 MeV for the m_{T}, p_{T}^e and $m_{\mathrm{T}} - p_{\mathrm{T}}$ distributions, respectively.

The two jet events create an irreducible background, when one of the jets is identified and reconstructed as an electron and a second jet is not reconstructed at all. Such events are called multi-jet (or QCD) background. The collected datasets are used to estimate the fraction and the shape of the multi-jet background using the matrix method

$$N^{\mathsf{Loose}} = N_W^{\mathsf{Loose}} + N_{\mathsf{QCD}}^{\mathsf{Loose}} \,, \tag{6.24}$$

$$N^{\mathsf{Tight}} = \varepsilon N_W^{\mathsf{Loose}} + f N_{\mathsf{QCD}}^{\mathsf{Loose}} \,, \tag{6.25}$$

where N^{Loose} and N^{Tight} are the numbers of events with loose and tight track matching requirements respectively, ε is the efficiency of a tight track match measured relatively to the loose track match criteria, f is the fake rate or the probability of a loose jet also passing the tight criteria.

N_W^{Loose} and $N_{\mathsf{QCD}}^{\mathsf{Loose}}$ are the unknown and therefore estimated numbers of signal events and background events within W candidates passing the loose requirements. The parameterizations of ε and f were taken from the runIIb12 analysis [146] and used to estimate the background in this analysis. The efficiency and fake-rates are parametrised with respect to p_{T}^e and η^e. The additional study of the ϕ_{det} dependence shows only a small effect on the fitted M_W value.

To estimate multi-jet background effects on M_W, the fake rate and efficiencies were varied according to the estimated uncertainties. The M_W value was extracted for each background variation and the difference between the values obtained was taken as the uncertainty. The effects were combined, this yields the largest uncertainty with 1 MeV per each distribution.

Process	Gen. events	Selected events	Fraction
$W \to e\nu$	354 291 401	24 139 889	$96.22\,\%$
$W \to \tau\nu$	345 645 976	2 186 168	$(1.668 \pm 0.001)\,\%$
$Z \to ee$	427 582 434	1 624 730	$(1.08 \pm 0.02)\,\%$
multi-jet	-	-	$(1.02 \pm 0.07)\,\%$

Table 6.9: *List of background predictions contributing to M_W measurement. The number of generated events, the number of unweighted events and final fraction of process is written in the second, third and fourth column, respectively.*

The uncertainty of the total background contamination was propagated to the

M_W measurement. The final background uncertainties are 1 MeV, 2 MeV, 1 MeV and 1 MeV for m_{T}, p_{T}^{e} and $m_{\mathrm{T}} - p_{\mathrm{T}}$, respectively. They were calculated as the squared sum over each background uncertainty. The list of calculated background fractions with their uncertainty can be found in Table 6.9. For Monte-Carlo samples there are also the number of events on generator level presented as well as the number of events which passed the W-candidate selection criteria.

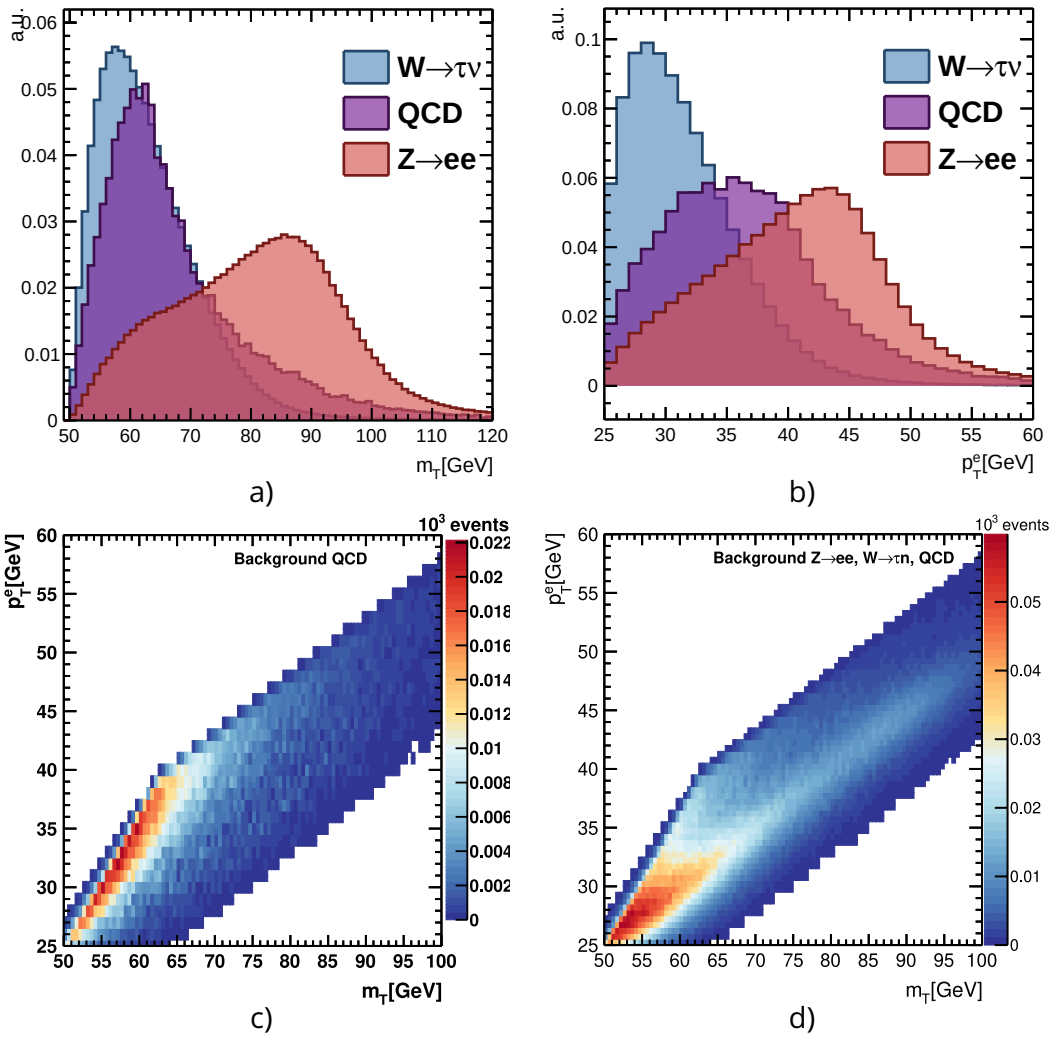

Figure 6.14: *Upper plots: Background shapes normalized to unity for transverse mass m_{T} (a) and electron transverse momentum p_{T}^{e} (b). The $W \to \tau\nu$, $Z \to ee$ and multi-jet background is represented by the blue, red and violet area, respectively. Lower plots: The shape of multi-jet (c) and total (d) background for the $m_{\mathrm{T}} - p_T$ distribution.*

The shapes of the background for the fitted distributions m_{T} and p_{T}^{e} are depicted on Figure 6.14 (a,b). The shape of multi-jet as well as the total background in the $m_{\mathrm{T}} - p_{\mathrm{T}}$ distribution is shown in Figure 6.14 (c,d).

In the following section, the background shapes are scaled by the estimated fraction and added to the signal prediction from PMCS. The combined signal and background prediction are compared to several measured distributions to check that predictions describes the data within estimated uncertainties.

The comparison of the simulated and the measured z-coordinate of the vertex in $W \to e\nu$ events is shown on plot Figure 6.15 (b). Due to the cuts applied and the

efficiencies the reconstructed shape of the z-coordinate distribution differs from a Gaussian distribution. The comparison of the measured and the modelled $W \to e\nu$ distributions of the parallel and the perpendicular projection of the hadronic recoil to the electron p_{T}^{e} direction are shown in Figure 6.16. The comparison of the measured and the modelled $W \to e\nu$ distributions of the pseudo-rapidity η_{det} and the transverse angle ϕ are shown on Figure 6.17. show good agreement between the measured data and the PMCS prediction.

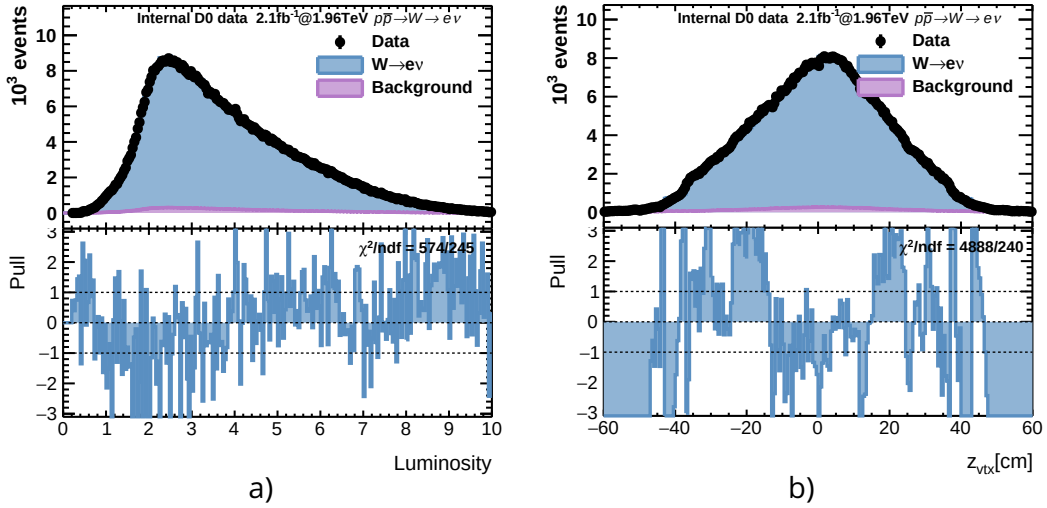

Figure 6.15: *Comparison of measured (black points) and predicted distributions (filled area) of luminosity (a) and vertex z-position (b) in $W \to e\nu$ events. Lower part of each figure shows pull-plot between data and prediction. Prediction was done by PMCS. The total background is showed as filled purple area.*

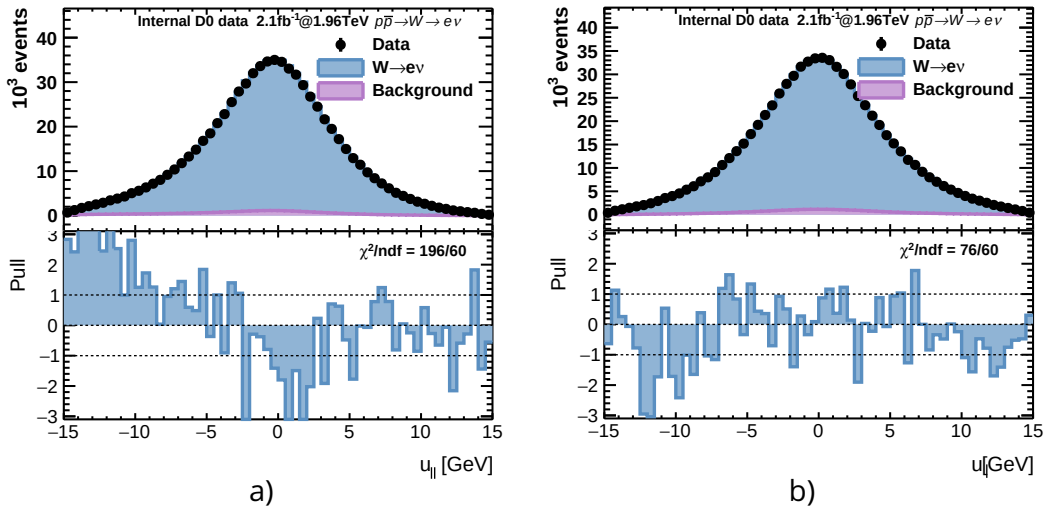

Figure 6.16: *Comparison of measured (black points) and predicted distributions (filled area) of hadronic parallel (a) and perpendicular (b) component w.r.t electron in $W \to e\nu$ events. Lower part of each figure shows pull-plot between data and prediction. Prediction was done by PMCS. The total background is showed as filled purple area.*

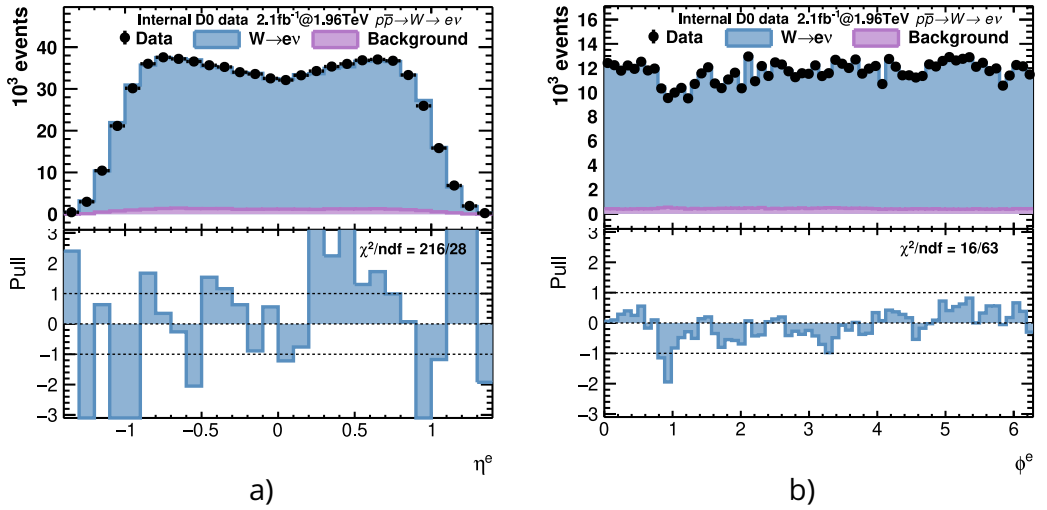

Figure 6.17: *Comparison of measured (black points) and predicted distributions (filled area) of electron pseudo-rapidity (a) and electron transverse angle (b) in $W \to e\nu$ events. Lower part of each figure shows pull-plot between data and prediction. Prediction was done by PMCS. The total background is showed as filled purple area.*

6.6 Results of W boson mass fit

The measurement of M_W using the runIIb3 data is described in this chapter. The new approach of extracting M_W from the two dimensional distribution was performed. Several tests and the results are summarized and compared to the one dimensional results. Finally, the fitted distributions are shown in Figure 6.18 and Figure 6.19.

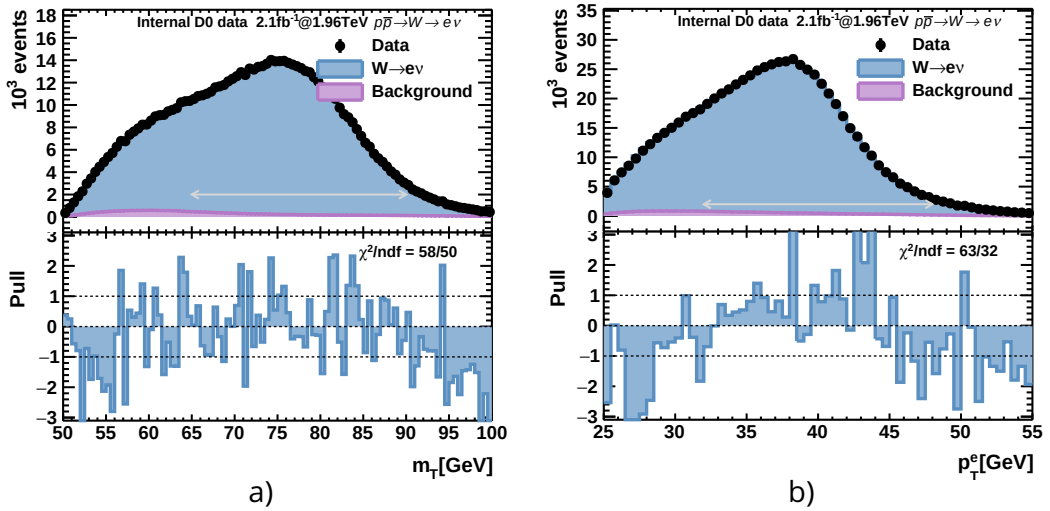

Figure 6.18: *Comparison of measured (black points) and predicted distributions (filled area) of transverse mass (a) and electron transverse momentum (b) in $W \to e\nu$ events. Lower part of each figure shows pull-plot between data and prediction. Prediction was done by PMCS. The total background is showed as filled purple area.*

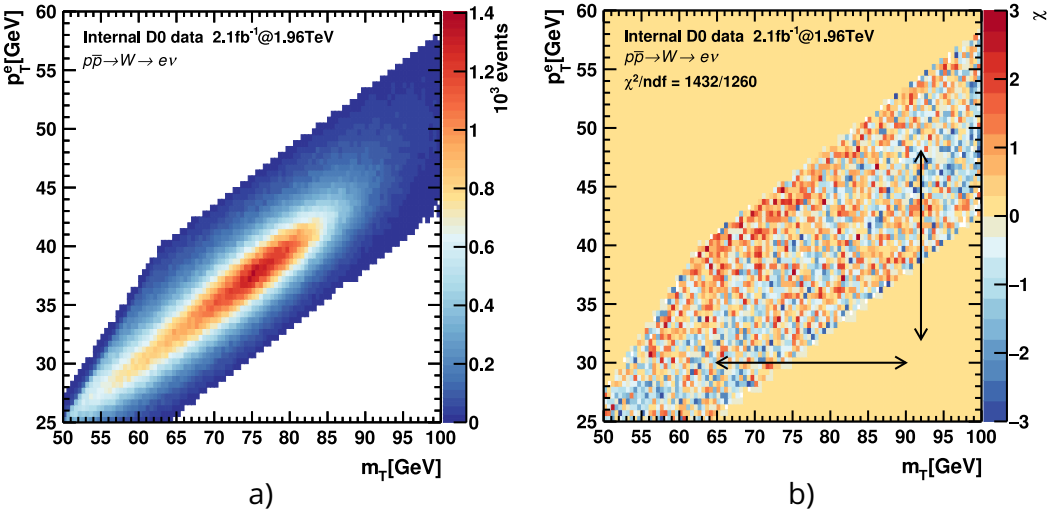

Figure 6.19: *Measured $m_{\mathrm{T}} - p_T$ distribution (a) and pull-plot between data and PMCS prediction including background.*

The values obtained from fitting the data with `wzfitter` are blinded, i.e. there is an unknown constant shift of the M_W value which is applied just before the program returns the fitted value. Neither the difference between two fitted values (e.g. between p_{T}^e and m_{T}) nor the uncertainties are affected by the blinding procedure. Therefore, the fitted results Equation 6.26, Equation 6.27, Equation 6.28 are presented as the

difference to the blinded value obtained from the $m_{\mathrm{T}} - p_{\mathrm{T}}$ fit $M_{\text{W-BLIND}}^{m_{\mathrm{T}}-p_{\mathrm{T}}} = 81.198\,\text{GeV}$. The additional shift per each distribution was applied compensating the new centrally profiled PDF (as observed in the profiling study Table 6.5).

$$\Delta M_W^{m_{\mathrm{T}}-p_{\mathrm{T}}} = 0 \pm 19_{\text{syst}} \pm 14_{\text{stat}}\text{MeV} \tag{6.26}$$

$$\Delta M_W^{m_{\mathrm{T}}} = 1 \pm 20_{\text{syst}} \pm 14_{\text{stat}}\text{MeV} \tag{6.27}$$

$$\Delta M_W^{p_{\mathrm{T}}^e} = -15 \pm 25_{\text{syst}} \pm 15_{\text{stat}}\text{MeV} \tag{6.28}$$

Within this thesis, not all systematic uncertainties could be evaluated. However, the dominant uncertainties have been studied in detail and are summarized in Table 6.10. The two-dimensional fit uncertainties can be compared to the combination of the one-dimensional uncertainties assuming the following correlations. The results of the previous analysis [43] estimate a 75% correlation between m_t and p_{T}^e for the electron energy scale and the hadronic recoil model. Using this correlation the combined one dimensional experimental uncertainty is 16 MeV. The only correlation between the theory uncertainties were the PDF uncertainties with 99% correlation. With respect to this the combined theoretical one-dimensional uncertainty is 18 Mev. The estimated experimental uncretainty from the two-dimensional fit is 17 MeV, which corresponds to the case when the experimental uncertainties are fully correlated. The two-dimensional theoretical uncertainties show the same results for m_t which are several times smaller than p_{T}^e. This can be interpreted that the m_t fit is more stable against the boson shape and the parton distribution function modeling the variations. This stability is also reflected in the $m_{\mathrm{T}} - p_{\mathrm{T}}$ fit. The correlation of the statistical uncertainties was estimated to be 66% and the combined one-dimensional statistical uncertainty is 14 MeV, which is in full agreement with the two-dimensional systematic uncertainty.

Uncertainty source [MeV]	$\delta M_W(m_{\mathrm{T}})$	$\delta M_W(p_{\mathrm{T}}^\ell)$	$\delta M_W(m_{\mathrm{T}} - p_{\mathrm{T}}^\ell)$
Electron Energy Scale	16	16	16
Recoil Model	9	3	6
Background	1	2	1
Experimental	18	16	17
PDF	6	14	6
Boson p_{T}-shape	3	14	3
Theoretical model	7	19	7
Systematic	20	25	19
Statistics	14	16	14
Total	24	30	23

Table 6.10: *List of studied uncertainties and their contribution per each distribution (column) and origin of uncertainty (row).*

An additional improvement of the two-dimensional fit would be an optimization of the fitting range to increase the sensitivity on the Jacobian peak. Consequently this would improvethe sensitivity to the value of the W mass. In this analysis a rectangular range was used but a trapezoidal would improve the measurement, because most of the events are situated on a diagonal of the $m_{\mathrm{T}} - p_{\mathrm{T}}$ distribution. Moreover, the fit-range with a trapezoidal shape would effectively cut off the multi-jet background (see Figure 6.14 (c)).

6.7 Preservation of W boson mass analysis for future revaluation

The following results were already presented on the EPS 2015 conference [147] and they were documented in DØ note [148].

The measurement of the W boson mass (M_W) will be one of the most lasting scientific results of the Do experiment, and it is expected to have an impact on the world average for at least the next decades. Even though the CERN Large Hadron Collider (LHC) experiments are currently in the process of preparing a new round of measurements, the expected experimental, theoretical, and model uncertainties will be, in the most optimistic scenario, on the order of 10 MeV. Hence, the most recent measurements of M_W at the Do experiment [149] based on $\int \mathcal{L}\mathrm{d}t = 4.3\,\mathrm{fb}^{-1}$ of data with a value of $M_W = (80.375 \pm 0.023)$ GeV will be relevant even in the long term. It should be noted that the model uncertainty is 13 MeV, where 11 MeV are due to the limited knowledge of parton density functions (PDF). In fact, the measurement currently under preparation, which will use the full data set, will be dominated by these PDF uncertainties.

In addition, measurements at the Tevatron and the LHC are complementary to a large extent, as different eigenvectors of the underlying PDFs dominate the W boson production in pp and $p\bar{p}$ collisions. It is expected that the knowledge of PDFs will improve significantly in the future, as new measurements of the differential production cross section of Z and W bosons become available and will be used for future PDF fits. Therefore, it was the aim of this work, which is summarized in the following, to preserve the DØ W boson mass analysis, allowing a reevaluation of the M_W measurement using newer PDF sets and a reduction of the overall systematic uncertainty.

The DØ collaboration is preparing long term storage of data and code for all major analyses. In addition to this centralized collaboration wide effort, it was decided to provide an independent method to rerun the M_W analysis, since it uses a large extent of highly specific code developments, e.g. the FastMC. To achieve this goal, a dedicated server for the M_W analysis preservation has been set up at the university of Mainz. The basic hardware parameters of the server are:

- Mainboard: with `AMD SR5690/SP5100` (Chipset `E-ATX`), on board: `VGA`, 2× Gbit-`LAN`, 6× `S-ATA` 3 Gb/s in `RAID`
- CPU: 2× `AMD Opteron 6344` (2 60GHz per 12-threads, 16 MB)
- RAM: 4× `Kingston DIMM DDR3 CL9` 8 GB 1333 MHz `PC3-10600 ECC`
- HDD: 4× 3 TB `HGST UltraStar 7K4000 Enterprise S-ATA` (64 MB, 7200 min^{-1}, `S-ATA` 6 Gb/s) `LSI` with `MegaRAID 9266-4i SAS/S-ATA`

This server contains all relevant data and code. In order to allow for a working operating system environment in the upcoming years, a `VirtualBox` [150] implementation was used. The `VirtualBox` can execute the operating system used by the analysis and thus allow for the compilation and the execution of the full DØ analysis software. To

make the interface user-friendly, we provide a basic set of scripts for the execution of the different analysis steps. Detailed documentation and help-pages are available directly after the login on the dedicated server. This also allows newcomers to rerun the DØ W boson mass analyses. The reproducibility of the analyses has been extensively tested. As an example, the resulting kinematic distributions of p_{T}^{e} and m_{T} after the M_W fit using the preservation analysis and the stored data are shown in Figure 6.20. They are in perfect agreement with the published results [149].

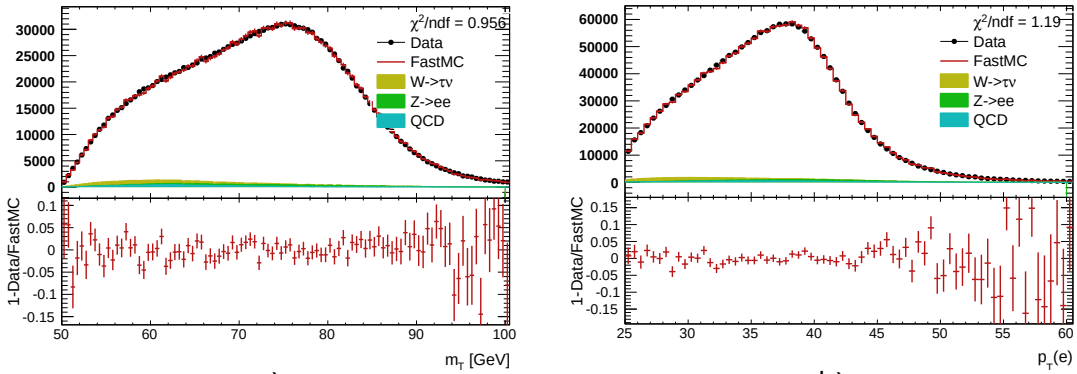

Figure 6.20: *The comparison of PMCS (red points) including background (filled area) and DATA (black points) using the* `CTEQ6.6` *grids. The plotted distributions are transverse mass (a) and transverse momentum of the electron (b). In lower part of every plot there is ratio plot between DATA and PMCS. Plot also in [148, 147].*

As an example of the reevaluation of M_W with a different PDF set, we determined M_W using the `MSTW08NLO` PDF set [151] instead of `CTEQ6.1` [152], which was used in the published analysis [149]. The results of M_W are shown in Figure 6.21, where the published values of M_W, the preserved values and the reevaluated values are indicated.

The preservation of the M_W mass measurement at the DØ detector allows the option to reevaluate the W boson mass using new parton density functions of the proton in future years. To provide the necessary infrastructure, a new server was installed at the University of Mainz in June 2014. It stores all data and software and is purely dedicated to the DØ W mass analysis preservation. For data-safety reasons, a mirror of this setup is duplicated at the Mogon-computer cluster infrastructure at the university of Mainz, guaranteeing a long term preservation of the analysis infrastructure. The setup has been extensively tested and has been demonstrated to successfully complete a reevaluation of the W boson mass with a different PDF set, allowing for potential future reductions in the theoretical uncertainties of the W boson mass value.

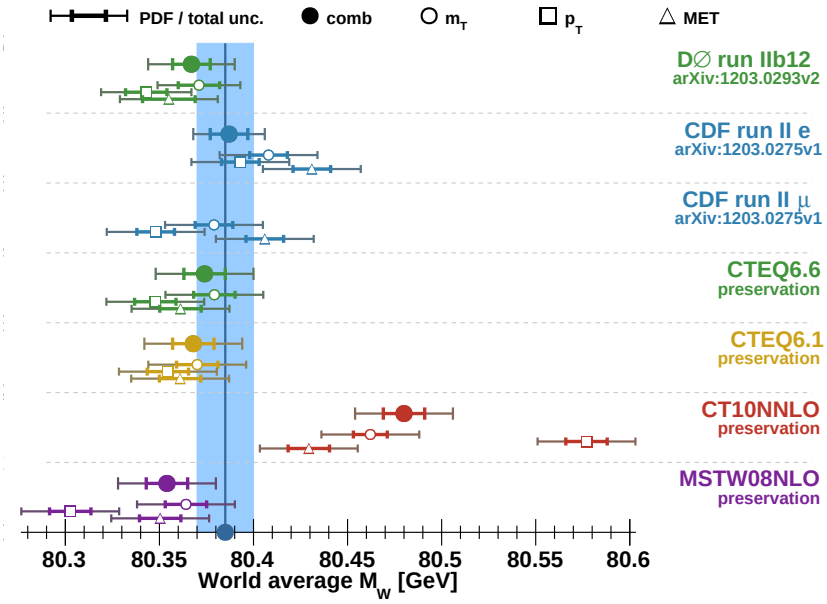

Figure 6.21: *The W boson mass fitted with preserved code using different PDF sets is compared to published results from DØ, CDF and world average [7]. Grey error bars represent total uncertainty, while colored error bands represents PDF uncertainty only. The mass fitted by m_{T}, p_{T}^{e} and $\not\!\!E_{\mathrm{T}}$ is shown as empty circle, square and triangle, respectively. Combined mass from all three distribution is marked by large filled circle. Values in each row with reference are taken from publication, otherwise were fitted by preserved analysis.*

7. Conclusion

This thesis focused on the study of the production of electroweak bosons in hadron collisions, as well as, the measurement of the W boson mass. The understanding of the former is a necessary requirement for the latter. Within this thesis, several approaches of the modeling of vector bosons have been studied and presented. Special focus was placed on higher order QCD calculations and the improvement of semi-analytical and numerical methods, which allow for precise prediction in a reasonable time. The starting point was the publicly available DYRES program, which was extended and improved, leading to the new calculation tool DYTURBO. The new improvements have been described together with benchmark studies which prove that the optimization procedures do not alter the underlying physics modeling.

The rapid speed improvements after code optimization and incorporation of different numerical methods opened a perspective to use DYTURBO as an unweighted particle generator for further precision studies at the LHC.

Even thought it has been proven that the predictions of DYTURBO are in agreement with DYRES, it is necessary to confront these predictions also with measured data. Hence the transverse momentum spectrum of Z bosons in the muon decay channel has been measured at a center of mass energy of 13 TeV, using data recorded by the ATLAS experiment at the LHC. In a second step, the measured spectrum was compared to the predictions of the optimized DYTURBO program, allowing for a new and innovative approach to extract the strong coupling constant. By fitting the measured p_{T}^{Z} distribution to different DYTURBO predictions at NNLL+NLO accuracy for different values of α_s, the strong coupling constant was determined to be

$$\alpha_s^{\mathrm{2D}}(M_Z^2) = 0.1177 \pm 0.0014_{\mathrm{syst+syst}} \pm 0.0086_{\mathrm{theo}} \,.$$

The precision of this measurement is comparable to other measurements of the ATLAS collaboration $\alpha_s^{\mathrm{TEEC}}(M_Z^2) = 0.1173 \pm 0.0010_{\mathrm{exp.}} \left(^{+0.0065}_{-0.0026}\right)_{\mathrm{theo}}$ [117]. An improvement of theoretical uncertainties is expected by using a formal accuracy at NNLL+NNLO in the strong coupling constant for the DYTURBO predictions.

The developed tools for the description of the electroweak boson production in hadron collisions can be used to improve the measurement of electroweak parameters like the W boson mass M_W. In this thesis, the W boson mass measurement was prepared for the latest data-set of the DØ experiment at the Tevatron collider. Since the mass of W boson cannot be measured directly due to an undetected neutrino, it is extracted via the kinematic energy distributions of the electron and the deposited hadronic energy. In this thesis a novel measurement technique was introduced, which relies on the two dimensional $m_{\mathrm{T}} - p_{\mathrm{T}}$ distribution of the transverse mass m_{T} and the electron transverse momentum p_{T}^{e} for the estimation of the W boson mass.

Currently only the half of unpublished DØ data was used in this thesis. Therefore, a blinding technique is used by introducing an unknown but constant offset during the mass fitting procedure. Once the internal review of the DØ collaboration has been successfully passed, this blinding offset will be removed. Since this was not yet done, only a blinded value is presented in this theses, where the value of the two-dimensional $m_{\mathrm{T}} - p_{\mathrm{T}}$ distribution was taken as a reference point. The resulting mass measurements with uncertainties are

$$\Delta M_W^{m_{\mathrm{T}}-p_{\mathrm{T}}} = 0 \pm 19_{\mathrm{syst}} \pm 14_{\mathrm{stat}} \mathrm{MeV}$$

$$\Delta M_W^{m_{\mathrm{T}}} = 1 \pm 20_{\mathrm{syst}} \pm 14_{\mathrm{stat}}\mathrm{MeV}$$

$$\Delta M_W^{p_{\mathrm{T}}^e} = -15 \pm 25_{\mathrm{syst}} \pm 15_{\mathrm{stat}}\mathrm{MeV}$$

The dominant uncertainty is due to the limited knowledge of the parton density functions of protons. By using measurements of the charge asymmetry of W bosons, this uncertainty can be reduced by profiling approaches, which have been also studied within the course of this thesis.

Future improvements on the knowledge of parton density functions as well as improved descriptions of the modeling of the vector boson production in hadron collisions will also reduce the theoretical uncertainties on the previously published values of M_W by the DØ collaboration. Therefore, a procedure for the preservation of previous M_W analyses was been developed. This preservation effort is not only storing already collected data locally in Mainz, but ensures that the software for the data processing and MC generation as well as the actual analyses can be repeated on future machines using new theoretical inputs. By this approach, we ensure a lasting impact on the measurement of a fundamental parameter of the Standard Model in future years.

Acknowledgement

I would like to say "thank you" to many people, but I did not write any name here. Instead, you should read carefully and find yourself. I tried to use the language accordingly.

Vďaka patrí mojej rodine za sarkazums, za jednoduché otázky a oporu keď bolo treba. Ďekuji přátelům za přísun podpůrnych látek, myšlenek a energie. Thanks to Lichtenbergers and Mainzers for all the (cake-, lunch-, coffee-, pizza-) meetings, (non-) scientific inspirations and awesome hard(ly) working team. Thanks to my colleages from DØ and ATLAS, because the knowledge that we have the common goal kept me in delivering the results. It won't be easy to break again the record for "the longest working time with people, who I never met". Grazie ai ragazzi, che mi hanno dimostrato, che gli italiani non sono solo grande fisico e ma anche buoni maestri e amici preziosi. Last but not least, my big thanks goes to my two bosses. Danke meine Doktorvater für enorme Geduld. Du hast mir gezeigt, dass es möglich ist, effektiv zu sein und Spaß zu haben. Merci à mon petit soleil, pour me montrer que le travail n'est pas ma vie. Thank you for your attention.

Work it harder, make it better,
do it faster makes us stronger.
More than ever hour after
our work is never over.

Daft Punk

Part III

Appendix

Bibliography

[1] UA1 Collaboration.
UA1: first Z event recorded (1983).
URL `https://cds.cern.ch/record/615824`

[2] UA1 Collaboration.
Ua1: W particle dacay (1982).
URL `https://cds.cern.ch/record/39467`

[3] R. Feynman, R. Leighton, and M. Sands.
The feynman lectures on physics (Mar 1963).
ISBN 9780201021165.

[4] S. L. Glashow.
The renormalizability of vector meson interactions.
Nucl. Phys., 10 107–117 (1959).
doi:10.1016/0029-5582(59)90196-8.

[5] A. Salam and J. C. Ward.
Weak and electromagnetic interactions.
Nuovo Cim., 11 568–577 (1959).
doi:10.1007/BF02726525.

[6] S. Weinberg.
A model of leptons.
Phys. Rev. Lett., 19 1264–1266 (Nov 1967).
doi:10.1103/PhysRevLett.19.1264.

[7] C. Patrignani et al.
Review of Particle Physics.
Chin. Phys., C40(10) 100001 (2016).
doi:10.1088/1674-1137/40/10/100001.

[8] R. P. Feynman.
Space-time approach to non-relativistic quantum mechanics.
Rev. Mod. Phys., 20 367–387 (Apr 1948).
doi:10.1103/RevModPhys.20.367.

[9] J. Schwinger.
On quantum-electrodynamics and the magnetic moment of the electron.
Phys. Rev., 73 416–417 (Feb 1948).
doi:10.1103/PhysRev.73.416.

[10] S. Tomonaga.
*On a relativistically invariant formulation of the quantum theory of wave fields**.
Progress of Theoretical Physics, 1(2) 27–42 (1946).
doi:10.1143/PTP.1.27.

[11] S. L. Glashow.
Partial-symmetries of weak interactions.

Nuclear Physics, 22(4) 579 – 588 (1961).
ISSN 0029-5582.
doi:http://dx.doi.org/10.1016/0029-5582(61)90469-2.

[12] F. Englert and R. Brout.
Broken symmetry and the mass of gauge vector mesons.
Phys. Rev. Lett., 13 321–323 (Aug 1964).
doi:10.1103/PhysRevLett.13.321.

[13] P. W. Higgs.
Broken symmetries and the masses of gauge bosons.
Phys. Rev. Lett., 13 508–509 (Oct 1964).
doi:10.1103/PhysRevLett.13.508.

[14] G. Aad et al.
Observation of a new particle in the search for the Standard Model Higgs boson with the ATLAS detector at the LHC.
Phys. Lett., B716 1–29 (2012).
doi:10.1016/j.physletb.2012.08.020.
1207.7214.

[15] S. Chatrchyan et al.
Observation of a new boson at a mass of 125 GeV with the CMS experiment at the LHC.
Phys. Lett., B716 30–61 (2012).
doi:10.1016/j.physletb.2012.08.021.
1207.7235.

[16] N. Cabibbo.
Unitary Symmetry and Leptonic Decays.
Phys. Rev. Lett., 10 531–533 (1963).
doi:10.1103/PhysRevLett.10.531.

[17] M. Kobayashi and T. Maskawa.
CP Violation in the Renormalizable Theory of Weak Interaction.
Prog. Theor. Phys., 49 652–657 (1973).
doi:10.1143/PTP.49.652.

[18] E. Fermi.
Tentativo di una teoria dell'emissione dei raggi beta.
Ric. Sci., 4 491–495 (1933).

[19] H. Fritzsch, M. Gell-Mann, and H. Leutwyler.
Advantages of the Color Octet Gluon Picture.
Phys. Lett., 47B 365–368 (1973).
doi:10.1016/0370-2693(73)90625-4.

[20] C. N. Yang and R. L. Mills.
Conservation of isotopic spin and isotopic gauge invariance.
Phys. Rev., 96 191–195 (Oct 1954).
doi:10.1103/PhysRev.96.191.

[21] G. Rodrigo and A. Santamaria.
QCD matching conditions at thresholds.
Phys. Lett., B313 441–446 (1993).

doi:10.1016/0370-2693(93)90016-B.
hep-ph/9305305.

[22] J. D. Bjorken and E. A. Paschos.
Inelastic electron-proton and γ-proton scattering and the structure of the nucleon.
Phys. Rev., 185 1975–1982 (Sep 1969).
doi:10.1103/PhysRev.185.1975.

[23] R. Feynman.
Photon-hadron interactions (Mar 1972).

[24] S. D. Drell and T.-M. Yan.
Massive lepton-pair production in hadron-hadron collisions at high energies.
Phys. Rev. Lett., 25 316–320 (Aug 1970).
doi:10.1103/PhysRevLett.25.316.

[25] F. Halzen and A. Martin.
Quarks and leptons: an introductory course in modern particle physics (Mar 1984).

[26] G. Breit and E. Wigner.
Capture of slow neutrons.
Phys. Rev., 49 519–531 (Apr 1936).
doi:10.1103/PhysRev.49.519.

[27] R. Hamberg, W. L. van Neerven, and T. Matsuura.
A complete calculation of the order $\alpha - s^2$ correction to the Drell-Yan K factor.
Nucl. Phys., B359 343–405 (1991).
doi:10.1016/S0550-3213(02)00814-3,10.1016/0550-3213(91)90064-5.
[Erratum: Nucl. Phys.B644,403(2002)].

[28] J. C. Collins and D. E. Soper.
Parton distribution and decay functions.
Nuclear Physics B, 194(3) 445 – 492 (1982).
ISSN 0550-3213.
doi:http://dx.doi.org/10.1016/0550-3213(82)90021-9.

[29] E. Mirkes.
Angular decay distribution of leptons from w-bosons at nlo in hadronic collisions.
Nuclear Physics B, 387(1) 3 – 85 (1992).
ISSN 0550-3213.
doi:http://dx.doi.org/10.1016/0550-3213(92)90046-E.

[30] J. C. Collins, D. E. Soper, and G. F. Sterman.
Transverse Momentum Distribution in Drell-Yan Pair and W and Z Boson Production.
Nucl. Phys., B250 199–224 (1985).
doi:10.1016/0550-3213(85)90479-1.

[31] F. Landry, et al.
Tevatron Run-1 Z boson data and Collins-Soper-Sterman resummation formalism.
Phys. Rev., D67 073016 (2003).
doi:10.1103/PhysRevD.67.073016.
hep-ph/0212159.

[32] M. Guzzi, P. M. Nadolsky, and B. Wang.
Nonperturbative contributions to a resummed leptonic angular distribution in inclusive neutral vector boson production.

Phys. Rev., D90(1) 014030 (2014).
doi:10.1103/PhysRevD.90.014030.
1309.1393.

[33] G. Bozzi, et al.
Transverse-momentum resummation and the spectrum of the Higgs boson at the LHC.
Nucl. Phys., B737 73–120 (2006).
doi:10.1016/j.nuclphysb.2005.12.022.
hep-ph/0508068.

[34] P. Flajolet and M. Golin.
Mellin transforms and asymptotics.
Acta Informatica, 31(7) 673–696 (Jul 1994).
ISSN 1432-0525.
doi:10.1007/BF01177551.
URL https://doi.org/10.1007/BF01177551

[35] S. Catani, D. de Florian, and M. Grazzini.
Universality of nonleading logarithmic contributions in transverse momentum distributions.
Nucl. Phys., B596 299–312 (2001).
doi:10.1016/S0550-3213(00)00617-9.
hep-ph/0008184.

[36] R. Wideröe.
Über ein neues prinzip zur herstellung hoher spannungen.
Archiv für Elektrotechnik, 21(4) 387–406 (Jul 1928).
ISSN 1432-0487.
doi:10.1007/BF01656341.

[37] Fermi National Accelerator Laboratory.
Fermilab History and Archives Project (Jan 2017).
URL http://history.fnal.gov/index.html

[38] C. Courier.
Farewell to the tevatron (Oct 2011).
URL http://cerncourier.com/cws/article/cern/47505

[39] F. N. A. Laboratory.
Fermilab tevatron accelerator (May 2014).
URL http://www.fnal.gov/pub/tevatron/tevatron-accelerator.html

[40] S. van der Meer.
Stochastic damping of betatron oscillations in the ISR.
Technical Report CERN-ISR-PO-72-31. ISR-PO-72-31, CERN, Geneva (Aug 1972).
URL http://cds.cern.ch/record/312939

[41] DO collaboration.
RunII Data Taking (Feb 2010).
URL http://d0server1.fnal.gov/Projects/Operations/D0RunII_DataTaking.xls

[42] V. M. Abazov et al.
Measurement of the w boson mass.

Phys. Rev. Lett., 103 141801 (Oct 2009).
doi:10.1103/PhysRevLett.103.141801.

[43] V. M. Abazov et al.
Measurement of the w boson mass with the do detector.
Phys. Rev. Lett., 108 151804 (Apr 2012).
doi:10.1103/PhysRevLett.108.151804.

[44] T. A. Aaltonen et al.
Combination of CDF and Do W-Boson Mass Measurements (2013).
doi:10.1103/PhysRevD.88.052018.
1307.7627.

[45] S. Abachi et al.
The do detector.
Nucl. Inst. Meth. A, 338(2) 185 – 253 (1994).
ISSN 0168-9002.
doi:http://dx.doi.org/10.1016/0168-9002(94)91312-9.

[46] DO Collaboration.
Drawings and pictures (Mar 2017).
URL https://www-d0.fnal.gov/Run2Physics/WWW/drawings.htm

[47] V. Abazov et al.
The upgraded do detector.
Nucl. Inst. Meth. A, 565(2) 463 – 537 (2006).
ISSN 0168-9002.
doi:http://dx.doi.org/10.1016/j.nima.2006.05.248.

[48] M. Abolins et al.
Design and implementation of the new do level-1 calorimeter trigger.
Nucl. Inst. Meth. A, 584(1) 75 – 97 (2008).
ISSN 0168-9002.
doi:http://dx.doi.org/10.1016/j.nima.2007.10.014.

[49] DO Collaboration.
Common analysis format environment (2008).
URL https://www-d0.fnal.gov/Run2Physics/cs/caf/

[50] S. Agostinelli et al.
GEANT4: A Simulation toolkit.
Nucl. Instrum. Meth., A506 250–303 (2003).
doi:10.1016/S0168-9002(03)01368-8.

[51] T. Sjostrand, S. Mrenna, and P. Z. Skands.
PYTHIA 6.4 Physics and Manual.
JHEP, 05 026 (2006).
doi:10.1088/1126-6708/2006/05/026.
hep-ph/0603175.

[52] C. Balazs and C. P. Yuan.
Soft gluon effects on lepton pairs at hadron colliders.
Phys. Rev., D56 5558–5583 (1997).
doi:10.1103/PhysRevD.56.5558.
hep-ph/9704258.

[53] R. Bailey.
An Application for Research: the Large Hadron Collider.
Proceedings, CAS - CERN Accelerator School: Ion Sources: Senec, Slovakia, May 29-June 8, 2012, pp. 565–574 (2013).
doi:10.5170/CERN-2013-007.565.
1404.0966.
URL https://inspirehep.net/record/1288545/files/arXiv:1404.0966.pdf

[54] CERN.
Proton beams are back in the LHC (Apr 2015).
URL http://cds.cern.ch/record/2015179

[55] ATLAS Collaboration.
Luminosity Public Results for Run 2 (2017).
URL https://twiki.cern.ch/twiki/bin/view/AtlasPublic/LuminosityPublicResultsRun2

[56] G. Aad et al.
The ATLAS Experiment at the CERN Large Hadron Collider.
JINST, 3 S08003 (2008).
doi:10.1088/1748-0221/3/08/S08003.

[57] M. Aaboud et al.
Performance of the ATLAS Trigger System in 2015.
Eur. Phys. J. C, 77(CERN-EP-2016-241. 5) 317. 76 p (Nov 2016).
URL https://cds.cern.ch/record/2235584

[58] ATLAS Collaboration.
Athena – ATLAS software framework (2017).
URL https://atlassoftwaredocs.web.cern.ch/athena/athena-intro/

[59] N. Metropolis and S. Ulam.
The Monte Carlo Method.
Journal of the American Statistical Association, 44(247) 335–341 (September 1949).
ISSN 01621459.
URL http://www.jstor.org/stable/2280232

[60] M. A. Dobbs et al.
Les Houches guidebook to Monte Carlo generators for hadron collider physics.
Physics at TeV colliders. Proceedings, Workshop, Les Houches, France, May 26-June 3, 2003, pp. 411–459 (2004).
hep-ph/0403045.
URL http://lss.fnal.gov/cgi-bin/find_paper.pl?conf-04-183

[61] P. Nason.
A New method for combining NLO QCD with shower Monte Carlo algorithms.
JHEP, 11 040 (2004).
doi:10.1088/1126-6708/2004/11/040.
hep-ph/0409146.

[62] J. Bellm et al.
Herwig 7.0/Herwig++ 3.0 release note.
Eur. Phys. J., C76(4) 196 (2016).
doi:10.1140/epjc/s10052-016-4018-8.
1512.01178.

[63] T. Gleisberg, et al.
Event generation with SHERPA 1.1.
JHEP, 02 007 (2009).
doi:10.1088/1126-6708/2009/02/007.
0811.4622.

[64] S. Catani, et al.
QCD matrix elements + parton showers.
JHEP, 11 063 (2001).
doi:10.1088/1126-6708/2001/11/063.
hep-ph/0109231.

[65] J. Alwall et al.
Comparative study of various algorithms for the merging of parton showers and matrix elements in hadronic collisions.
Eur. Phys. J., C53 473–500 (2008).
doi:10.1140/epjc/s10052-007-0490-5.
0706.2569.

[66] K. Hamilton, P. Nason, and G. Zanderighi.
MINLO: Multi-Scale Improved NLO.
JHEP, 10 155 (2012).
doi:10.1007/JHEP10(2012)155.
1206.3572.

[67] S. Alioli, et al.
Combining Higher-Order Resummation with Multiple NLO Calculations and Parton Showers in GENEVA.
JHEP, 09 120 (2013).
doi:10.1007/JHEP09(2013)120.
1211.7049.

[68] G. Bozzi, et al.
Production of Drell-Yan lepton pairs in hadron collisions: Transverse-momentum resummation at next-to-next-to-leading logarithmic accuracy.
Phys. Lett., B696 207–213 (2011).
doi:10.1016/j.physletb.2010.12.024.
1007.2351.

[69] T. Becher, M. Neubert, and D. Wilhelm.
Electroweak Gauge-Boson Production at Small q_T: Infrared Safety from the Collinear Anomaly.
JHEP, 02 124 (2012).
doi:10.1007/JHEP02(2012)124.
1109.6027.

[70] S. Frixione and B. R. Webber.
Matching NLO QCD computations and parton shower simulations.
JHEP, 06 029 (2002).
doi:10.1088/1126-6708/2002/06/029.
hep-ph/0204244.

[71] P. Nason.
A New method for combining NLO QCD with shower Monte Carlo algorithms.

JHEP, 11 040 (2004).
doi:10.1088/1126-6708/2004/11/040.
hep-ph/0409146.

[72] M. L. Mangano, et al.
ALPGEN, a generator for hard multiparton processes in hadronic collisions.
JHEP, 07 001 (2003).
doi:10.1088/1126-6708/2003/07/001.
hep-ph/0206293.

[73] J. Alwall, et al.
The automated computation of tree-level and next-to-leading order differential cross sections, and their matching to parton shower simulations.
JHEP, 07 079 (2014).
doi:10.1007/JHEP07(2014)079.
1405.0301.

[74] J. M. Campbell and R. K. Ellis.
An Update on vector boson pair production at hadron colliders.
Phys. Rev., D60 113006 (1999).
doi:10.1103/PhysRevD.60.113006.
hep-ph/9905386.

[75] R. Gavin, et al.
W Physics at the LHC with FEWZ 2.1.
Comput. Phys. Commun., 184 208–214 (2013).
doi:10.1016/j.cpc.2012.09.005.
1201.5896.

[76] M. Schott and M. Dunford.
Review of single vector boson production in pp collisions at $\sqrt{s} = 7$ TeV.
Eur. Phys. J., C74 2916 (2014).
doi:10.1140/epjc/s10052-014-2916-1.
1405.1160.

[77] G. A. Ladinsky and C. P. Yuan.
The Nonperturbative regime in QCD resummation for gauge boson production at hadron colliders.
Phys. Rev., D50 R4239 (1994).
doi:10.1103/PhysRevD.50.R4239.
hep-ph/9311341.

[78] RESBOS Collaboration.
RESBOS program branch CP (Jun 2015).
URL http://hep.pa.msu.edu/resum//code/resbos_cp/resbos_060315.tar.bz2

[79] G. P. Lepage.
A new algorithm for adaptive multidimensional integration.
Journal of Computational Physics, 27(2) 192 – 203 (1978).
ISSN 0021-9991.
doi:http://dx.doi.org/10.1016/0021-9991(78)90004-9.

[80] S. Catani, et al.
Vector boson production at hadron colliders: transverse-momentum resummation and leptonic decay.

JHEP, 12 047 (2015).
doi:10.1007/JHEP12(2015)047.
1507.06937.

[81] T. Hahn.
CUBA: A Library for multidimensional numerical integration.
Comput. Phys. Commun., 168 78–95 (2005).
doi:10.1016/j.cpc.2005.01.010.
hep-ph/0404043.

[82] Johnson, Steve G.
Cubature Multi-dimensional integration (2017).
URL http://ab-initio.mit.edu/wiki/index.php/Cubature_(Multi-dimensional_integration)

[83] R. Brun and F. Rademakers.
ROOT: An object oriented data analysis framework.
Nucl. Instrum. Meth., A389 81–86 (1997).
doi:10.1016/S0168-9002(97)00048-X.

[84] G. D'Agostini.
A multidimensional unfolding method based on bayes' theorem.
Nuclear Instruments and Methods in Physics Research Section A: Accelerators, Spectrometers, Detectors and Associated Equipment, 362(2) 487–498 (1995).
ISSN 0168-9002.
doi:https://doi.org/10.1016/0168-9002(95)00274-X.

[85] The Scipy community.
Multivariate data interpolation (2017).
URL https://docs.scipy.org/doc/scipy/reference/tutorial/interpolate.html#multivariate-data-interpolation-griddata

[86] Python software foundation.
Python programming language v3.4.2 (Oct 2014).
URL http://python.org/

[87] J. Cúth.
Extraction of α_S from p_{T}^Z (Dec 2016).
URL https://gitlab.cern.ch/LichtenbergGroup/LGNtupleMaker/blob/Base-2.4.22/LGAnalysis/Zpt13TeVAnalysis/scripts/alphaS.py

[88] E. Jones, et al.
SciPy vo.18.1: Open source scientific tools for Python (Sep 2016).
URL http://www.scipy.org/

[89] Matplotlib Developers.
Matplotlib: v1.5.3 (Sep 2016).
URL http://matplotlib.org/

[90] ATLAS collaboration.
Luminosity Calculator.
web page (Dec 2016).
URL https://atlas-lumicalc.cern.ch/

[91] ATLAS collaboration.
Combined Performance Tools for Physics Analysis.
Twiki page (Dec 2016).
URL https://twiki.cern.ch/twiki/bin/viewauth/AtlasProtected/PhysicsAnalysisWorkBookRel20CPRec

[92] ATLAS collaboration.
RootCore version Base-2.4.22.
software framework (Dec 2016).
URL https://svnweb.cern.ch/cern/wsvn/atlasoff/PhysicsAnalysis/D3PDTools/RootCore/tags/RootCore-00-04-62

[93] Gustaaf Brooijmans.
List of xAOD Derivation (2017).
URL https://docs.google.com/spreadsheets/d/1vzqMXKpu5yuXGAX0Pbb6NmY35aQa_jU_sj0kFU29mwI/edit#gid=1484460466

[94] ATLAS collaboration.
Combined Performance Tools for Physics Analysis – Event Cleaning.
Twiki page (Dec 2016).
URL https://twiki.cern.ch/twiki/bin/view/AtlasProtected/PhysicsAnalysisWorkBookRel20CPRec#Event_cleaning

[95] ATLAS collaboration.
data15_13TeV.periodAllYear_DetStatus-v79-repro20-02_DQDefects-00-02-02_PHYS_StandardGRL_All_Good_25ns.xml.
XML file (Dec 2016).
URL https://twiki.cern.ch/twiki/bin/view/AtlasProtected/GoodRunListsForAnalysisRun2#2015_13_TeV_pp_data_taking_summa

[96] ATLAS collaboration.
GoodRunsList.
software package (Dec 2016).
URL https://svnweb.cern.ch/cern/wsvn/atlasoff/DataQuality/GoodRunsLists/tags/GoodRunsList-00-01-34/

[97] ATLAS collaboration.
Muon physics Trigger Recommendations 2015.
Twiki page (Dec 2016).
URL https://twiki.cern.ch/twiki/bin/view/Atlas/MuonTriggerPhysicsTriggerRecommendations2015

[98] ATLAS collaboration.
Track to Vertex Association.
Twiki page (Dec 2016).
URL https://twiki.cern.ch/twiki/bin/view/AtlasProtected/TrackingCPPreRecs2016#Track_to_Vertex_Association

[99] ATLAS collaboration.
MuonSelectorTools.
software package (Dec 2016).
URL https://svnweb.cern.ch/cern/wsvn/atlasoff/PhysicsAnalysis/MuonID/MuonSelectorTools/tags/MuonSelectorTools-00-05-33

[100] ATLAS collaboration.
MuonSelectionTool.

Twiki page (Dec 2016).
URL https://twiki.cern.ch/twiki/bin/view/Atlas/MuonSelectionTool

[101] G. Aad et al.
Muon reconstruction performance of the ATLAS detector in proton–proton collision data at $\sqrt{s}$ = 13 TeV.
Eur. Phys. J., C76(5) 292 (2016).
doi:10.1140/epjc/s10052-016-4120-y.
1603.05598.

[102] A. Collaboration.
Twiki: Isolation selection tool (2017).
URL https://twiki.cern.ch/twiki/bin/viewauth/AtlasProtected/IsolationSelectionTool

[103] ATLAS Collaboration.
Twiki: Muon Isolation Efficiency (2017).
URL https://twiki.cern.ch/twiki/bin/view/AtlasProtected/MCPAnalysisGuidelinesMC15#Muon_reconstruction_efficiency_s

[104] M. Aaboud et al.
Measurements of top-quark pair to Z-boson cross section ratios at $\sqrt{s} = 13, 8, 7$ TeV with the ATLAS detector.
JHEP, 02 117 (2017).
doi:10.1007/JHEP02(2017)117.
1612.03636.

[105] M. Grazzini, et al.
$W^{\pm}Z$ production at hadron colliders in NNLO QCD.
Phys. Lett., B761 179–183 (2016).
doi:10.1016/j.physletb.2016.08.017.
1604.08576.

[106] F. Cascioli, et al.
ZZ production at hadron colliders in NNLO QCD.
Phys. Lett., B735 311–313 (2014).
doi:10.1016/j.physletb.2014.06.056.
1405.2219.

[107] M. Aaboud et al.
Measurement of the $t\bar{t}$ production cross section using $e\mu$ events with b-tagged jets in pp collisions at $\sqrt{s}$=13 TeV with the ATLAS detector.
Phys. Lett., B761 136–157 (2016).
doi:10.1016/j.physletb.2016.08.019,10.1016/j.physletb.2017.09.027.
[Erratum: Phys. Lett.B772,879(2017)], 1606.02699.

[108] ATLAS Collaboration.
ATLAS Metadata Interface (2017).
URL https://ami.in2p3.fr/

[109] ATLAS Collaboration.
Twiki: Extended Pileup reweighting (2017).
URL https://twiki.cern.ch/twiki/bin/view/AtlasProtected/ExtendedPileupReweighting#Recommended_settings_version_00

[110] ATLAS Collaboration.
Twiki: Muon momentum scale and resolution (2017).
URL https://twiki.cern.ch/twiki/bin/view/AtlasProtected/MCPAnalysisGuidelinesMC15#Muon_momentum_scale_and_resoluti

[111] G. Aad et al.
Muon reconstruction performance of the atlas detector in proton–proton collision data at $\sqrt{s}$ = 13 tev.
The European Physical Journal C, 76(5) 292 (May 2016).
ISSN 1434-6052.
doi:10.1140/epjc/s10052-016-4120-y.

[112] ATLAS collaboration.
MuonEfficiencyCorrections.
software package (Dec 2016).
URL https://svnweb.cern.ch/cern/wsvn/atlasoff/PhysicsAnalysis/MuonID/MuonIDAnalysis/MuonEfficiencyCorrections/tags/MuonEfficiencyCorrections-04-00-02

[113] M. Aaboud et al.
Performance of the atlas trigger system in 2015.
The European Physical Journal C, 77(5) 317 (May 2017).
ISSN 1434-6052.
doi:10.1140/epjc/s10052-017-4852-3.

[114] G. Aad et al.
Measurement of the transverse momentum and ϕ^*_η distributions of Drell–Yan lepton pairs in proton–proton collisions at $\sqrt{s} = 8$ TeV with the ATLAS detector.
Eur. Phys. J., C76(5) 291 (2016).
doi:10.1140/epjc/s10052-016-4070-4.
1512.02192.

[115] T. Adye.
Roounfold: Root unfolding framework (2017).
URL http://hepunx.rl.ac.uk/~adye/software/unfold/RooUnfold.html

[116] S. Alekhin et al.
HERAFitter, Open Source QCD Fit Project.
Eur. Phys. J., C75(7) 304 (2015).
doi:10.1140/epjc/s10052-015-3480-z.
1410.4412.
URL https://www.xfitter.org/xFitter/

[117] G. Aad et al.
Measurement of transverse energy-energy correlations in multi-jet events in pp collisions at $\sqrt{s} = 7$ TeV using the ATLAS detector and determination of the strong coupling constant $\alpha_s(m_Z)$.
Phys. Lett., B750 427–447 (2015).
doi:10.1016/j.physletb.2015.09.050.
1508.01579.

[118] M. Aaboud et al.
Measurement of the W-boson mass in pp collisions at $\sqrt{s} = 7$ TeV with the ATLAS detector (2017).
1701.07240.

[119] D. Collaboration.
Cafe package: wzfitter (2016).
URL cdcvs.fnal.gov:/cvsroot/d0cvs/wzfitter

[120] F. James.
MINUIT Function Minimization and Error Analysis: Reference Manual Version 94.1 (1994).

[121] T. Andeen et al.
Measurement of electron energy scale and offset with $z \to ee$ full monte carlo and data.
Do Note 5662 (Version 3.0) (2009).

[122] J. Hobbs.
Modeling the hadronic recoil in the run iib w mass.
Do Note 6283 (v 01.01.02) (2012).

[123] P. Golonka and Z. Was.
PHOTOS Monte Carlo: A Precision tool for QED corrections in Z and W decays.
Eur. Phys. J., C45 97–107 (2006).
doi:10.1140/epjc/s2005-02396-4.
hep-ph/0506026.

[124] Z. Was.
TAUOLA for simulation of tau decay and production: perspectives for precision low energy and LHC applications.
Nucl. Phys. Proc. Suppl., 218 249–255 (2011).
doi:10.1016/j.nuclphysbps.2011.06.040.
1101.1652.

[125] D. Collaboration.
Cafe package: wz_epmcs (2016).
URL cdcvs.fnal.gov:/cvsroot/d0cvs/wz_epmcs

[126] D. Collaboration.
Cafe package: wmass_tools (2016).
URL cdcvs.fnal.gov:/cvsroot/d0cvs/wmass_tools

[127] D. Collaboration.
Cafe package: wmass_analysis (2016).
URL cdcvs.fnal.gov:/cvsroot/d0cvs/wmass_analysis

[128] J. Cuth.
Analysis repository for w mass measurement (2017).
URL https://gitlab.com/jakubkocutik/cafe_2S.git(fetch)

[129] D. Boline et al.
Measurement of the w boson mass using run iib1/2 data.
Do Note 6268 (v1.00) (2012).

[130] R. Collaboration.
Legacy grids for cteq6.6 (2014).
URL http://hep.pa.msu.edu/resum/grids/resbos_p/w_z/tev2/general_purpose/w+/before_2011/45_PDFs

[131] RESBOS Collaboration.
LEGACY grids for CT10nnlo and g-parameter variation (2014).
URL http://hep.pa.msu.edu/resum/grids/resbos_p/w_z/tev2/general_purpose/w+/2012/nnlo_pdfs/

[132] M. Guzzi.
private communication (2014).

[133] M. Guzzi, P. M. Nadolsky, and B. Wang.
Nonperturbative contributions to a resummed leptonic angular distribution in inclusive neutral vector boson production.
Phys. Rev., D90(1) 014030 (2014).
doi:10.1103/PhysRevD.90.014030.
1309.1393.

[134] P. M. Nadolsky et al.
Implications of CTEQ global analysis for collider observables.
Phys. Rev., D78 013004 (2008).
doi:10.1103/PhysRevD.78.013004.
0802.0007.

[135] D. Boline et al.
Understanding pdf uncertainties in the do w boson mass measurement.
Do Note 6147 (2012).

[136] H. Paukkunen and P. Zurita.
PDF reweighting in the Hessian matrix approach.
JHEP, 12 100 (2014).
doi:10.1007/JHEP12(2014)100.
1402.6623.

[137] S. Camarda et al.
QCD analysis of W- and Z-boson production at Tevatron.
Eur. Phys. J., C75(9) 458 (2015).
doi:10.1140/epjc/s10052-015-3655-7.
1503.05221.

[138] V. M. Abazov et al.
Measurement of the shape of the boson rapidity distribution for $p\bar{p} \to Z/gamma^* \to e^+e^-$ + X events produced at $\sqrt{s}$ of 1.96-TeV.
Phys. Rev., D76 012003 (2007).
doi:10.1103/PhysRevD.76.012003.
hep-ex/0702025.

[139] T. A. Aaltonen et al.
Measurement of $d\sigma/dy$ of Drell-Yan e^+e^- pairs in the Z Mass Region from $p\bar{p}$ Collisions at $\sqrt{s} = 1.96$ TeV.
Phys. Lett., B692 232–239 (2010).
doi:10.1016/j.physletb.2010.06.043.
0908.3914.

[140] V. M. Abazov et al.
Measurement of the muon charge asymmetry in $p\bar{p} \to W + X \to \mu\nu + X$ events at $\sqrt{s}$ = 1.96 TeV.
Phys. Rev., D88 091102 (2013).

doi:10.1103/PhysRevD.88.091102.
1309.2591.

[141] T. Aaltonen et al.
Direct Measurement of the W Production Charge Asymmetry in $p\bar{p}$ Collisions at $\sqrt{s} = 1.96$ TeV.
Phys. Rev. Lett., 102 181801 (2009).
doi:10.1103/PhysRevLett.102.181801.
0901.2169.

[142] V. M. Abazov et al.
Measurement of the W Boson Production Charge Asymmetry in $p\bar{p} \to W+X \to e\nu+X$ Events at $\sqrt{s} = 1.96$ TeV.
Phys. Rev. Lett., 112(15) 151803 (2014).
doi:10.1103/PhysRevLett.114.049901,10.1103/PhysRevLett.112.151803.
[Erratum: Phys. Rev. Lett.114,no.4,049901(2015)], 1312.2895.

[143] T. e. a. Andeen.
Modeling the hadronic recoil for a precision measurement of the w mass in the run iia analysis at d (method i).
Do Note 5668 (2007).

[144] S. Yaacob et al.
Preparation of zero bias events for overlay onto monte carlo as part of the do runiib w mass analysis.
Do Note 5875 (2009).

[145] D. Boline.
W mass measurement in full geant monte carlo in run iib.
Do Note 6267 (Version 1.2.0) (2012).

[146] D. Boline and A. Melnitchouk.
Background model for runiib w mass measurement.
Do Note 6084 (Version 2.1) (February 2012).

[147] J. Cúth (on behalf of Do collaboration) and M. Schott.
Preservation of the Do W mass measurement to incorporate future PDF and physics models.
Proceedings of Science (EPS-HEP2015), 339 (2015).
URL http://pos.sissa.it/archive/conferences/234/339/EPS-HEP2015_339.pdf

[148] J. Cúth and M. Schott.
Preservation of the w boson mass analysis of the do experiment.
Do note 6454 (Version 1.00) (2015).

[149] V. M. Abazov et al.
Measurement of the W boson mass with the Do detector.
Phys. Rev., D89(1) 012005 (2014).
doi:10.1103/PhysRevD.89.012005.
1310.8628.

[150] Oracle VM.
Virtualbox (2015).
URL https://www.virtualbox.org/

[151] A. D. Martin, et al.
Parton distributions for the LHC.
Eur. Phys. J., C63 189–285 (2009).
doi:10.1140/epjc/s10052-009-1072-5.
0901.0002.

[152] D. Stump, et al.
Inclusive jet production, parton distributions, and the search for new physics.
JHEP, 10 046 (2003).
doi:10.1088/1126-6708/2003/10/046.
hep-ph/0303013.

List of Figures

2.1 Feynman diagrams for interaction vertices of electroweak bosons and fermions. . . . 8
2.2 The list of α_s measuements with respect to scaled of studied process. The plot is from [7]. . . . 10
2.3 Diagram of the vector boson $W/Z/\gamma$ production in collision of two hadrons $h_{1,2}$ and its decay to lepton pairs $\ell_{i,j}$. The four-momenta of interacting partons $q_{a,b}$ are defined by the four-momenta of colliding hadrons $P_{1,2}^{\alpha,\beta}$ and the fraction $x_{1,2}$. The four-momentum of intermediating boson and four-momenta of leptons are denoted by q^{κ} and $p_{3,4}^{\mu,\nu}$, respectively. The latin indices a, b, i, j represents the fermion flavour and greek indices α, β, μ, ν represent the bispinor space. . . . 11
2.4 Example of diagrams contributing to born level (a), boson and gluon (b), boson and quark (c). The leading order is indicated as blue, one-loop correction as light blue and two-loop correction as faint blue. The Electroweak vertex and boson are shown as black. . . . 14
2.5 Illustration of Collins-Soper frame. Blue lines represents the incoming partons, red vectors represents the outgoing lepton. The other lepton momentum vector is symmetric with respect to origin of coordinates. 14
2.6 Comparison of resummation (a) and fixed order (b) diagrams. The dotted line represents the infinite series of gluon emmisions, which is resummed. . . . 16
2.7 A sketch of the differential cross section with respect to the transverse momentum of the vector boson q_{T}. . . . 16

3.1 Coordinate systems: Cartesian depicted by green, spherical is red. Blue color represents described vector. . . . 21
3.2 Schematic view of the Fermilab accelerator complex. Plot adapted from [38] data from [39]. . . . 23
3.3 Integrated luminosity of runIIb delivered by Tevatron (green) and recorded by DØ experiment (blue). The data was taken from [41]. . . . 24
3.4 Cross section view of the DØ showing the sub-detector parts. Plot from [45]. . . . 25
3.5 Schematic view of the tracking detector. Plot colorized and taken from [46] 26
3.6 Cut-away view of DØ calorimeters. The beam line is marked by thin red line. For more information see text. Plot taken from [46] 27
3.7 Schematic view of calorimeter cell. Plot taken from [47]. . . . 28
3.8 Technical drawing of calorimeter cells with pseudo-rapidity lines. The cells shading pattern follows the read-out structure. The electromagnetic cells are yellow, blue are fine hadronic cells, faint blue are coarse hadronic cells. The pre-shower detectors are marked red, the position of ICD is marked green. Plot taken from [47] and colorized. . . . 29
3.9 DØ trigger with the corresponding rates at each stage. Plot taken from [48]. . . . 31
3.10 Schematic view of CERN accelerator complex 34

3.11 Integrated luminosity with respect to time for different production years. Figure taken from [55]. 35

3.12 Cut-away view of ATLAS detector.Figure taken from [56]. 36

3.13 Cut-away view of ATLAS inner detector system. 37

3.14 Cut-away view of ATLAS calorimeter system. 38

3.15 The cut-away view of ATLAS muons spectrometer 39

4.1 Differential cross section (upper part) and ratio (lower part) with respect to p_{T} of the Z (a,b), W^+ (c,d) and W^- (e,f) bosons. The prediction of DYRES, DYTURBO with polynomial and DYTURBO with numerical transformation of PDF is marked by green, orange and blue color. Further information is given in the text. 56

4.2 Differential cross section (upper part) and ratio (lower part) with respect to p_{T} of the Z boson. The integration using VEGAS and quadrature rule is marked by blue and green color, resp. 57

5.1 Comparison of p_{T}^{Z} distribution shapes for different values of α_S (a), g_{NP} (b) parameters and variation of renormalization and factorization scales (c). The lower part of each plot shows the ratio with respect to $\alpha_S = 0.1180$, $g_{\mathrm{NP}} = 0.8\,\mathrm{GeV}^2$ and $\mu_R = \mu_F = 1$. 63

5.2 Plots on the left hand side show the fitted $\Delta\chi^2$ parabola w.r.t α_S (a) and g_{NP} (c) and the 68%, 95% and 99% CL regions of the 2D α_S-g_{NP} fit (e). The blue points mark the value of the template where χ^2 was evaluated. The pseudo-data is the MC prediction with values $\alpha_S = 0.1182$ and $g_{\mathrm{NP}} = 1.1\,\mathrm{GeV}^2$. The plots on the right hand side show the ratio of the p_{T}^{Z} shape between the pseudo-data and the spline from the best fitted value of α_S (b) g_{NP} (d) and both (f). The yellow line and band represent the pseudo-input uncertainty from the statistics of the prediction. The blue band and line represent the uncertainty on the fitted shape. . . . 66

5.3 The number of observed events with respect to the average number of interactions per bunch crossing $\langle\mu\rangle$. The collected data is compared to Monte-Carlo predictions including backgrounds. The lower part of the plot shows the ratio of Monte-Carlo and data. Grey bands represent systematic uncertainties and error bars represent statistic uncertainty on both parts of the plot. 73

5.4 Muon resolution $\sigma(m_{\mu\mu})$ (a) and muon scale $\mu(m_{\mu\mu})$ (b) with respect to $\eta^{\text{lead-}\mu}$ before (blue) and after (green) p_{T}^{μ} corrections compared to data (red). The lower part of the plot shows the ratio of data and Monte-Carlo. 74

5.5 Scaling factors for reconstruction (green), isolation (violet) and trigger (cyan) efficiencies with respect to the $\eta^{\mathrm{lead}-\mu}$ (a) and $p_{\mathrm{T}}^{\mathrm{lead}-\mu}$ (b) used for the analysed events. The combined correction are depicted in red. . . 75

5.6 Distribution of p_{T}^{Z} (a) and y^{Z} (b) before (fuchsia) and after (grey) the application of p_{T}^{Z}-y^{Z} re-weighting. The collected data is compared to Monte-Carlo predictions including backgrounds. The lower part of the plot shows the ratio of Monte-Carlo and data. Grey bands represent systematic uncertainties and error bars represent statistic uncertainty on both parts of the plot. 75

5.7 Number of observed muons with respect to muon transverse momentum (a) and muon pseudorapidy (b). The collected data is compared to Monte-Carlo predictions including backgrounds. The lower part of the plot shows the ratio of Monte-Carlo and data. Grey bands represent systematic uncertainties and error bars represent statistic uncertainty on both parts of the plot. 76
5.8 The number of observed events with respect to rapidy (a), mass (b) and transverse momentum (c) of the Z candidate.The collected data is compared to Monte-Carlo predictions including backgrounds. The lower part of the plot shows the ratio of Monte-Carlo and data. Grey bands represent systematic uncertainties and error bars represent statistic uncertainty on both parts of the plot. 77
5.9 Two-dimensional representation of the response matrix (a) normalized to number of events in reconstructed bin and Purity and stability (b) per p_{T}^{Z} bin in percent. 78
5.10 Sanity (a,c) and closure (b,d) tests of Bin-by-Bin (a,b) and Bayesian unfolding (c,d). The pseudo-data fiducial (red) and reconstructed (cyan) distributions are compared to the fiducial distributions of training (green) and unfolded (voilet) shapes of the p_{T}^{Z} distribution. The lower part of each plot shows the ratio of shapes with respect to the fiducial of the pseudo-data. 80
5.11 Relative uncertainty contribution to the unfolded p_{T}^{Z} distribution from each source (a). Comparison of the theory predictions to the unfolded data (b), with a predicted value of α_s = 0.1182. 81
5.12 A comparison of $\alpha_s(M_Z^2)$ measurements with the world average (gray band and line). The value from this measurement is named $p_{\mathrm{T}}(Z)$. The other values are taken from [7]. 84
5.13 The plots on the left hand side: Fitted $\Delta\chi^2$ parabola w.r.t α_s (a) and g_{NP} (c), and the 68%, 95% and 99%CL regions of the 2D α_s-g_{NP} fit (e). The blue points (1D) and colored areas (2D) mark values of the template where the χ^2 was calculated. The plots on the right right hand side: The ratio of the p_{T}^{Z} shape between the data (yellow line) and spline (blue line) from the best fitted value of α_s (b) g_{NP} (d) and both simultaneously (f). The yellow band represents the experimental uncertainty. The blue bands represent the uncertainty of the prediction (dark blue) and the total prediction uncertainty including scale uncertainties. 85

6.1 The indirect estimation of M_W with a global electroweak fit (blue parabola) compared to the world average (orange point), new ATLAS measurement [118] (blue square) and personal combination with an assumption of a 50% correlation (green square). 88
6.2 Shapes of the transverse mass m_{T} (a) and the lepton transverse momentum p_{T}^{ℓ} (b) distributions. The blue filled area shows the truth distribution in the lab system ($q_{\mathrm{T}} \neq 0$), the green line shows the distribution in the W rest frame ($q_{\mathrm{T}} = 0$) and the red line shows the distribution after the detector simulation. The plots were created with RESBOS and PMCS (see text). All distributions are scaled to unity. 89
6.3 The reconstructed distribution of the W transverse mass (a) and electron transverse momentum (b) for different values of M_W. The upper part of each plot shows distributions normalized to unity. The lower part of each plot shows the ratio with respect to $M_W = 80.399\,\mathrm{GeV}$. . . 90

6.4 Schematic view of a $Z \to ee$ (left) and a $W \to e\nu$ (right) event in the transversal plane. The inner part of each schema shows the truth momentum vectors and the outer part shows the simulated detector response. The electron response in the calorimeter is depicted as a red area, while the blue area represents the rest of measured activity in the calorimeter (hadronic recoil). The plot was taken from [43] and extended. 91
6.5 Block diagram of PMCS inputs and outputs. Orange arrows represent inputs to parametrization and tuning. Blue arrows represent the event processing. More description is in the text. 91
6.6 The shapes of the p_{T}^{W} distribution without any fiducial cut as obtained from RESBOS CT10nnlo g_{NP} variations for fixed (red and green) and varied (cyan and violet) perturbative scales. The non-physical shape is marked by "kink". 94
6.7 Squared contribution $(\Delta M_i)^2$ to PDF envelope of m_{T} (a) and $m_{\mathrm{T}} - p_{\mathrm{T}}$ (b) per each eigenvalue. The symmetric term $(\Delta M_i)^2$ is represented as blue bars and positive (negative) term $(\Delta^{\pm} M_i)^2$ is represented as green (red) bars. 96
6.8 Fitted values of M_W from m_{T} (a) and $m_{\mathrm{T}} - p_{\mathrm{T}}$ (b) per each eigenvalue (points and green band) with the central value (black dashed line) and final scaled PDF envelope (blue band). Error bars and dark blue band represent the statistical uncertainty of the generated sample. 97
6.9 Distribution of Z transverse momentum from (black points) runIIb3 (a) and runIIb4.b) data compared to PMCS predictions using CT14nnlo (brown points) and CTEQ6.6 (blue points) PDF set. 97
6.10 Distribution of hadronic recoil in $W \to e\nu$ events from runIIb3 data compared to CTEQ6.6 (a) and CT14nnlo (b) PMCS prediction. The lower part shows a pull plot between data as PMCS. 98
6.11 Fitted values of M_W from m_{T} (a) and $m_{\mathrm{T}} - p_{\mathrm{T}}$ (b) per each eigenvalue are represented by points. Original and profiled CTEQ6.6 is depicted by orange and green color, respectively. The blue band represents the scaled symmetric PDF envelope. 100
6.12 Comparison of original (green) and profiled CTEQ6.6 (blue) and CT14nnlo (brown) PDF uncertainties for m_{T} (circle) p_{T}^{e} (square) $m_{\mathrm{T}} - p_{\mathrm{T}}$ (triangle) distributions. The shift ΔM_W is estimated by fitting central distributions of each PDF sample with CTEQ6.6 templates. 101
6.13 Comparison of measured (black points) and predicted distributions (filled area) of Z-candidate invariant mass (a), Z-candidate transverse momentum (b), electron transverse momentum (c), electron pseudo-rapidity (d), and hadronic recoil x- (e) and y- (f) components in runIIb3 $Z \to ee$ events. Lower part of each figure shows pull-plot between data and prediction. Prediction was done by PMCS. 107
6.14 Upper plots: Background shapes normalized to unity for transverse mass m_{T} (a) and electron transverse momentum p_{T}^{e} (b). The $W \to \tau\nu$, $Z \to ee$ and multi-jet background is represented by the blue, red and violet area, respectively. Lower plots: The shape of multi-jet (c) and total (d) background for the $m_{\mathrm{T}} - p_{\mathrm{T}}$ distribution. 110
6.15 Comparison of measured (black points) and predicted distributions (filled area) of luminosity (a) and vertex z-position (b) in $W \to e\nu$ events. Lower part of each figure shows pull-plot between data and prediction. Prediction was done by PMCS. The total background is showed as filled purple area. 111

6.16 Comparison of measured (black points) and predicted distributions (filled area) of hadronic parallel (a) and perpendicular (b) component w.r.t electron in $W \to e\nu$ events. Lower part of each figure shows pull-plot between data and prediction. Prediction was done by PMCS. The total background is showed as filled purple area. 112

6.17 Comparison of measured (black points) and predicted distributions (filled area) of electron pseudo-rapidity (a) and electron transverse angle (b) in $W \to e\nu$ events. Lower part of each figure shows pull-plot between data and prediction. Prediction was done by PMCS. The total background is showed as filled purple area. 112

6.18 Comparison of measured (black points) and predicted distributions (filled area) of transverse mass (a) and electron transverse momentum (b) in $W \to e\nu$ events. Lower part of each figure shows pull-plot between data and prediction. Prediction was done by PMCS. The total background is showed as filled purple area. 113

6.19 Measured $m_{\mathrm{T}} - p_{\mathrm{T}}$ distribution (a) and pull-plot between data and PMCS prediction including background. 113

6.20 The comparison of PMCS (red points) including background (filled area) and DATA (black points) using the CTEQ6.6 grids. The plotted distributions are transverse mass (a) and transverse momentum of the electron (b). In lower part of every plot there is ratio plot between DATA and PMCS. Plot also in [148, 147]. 116

6.21 The W boson mass fitted with preserved code using different PDF sets is compared to published results from DØ, CDF and world average [7]. Grey error bars represent total uncertainty, while colored error bands represents PDF uncertainty only. The mass fitted by m_{T}, p_{T}^{e} and $\not{E}_{\mathrm{T}}$ is shown as empty circle, square and triangle, respectively. Combined mass from all three distribution is marked by large filled circle. Values in each row with reference are taken from publication, otherwise were fitted by preserved analysis. 117

A.1 The plot (a) shows ratio (lower) and total events of measured and modelled Z candidate events with respect to mean number of interaction per bunch crossing $\langle\mu\rangle$. The plot (b) interprets the nominal response matrix used for unfolding to fiducial level. 160

A.2 Comparison of measured Z candidates and Monte-Carlo predcition for distribution of muon track perpendicular distance from beam line d_0^{μ} (a), muon pseudorapidity η^{μ} with logarithmic (b) and linear (c) axis and muon transverse momentum distribution p_{T}^{μ} with logarithmic (d) and linear (e) axis. The lower part of plots shows the ratio and colored area symbolize the background. 161

A.3 Comparison of measured Z candidates and Monte-Carlo predcition for distribution of dimuon invariant mass m^{Z} with logarithmic (a) and linear axis (b), dimuon transverse momentum p_{T}^{Z} with logarithmic (c) and linear axis (d) and dimuon rapidity y^{Z} (e). The lower part of plots shows the ratio and colored area symbolize the background. 162

B.1 Comparison of measured (black points) and predicted (filled area) $W \to e\nu$ events with respect to instantaneous luminosity (a), z-vertex position (b), angular angle of W candidate (c), hadronic recoil (d). 163

B.2 Comparison of measured (black points) and predicted (filled area) $W \to e\nu$ events with respect to angular difference between electron and missing transverse energy (a) angular difference between electron and hadronic recoil (b) angular difference between missing transverse and hadronic recoil (c) . . . 164
B.3 Comparison of measured (black points) and predicted (filled area) $W \to e\nu$ events with respect to electron pseudorapidity without (a) and with (b) detector level corrections, electron transverse angle without (c) and with (d) detector level corrections and electron transverse energy (e). . 165
B.4 Comparison of measured (black points) and predicted (filled area) $W \to e\nu$ events with respect to scalar sum of deposited energy in calorimeter (a), missing transverse energy size (b), angle (c), x-component (d) and y-component (e). . . . 166
B.5 Comparison of measured (black points) and predicted (filled area) $W \to e\nu$ events with respect to hadronic recoil parallel projection (a), hadronic recoil perpendicular projection (b) and transversal mass of candidate (c). 167
B.6 Comparison of measured (black points) and predicted (filled area) $W \to e\nu$ events with respect to hadronic recoil size (a) and its azimuthal angle (b) x-component (c) and y-component (d). . . . 168
B.7 Measured (a) and predicted (b) two dimensional $m_{\mathrm{T}} - p_{\mathrm{T}}$ distribution. Pull-plot comparing data and Monte-Carlo prediction with respect to $m_{\mathrm{T}} - p_{\mathrm{T}}$ (c). Estimated total background (d) and multi-jet background (e) yields for two dimensional $m_{\mathrm{T}} - p_{\mathrm{T}}$ distributions. . . . 169
B.8 Comparison of measured (black points) and predicted (filled area) $W \to e\nu$ events with respect to instantaneous luminosity (a), z-vertex position (b), angular angle of W candidate (c), hadronic recoil (d). . . . 170
B.9 Comparison of measured (black points) and predicted (filled area) $W \to e\nu$ events with respect to angular difference between electron and missing transverse energy (a) angular difference between electron and hadronic recoil (b) angular difference between missing transverse and hadronic recoil (c) . . . 171
B.10 Comparison of measured (black points) and predicted (filled area) $W \to e\nu$ events with respect to electron pseudorapidity without (a) and with (b) detector level corrections, electron transverse angle without (c) and with (d) detector level corrections and electron transverse energy (e). . 172
B.11 Comparison of measured (black points) and predicted (filled area) $W \to e\nu$ events with respect to scalar sum of deposited energy in calorimeter (a), missing transverse energy size (b), angle (c), x-component (d) and y-component (e). . . . 173
B.12 Comparison of measured (black points) and predicted (filled area) $W \to e\nu$ events with respect to hadronic recoil parallel projection (a), hadronic recoil perpendicular projection (b) and transversal mass of candidate (c). 174
B.13 Comparison of measured (black points) and predicted (filled area) $W \to e\nu$ events with respect to hadronic recoil size (a) and its azimuthal angle (b) x-component (c) and y-component (d). . . . 175
B.14 Measured (a) and predicted (b) two dimensional $m_{\mathrm{T}} - p_{\mathrm{T}}$ distribution. Pull-plot comparing data and Monte-Carlo prediction with respect to $m_{\mathrm{T}} - p_{\mathrm{T}}$ (c). Estimated total background (d) and multi-jet background (e) yields for two dimensional $m_{\mathrm{T}} - p_{\mathrm{T}}$ distributions. . . . 176

C.1 Fitted values of M_W with respect to PDF members for m_{T} (a), $m_{\mathrm{T}} - p_{\mathrm{T}}$ (b) and p_{T} (c). . . . 177

C.2 Squared contribution to total uncertainty with respect to PDF members for m_{T} (a), $m_{\mathrm{T}} - p_{\mathrm{T}}$ (b) and p_{T} (c). 177
C.3 Fitted values of M_W with respect to PDF members for m_{T} (a), $m_{\mathrm{T}} - p_{\mathrm{T}}$ (b) and p_{T} (c). 178
C.4 Squared contribution to total uncertainty with respect to PDF members for m_{T} (a), $m_{\mathrm{T}} - p_{\mathrm{T}}$ (b) and p_{T} (c). 179
C.5 Fitted values of M_W with respect to PDF members for m_{T} (a), $m_{\mathrm{T}} - p_{\mathrm{T}}$ (b) and p_{T} (c). 180
C.6 Squared contribution to total uncertainty with respect to PDF members for m_{T} (a), $m_{\mathrm{T}} - p_{\mathrm{T}}$ (b) and p_{T} (c). 180

D.1 Pull-plot for profiling result values of fitted and input parameters. . . . 182
D.2 Prediction with original and profiled PDF is compared to input data from CDF Z rapidity (a), Do Z rapidity (b), Do W asymmetry (c), Do $W \to \mu\nu$ lepton asymmetry (d) and CDF W asymmetry (e) measurement. 183
D.3 Comparison of original (blue) and profiled (red) PDF with respect to Bjorken-x at $Q^2 = M_W^2$. Compared distributions are: ratio d/u quark parton function (a), double ratio of d/u functions (b), difference $d - u$ functions (c) and ratio of $d - u$ difference (d). 184

List of Tables

2.1 List of fixed order calculation diagrams up to $\mathcal{O}\left(\alpha_s^2\right)$. Taken from [27]. 13

4.1 Selected Drell-Yan generators with the highest implemented order and used method of calculation. A possible interface to a parton shower program is marked by $(+PS)$. The table is adapted from [76], with data obtained from reference present in each row. 47
4.2 List of terms needed per each order and input settings of parameters `order` and `fixedorder`. 50
4.3 List of available integrand implementations inside DYTURBO. 52
4.4 Comparison between DYRES and DYTURBO differential cross section of resummed term at fixed values of $y = 0$, $m = m_V$, $\cos\theta = 0$, and various values of p_T. The differential cross section are given in fb/GeV^2. 55

5.1 Event selection table for data (cut-flow). The number of events in data (second column) fulfilling the cut is shown in the first column. From the second to the last column the fraction calculated with respect to first row below the horizontal line is shown. The values in the last column are calculated as fraction with respect to first row (xAOD). 69
5.2 List of used samples with full dataset name. In the case of a data sample the `periodX` is substituted by corresponding period from D-J. 70
5.3 Definition of regions for the multi-jet background estimation together with the number of observed events in each region. The last row represents the estimated multi-jet background. 71
5.4 Used Monte-Carlo samples for each process. The cross section are obtained from the `AMI` [108] database and the uncertainties are from stated reference. Number of xAOD events is taken from DxAOD `CutBookKeeper` and the C-factor represents the scale applied to histograms before comparing with data. 72
5.5 Table of bin-edges, unfolded shape and relative uncertainty (statistical, systematic and total) per each bin of p_{T}^Z. 82

6.1 Values of perturbative and non-perturbative parameters of CTEQ6.6 grid files [130]. The values of parameters were taken from the grid file header. 93
6.2 Values of parameters for updated CT10nnlo grids [132] with different perturbative regimes. The values were taken from the header of available grid files except for the values for fixed $C_{1,3} = b_0$ which were taken from [32]. 94
6.3 Calculated p_{T}-shape uncertainties from available non-perturbative parameter variations. The main value is the symmetric uncertainty and the subscript (superscript) is the negative (positive) difference from the central sample. The last row represents a conservative squared sum of these uncertainties. 95
6.4 List of Tevatron measurements used for constraining the CTEQ6.6 PDF set. 100

6.5 Estimated PDF uncertainty δ_{PDF} and fitted M_W from central sample of each PDF set using templates from CTEQ6.6 prediction ΔM_W^{fit} 101
6.6 Fitted values with uncertainties of the hadronic recoil parameters and their correlation. 103
6.7 Results of the fits for electron energy scale and offset to the data runIIb3. The instantaneous luminosity unit $\mathcal{L}$ is $36{\cdot}10^{30}\,\text{cm}^{-2}\text{s}^{-1}$. 104
6.8 Number of selected data in runIIb3 and fraction to events recorded in EMMET stream. All events means all collected by minimum bias trigger. 108
6.9 List of background predictions contributing to M_W measurement. The number of generated events, the number of unweighted events and final fraction of process is written in the second, third and fourth column, respectively. 109
6.10 List of studied uncertainties and their contribution per each distribution (column) and origin of uncertainty (row). 114

C.1 Fitted values for each PDF member per each studied distribution. . . . 178
C.2 Final value of estimated PDF uncertainties per studied distribution . . 178
C.3 Fitted values for each PDF member per each studied distribution. . . . 179
C.4 Final value of estimated PDF uncertainties per studied distribution . . 179
C.5 Fitted values for each PDF member per each studied distribution. . . . 181
C.6 Final value of estimated PDF uncertainties per studied distribution . . 181

D.1 Minimization result χ^2 agreement between data and predictions from nominal and profiled PDF 183

List of Abbreviations

Symbols | A | C | D | E | F | G | H | I | L | M | N | P | Q | R | S | T | V | X | Z

Symbols

$-\ln \mathcal{L}$
: negative log-likelihood function. 90

A

ABCD
: Method for estimation of background. 72

ALICE
: A Large Ion Collider Experiment. 34

ATLAS
: A Thoroidal LHC AparatuS. 7, 20, 21, 33–40, 67, 83, 120, 145

C

CC
: Central Calorimeter. 27, 28

CDF
: Collider Detector at Fermilab. 24

CERN
: European Organization for Nuclear Research. 20, 33, 34, 144

CFT
: Central Fiber Tracker. 25, 26, 30

CKM
: Cabibbo-Kobayashi-Maskawa mixing matrix. 7, 8, 12

CL
: Confidence Level. 66, 83, 85, 145, 146

CMS
: Compact Muon Solenoid. 34

CPS
: Central Pre-Shower. 27, 28

CS
: Collins-Soper frame. 15

CSC

Cathode Strip Chambers. 38, 39

CSS

Collins-Soper-Sterman resummation formalism. 16, 17, 48, 51, 92

D

DØ

detector at the Tevatron collider. 20, 21, 24, 25, 144

DAQ

Data AcQuisition system. 22, 67

DOFO

Magnets opposite to the FODO lattice. 23

Drell-Yan

Process of massive lepton pair production at hadron collision. 6, 10, 11, 15, 46–48, 90, 92, 151

DxAOD

Extended Analysis Objects Data format derivation. 67, 69, 72, 151

DYRES

Drell-Yan Monte-Carlo integrator. 48–50, 53–56, 120, 145, 151

DYTURBO

Drell-Yan Monte-Carlo integrator. 48–56, 62, 81, 83, 84, 120, 145, 151

E

E1_SHT25

Single electron trigger with 25 GeV cut. 31

E1_SHT27

Single electron trigger with 27 GeV cut. 31

EC

End-cap Calorimeter. 27, 28

EF

Event Filter - precise software trigger. 40

Electroweak

quantum field theory of electromagnetic and weak interaction. 7, 8, 14, 144

EM

Electromagnetic layers of calorimeter. 28, 32, 106

F

Fermilab
Fermi National Laboratory. 20, 22, 23, 144

FODO
focusing and defocusing quadrupole magnet lattice. 22

FPS
Forward Pre-Shower. 27, 28

FSR
Final State Radiation. 92, 103

FullMC
full Monte-Carlo simulation. 33, 92, 102

G

GRL
Good-Runs-List. 67

H

HLT
High Level Trigger. 40, 67, 74

I

IBL
Insertable b-layer. 36

ICD
Inter-Cryostat Detector. 27–29, 144

ID
Inner Detector. 35–38, 40, 41, 68, 74

ISR
Initial State Radiation. 46

L

L1
First Hardware trigger. 30, 31, 40, 67, 74

L2
Second Hardware trigger. 30, 31

L2
Fast software trigger. 40

L3
Software trigger. 30, 31, 105

LAr

Liquid-Argon Calorimeter. 27, 37, 67

LEP

Large Electron-Positron collider. 33

LHAPDF

Les Houches Parton Distribution Function format. 62

LHC

Large Hadron Collider. 20, 21, 33–35, 41, 120

LHCb

Large Hadron Collider beauty. 34

LINAC

LINear ACcelerator in Fermilab. 22

LINAC2

LINear ACcelerator at CERN. 33

LO

Leading order. 13

Lumi-block

Time period of run, when beam condition are constant. 67

M

MBLibrary

Minimum Bias Library. 102

MDT

Mini Drift Tubes. 30

MDT

Monitored Drift Tubes. 38–41

Monte-Carlo

Random sampling numerical integration method. 41, 46, 51, 61, 70–77, 79, 81, 90, 105, 110, 145, 146, 148, 149, 151, 154–157, 163, 164, 170

MS

Muon Spectrometer. 35, 37–41, 68, 74

N

NLO

Next-to-Leading order. 13, 47, 49, 81, 84

NNLL

Next-to-Next-to-Leading logarithms. 49, 81, 84

NNLO

Next-to-Next-to-Leading order. 13, 49, 84

P

p.d.f.

probability density function. 51

PDF

Parton Distribution Function. 10, 50, 53, 81, 83, 90, 92, 94–97, 99–101, 114, 116, 147, 149–152, 171–175, 177, 178

PDT

Proportional Drift Tubes. 30

PHOTOS

QED FSR Monte-Carlo generator. 108

pile-up

Other than primary interaction vertices during one bunch-crossing.. 68, 92, 102

Pixel

Pixel detector. 36, 68

PMCS

Parameterised Monte-Carlo Simulation. 33, 89–92, 96, 98, 101, 102, 104, 106–113, 116, 146–148, 157, 164

primary vertex

Vertex with largest sum of track transverse momentum.. 68

PS

Proton Synchrotron. 33

PSB

Proton Synchrotron Booster. 33

PYTHIA

General purpose Monte-Carlo generator. 102

Q

QCD

quantum field theory of the strong interaction – Quantum Chromodynamics. 9–12, 17, 46, 54, 60, 71, 92, 93

QED

Quantum Electrodynamics. 7, 9, 11, 92, 108

R

RAW

raw stream from detector electronics. 41

RESBOS

Drell-Yan Monte-Carlo generator using resummation calculation. 48, 89, 91–94, 96, 108, 109, 146, 147

RF

radio frequency. 20, 22, 23, 34

RMS

Root Mean Square. 32

RoI

Region of Interest. 31, 40

RPC

Resistive Plate Chambers. 38, 39

runIIb1

Tevatron run period from June 2006 to July 2007. 24

runIIb12

Tevatron run period from June 2006 to June 2009. 103, 108, 109

runIIb2

Tevatron run period from November 2007 to June 2009. 24

runIIb3

Tevatron run period from September 2009 to June 2010. 24, 97, 98, 104–108, 113, 147, 152

runIIb4

Tevatron run period from August 2010 to September 2011. 24, 97, 147

S

SCT

Semiconductor Tracker. 26, 36, 68

SM

quantum field theory of particle physics – Standard Model. 6, 7, 88

SMT

Silicon Microstrip Tracker. 25, 26, 36, 106

SPS

Super Proton Synchrotron. 33

T

tag-and-probe
Method for estimation of efficiencies. 74

Tevatron
hadron collider at Fermilab. 20–24, 30, 48, 88, 93, 99, 100, 105, 120, 144, 151

TGC
Thin Gap Chambers. 38, 39

Tile
Tile Calorimeter. 67

ToyMC
Method for estimation of statistical uncertainty. 90, 104

track-to-vertex distance
distance between vertex and point of track nearest to beam-line.. 68

TRT
Transition Radiation Tracker. 36, 37, 68

V

Vegas
Monte-Carlo integration method. 48, 49, 52

X

xAOD
Extended Analysis Objects Data format. 67, 69, 70, 72, 151

Z

ZBLibrary
Zero Bias Library. 102

A.

ATLAS p_{T}^{Z} control distributions

This appendix contains additional control distributions extending Chapter 5. All distributions are comparing measured data and Monte-Carlo prediction after applictaion of all discussed correction.

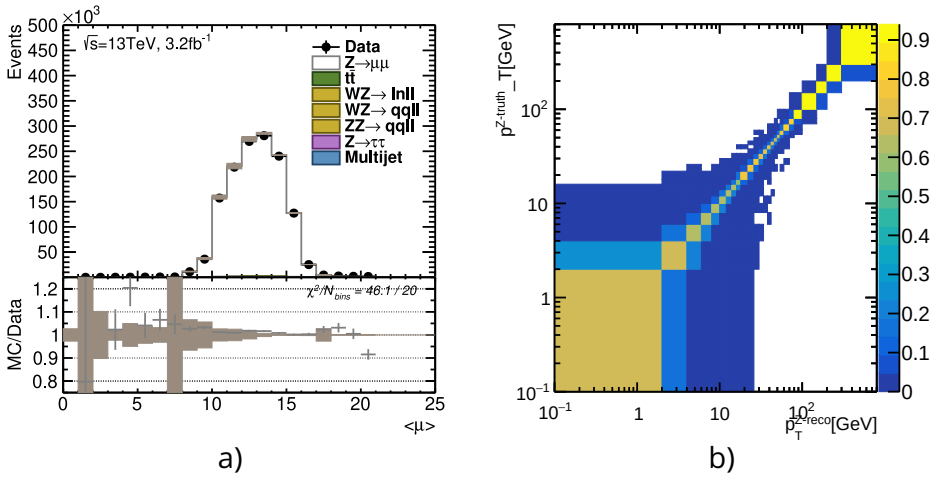

Figure A.1: *The plot (a) shows ratio (lower) and total events of measured and modelled Z candidate events with respect to mean number of interaction per bunch crossing $\langle\mu\rangle$. The plot (b) interprets the nominal response matrix used for unfolding to fiducial level.*

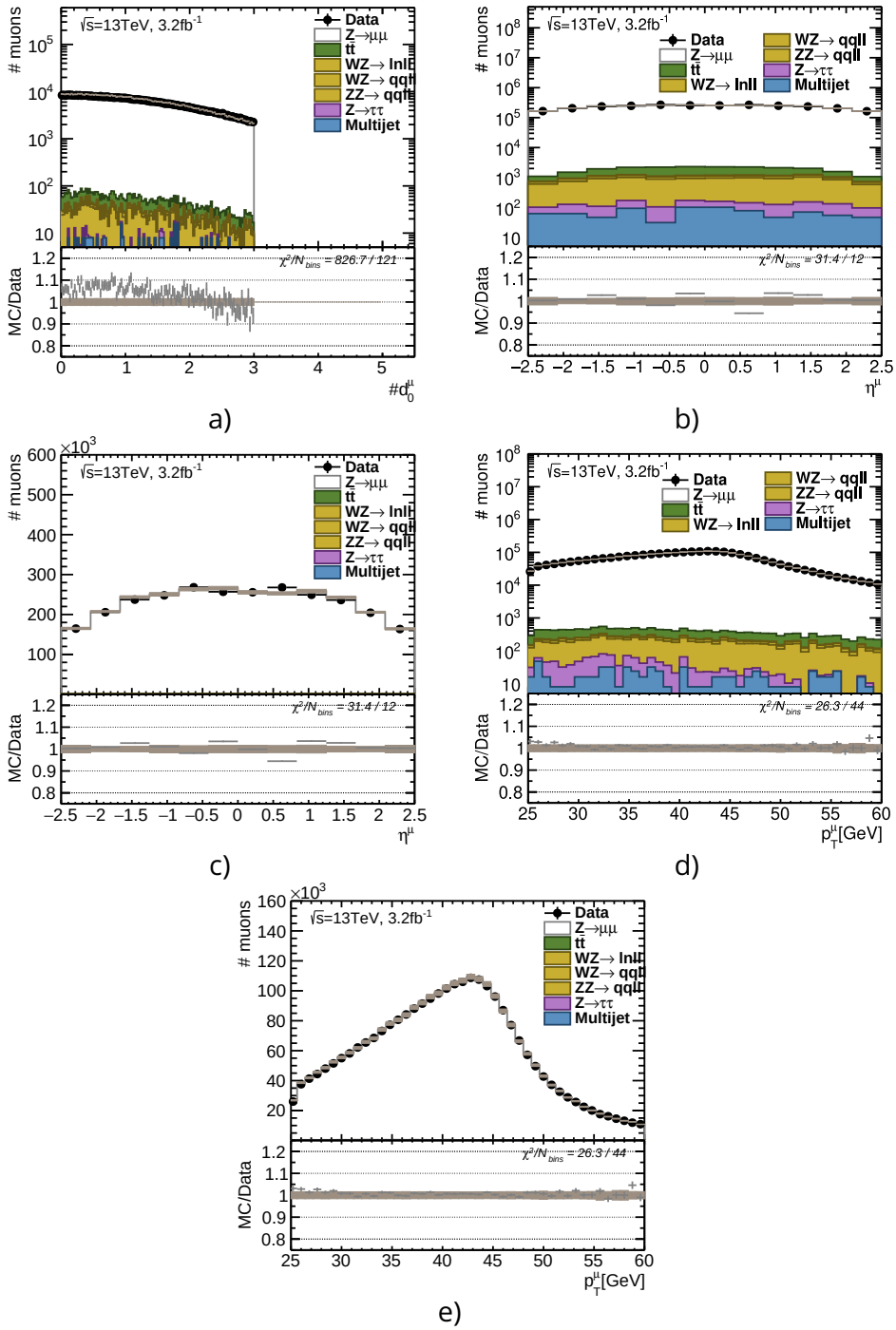

Figure A.2: *Comparison of measured Z candidates and Monte-Carlo predcition for distribution of muon track perpendicular distance from beam line d_0^{μ} (a), muon pseudorapidity η^{μ} with logarithmic (b) and linear (c) axis and muon transverse momentum distribution p_{T}^{μ} with logarithmic (d) and linear (e) axis. The lower part of plots shows the ratio and colored area symbolize the background.*

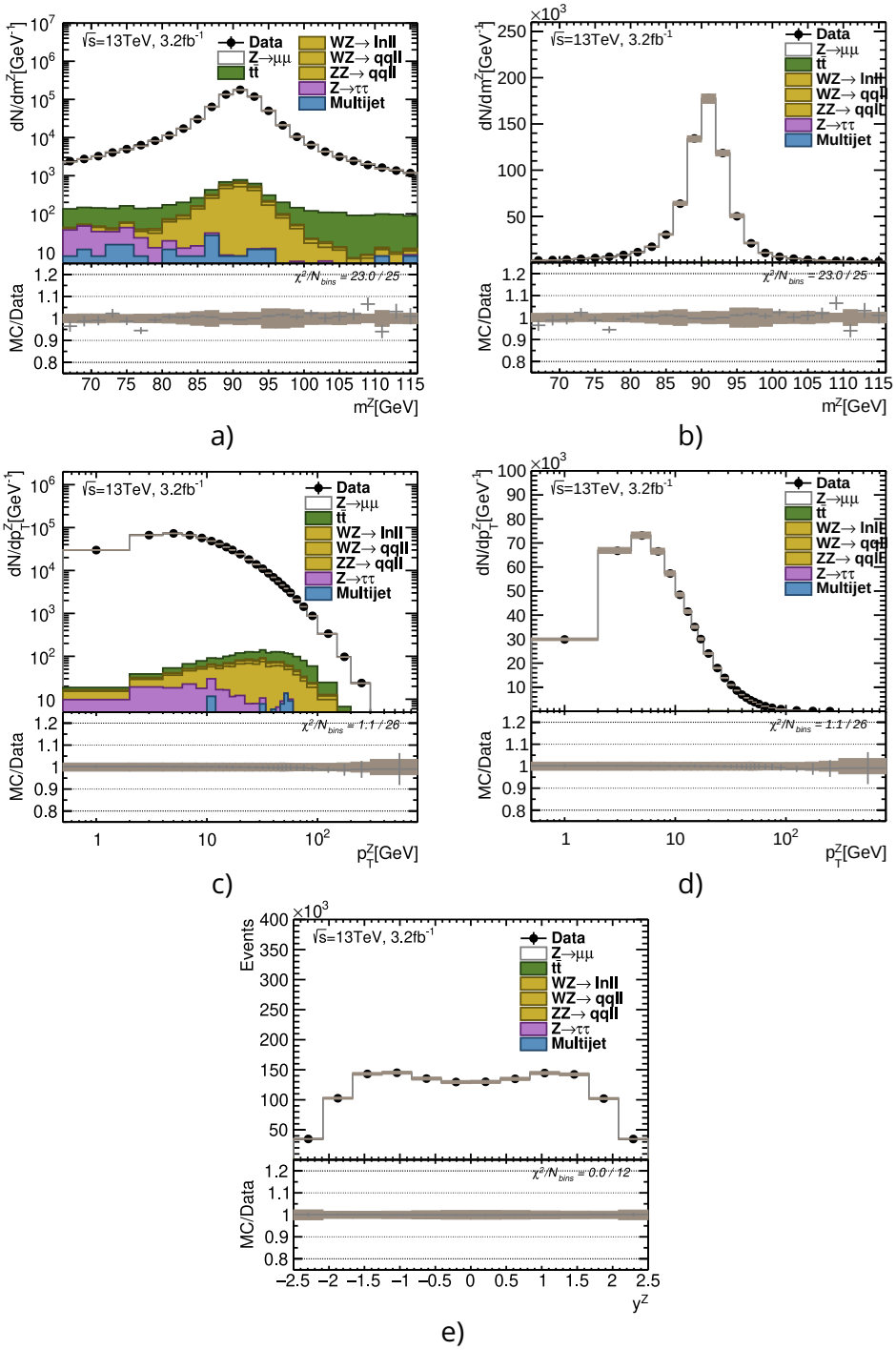

Figure A.3: *Comparison of measured Z candidates and Monte-Carlo predcition for distribution of dimuon invariant mass m^Z with logarithmic (a) and linear axis (b), dimuon transverse momentum p_{T}^Z with logarithmic (c) and linear axis (d) and dimuon rapidity y^Z (e). The lower part of plots shows the ratio and colored area symbolize the background.*

B. W mass control plots

This appendix contains extensive list of control distribution for W boson mass analysis, which is described in Chapter 6

B.1 Comparison of data from RunIIb3 with CTEQ6.6

List of distribution showing the level of agreement between measured data and Monte-Carlo prediction is presented in this section. The predictions are done by PMCS using CTEQ6.6 PDF set. And the lower part of each figure shows pull-plot between data and prediction.

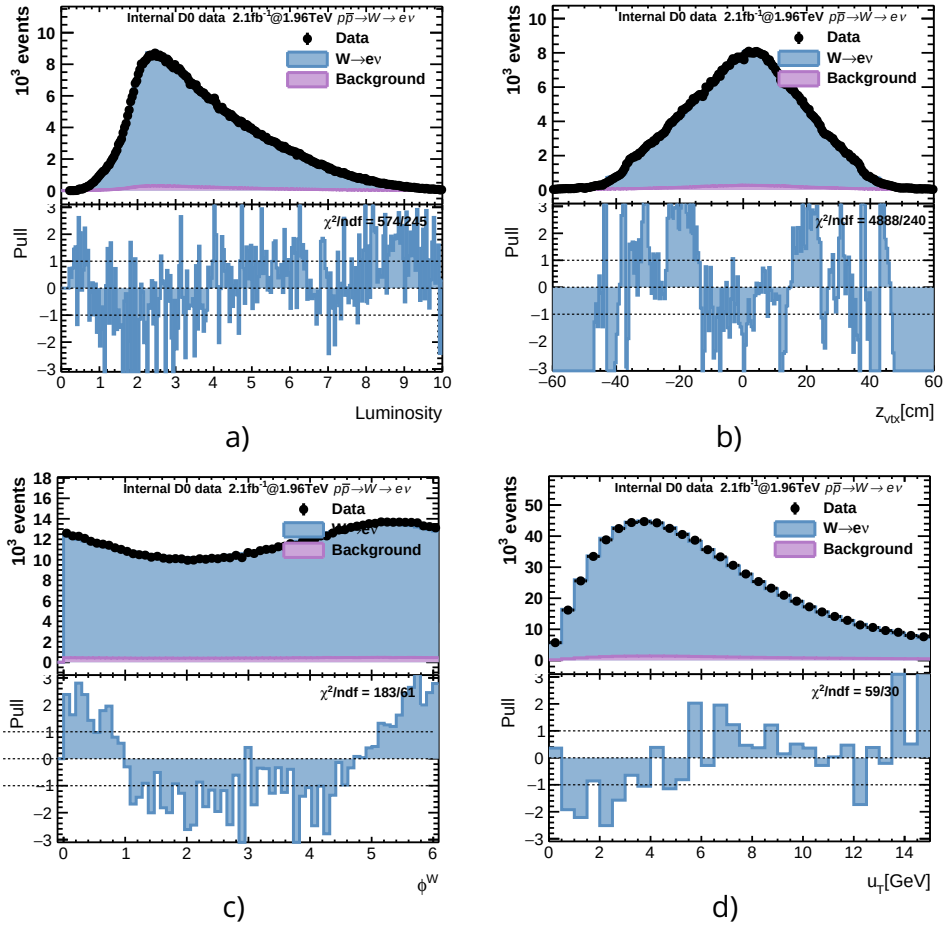

Figure B.1: *Comparison of measured (black points) and predicted (filled area) $W \to e\nu$ events with respect to instantaneous luminosity (a), z-vertex position (b), angular angle of W candidate (c), hadronic recoil (d).*

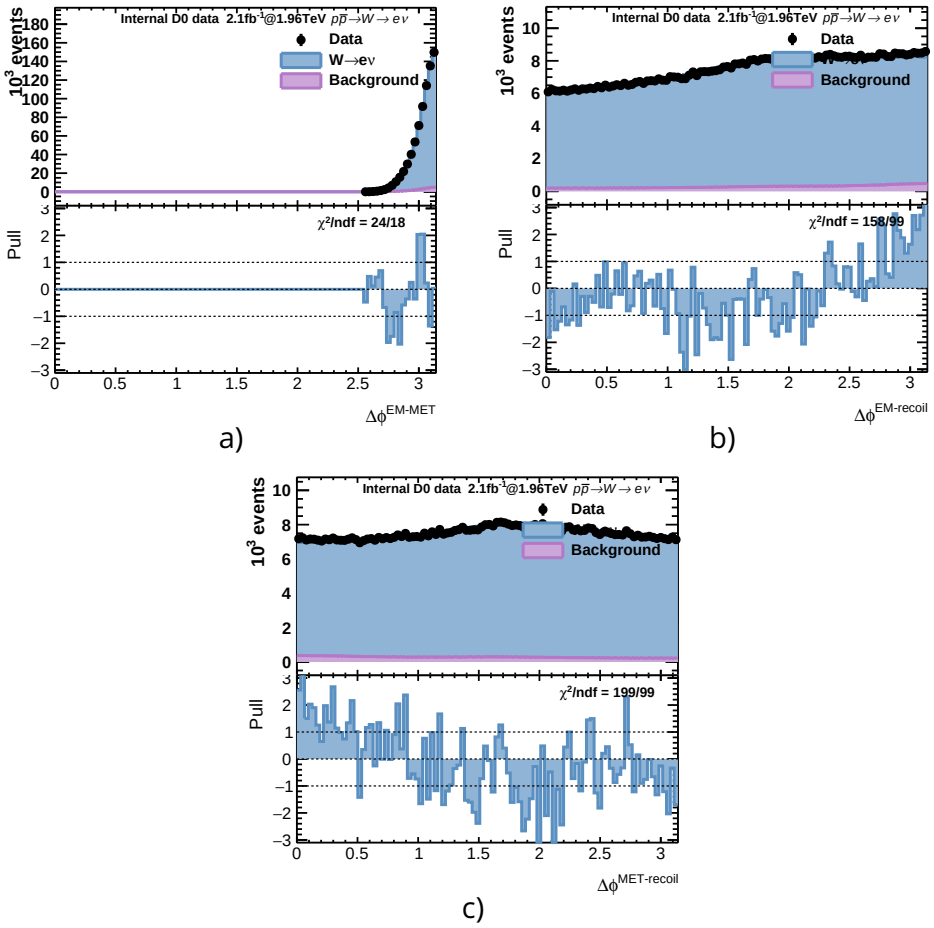

Figure B.2: *Comparison of measured (black points) and predicted (filled area) $W \to e\nu$ events with respect to angular difference between electron and missing transverse energy (a) angular difference between electron and hadronic recoil (b) angular difference between missing transverse and hadronic recoil (c)*

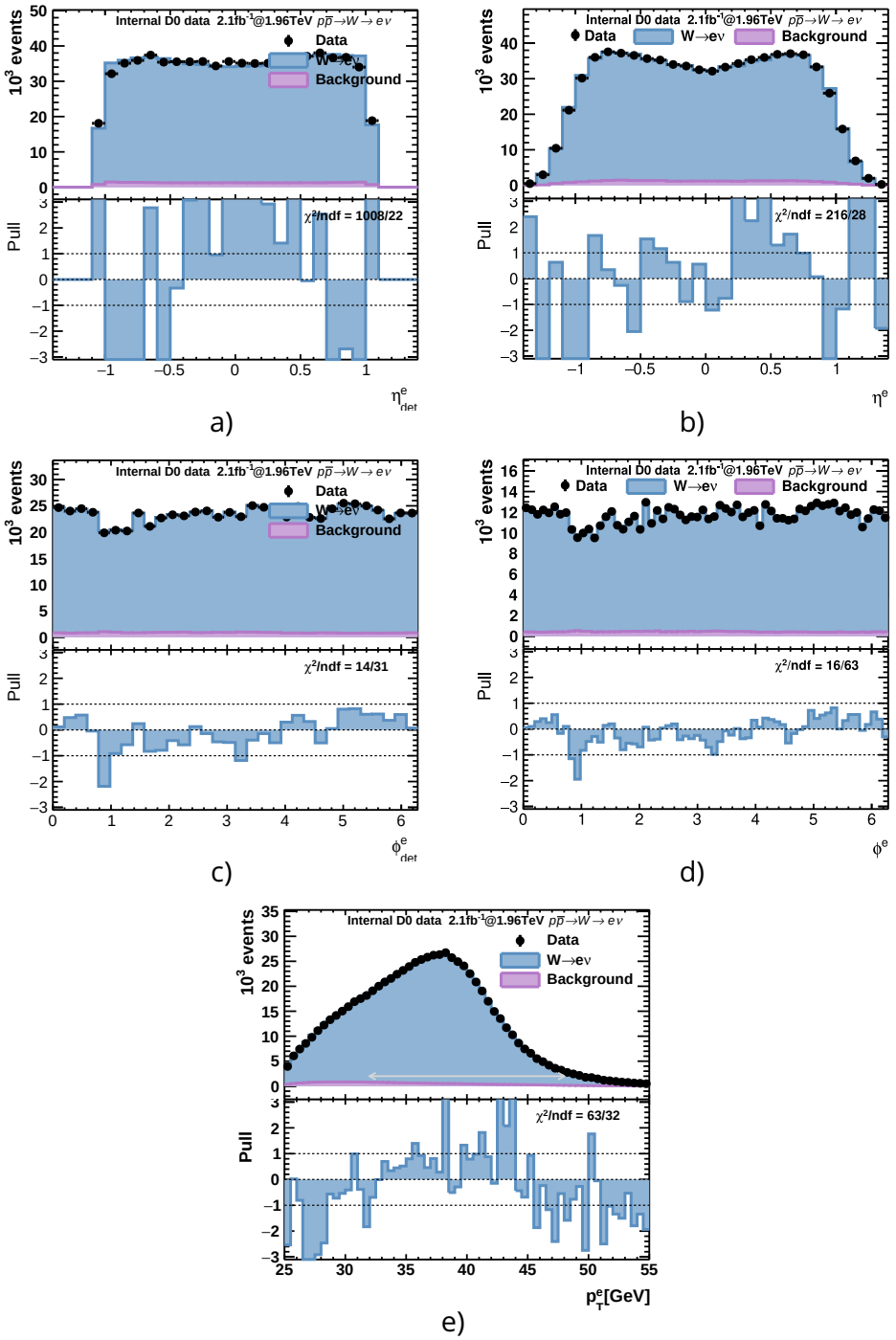

Figure B.3: *Comparison of measured (black points) and predicted (filled area) $W \to e\nu$ events with respect to electron pseudorapidity without (a) and with (b) detector level corrections, electron transverse angle without (c) and with (d) detector level corrections and electron transverse energy (e).*

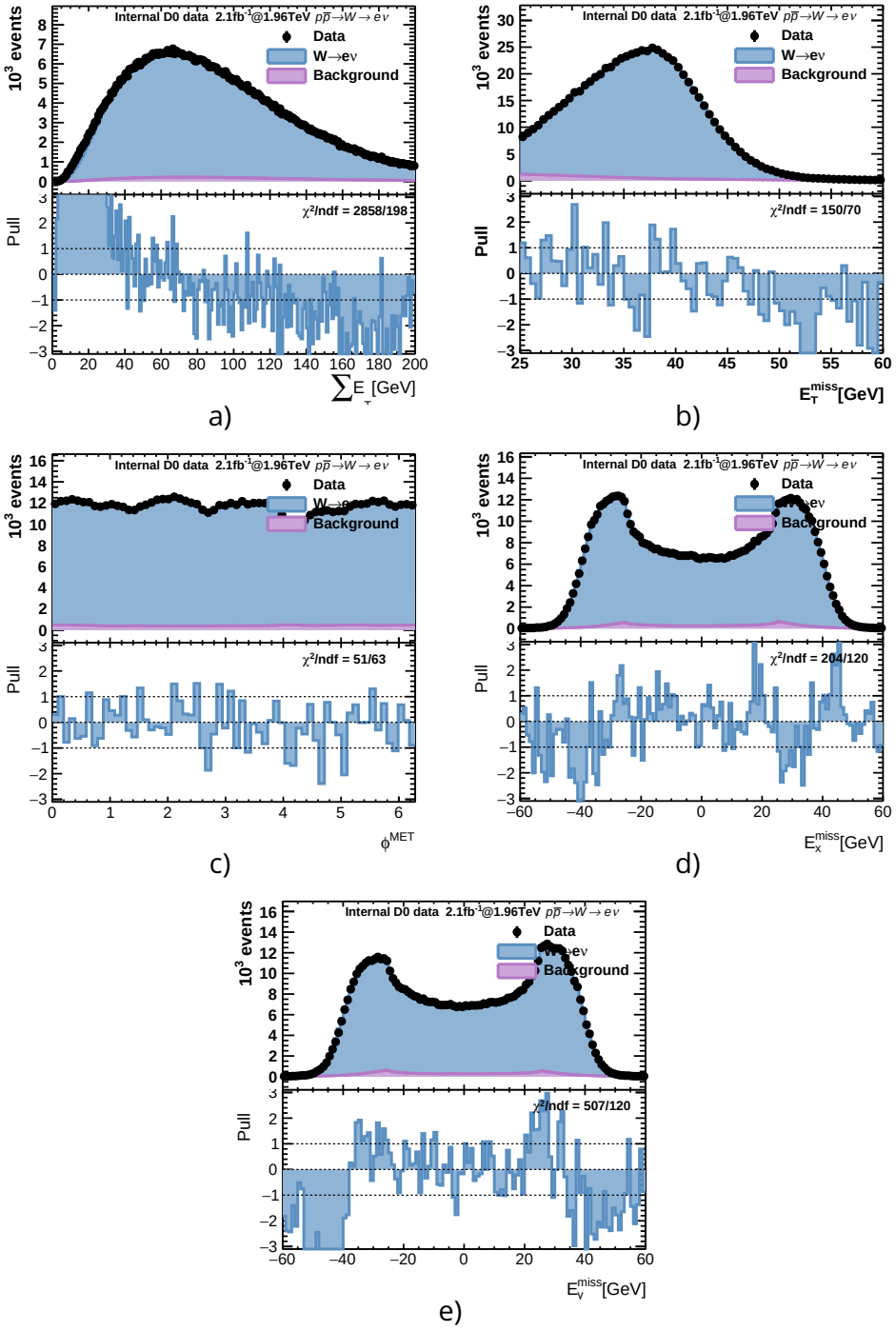

Figure B.4: *Comparison of measured (black points) and predicted (filled area) $W \to e\nu$ events with respect to scalar sum of deposited energy in calorimeter (a), missing transverse energy size (b), angle (c), x-component (d) and y-component (e).*

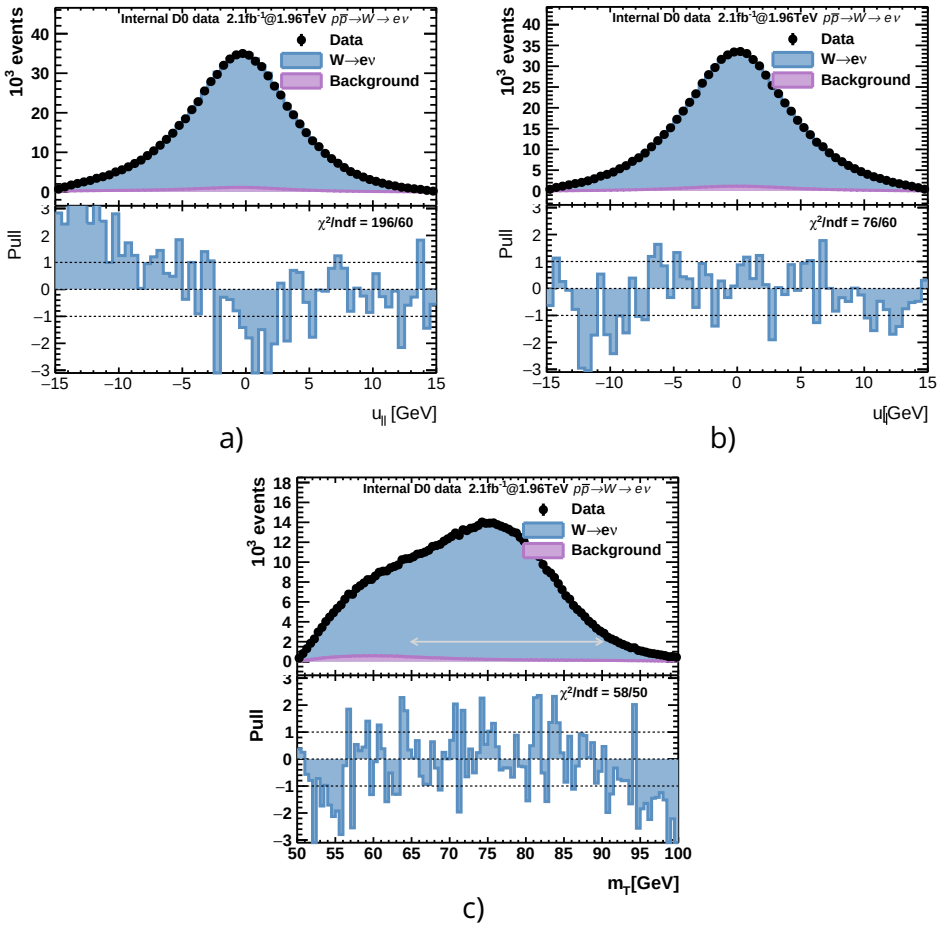

Figure B.5: *Comparison of measured (black points) and predicted (filled area) $W \to e\nu$ events with respect to hadronic recoil parallel projection (a), hadronic recoil perpendicular projection (b) and transversal mass of candidate (c).*

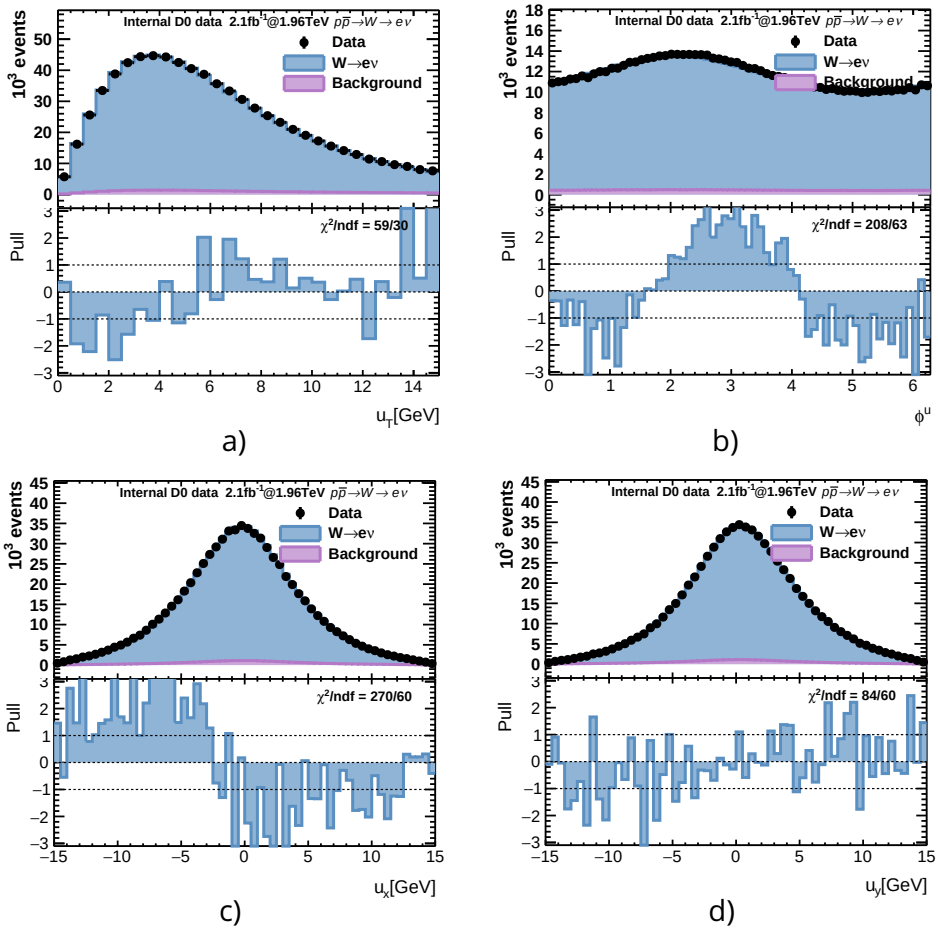

Figure B.6: *Comparison of measured (black points) and predicted (filled area) $W \to e\nu$ events with respect to hadronic recoil size (a) and its azimuthal angle (b) x-component (c) and y-component (d).*

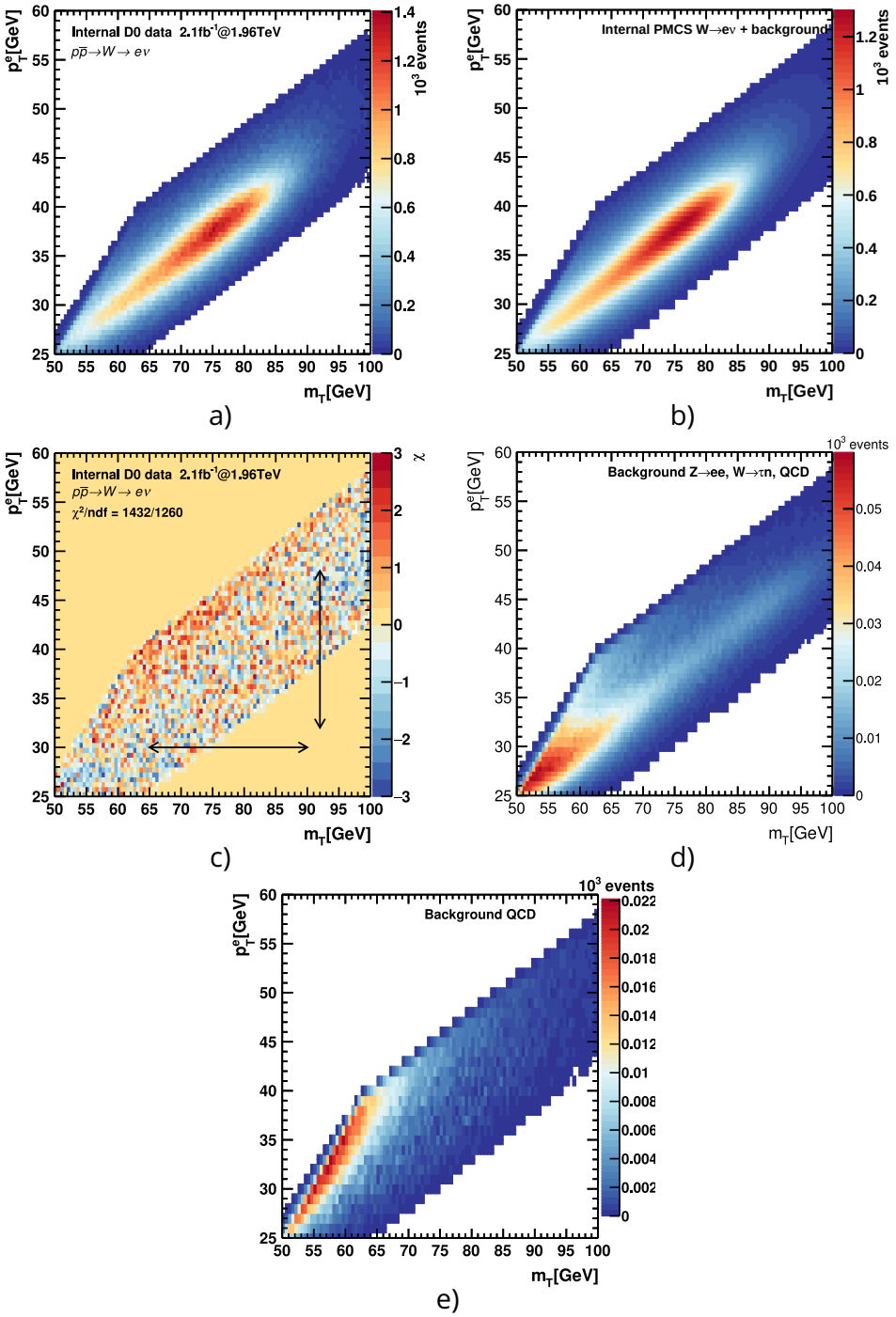

Figure B.7: *Measured (a) and predicted (b) two dimensional $m_{\mathrm{T}} - p_T$ distribution. Pull-plot comparing data and Monte-Carlo prediction with respect to $m_{\mathrm{T}} - p_T$ (c). Estimated total background (d) and multi-jet background (e) yields for two dimensional $m_{\mathrm{T}} - p_T$ distributions.*

B.2 Comparison of data from RunIIb3 with CT14nnlo

List of distribution showing the level of agreement between measured data and Monte-Carlo prediction is presented in this section. The predictions are done by PMCS using CT14nnlo PDF set. And the lower part of each figure shows pull-plot between data and prediction.

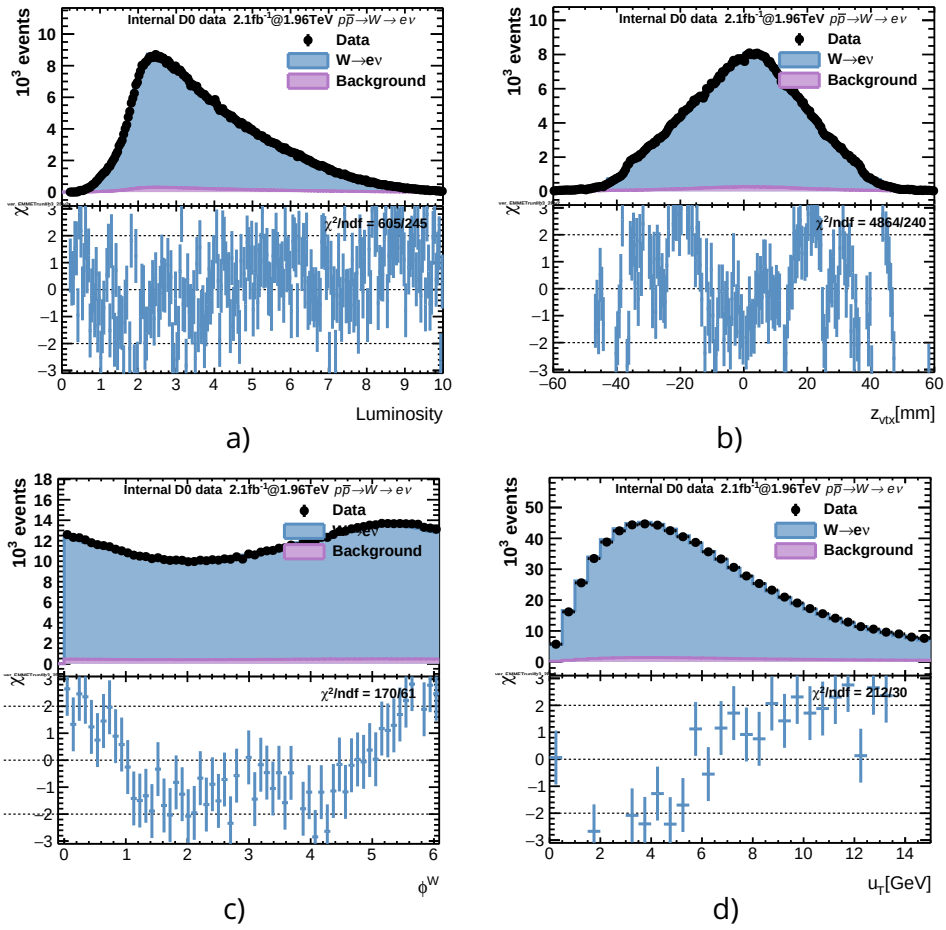

Figure B.8: *Comparison of measured (black points) and predicted (filled area) $W \to e\nu$ events with respect to instantaneous luminosity (a), z-vertex position (b), angular angle of W candidate (c), hadronic recoil (d).*

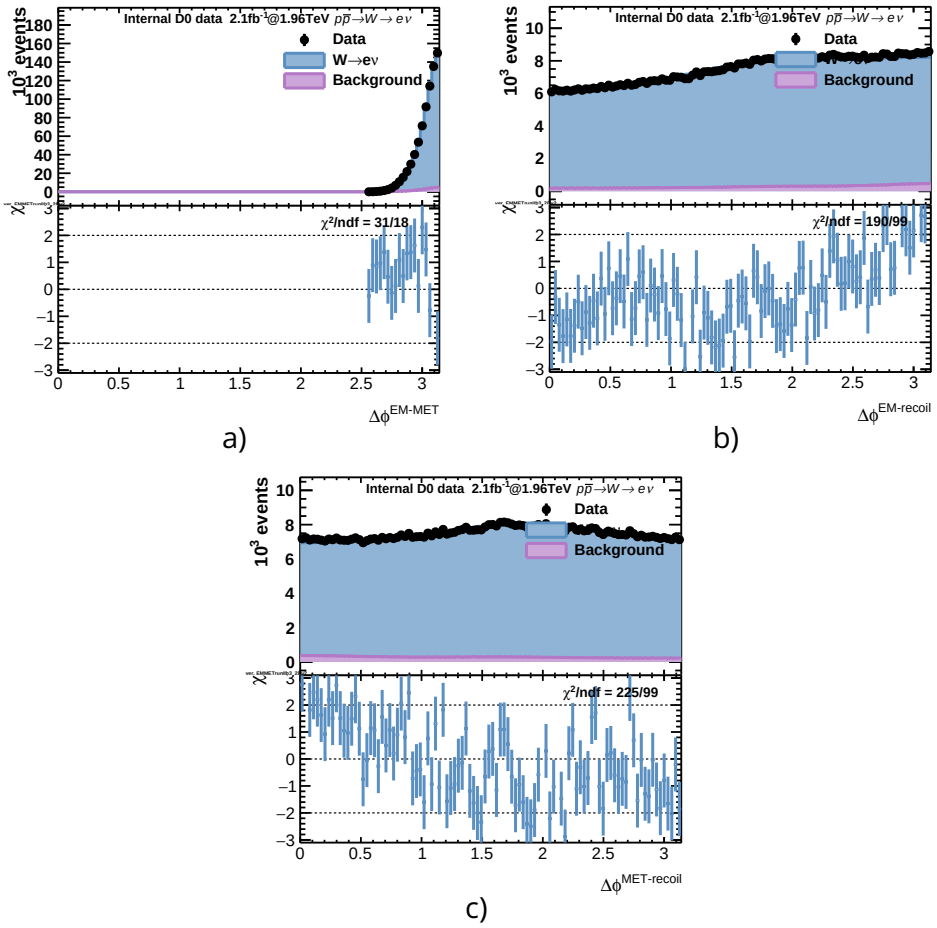

Figure B.9: *Comparison of measured (black points) and predicted (filled area) $W \to e\nu$ events with respect to angular difference between electron and missing transverse energy (a) angular difference between electron and hadronic recoil (b) angular difference between missing transverse and hadronic recoil (c)*

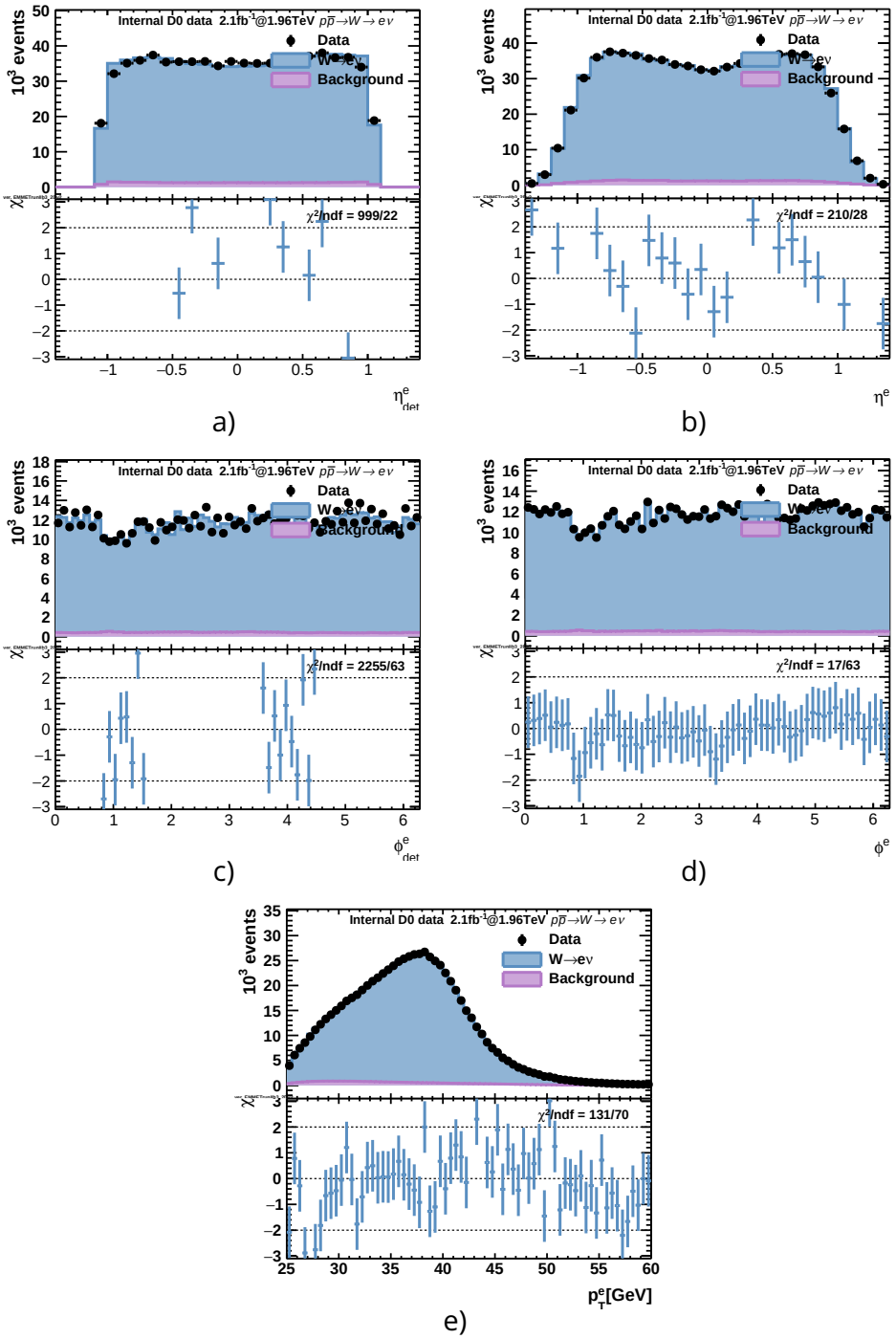

Figure B.10: *Comparison of measured (black points) and predicted (filled area) $W \to e\nu$ events with respect to electron pseudorapidity without (a) and with (b) detector level corrections, electron transverse angle without (c) and with (d) detector level corrections and electron transverse energy (e).*

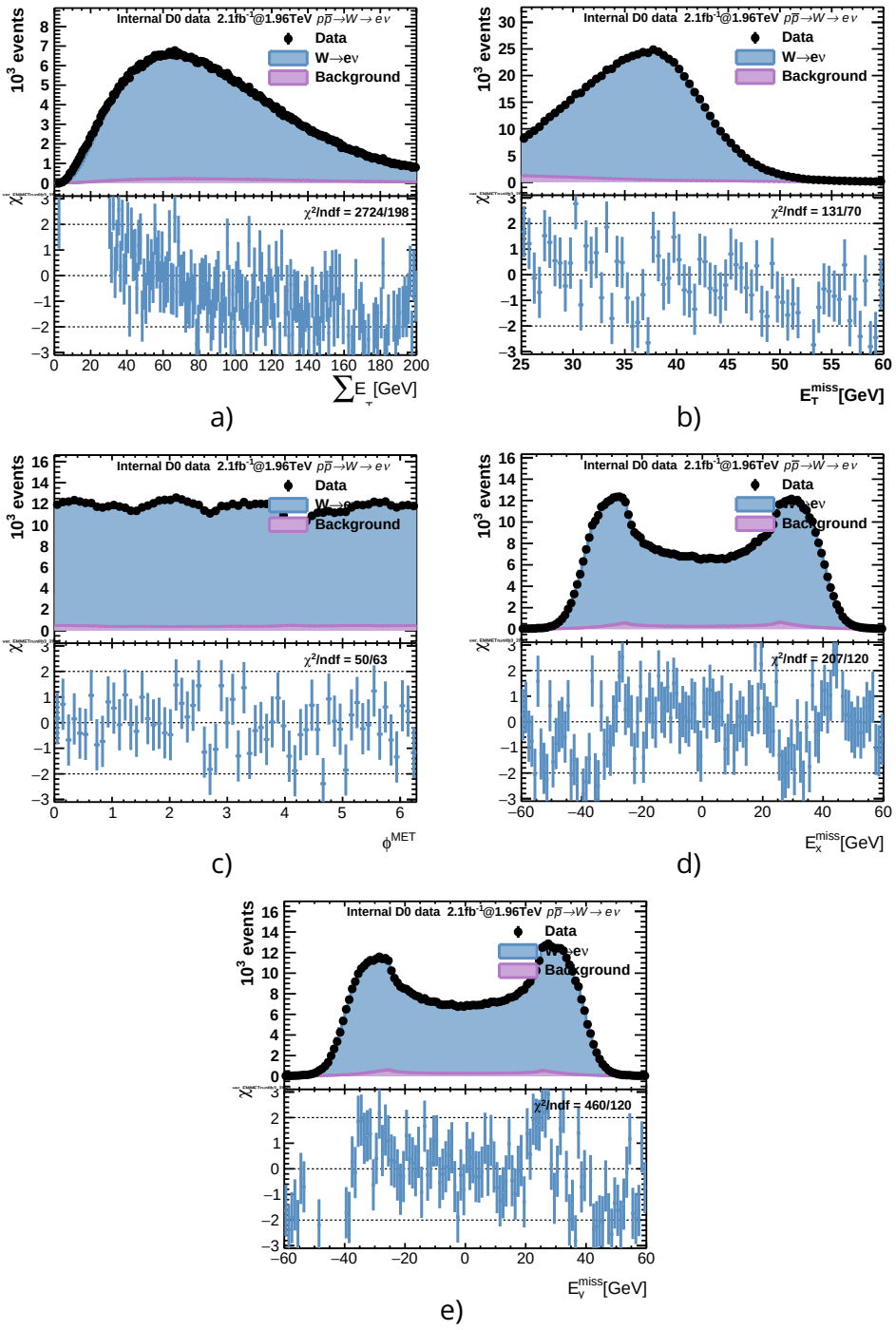

Figure B.11: *Comparison of measured (black points) and predicted (filled area) $W \to e\nu$ events with respect to scalar sum of deposited energy in calorimeter (a), missing transverse energy size (b), angle (c), x-component (d) and y-component (e).*

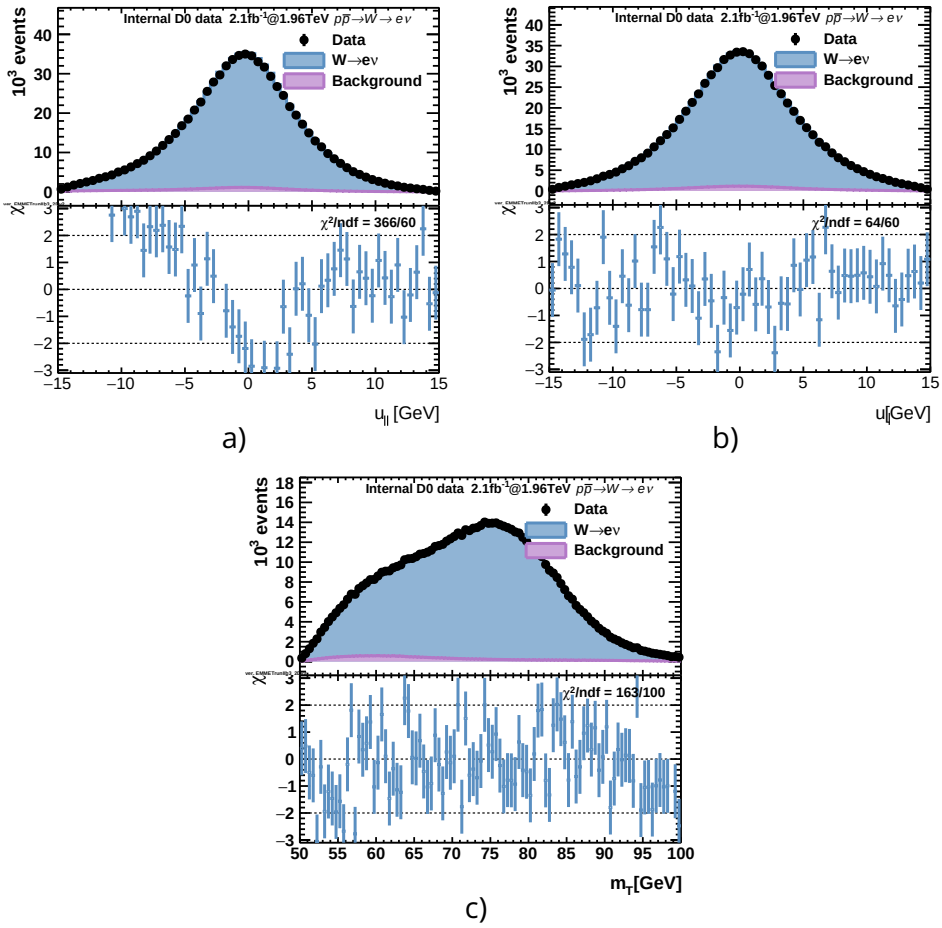

Figure B.12: *Comparison of measured (black points) and predicted (filled area) $W \to e\nu$ events with respect to hadronic recoil parallel projection (a), hadronic recoil perpendicular projection (b) and transversal mass of candidate (c).*

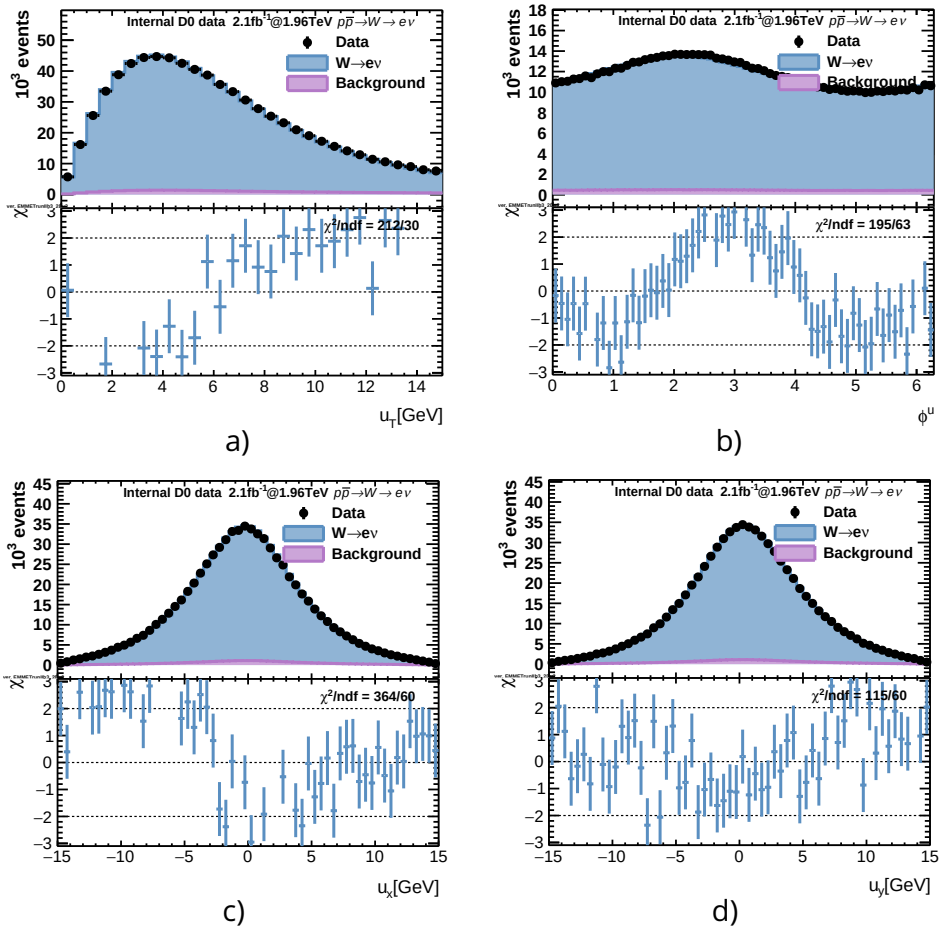

Figure B.13: *Comparison of measured (black points) and predicted (filled area) $W \to e\nu$ events with respect to hadronic recoil size (a) and its azimuthal angle (b) x-component (c) and y-component (d).*

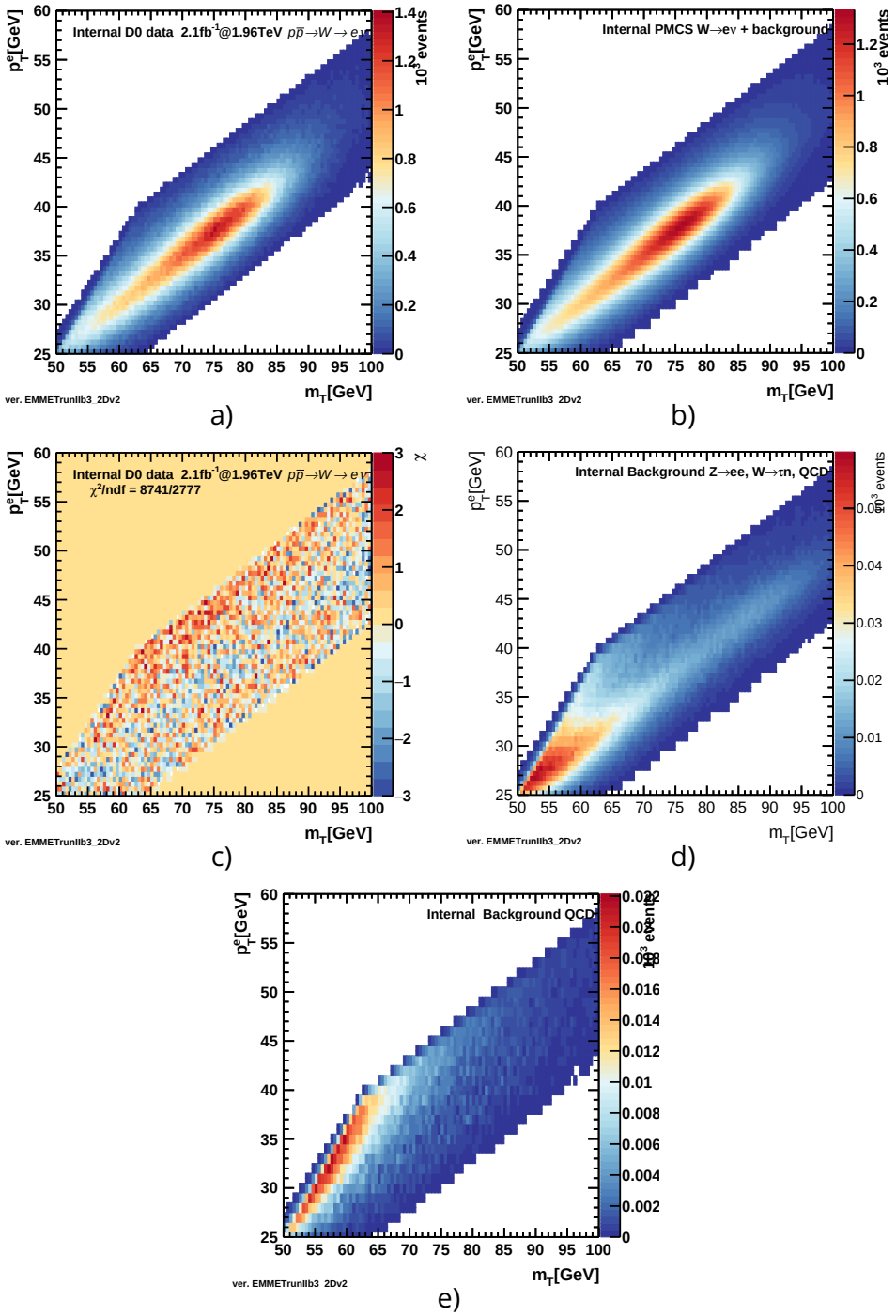

Figure B.14: *Measured (a) and predicted (b) two dimensional $m_{\mathrm{T}} - p_T$ distribution. Pull-plot comparing data and Monte-Carlo prediction with respect to $m_{\mathrm{T}} - p_T$ (c). Estimated total background (d) and multi-jet background (e) yields for two dimensional $m_{\mathrm{T}} - p_T$ distributions.*

C. W boson mass theory uncertainty plots

This appendix presents the additional plots for estimation of W boson mass uncertainty, which origins from internal structure of colliding hadrons.

C.1 Uncertainty estimated from CTEQ6.6

This section presents intermediate steps for calculating PDF uncertainty from CTEQ6.6.

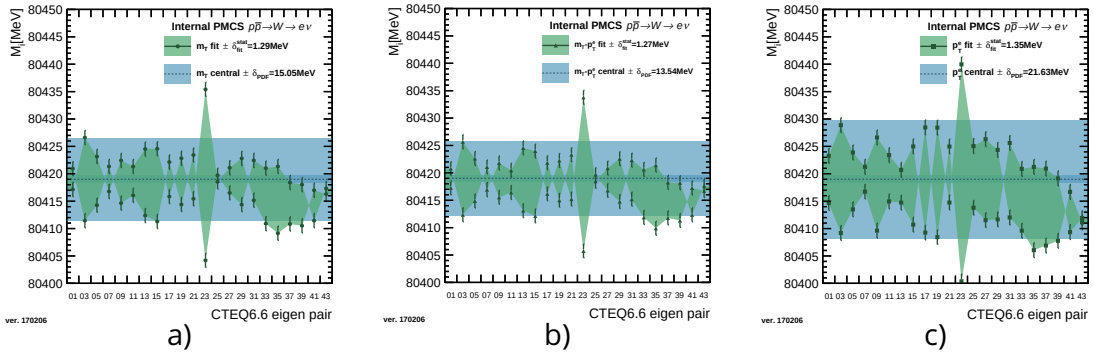

Figure C.1: *Fitted values of M_W with respect to PDF members for m_{T} (a), $m_{\mathrm{T}} - p_T$ (b) and p_{T} (c).*

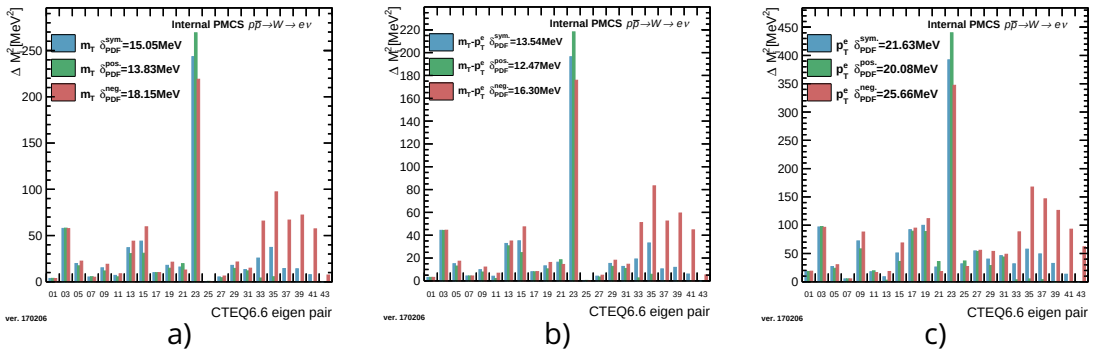

Figure C.2: *Squared contribution to total uncertainty with respect to PDF members for m_{T} (a), $m_{\mathrm{T}} - p_T$ (b) and p_{T} (c).*

pair	ilo	ihi	m_T lo	m_T hi	m_T Δ^2	p_T^e lo	p_T^e hi	p_T^e Δ^2	$m_T - p_T^e$ lo	$m_T - p_T^e$ hi	$m_T - p_T^e$ Δ^2
1	01	02	80417.12	80420.93	3.62	80423.27	80414.67	18.49	80417.26	80420.77	3.08
2	03	04	80426.62	80411.42	57.74	80428.88	80409.19	96.92	80425.66	80412.35	44.29
3	05	06	80423.16	80414.27	19.74	80423.89	80413.51	26.92	80422.62	80414.86	15.05
4	07	08	80416.77	80421.34	5.22	80421.27	80416.73	5.15	80416.94	80421.09	4.30
5	09	10	80422.42	80414.65	15.12	80426.62	80409.62	72.27	80421.80	80415.53	9.81
6	11	12	80421.32	80416.06	6.93	80423.40	80414.96	17.83	80420.47	80416.42	4.10
7	13	14	80424.52	80412.37	36.88	80420.70	80414.73	8.92	80424.55	80413.10	32.79
8	15	16	80424.56	80411.29	44.00	80424.99	80410.71	50.97	80423.99	80412.13	35.12
9	17	18	80415.85	80422.14	9.90	80409.26	80428.46	92.11	80416.16	80421.83	8.03
10	19	20	80422.83	80414.39	17.81	80428.42	80408.44	99.81	80422.26	80414.99	13.18
11	21	22	80415.43	80423.43	15.98	80414.75	80424.98	26.16	80415.22	80423.31	16.38
12	23	24	80435.41	80404.20	243.44	80439.98	80400.36	392.30	80433.78	80405.75	196.41
13	25	26	80418.53	80419.74	0.37	80425.07	80413.80	31.75	80418.46	80419.67	0.36
14	27	28	80421.10	80416.50	5.28	80426.32	80411.54	54.62	80420.86	80416.78	4.16
15	29	30	80422.81	80414.37	17.78	80424.35	80411.67	40.18	80422.58	80414.76	15.29
16	31	32	80415.16	80422.43	13.22	80412.02	80425.62	46.22	80415.19	80422.31	12.67
17	33	34	80410.90	80421.03	25.67	80409.61	80420.88	31.80	80411.87	80420.63	19.21
18	35	36	80409.14	80421.33	37.18	80406.06	80421.25	57.72	80409.89	80421.42	33.24
19	37	38	80410.83	80418.40	14.33	80406.89	80420.94	49.34	80411.77	80418.26	10.53
20	39	40	80410.50	80418.01	14.10	80407.77	80419.16	32.46	80411.30	80418.19	11.86
21	41	42	80416.99	80411.43	7.72	80416.69	80409.36	13.44	80417.24	80412.33	6.03
22	43	44	80416.29	80417.32	0.26	80411.13	80411.91	0.15	80416.73	80417.63	0.20

Table C.1: *Fitted values for each PDF member per each studied distribution.*

m_T [MeV]	p_T^e [MeV]	$m_T - p_T^e$ [MeV]
$15.05^{+13.83}_{-18.15}$	$21.63^{+20.08}_{-25.66}$	$13.54^{+12.47}_{-16.30}$

Table C.2: *Final value of estimated PDF uncertainties per studied distribution*

C.2 Uncertainty estimated from CTEQ6.6 profiled

This section presents intermediate steps for calculating PDF uncertainty from profiled CTEQ6.6.

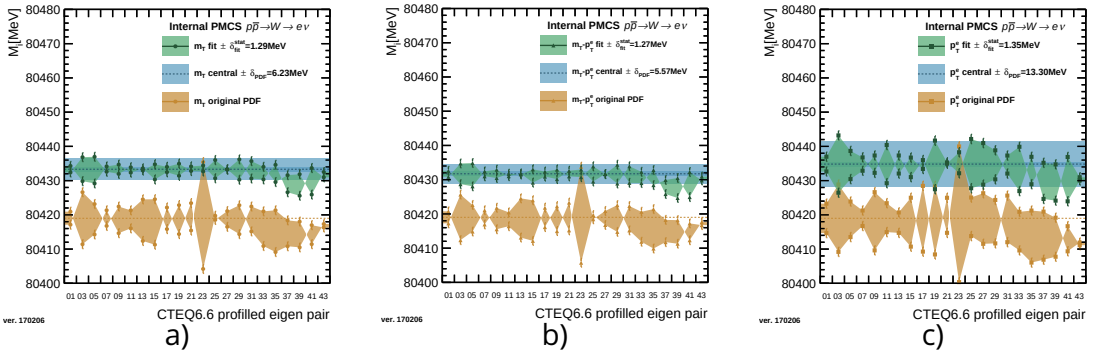

Figure C.3: *Fitted values of M_W with respect to PDF members for m_T (a), $m_T - p_T$ (b) and p_T (c).*

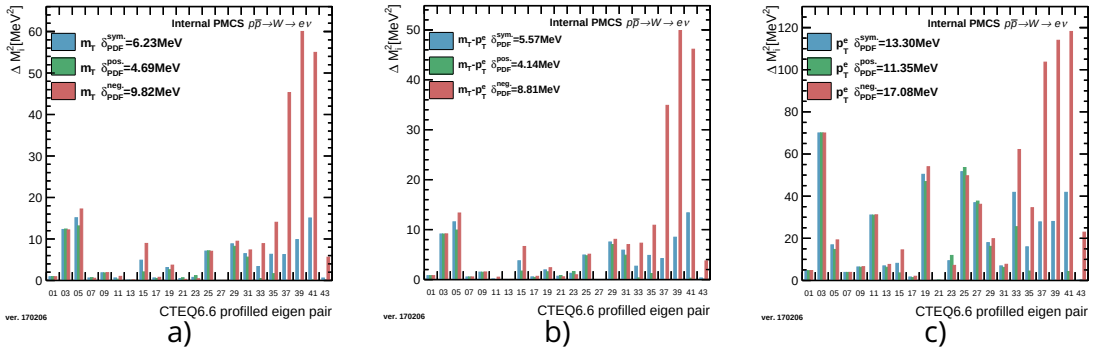

Figure C.4: *Squared contribution to total uncertainty with respect to PDF members for m_{T} (a), $m_{\mathrm{T}} - p_T$ (b) and p_{T} (c).*

pair	ilo	ihi	m_T lo	m_T hi	m_T Δ^2	p_T^e lo	p_T^e hi	p_T^e Δ^2	$m_T - p_T^e$ lo	$m_T - p_T^e$ hi	$m_T - p_T^e$ Δ^2
1	01	02	80432.38	80434.29	0.91	80436.98	80432.66	4.67	80430.84	80432.60	0.78
2	03	04	80436.85	80429.84	12.29	80443.20	80426.46	70.00	80434.74	80428.70	9.13
3	05	06	80436.95	80429.18	15.12	80438.67	80430.44	16.91	80434.87	80428.07	11.56
4	07	08	80432.60	80434.15	0.60	80436.78	80432.87	3.82	80431.00	80432.44	0.52
5	09	10	80431.96	80434.68	1.85	80432.27	80437.33	6.41	80430.49	80432.93	1.49
6	11	12	80433.90	80432.33	0.61	80440.40	80429.25	31.07	80431.74	80431.03	0.13
7	13	14	80432.95	80433.57	0.10	80432.07	80437.33	6.93	80431.54	80431.83	0.02
8	15	16	80434.77	80430.34	4.90	80436.72	80431.02	8.13	80433.03	80429.15	3.76
9	17	18	80434.02	80432.45	0.62	80433.41	80435.99	1.66	80432.38	80430.92	0.54
10	19	20	80434.94	80431.41	3.12	80441.68	80427.48	50.38	80432.97	80430.18	1.94
11	21	22	80432.81	80434.14	0.44	80435.30	80434.96	0.03	80430.98	80432.62	0.67
12	23	24	80432.68	80434.41	0.75	80432.15	80438.28	9.37	80430.75	80432.99	1.26
13	25	26	80436.00	80430.67	7.09	80442.15	80427.78	51.62	80433.90	80429.47	4.92
14	27	28	80433.20	80433.34	0.01	80440.97	80428.82	36.91	80431.63	80431.66	0.00
15	29	30	80436.20	80430.25	8.84	80438.85	80430.38	17.96	80434.37	80428.88	7.53
16	31	32	80430.62	80435.70	6.46	80432.06	80437.32	6.93	80429.08	80433.93	5.89
17	33	34	80430.35	80434.01	3.36	80426.95	80439.88	41.83	80429.02	80432.30	2.68
18	35	36	80434.61	80429.58	6.32	80436.95	80428.95	15.98	80432.82	80428.42	4.83
19	37	38	80426.60	80431.60	6.25	80424.65	80435.20	27.81	80425.82	80429.92	4.20
20	39	40	80425.58	80431.86	9.85	80424.15	80434.74	28.00	80424.66	80430.49	8.48
21	41	42	80433.68	80425.91	15.07	80436.89	80423.96	41.83	80432.24	80424.93	13.36
22	43	44	80430.96	80432.50	0.60	80430.98	80430.04	0.22	80429.79	80430.92	0.32

Table C.3: *Fitted values for each PDF member per each studied distribution.*

m_T [MeV]	p_T^e [MeV]	$m_T - p_T^e$ [MeV]
$6.23^{+4.69}_{-9.82}$	$13.30^{+11.35}_{-17.08}$	$5.57^{+4.14}_{-8.81}$

Table C.4: *Final value of estimated PDF uncertainties per studied distribution*

C.3 PDF CT14nnlo

This section presents intermediate steps for calculating PDF uncertainty from CT14nnlo.

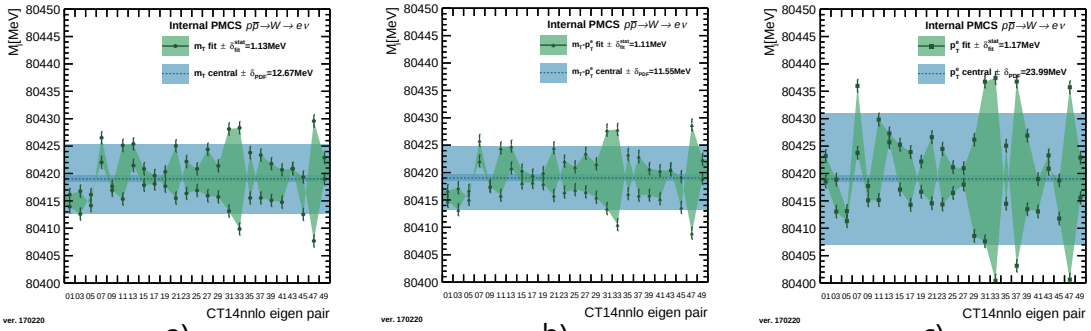

Figure C.5: *Fitted values of M_W with respect to PDF members for m_{T} (a), $m_{\mathrm{T}}-p_T$ (b) and p_{T} (c).*

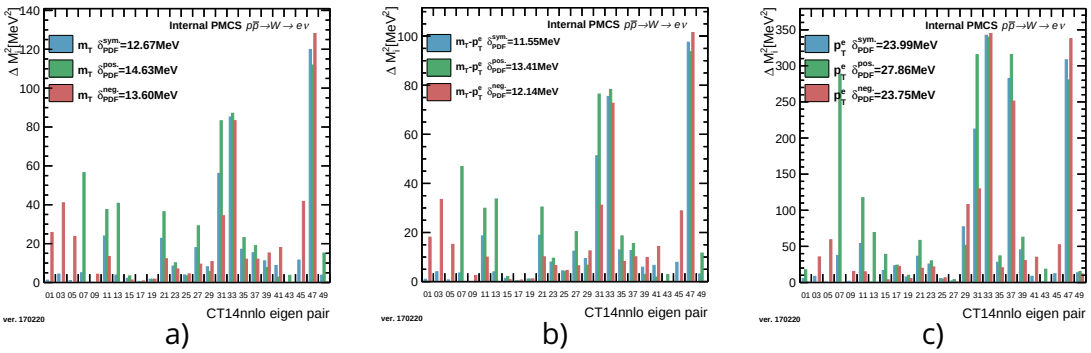

Figure C.6: *Squared contribution to total uncertainty with respect to PDF members for m_{T} (a), $m_{\mathrm{T}}-p_T$ (b) and p_{T} (c).*

pair	ilo	ihi	m_T lo	m_T hi	m_T Δ^2	p_T^e lo	p_T^e hi	p_T^e Δ^2	$m_T - p_T^e$ lo	$m_T - p_T^e$ hi	$m_T - p_T^e$ Δ^2
1	01	02	80413.92	80416.14	1.23	80418.55	80423.19	5.40	80414.75	80416.70	0.95
2	03	04	80412.60	80416.77	4.35	80413.05	80418.88	8.52	80413.22	80417.23	4.01
3	05	06	80416.13	80414.13	1.00	80411.31	80413.13	0.83	80416.79	80415.12	0.70
4	07	08	80422.03	80426.52	5.03	80423.74	80435.99	37.49	80422.11	80425.86	3.52
5	09	10	80416.93	80417.62	0.12	80415.09	80417.71	1.71	80417.44	80417.65	0.01
6	11	12	80415.34	80425.13	23.93	80415.15	80429.84	53.92	80415.85	80424.48	18.61
7	13	14	80421.46	80425.38	3.85	80425.69	80427.32	0.66	80420.83	80424.81	3.96
8	15	16	80417.87	80420.85	2.22	80417.07	80425.24	16.68	80418.13	80420.44	1.33
9	17	18	80418.08	80419.62	0.59	80414.28	80423.91	23.18	80418.20	80419.55	0.46
10	19	20	80420.30	80417.69	1.71	80422.17	80416.64	7.63	80420.01	80417.96	1.06
11	21	22	80425.03	80415.50	22.72	80426.64	80414.57	36.41	80424.52	80415.83	18.88
12	23	24	80416.36	80422.18	8.48	80414.36	80424.48	25.60	80416.46	80422.10	7.96
13	25	26	80416.89	80420.84	3.89	80416.44	80421.15	5.53	80416.88	80421.05	4.36
14	27	28	80415.92	80424.40	17.96	80417.97	80420.97	2.24	80416.48	80423.52	12.41
15	29	30	80415.71	80421.39	8.06	80408.61	80426.17	77.10	80415.47	80421.60	9.37
16	31	32	80413.14	80428.12	56.15	80407.61	80436.76	212.37	80413.43	80427.75	51.28
17	33	34	80409.87	80428.33	85.17	80400.43	80437.43	342.25	80410.49	80427.86	75.44
18	35	36	80423.81	80415.53	17.13	80425.07	80414.48	28.05	80423.33	80416.14	12.90
19	37	38	80415.53	80423.35	15.30	80403.15	80436.77	282.50	80415.83	80422.95	12.66
20	39	40	80415.10	80421.77	11.13	80413.48	80426.92	45.14	80415.88	80420.72	5.87
21	41	42	80414.76	80420.68	8.77	80413.08	80418.98	8.71	80415.23	80420.37	6.61
22	43	44	80420.92	80420.86	0.00	80420.85	80423.30	1.50	80420.70	80420.45	0.02
23	45	46	80412.54	80419.34	11.55	80418.73	80411.77	12.11	80413.64	80419.25	7.86
24	47	48	80429.58	80407.68	119.86	80435.75	80400.63	308.36	80428.69	80408.94	97.53
25	49	50	80422.89	80418.99	3.81	80422.91	80415.56	13.51	80422.42	80418.89	3.11

Table C.5: *Fitted values for each PDF member per each studied distribution.*

m_T [MeV]	p_T^e [MeV]	$m_T - p_T^e$ [MeV]
$12.67^{+14.63}_{-13.60}$	$23.99^{+27.86}_{-23.75}$	$11.55^{+13.41}_{-12.14}$

Table C.6: *Final value of estimated PDF uncertainties per studied distribution*

D. CTEQ 6.6 profiling control plots

This appendix contains additional plots and results of the CTEQ6.6 profiling procedure.

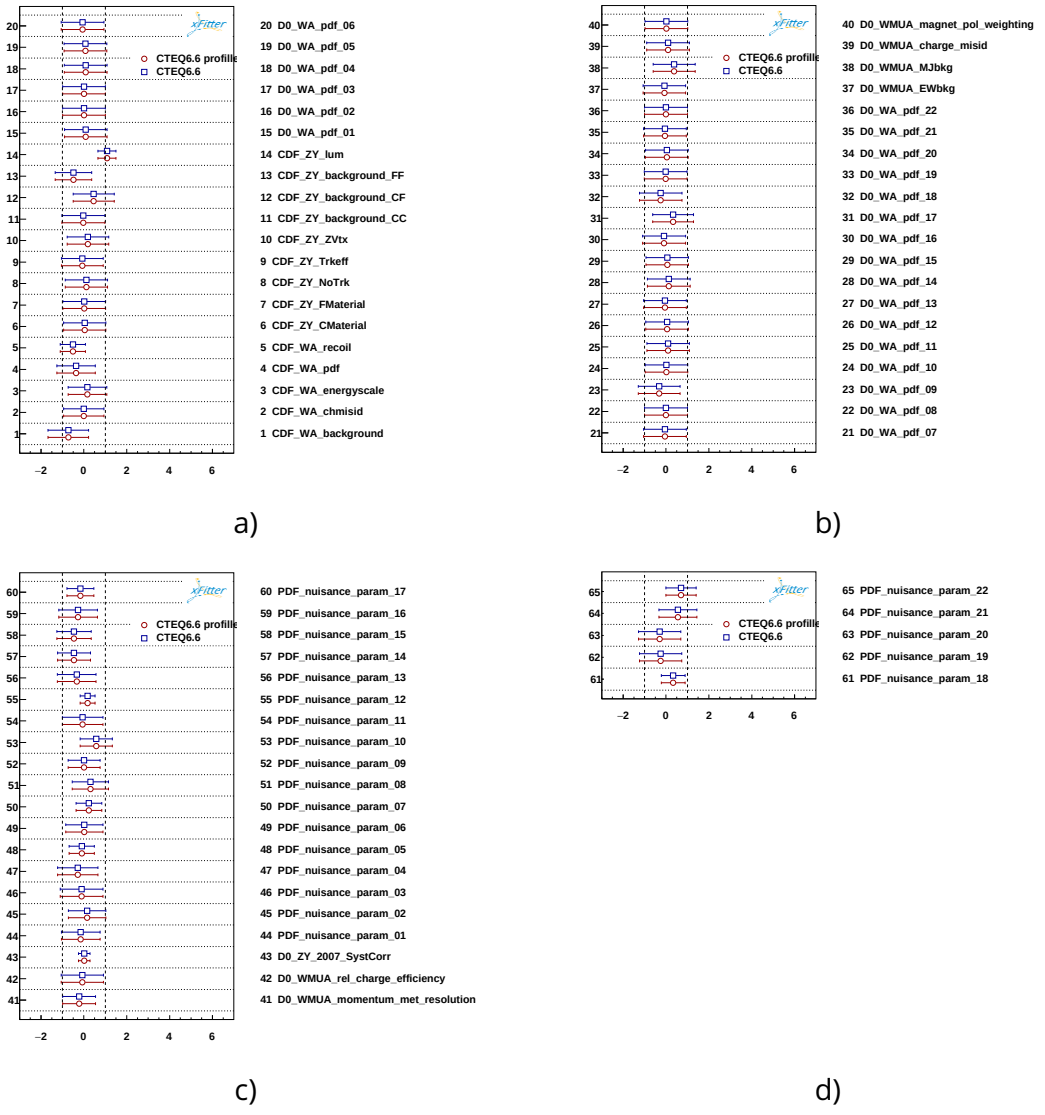

Figure D.1: *Pull-plot for profiling result values of fitted and input parameters.*

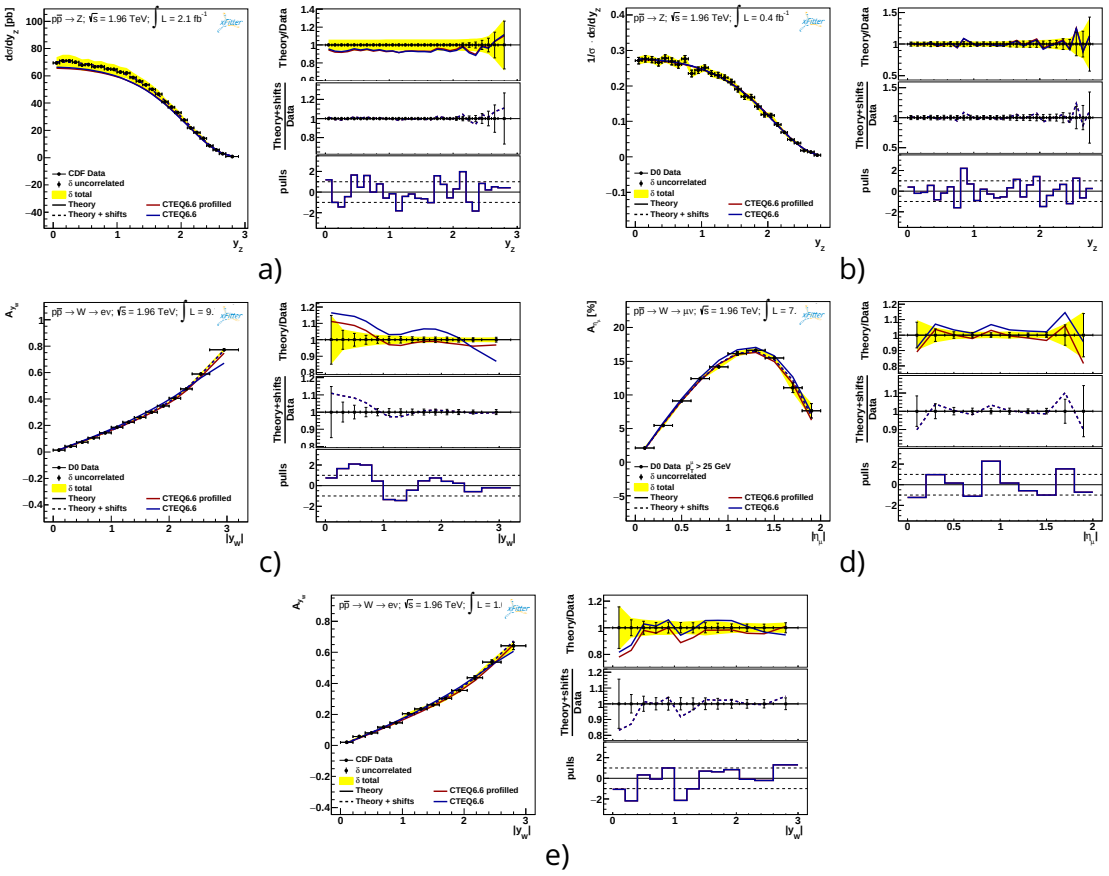

Figure D.2: *Prediction with original and profiled PDF is compared to input data from CDF Z rapidity (a), Do Z rapidity (b), Do W asymmetry (c), Do $W \to \mu\nu$ lepton asymmetry (d) and CDF W asymmetry (e) measurement.*

Dataset	CTEQ6.6 profilled	CTEQ6.6
CDF Z rapidity 2010	29 / 28	29 / 28
Do Z rapidity 2007	22 / 28	22 / 28
Do W asymmetry 2013	14 / 14	14 / 14
Do $W \to \mu\nu$ lepton asymmetry $p_{\mathrm{T}}^{\ell} > 25$ GeV	13 / 10	13 / 10
CDF W asymmetry 2009	16 / 13	16 / 13
Correlated χ^2	3.2	5.5
Log penalty χ^2	-1.52	-1.52
Total χ^2 / dof	96 / 93	98 / 93
χ^2 p-value	0.40	0.34

Table D.1: *Minimization result χ^2 agreement between data and predictions from nominal and profiled PDF*

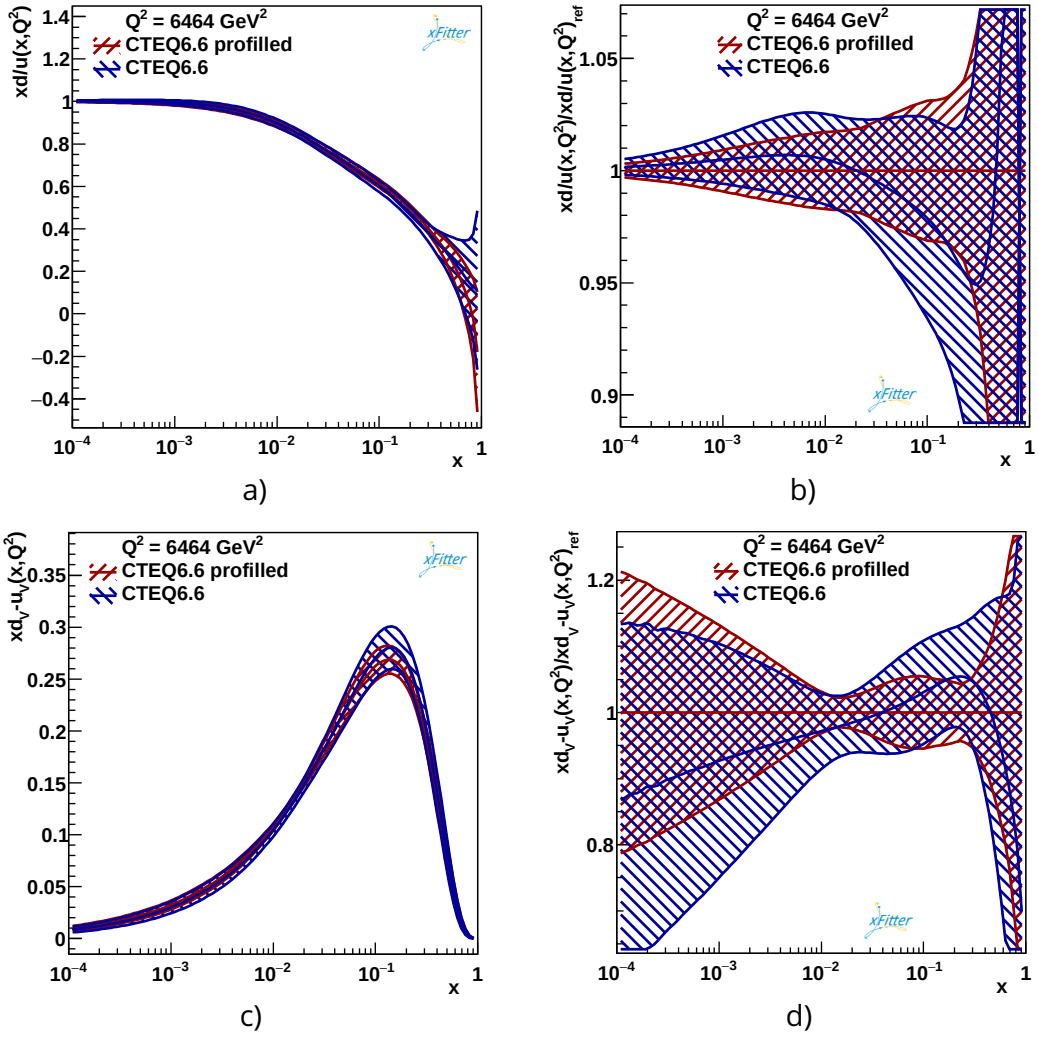

Figure D.3: *Comparison of original (blue) and profiled (red) PDF with respect to Bjorken-x at $Q^2 = M_W^2$. Compared distributions are: ratio d/u quark parton function (a), double ratio of d/u functions (b), difference $d - u$ functions (c) and ratio of $d - u$ difference (d).*